This is to certify that the

dissertation entitled

Microwave Processing of Epoxy Resins and Graphite Fiber/Epoxy Composites in a Cylindrical Tunable Resonant Cavity

presented by

Jianghua Wei

has been accepted towards fulfillment of the requirements for

Ph.D. degree in Chemical Engineering

Major professor

Date 11/6/92

DATE DUE	DATE DUE	DATE DUE
JUN 1 3 1998 S27 26		
FEB 0 7 1996		
249 JUN 0 9 1996		
070201 JUN 1 4 2001 121 0844		
NOV 2 8 2007 0825 07		

Microwave Processing of Epoxy Resins and Graphite Fiber/Epoxy Composites in a Cylindrical Tunable Resonant Cavity

By

Jianghua Wei

A DISSERTATION

Submitted to

Michigan State University

in partial fulfillment of the requirement

for the degree of

DOCTOR OF PHILOSOPHY

Department of Chemical Engineering

1992

ABSTRACT

Microwave Processing of Epoxy Resins and Graphite Fiber/Epoxy Composites in a Cylindrical Tunable Resonant Cavity

By

Jianghua Wei

This dissertation presents a systematic study for the use of microwave energy as an alternative to thermal energy in the processing of polymers and composites, including the results of the neat resin study, various microwave processing technique, and processing model.

In the cure study of neat epoxy resins, two stoichiometric epoxy/amine systems were studied, diglycidyl ether of bisphenol A (DGEBA, Dow Chemical DER 332) with diaminodiphenyl sulfone (DDS, Aldrich Chemical) and DGEBA with meta phenylene diamine (MPDA, Aldrich Chemical). Comparative isothermal cures were conducted using microwave and thermal energy. Compared to thermal cure, microwave cure increased reaction rates and glass transition temperature of both DGEBA/DDS and DGEBA/mPDA systems. The increase is much more significant in the DGEBA/DDS system than in the DGEBA/mPDA system. The microwave and thermal cure of both systems were successfully described by second order autocatalytic reaction kinetics.

Batch, scale up of batch, and continuous processing techniques were also studied using microwave energy. In the study of batch processing, 24-ply Hercules AS4/3501-6 graphite fiber/epoxy laminates were processed in a 17.78 cm diameter cylindrical tunable resonant cavity using 2.45 GHz microwave radiation. The temperature uniformity across the laminate was a strong function of the electromagnetic (EM) heating modes. With proper choice of the heating mode, 3.8 cm thick composites were uniformly heated. The mechanical properties of microwave processed composites were higher than those of

thermally processed samples using similar processing temperature cycles. Better bonding between the graphite fibers and the matrix was observed in the microwave processed composites than in the thermally processed samples. The scale up of batch processing was studied using a 17.78 cm cavity with 2.45 GHz microwave radiation and a 45.72 cm cavity with 915 MHz microwave radiation. For low to medium loss materials, the location of a given resonant mode can be scaled up accordingly, that is with the same electromagnetic field pattern and the heating characteristics, when every dimensions of the sample was scaled by the scale-up factor of the cavities. A unique microwave applicator was invented for continuous processing of conductor and nonconductor reinforced composites using microwave energy without microwave leakage.

A five parameter microwave power absorption model and a one dimensional composite processing model were developed. The process model was numerically coded use FORTRAN and used in various simulations of microwave and thermal processing. Simulation results show that: 1) the thickest Hercules AS4/3501-6 composite that can be processed using the manufacture's cure cycle is 4 cm, 2) good heat convection at the composite surface is very important in reducing the temperature excursion during thermal processing, 3) microwave processing is much better than thermal processing in process controllability, process speed, and temperature uniformity inside the composite.

To my wife

Qianqian

ACKNOWLEDGEMENT

I wish to thank Prof. Martin C. Hawley for his wisdom and guidance during the course of this research. Thanks are also extended to Prof. Dennis Nyquist and Dr. Jinder Jow for their many discussions and valuable suggestions, and to Mr. Brook Thomas for his proofreading of the dissertation. Finally, I would like to thank my wife for her understanding, caring, support, and endless love through the duration of this work.

This research was supported in part by DARPA.

TABLE OF CONTENTS

LIST OF TABLES

LIST OF FIGURES

CHAPTER 1
INTRODUCTION

Because of their superior specific properties and high performance, graphite fiber reinforced epoxy composites are widely used in aerospace, military, recreation, transportation, and other industries [1,2]. This type of composite is usually processed in the autoclave by first arranging uncured prepreg into a designed shape and then curing at elevated temperatures and pressures using thermal energy. However, autoclave curing requires long cure cycles, such as 4.5 to 8.5 hours for Hercules AS4/3501-6 composites, and even this long cure cycle is only suitable for thin parts because of the nature of thermal heating and large exotherm resulting from the polymerization reaction. To shorten the processing time and to process thick-section composites, new processing techniques need to be developed.

1.1 Characteristics of Microwave and Thermal Heating

Thermal heating is characterized by surface-driven, non-selective heating. The heating efficiency is controlled by the heat transfer coefficient at composite surface and the thermal conductivity of the composite. During processing, the heat front moves from the surface to the interior of the composite. For thermoset polymers, the heat initiates the exothermic polymerization reaction. The thermoset undergoes liquefaction, gelation and vitrification as the reaction proceeds. The direction of the heat front represents, to a certain degree, the direction of the vitrification front. Once the thermoset matrix reaches vitrification, the extra resin and trapped gases in the interior will remain inside the composite. This processing drawback will reduce the mechanical properties of the processed composites. Also as the polymerization of thermoset is a strong exothermic reaction, the exotherm not only accelerates the movement of the heat front, but also creates a large temperature excursion in the

interior of the composite. The temperature excursion in the interior may cause thermal degradation of the matrix. To reduce the temperature excursion and remove the extra resin, slow heating rates and long cure cycles with several relatively low soak temperatures are required. The temperature excursion can be eliminated if the heat source can be readily removed when the thermal excursion occurs, which is impossible during thermal processing.

To overcome the disadvantages of thermal heating, microwave heating has been studied as an alternative in the processing of polymer composites [3-38]. Table 1.1 shows one-to-one comparison between microwave and thermal heating characteristics.

Table 1.1 Comparison of Microwave and Thermal Heating Characteristics

	Thermal Heating	Microwave Heating
Heating Rate	SLOW, Controlled by heat transfer	FAST, Direct coupling of energy into molecules
Selectivity	NO, Heating is due to the temperature gradient	YES, Heating is proportional to material loss factor and input power
Heat Movement	OUT TO IN, Surface driven heating from hot to cold	IN TO OUT, Volumetric heating with boundary heat loss
Controllability	NO, Heat source can't be readily controlled.	YES, Microwave energy can be readily removed

The advantages of microwave heating over thermal heating in Table 1.1 can be easily explained by microwave power absorption in the material. The power absorption rate, P, (in W/m^3) inside a homogeneous material is [7]

$$P = \frac{1}{2} \epsilon_0 \epsilon'' \omega \, |\vec{E}|^2 \qquad (1\text{-}1)$$

where $\vec{E}$ is the electric field strength inside the material, V/m.

ω is the frequency, rad/sec. $\omega = 2\pi f$, f is the frequency Hz.

ϵ_0 is the permittivity of free space, $\epsilon_0 = 1/(36\pi) \times 10^{-9}$ F/m.

ϵ' is the effective relative loss factor, $\epsilon' = \epsilon_d' + \sigma/(\epsilon_0 \omega)$,

ϵ_d' is relative loss factor due to dipolar contribution,

σ is the material conductivity, S/m.

Clearly, ϵ'' is responsible for selective heating. $\vec{E}$ is responsible for fast heating and controllability. Because the electric field can penetrate into the material as far as its skin depth, the microwave heating is volumetric. The volumetric heating and high controllability of microwave heating not only eliminate the temperature excursion during processing but also allow higher curing temperatures. Figure 1.1 shows the comparison of temperature profiles during microwave and thermal curing of pure epoxy resin, diglycidyl ether of bisphenol A (DGEBA)/ diaminodiphenyl sulfone (DDS). The thermal curve was obtained when the epoxy sample was placed in a thermal oven at 200°C. The two microwave curves were obtained using continuous power input to heat the resin to the control temperature, 190°C or 230°C, then using pulsed power input to maintain the resin temperature at the control temperature. As shown in the Figure 1.1, the initial heating rate is much faster in the microwave cure than in the thermal cure due to the different heating mechanism. No temperature excursions were observed during microwave cure while a temperature excursion of 40°C was observed during thermal cure. Because the temperature excursion can be eliminated during microwave cure, higher cure temperatures can be used to process thermoset composites. If the thermal degradation temperature is 240°C as shown in Figure 1.1, the maximum cure temperature that can be used in microwave cure is 230°C while that in thermal cure is only 200°C.

The volumetric and inside-out characteristics of microwave heating cause an inside out movement of the heat and vitrification fronts. This allows both excess resin and trapped gases to be fully removed from the interior. A highly consolidated composite with better mechanical properties can be expected from microwave processing. The selective characteristic of microwave heating results in a higher temperature in the graphite fiber than the surrounding matrix. This unique temperature profile improves the interfacial bonding between graphite fiber and epoxy matrix [5,6].

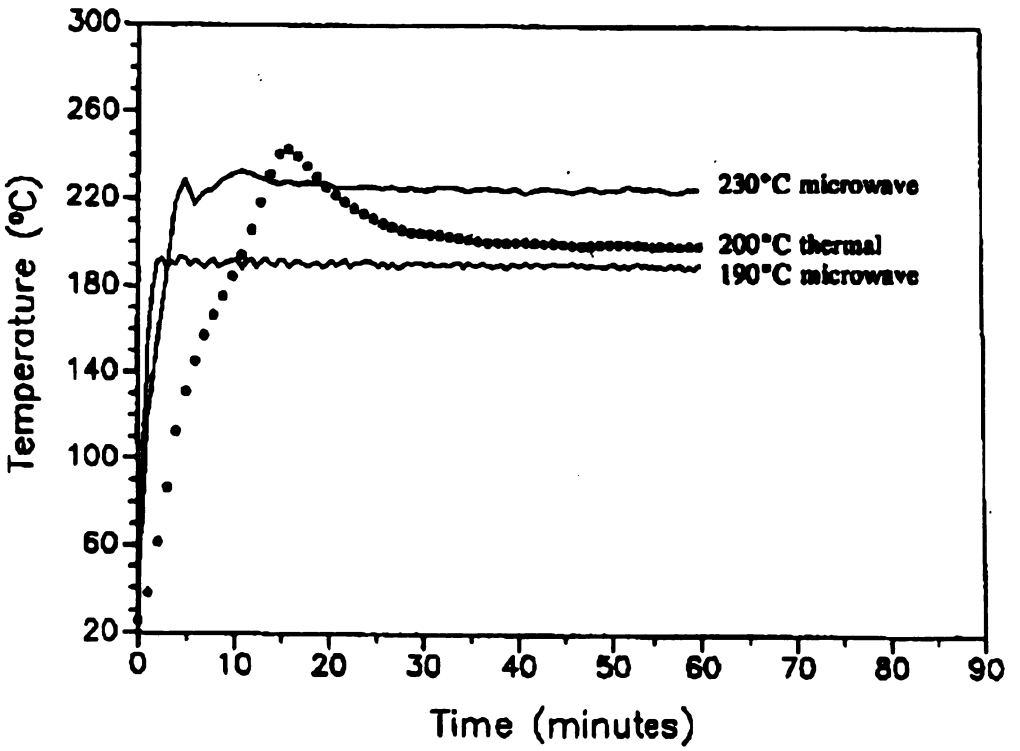

Figure 1.1 Temperature profiles during microwave and thermal cure of pure epoxy resins

The above comparison shows that microwave heating is superior to thermal heating in processing of thermoset and thermoset based composites. A technique based on microwave heating is highly desirable for composite processing in order to

obtain composites of superior properties, to process thick-section composites, and to shorten processing cycles.

1.2 Research Topics

The main objective of this research is to develop a low-cost, high-speed composite processing technique using microwave energy. In order to understand the full potential of microwave curing, the interaction between microwave radiation and material is studied and different processing techniques are developed. Specifically, the following sub-objectives are used to support the core objective:

1. To investigate the microwave radiation effects on epoxy curing rates and the glass transition temperatures of the cured epoxy samples.

2. To demonstrate the possibility of using microwave energy to batch process graphite fiber/epoxy composites using 2.45GHz microwave radiation.

3. To study the scalability of the batch microwave process technique by comparing the heating in a 17.78 cm cavity and a 45.72 cm cavity.

4. To demonstrate the possibility of continuous processing of continuous graphite fiber reinforced epoxy composites using microwave energy.

5. To develop a microwave power absorption model for prediction and controlling of the energy coupling during microwave processing.

6. To develop a microwave and thermal process model for precess simulation and control.

CHAPTER 2
BACKGROUND FOR MICROWAVE PROCESSING

2.1 Introduction

The name "Microwave" generally refers to electromagnetic waves in the frequency range of 300MHz to 300GHz or the characteristic wavelength range of 1.0 m to 1 mm. Although the microwave generator was first invented by Kassner in 1937[39], substantial industrial use did not start until after World War II[40]. Heating is one of the major non-communication applications of microwave power. However, heating is confined to officially assigned ISM frequencies, such as 915MHz and 2.45GHz. To fully illustrate the microwave heating mechanism and its advantages, the basic principles of microwave heating are reviewed in this chapter.

2.2 Interactions Between Electromagnetic Radiation and Materials

Most polymers and composites are non-magnetic. For non-magnetic materials, the electromagnetic (EM) energy loss in a given material is only dependent upon the electric field. All non-magnetic materials are cataloged as dielectrics, conductors, and composite materials consisting of dielectrics and conductors. For conductors, the conductivity determines the interaction between EM radiation and the material. For a perfect conductor, the conductivity is infinite and all incident EM radiation will be perfectly reflected. For a conductor of finite conductivity, the incident EM radiation can penetrate into the conductor as deep as its skin depth, Z_o. The skin depth is defined as the distance from the surface at which the field strength falls to 1/e of its strength at the surface. The skin depth in a conductor can be calculated as

$$Z_o = \sqrt{\frac{2}{\omega \mu_o \sigma}} \tag{2-1}$$

where ω is the frequency of the EM waves in rad/sec, μ_o is the permeability of the free space, $4\pi x10^{-7}$ H/m, and σ is the conductivity of the conductor in mhos/meter. The field strength beyond the skin depth is usually negligible. For graphite fiber, $\sigma=7x10^4$ mhos/meter, and Z_o is 38.4 μm at 2.45GHz. The skin depth for AS4 graphite fiber at 2.45GHz is therefore about four times the fiber diameter. The total EM power loss in a unit conductor element of infinite length can be calculated by:

$$P = \frac{1}{2}\sqrt{\frac{\omega \mu_o}{2\sigma}}\, H_o \tag{2-2}$$

where H_o is the magnetic field strength at the surface in Amperes/meter.

For dielectrics, the interaction between EM radiation and the dielectrics are determined by the dielectric properties of the materials, $\epsilon^*=\epsilon'-j\epsilon''$, at corresponding EM frequency. ϵ' is the dielectric constant representing electrical polarizability which reflects the ability of a material to store electric energy, and ϵ'' is the dielectric loss factor, representing the molecular relaxation phenomenon which reflects the ability of a material to dissipate electrical energy. The skin depth for dielectric materials is

$$Z_o = \frac{2}{\omega \epsilon'' \sqrt{\frac{\mu_o}{\epsilon'}}} \tag{2-3}$$

For fully cured DGEBA/DDS epoxy, $\epsilon^*=\epsilon_0$ (3.5-j 0.1), the skin depth z_0 =0.729m at 2.45GHz. The microwave power loss in a dielectric can be calculated using Equation (1-1). For homogeneous materials in general, the skin depth is calculated by[41]

$$Z_o=\frac{1}{2\omega}\left[\frac{2}{\mu_0\mu'\varepsilon_0\varepsilon'}\right]^{\frac{1}{2}}\left[\left(1+\left(\frac{\varepsilon''}{\varepsilon'}\right)^2\right)^{\frac{1}{2}}-1\right]^{-\frac{1}{2}} \tag{2-4}$$

The skin depth in an anisotropic composite can be calculated in its principal directions using Equation (2-4). For AS4/3501-6, the effective complex permittivity along the

fiber direction is $\epsilon^*=\epsilon_0$ (1-j2500), and perpendicular to fiber direction is $\epsilon^*=\epsilon_0$ (14.5-j75.8) [8]. Assuming the fiber direction is the principal direction, the skin depth for this type of composite is 9.8mm and 3.2m for electric fields along and perpendicular to the fiber direction, respectively. The power absorption rate inside the composite can be calculated by Poynting's theorem[42]

$$P = \frac{1}{2}\omega\epsilon_o \vec{E}\cdot\bar{\bar{\epsilon}}''_{eff}\cdot\vec{E}^*$$
$$\bar{\bar{\epsilon}}''_{eff} = \bar{\bar{\epsilon}}''_d + \frac{\bar{\bar{\sigma}}}{\epsilon_o\omega} \qquad (2\text{-}5)$$

where $\bar{\bar{\epsilon}}''_{eff}$ and $\bar{\bar{\epsilon}}''_d$ are relative effective dyadic loss factor and relative dyadic loss factor

due to dipolar distribution,

$\bar{\bar{\sigma}}$ is the dyadic conductivity, S/m, and

$\vec{E}^*$ is the conjugate electric field vector, V/m.

When a conductor is placed in an alternating EM field, the free electrons will move against the applied field at the alternating frequency. When a dielectric is placed in an alternating EM field, the dielectric material will undergo four different kinds of polarization.
The four polarizations are electron or optical, atomic, orientational or dipolar, and interfacial or space-charge orientations.

2.2.1 Electron or Optical Polarization

This type of polarization is due to the shift of the nuclei center of electron orbits caused by the applied electric field, as shown in Figure 2.1 (a). When no external field is present, the center of positive charges, which are concentrated in the

nucleus, coincides with the center of negative charges, which are circulating around the nucleus. When an external field is applied, the electrons are pushed away from their original path and a dipole moment, $\vec{\mu}$, is induced opposite to the applied electric field. The induced dipole moment is proportional to the field strength, $\vec{E}$, but independent of the frequency. There is no phase displacement with regard to the electric field and therefore no dielectric losses will occur. The typical relaxation time for electron polarization is 10^{-15} sec[43]. This type of polarization occurs in all materials and is responsible for refraction of visible light. The breakdown of this polarization occurs in the ultra-violet and visible range of EM spectrum.

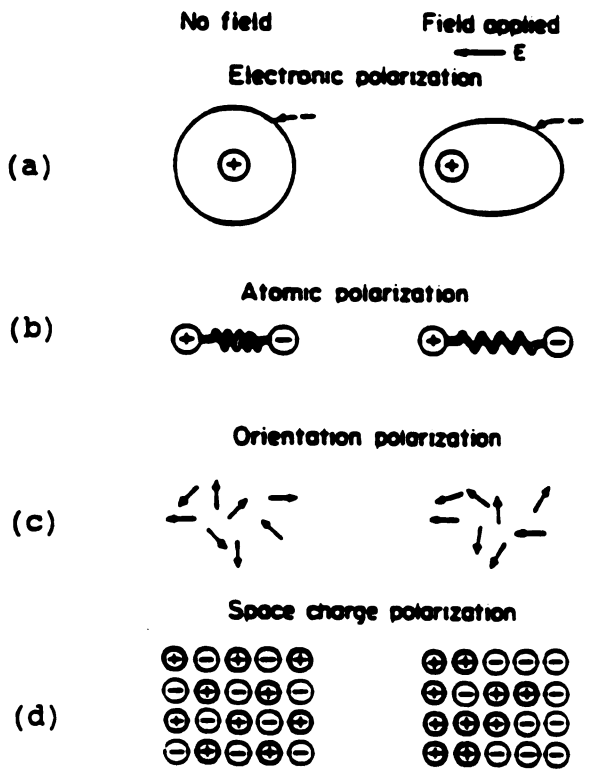

Figure 2.1 Four Types of Polarization Mechanisms

2.2.2 Atomic Polarization

This type of polarization is observed when molecules consisting of two different kinds of atoms are placed in the electric field, as shown in Figure 2.1 (b). When there is no external electric field, the molecule is neutral as a whole either because the center of the positive and negative charges coincides, as in a non-ionic molecule, or because individuals ions are not freely mobile due to a strong internal electric field (or dipole moment), as in an ionic molecule. When an external electric field is applied, the positive charges move in the direction of the field while the negative ones move in the opposite direction. The displacement from their rigid position of equilibrium is proportional to the external electric field strength. This type of polarization mainly causes the bending and twisting motion of the molecules. For example, the elastically joined molecule, such as Na^+Cl^-, can be excited into compulsory oscillation which behaves as resonators with very small attenuation under an alternating electric field. The magnitudes of atomic polarization of non-ionic, or non-partially ionic polymers are much less than those of ionic or partially ionic polymers. The typical relaxation time of this type of polarization is 10^{-13} sec. The breakdown of atomic polarization occurs in the infra-red region of the EM spectrum.

2.2.3 Orientation or Dipole Polarization

This type of polarization only occurs when dipolar or polar molecules are placed in the electric field, as shown in Figure 2.1 (c). In dipolar molecules, the centers of gravity of the positive and negative charges do not coincide but are separated by a small distance. The strength of this permanent polarity is measured as a dipole moment, $\vec{\mu}$. When there is no external electric field applied, the material as whole is neutral due to the random motion of molecules. When an external electric field is applied, the dipolar molecules will rotate until they are aligned in the direction

of the field. Orientation polarization is fundamentally different from electronic and atomic polarization. The latter is due to the displacing force exercised by the external field upon the electrons and atoms via the induced dipole moments, while the orientation polarization is due to the torque action of the field on the pre-existing permanent dipole moments of the molecules. The dielectric loss of orientation polarization is mainly due to the frictional resistance of the medium during dipole rotation. The typical relaxation time of this type of polarization is 10^{-9} sec. The breakdown of this polarization occurs in the microwave range of the EM spectrum. This type of polarization has most interesting to us because it occurs in the microwave range. The calculation of dielectric properties for polar materials will be presented in further detail in section 2.3.

2.2.4 Interfacial or Space-charge Polarization

The previously discussed polarizations; electronic, atomic, and orientation are caused by the displacement or orientation of bound charge carriers. The atoms and molecules are affected by the local field and modulated by the polarization of the surroundings. Interfacial polarization is caused by the migration of charges inside and at the interface of dielectrics under a large scale field. It occurs at radio frequency range.

2.3 Dielectric Properties of Polar Materials

The dielectric properties of a material are characterized by a dielectric constant, ϵ', and a dielectric loss factor, ϵ''. ϵ' is defined as the ratio between the capacitance of a condenser filled with dielectrics and the capacitance of the same condenser when empty (Faraday called ϵ' specific inductive capacity). The higher the polarizability of a molecule, the higher its dielectric constant.

Figure 2.2 shows the frequency dependence of ϵ', and ϵ''. At low frequencies, all types of polarization can reach the steady state values as they would in a static field. Therefore polarizability or ϵ' is high. As frequency increases, some types of polarization may no longer have time to reach their static field values and the polarizability, that is ϵ', is decreased. The polarization fails at its natural frequency ω_m which is the reciprocal of the polarization relaxation time. This is related to the occurrence of electric energy dissipation due to dielectric relaxation at the frequency, ω_m. At the breakdown of a polarization, ϵ', ϵ'' is usually increased dramatically.

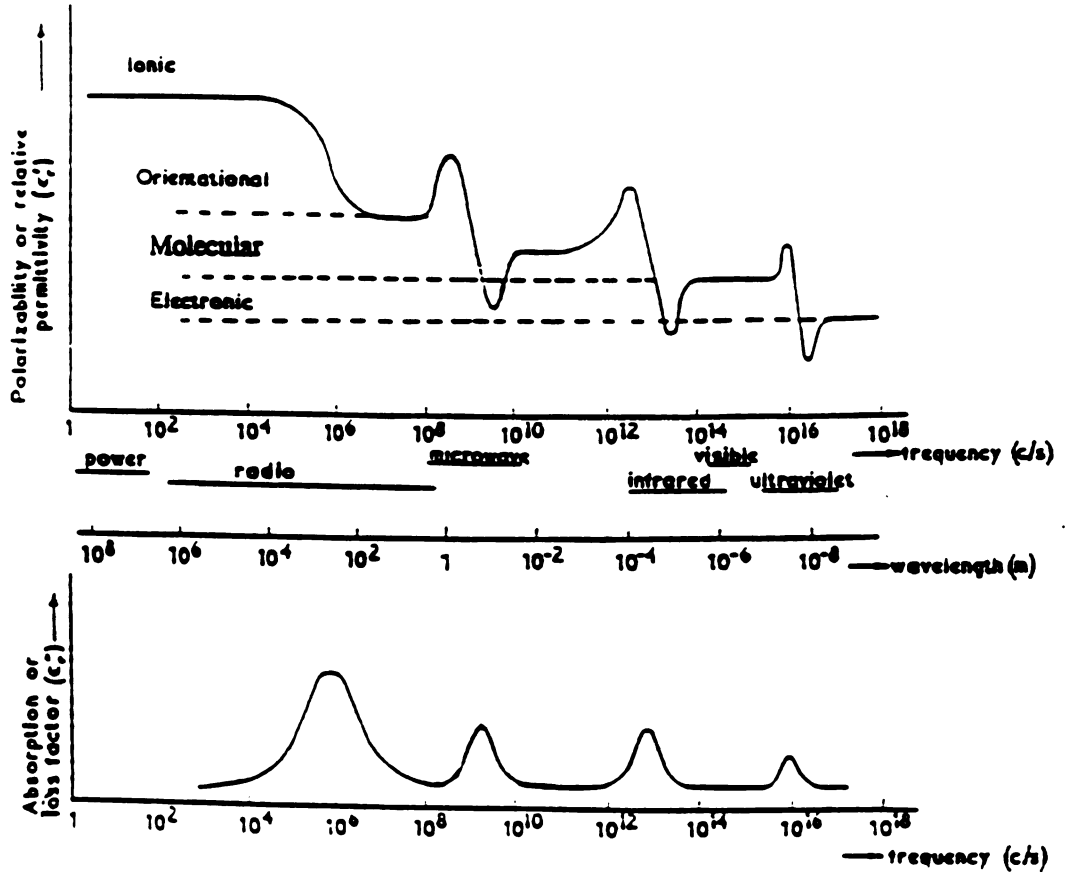

Figure 2.2 Frequency Dependance of ϵ' and ϵ''

The dielectric properties of the material is very important in understanding how the microwave energy is coupled into the dielectric materials. For polar molecules in a liquid or solid, Debye derived formulae for the dielectric constant ϵ' and the dielectric loss factor ϵ''[44].

$$\epsilon' = \epsilon_o \frac{K_s' + K_\infty' \omega^2 \tau_e^2}{1 + \omega^2 \tau_e^2}$$
$$\epsilon'' = \epsilon_o \frac{(K_s' - K_\infty') \omega \tau_e}{1 + \omega^2 \tau_e^2} \qquad (2\text{-}6)$$

with

$$\tau_e = \tau \frac{K_s' + 2}{K_\infty' + 2}$$
$$\tau = \frac{4 \pi r^3 \eta}{\kappa T}$$

where $\kappa = 1.380 \times 10^{-23}$ J/°K, Boltzmann's constant,

K_s' and K_∞' are the relative static and optical permittivities,

τ is the dipole relaxation time, in sec.,

r is the radius of the assumed spherical molecules, in m,

η is the viscosity of the medium, in poise (J/m^2), and

T is the temperature, in °K.

The dielectric conductivity σ_d, and dielectric loss tanδ of the material are

$$\sigma_d = \omega \epsilon''$$
$$\tan\delta = \frac{\epsilon''}{\epsilon'} = \frac{(K_s' - K_\infty') \omega \tau_e}{K_s' + K_\infty' \omega^2 \tau_e^2} \qquad (2\text{-}7)$$

Other equations for the determination of relaxation time of polymers are the Arrhenius relation and the WLF relation. The Arrhenius relation is for relaxation dominated by local molecular transitions while the WLF relation is for relaxation

dominated by structural transitions. Their expressions are

Arrhenius relation: $\tau = \tau_o e^{-\frac{E}{RT}}$

WLF relation: $\tau = \tau_o e^{-\frac{A(T-T_g)}{B+T-T_g}}$

where E is the activation energy in cal/mole, Tg is the glass transition temperature in °K, T is polymer temperature in °K, R is the gas constant, R=1.987 cal/mole/°K, and A,B are constants.

2.4 Microwave Heating Applications

The usage of microwave energy can be classified into communication and non-communication applications. The major non-communication applications of microwave energy are in medicine and heating. Microwave heating has been used in food processing, drying, material processing, waste treatment, and organic synthesis.

In the forest industry, microwave energy has been used to process large bundles of wood and plywood veneer[45]. In the food industry, microwave energy has been used to dry potato chips since the 1960's[46]. Other materials studied in microwave drying included acid hydrolysis of corn stover[47], 13X zeolites[48], and polymers[49]. All of these studies show that microwave drying is significantly faster than conventional thermal drying. However, extra care is required during microwave drying. For example, the bound water inside nylons is very difficult to remove and may cause thermal runaway in the material if the microwave drying is not well monitored[49].

The most common applications of microwave processing are food processing, polymer and composite processing, coal processing, and ceramics processing. In food

processing, bacon cooking and meat tempering accounted for 79% of installed microwave heating capacity as of 1984[50]. Other applications in food processing are seed treatment for insect control[51] and soybean treatment for quality improvement[52]. In the processing of polymers and composites, microwave energy enhanced the polymerization rate of epoxy[10,14,16,20,22,26,53], increased glass transition temperature (T_g) of cured epoxy[10,16], improved the interfacial bonding between graphite fiber and matrix[5,6], and increased the mechanical properties of the composites[3,9]. However, no increase in reaction rates in microwave curing of epoxy were also reported as compared to those of thermal curing[18,19]. In the processing of coal, microwave energy was able to produce a greater number of low molecular weight hydrocarbons than is possible in thermal processing[41]. Microwave energy was able to change non-magnetic pyritic sulfur into magnetic material. Microwave energy was also used to process ceramics and a much faster heating rate and better properties of sintered ceramics were observed[39]. Overviews of microwave heating in the processing of polymers[54] and ceramics[55] have recently been published.

Microwave heating was effectively applied to the processing of waste materials[56,57,58]. A wide range of waste materials has been studied, including infectious medical waste, solvent-laden waste, sludge, used rubber tires, contaminated soils, petroleum products, coal, activated carbon, gases, plastics/elastomers, nuclear waste, and sewage/waste water[59]. A faster processing speed and lower processing cost were reported. Microwave heating was also used as an alternative to thermal heating in organic synthesis[60,61,62,63]. Again, a significant reduction in the time necessary to complete the reaction under microwave conditions was observed, especially when lossy solvents were involved.

2.5 Microwave Heating Systems

Three kinds of microwave applicators, waveguides, commercial multimode microwave ovens, and tunable resonant cavities are commonly used in the microwave processing of materials. All the three kinds of applicator have been studied in microwave heating of polymers and composites. However, only the resonant cavity can easily focus the microwave power into materials and was successfully used in processing of crossply and thick-section graphite fiber reinforced composites[3,5,9]. Cylindrical tunable resonant cavities were used in the present study. The characteristics of resonant cavities, microwave circuit systems, and electric field patterns inside a cavity are discussed in this section.

2.5.1 Cylindrical Tunable Resonant Cavity

The cylindrical cavity in this study is made out of a length of metal circular waveguide with both ends shorted by the same metal, such as copper or aluminum, as shown in Figure 2.3. The top short-plate is adjustable so that the cavity length L_c can be changed. The bottom plate is removable for sample loading. The microwave energy is introduced into the cavity by a coaxial coupling probe. The coaxial coupling probe is adjustable in the radial direction so that the coupling probe depth L_p can be changed for locating critical coupling conditions.

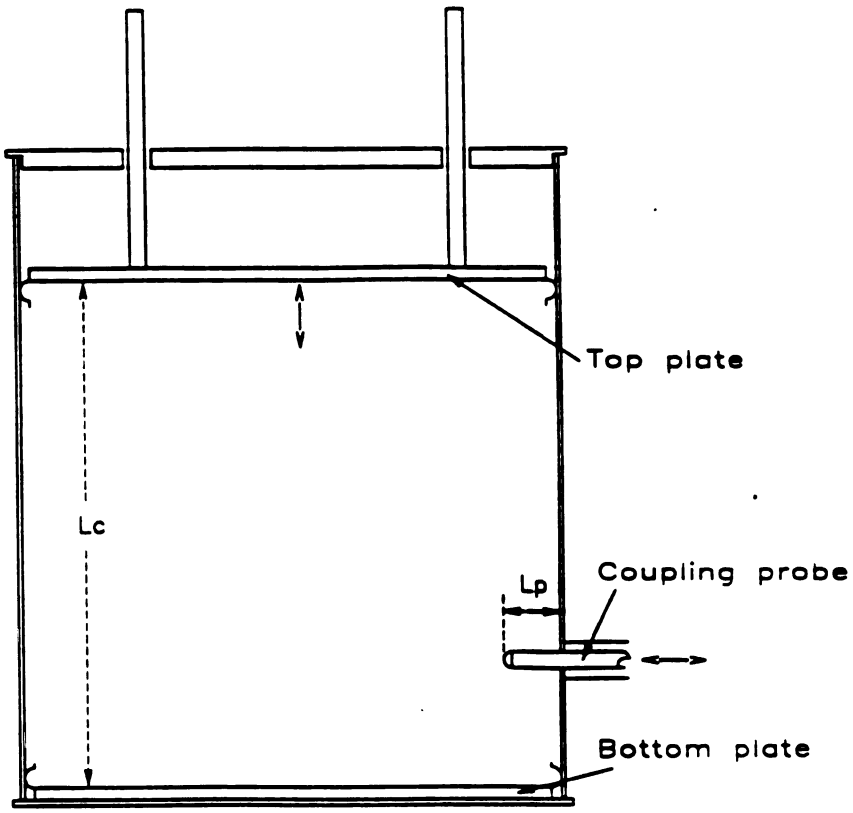

Figure 2.3 Diagram of Cylindrical Tunable Resonant Cavity

In order to confine microwave energy inside the cavity, the ratio of cavity length/cavity radius must be such that the electric field patterns inside the cavity reach a resonant condition. The resonant electric field inside an empty cavity can be theoretically calculated according to Maxwell's equations and the electric and magnetic boundary conditions at the cavity wall. The boundary conditions at the cavity wall are that the electric field, $\vec{E}$, has only a normal component while the magnetic field, $\vec{H}$, has only a tangential component. There are two types of resonant conditions or modes. Transverse electric (TE) and transverse magnetic (TM). For TE modes, the electric field is aligned perpendicular to the axial direction. For TM modes, the electric field is aligned along the axial direction. Three subscripts, n,p,q,

are used as mode nomenclature to represent the physical appearance of the corresponding mode in an empty cavity, i.e. TE_{npq} and TM_{npq}. n denotes the number of the periodicity in the circumferential direction, n=0,1,2,..... p denotes the number of field zeroes in the radial direction, p=1,2,3,.... q denotes the number of half wavelengths of the equivalent circular waveguide, q=0,1,2,... for TM modes and q=1,2,3,... for TE modes. Figure 2.4 shows the physical appearance of the EM field of the TM_{012} mode. The dashed line represents the magnetic field while the solid line represents the electric field. In the diagram, the higher the density of the lines, the stronger the local field is. This mode is very efficient for heating rod shaped materials when the rod is placed at the center of the cavity.

The relationship between the cavity diameter/length ratio and the product of cavity diameter and frequency for a given resonant mode can be calculated theoretically and presented as a mode chart. The theoretical equations for TM and TE modes in an empty circular cylindrical cavity are[42]

$$(fd)^2_{TM_{npq}} = \frac{x_{np}^2}{\pi^2 \varepsilon_o \mu_o} + \frac{q^2}{4\varepsilon_o \mu_o}\left(\frac{d}{L_c}\right)^2 \tag{2-8}$$

$$(fd)^2_{TE_{npq}} = \frac{x'^2_{np}}{\pi^2 \varepsilon_o \mu_o} + \frac{q^2}{4\varepsilon_o \mu_o}\left(\frac{d}{L_c}\right)^2 \tag{2-9}$$

where f is the frequency, Lc is the cavity length for the resonant mode, d is the diameter of the cavity, x_{np} and x_{np}' are the ordered zeros of the Bessel function $J_n(x)$ and its derivative $J_n'(x')$ with the first subscript referring to the order of the Bessel function and the second to the order of the zero, and μ_o is the permeability of free space. Figure 2.5 shows the mode chart. For a given cavity, the cavity length of a certain mode is strongly dependent on the frequency, except for those TM modes with q=0.

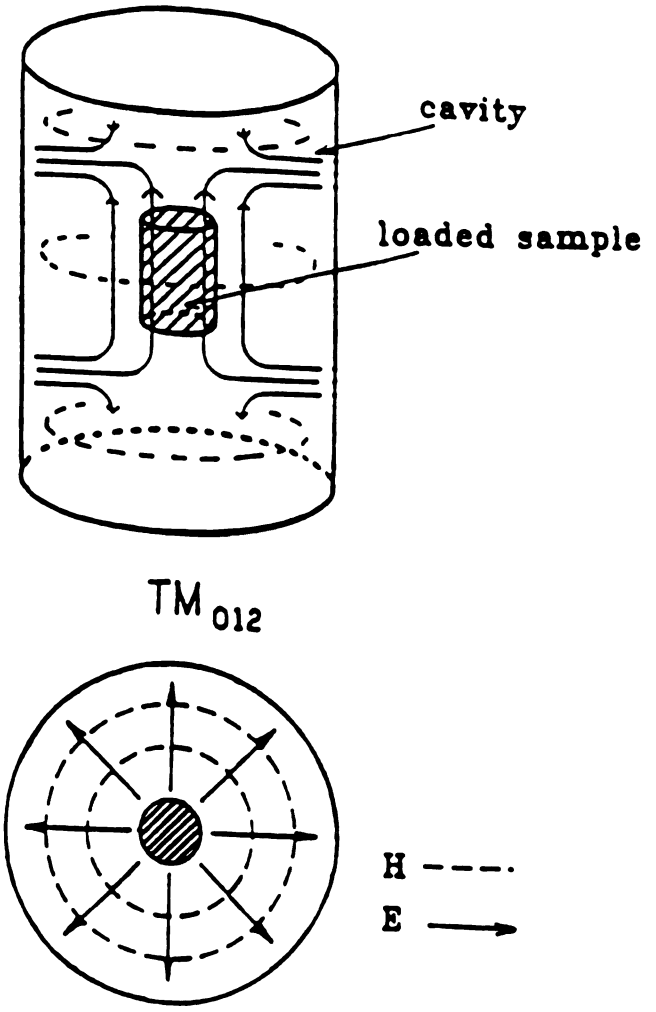

Figure 2.4 Theoretical EM Field of TM_{012} in a Cylindrical Empty Cavity

In this study, three sizes of cylindrical tunable resonant cavities are used. Their inner diameters are 15.24, 17.78, 45.72 cm. Both 15.24 and 17.78 cavities are made from brass and the 45.72 cavity is made from aluminum. Figures 2.6, 2.7, and 2.8 show the cavity length versus frequency mode chart for the empty 15.24, 17.78, 45.72 cm cavities, respectively. The 15.24 cm cavity was used for polymer kinetics study and the 17.78 cm and 45.72 cm cavities were used for the processing study. A thin film sample was used in the 15.24 cm cavity during the kinetics study

and the electromagnetic field inside the cavity is very close to that of the empty cavity. During the processing studies in the 17.78 cm and 45.72 cm cavities, the sample size was relatively large and the electromagnetic fields were greatly perturbed, especially when the loaded material is graphite fiber composites. In these cases, the location of the coupling probe is also important. For 17.78 cm cavity, the coupling probe was located 5.461 cm above the bottom plate. To measure the radial electric field strength along the axial and circumferential direction, holes 0.216 cm in diameter were drilled in the cavity wall. To prevent microwave leakage from the holes, a 1.27 cm thick copper strip was used to surround the holes. In the axial direction, the holes were drilled in the cavity wall with 90° respect to the coupling probe. The first hole was drilled 0.605 cm above the bottom plate and the rest of the holes were drilled 0.922 cm apart from each other. In the circumferential direction, three rows of holes were drilled at the heights of the third, fourth, and fifth holes of the axial hole line because the composites were usually loaded at this height, 2.5 to 4.3 cm above the bottom plate. Using the axial hole line as reference, the holes were drilled every 10° in the circumferential direction. For the 45.72 cm cavity, the coupling probe was located 10 cm above the bottom plate. Only an axial hole line was drilled with first hole at 3.13 cm and the rest of the holes were 0.922 cm apart from each other.

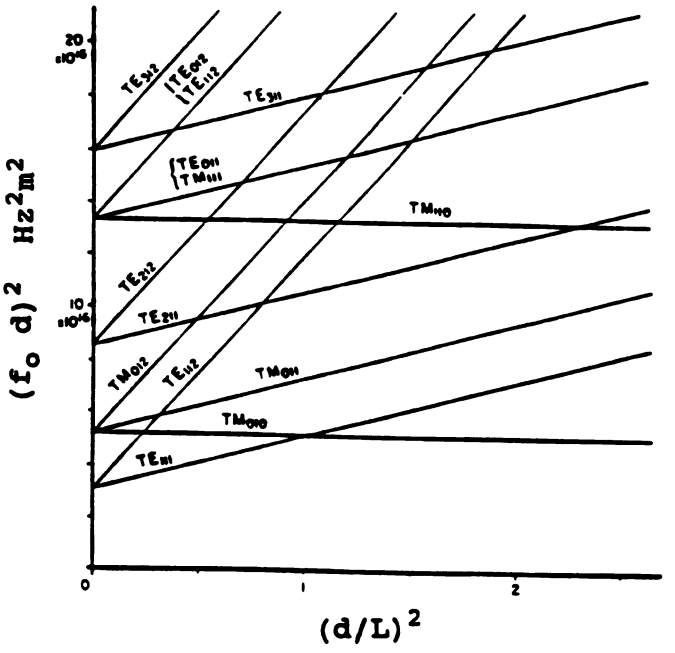

Figure 2.5 Mode Chart for Circular Cylindrical Cavities

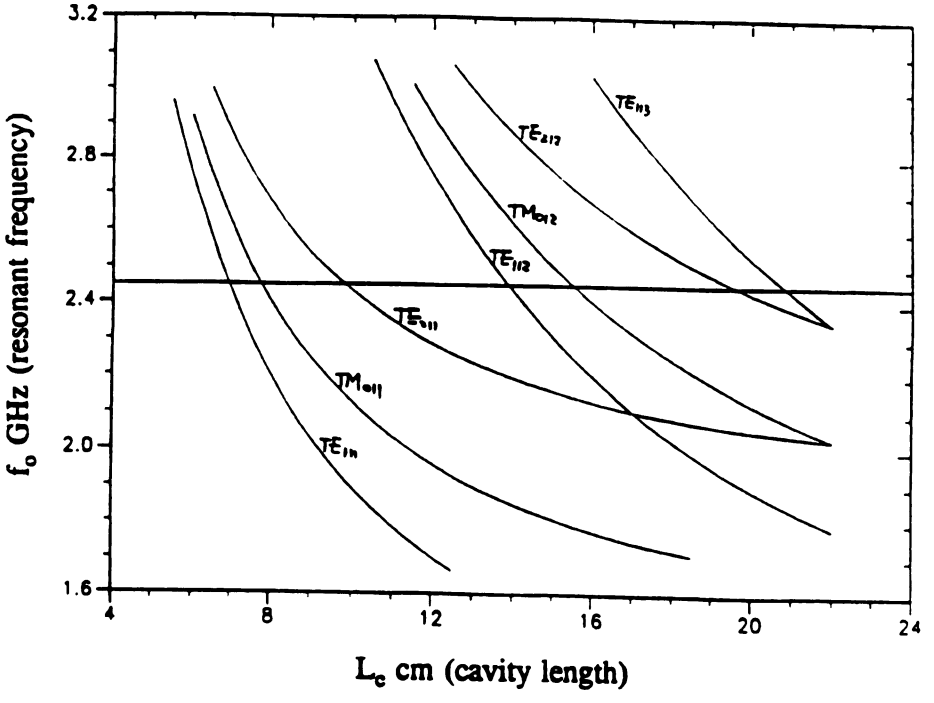

Figure 2.6 Mode Chart for 15.24 cm Cylindrical Cavity

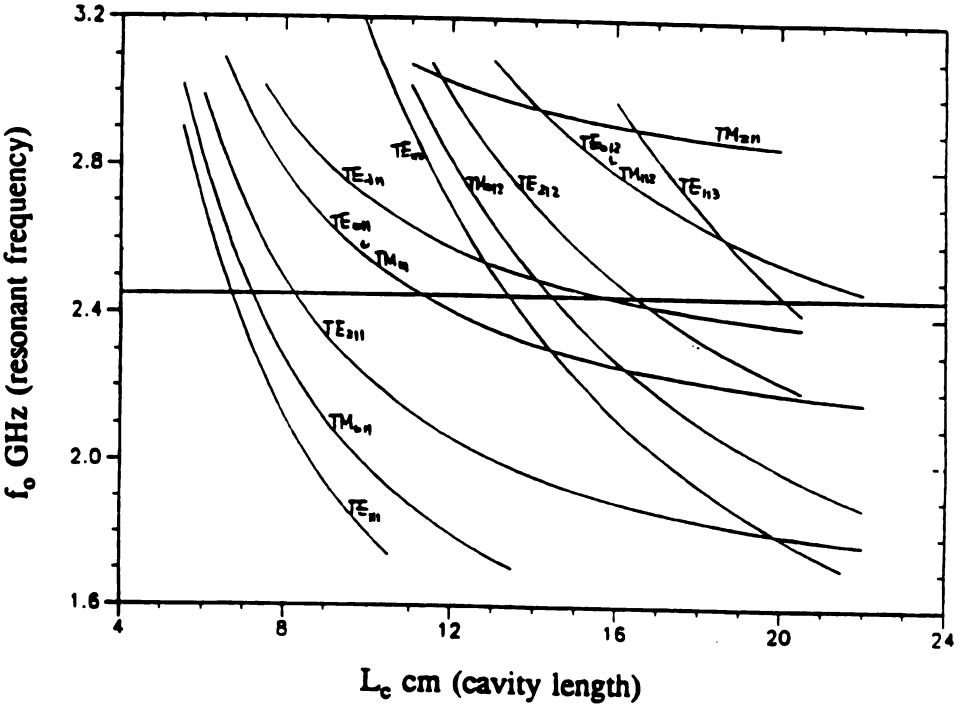

Figure 2.7 Mode Chart for 17.78 cm Cylindrical Cavity

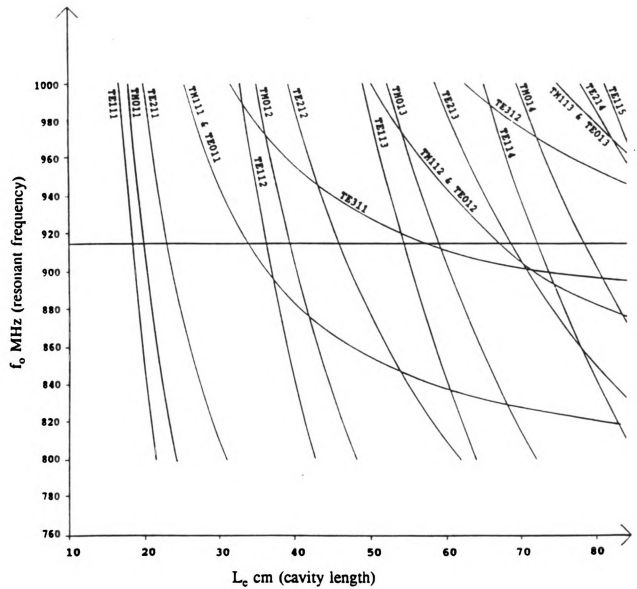

Figure 2.8 Mode Chart for 45.72 cm Cylindrical Cavity

2.5.2 Q Factor of the Resonant Cavity

The Q factor of the resonant cavity is defined as ratio of the energy stored inside the cavity to the energy lost at the cavity wall per unit time.

$$Q = 2\pi f_o \frac{energy\ stored}{energy\ lost} = 2\pi f_o \frac{\varepsilon \int_v |E|^2 d\tau}{R \oint_s |H|^2 ds} \tag{2-10}$$

where R is the intrinsic wave resistance of the metal walls.

The Q factor of the resonant cavity in the microwave frequency range is usually very high, 10^4 or more[64], and is a function of the resonant modes. The Q factor of a single mode cylindrical cavity of finite conducting walls can be derived theoretically using the cavity-wall perturbation method[42].

$$(Q_c)^{TM}_{np0} = \frac{\eta x_{np}}{2R(1+a/L_c)} \tag{2-11}$$

$$(Q_c)^{TM}_{npq} = \frac{\eta \sqrt{x_{np}^2 + \left(\frac{q\pi a}{L_c}\right)^2}}{2R(1+a/L_c)} \tag{2-12}$$

$$(Q_c)^{TE}_{npq} = \frac{\eta \left(x'^{\,2}_{np} + \left(\frac{q\pi a}{L_c}\right)^2\right)^{3/2} (x'^{\,2}_{np} - n^2)}{2R\left(\left(\frac{nq\pi a}{L_c}\right)^2 + x'^{\,4}_{np} + 2\frac{a}{L_c}\left(\frac{q\pi a}{L_c}\right)^2 (x'^{\,2}_{np} - n^2)\right)} \tag{2-13}$$

where η is the intrinsic impedance of the dielectric, R is the intrinsic wave resistance of the metal wall, a is the cavity radius. However, the theoretical Q values are higher than the Q factors of the actual cavity because the actual cavity has the coaxial coupling probe at the side wall and the finger stock at the top and bottom plates. The Q factor of the actual cavity is usually measured experimentally from the power absorption curve, as shown in Figure 2.9. The procedure is first to locate the desired resonant mode at frequency f_o by adjusting the coupling probe depth, L_p, and the cavity length, L_c, using a swept frequency microwave source, then measuring the bandwidth at the half power points δf. The Q factor for a cavity in a single resonant mode can be determined as

$$Q = 2\frac{f_o}{\delta f} \tag{2-14}$$

Equation (2-14) can not be used to determine the Q factor for a cavity resonated in multimode conditions.

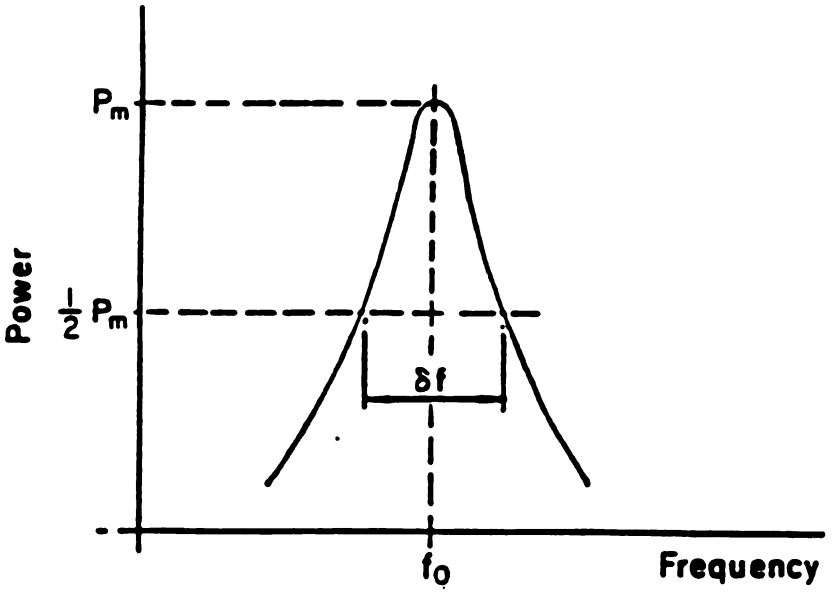

Figure 2.9 Q-factor Determination From Power Absorption Curve

2.5.3 Electromagnetic Field Inside the Resonated Cavity

In a homogeneous, source-free cylindrical cavity with perfectly conducting walls, the EM field inside the cavity can be derived from Maxwell's equations and the boundary conditions[42]. For TM modes:

$$\begin{aligned} E_\rho &= \frac{1}{\hat{y}}\frac{\partial^2 \psi_{npq}}{\partial \rho \partial z} & H_\rho &= \frac{1}{\rho}\frac{\partial \psi_{npq}}{\partial \phi} \\ E_\phi &= \frac{1}{\hat{y}}\frac{1}{\rho}\frac{\partial^2 \psi_{npq}}{\partial \phi \partial z} & H_\phi &= -\frac{\partial \psi_{npq}}{\partial \rho} \\ E_z &= \frac{1}{\hat{y}}\left(\frac{\partial^2}{\partial z^2} + k^2\right)\psi_{npq} & H_z &= 0 \end{aligned} \tag{2-15}$$

where $k^2 = \omega^2 \mu_o \epsilon$ and ψ_{npq} is the wave potential for TM_{npq} modes.

$$\psi_{npq} = J_n\left(\frac{x_{np}\rho}{a}\right)\begin{Bmatrix}\sin n\phi \\ \cos n\phi\end{Bmatrix}\cos\left(\frac{q\pi}{d}z\right) \tag{2-16}$$

For TE modes:

$$\begin{aligned} H_\rho &= \frac{1}{\hat{z}}\frac{\partial^2\psi_{npq}}{\partial\rho\partial z} & E_\rho &= -\frac{1}{\rho}\frac{\partial\psi_{npq}}{\partial\phi} \\ H_\phi &= \frac{1}{\hat{z}}\frac{1}{\rho}\frac{\partial^2\psi_{npq}}{\partial\phi\partial z} & E_\phi &= \frac{\partial\psi_{npq}}{\partial\rho} \\ H_z &= \frac{1}{\hat{z}}\left(\frac{\partial^2}{\partial z^2}+k^2\right)\psi_{npq} & E_z &= 0 \end{aligned} \tag{2-17}$$

where ψ_{npq} is the wave potential for TE_{npq} modes.

$$\psi_{npq} = J_n\left(\frac{x'_{np}\rho}{a}\right)\begin{Bmatrix}\sin n\phi \\ \cos n\phi\end{Bmatrix}\sin\left(\frac{q\pi}{d}z\right) \tag{2-18}$$

For the loaded cavity, Equation (2-15) to (2-18) are no longer applicable. Cavity perturbation theory is usually used to calculate the EM field in a cavity loaded with a small object which only perturbs the resonant frequency by a few percent. The object can be dielectric, magnetizable, or conducting. Using the material-cavity perturbation method, a cylindrical cavity resonated in the TM_{012} mode has been used for measurement of material dielectric properties[7]. For a cavity coaxially loaded with homogeneous lossy materials, a mode-matching method was used to calculate the EM field inside the cavity[65]. However, for a cavity loaded with an anisotropic composite plate, especially graphite fiber reinforced composite, the EM field inside the cavity is very complicated. A five parameter formula for calculating the electric field inside the loaded composite is presented in Chapter 8.

2.5.4 Microwave Processing System

Two microwave systems, one operating at 2.45GHz with 15.24cm and 17.78cm inner diameter cavities and one operating at 915MHz with a 45.72cm inner

diameter cavity, were used in this study. Figure 2.9 shows the microwave circuit setup for each of these systems. Both systems have four basic units; a microwave source circuit, a tunable circular cylindrical cavity, a data acquisition unit, and a temperature and electric field (E-field) measurement unit. Either a Luxtron 755 multichannel fluoroptic thermometer or an infrared thermometer was used to measure the temperatures and an antenna probe was used to measure the E-field strength. The radial E-field strength in the axial direction and the axial E-field at the top of the cavity can be measured. The input power, P_i, reflected power, P_r, and the detected power at cavity wall, P_b, are measured by power meters (HP4356). The data acquisition unit is a data collection board in a personal computer driven by software described elsewhere[7]. Each microwave source circuit consists of two parts: a swept frequency, low power microwave source circuit and single frequency, high power microwave source circuit.

In the 2.45GHz system, the swept frequency microwave source is a HP 8350B Sweep Oscillator with the HP 86235A RF Plug-In (frequency range 1.7 to 4.3 GHz). A power absorption curve is observed on an oscilloscope (Tektronix 2213) over a swept range of microwave frequencies from the power reflected back into the microwave circuit from the cavity. Resonant modes exist at those locations on the oscilloscope trace where there is zero reflected power. The dimensions of the cavity are adjusted so that zero reflected power is observed at 2.45GHz. Once the resonance condition at 2.45GHz is found, single frequency microwave power from an Opthos MPG-4M is introduced into the cavity for processing.

In the 915MHz system, the swept frequency microwaves are generated by a HP 8350B Sweep Oscillator with HP 86220A RF Plug-In (frequency range 10 to 1300MHz). The power absorption curve is displayed on a Tektronix 465 Oscilloscope. High power is generated by supplying a continuous wave of 915MHz from the sweep oscillator to a Logimetrics Model A610/P (frequency range .5 to 1.0 GHz) microwave power amplifier.

915 MHz system

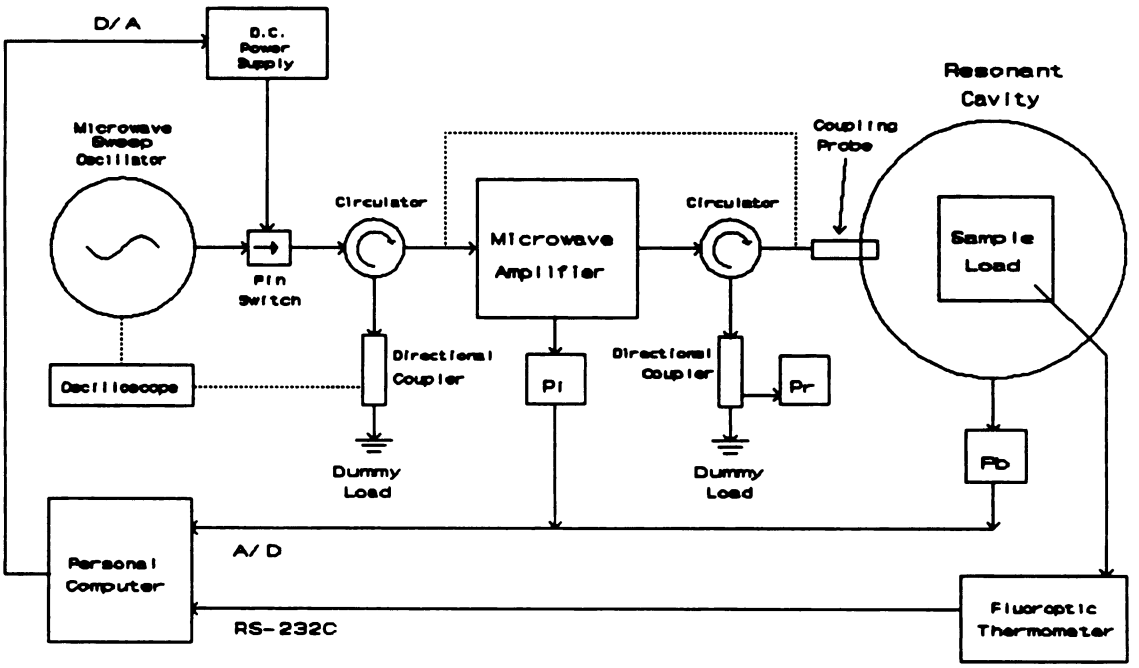

2.45 GHz system

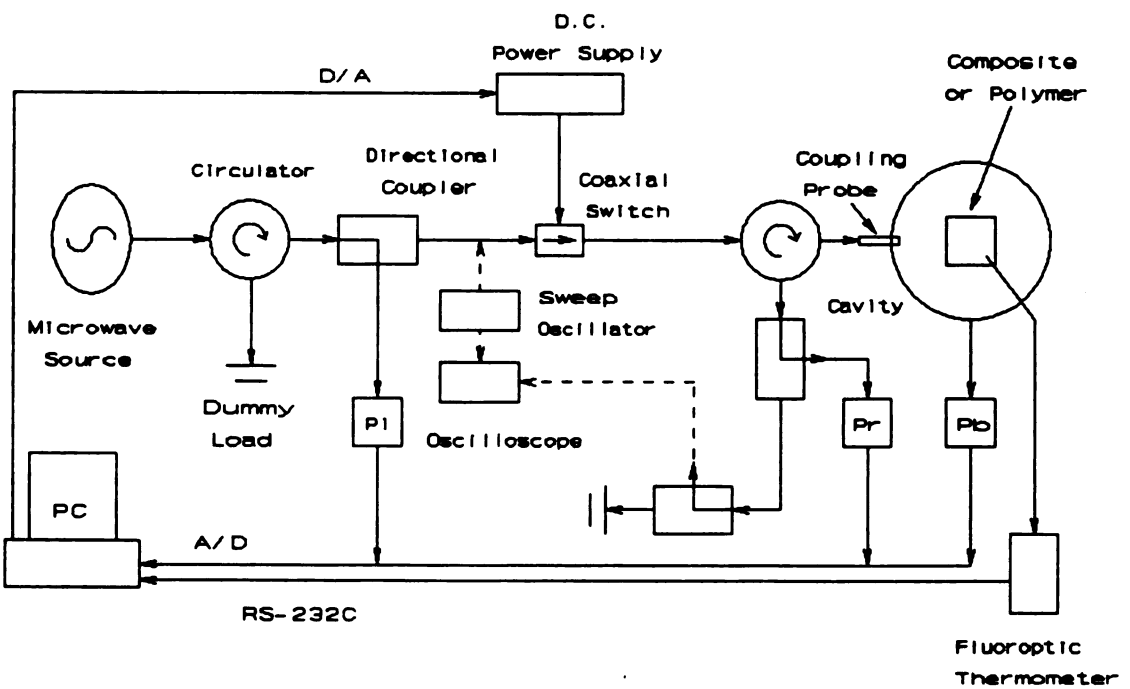

Figure 2.10 Microwave Processing Systems

A coaxial switch (micronetics RSN-2D-I/12V) is installed in the 2.45GHz microwave source circuit to turn the microwave power on and off for maintaining isothermal conditions after the sample has reached the control temperature. The switch is regulated by a dc power supply (Electronic Measurements HCR-30-8-111) which is controlled by an I/O interface board (Omega DAS-16) in a personal computer. Actuation of the on/off switch is in response to temperature feedback from a fluoroptic temperature sensing system (Luxtron 755).

For an empty cavity, the power absorption curves are usually single peak curves and the location of zero reflected power can be calculated theoretically. When either a polymer or composite plate was loaded into the cavity, however, the power absorption curve on the oscilloscope was not always a single peak curve. Especially when the resonant standing electromagnetic fields interact with an anisotropic composite, the electric field strength distribution inside and outside the composite is complicated. The resonant heating modes in a composite loaded cavity are not identical to any theoretical TM or TE modes. A power absorption curve with several resonant peaks (at different frequencies) can be generated by adjusting the cavity length and the coupling probe depth. The position of resonant peaks changes and the number of resonant peaks is increased or decreased as the cavity length or/and coupling probe depth are changed. The cavity length and coupling probe depth, however, play different roles in the presence of resonance condition. The cavity length determines the possibility of resonance at a given frequency and the coupling probe depth determines the realizability of the resonance. With improper cavity length, the resonance condition can not be achieved no matter what the coupling probe depth is. With proper cavity length, the resonance condition can be obtained only at a certain coupling probe depth. For a given loaded cavity, the presence of resonant peaks was a function of frequency, cavity length and the probe depth. Each peak corresponded to a resonant heating mode of a particular electric field strength and pattern as well as the cavity length, probe length and the resonant operating frequency. At the fixed frequency, several resonant heating modes were

generated depending on the combination of cavity length and probe depth. Based on the appearances and behaviors of the resonant peaks, three types of resonant heating mode, pseudo-single (PS), controlled-hybrid (CH), and uncontrolled-hybrid (UH) resonant modes, were observed on the oscilloscope as shown in Figure 2.11. The pseudo-single mode looks and behaves as an empty cavity mode. The hybrid mode curves look like curves of two or more peaks coalesced and each peak represents a different resonant mode. If all peaks can be located at 2.45 GHz for processing, the hybrid mode is a controlled-hybrid mode. If only one peak can be located at 2.45 GHz for processing, the hybrid mode is a uncontrolled-hybrid mode. When a hybrid mode was used to process the composite, the resonance of the loaded cavity could be maintained at a chosen peak (mode) by properly adjusting the cavity length and coupling probe depth constantly during the processing.

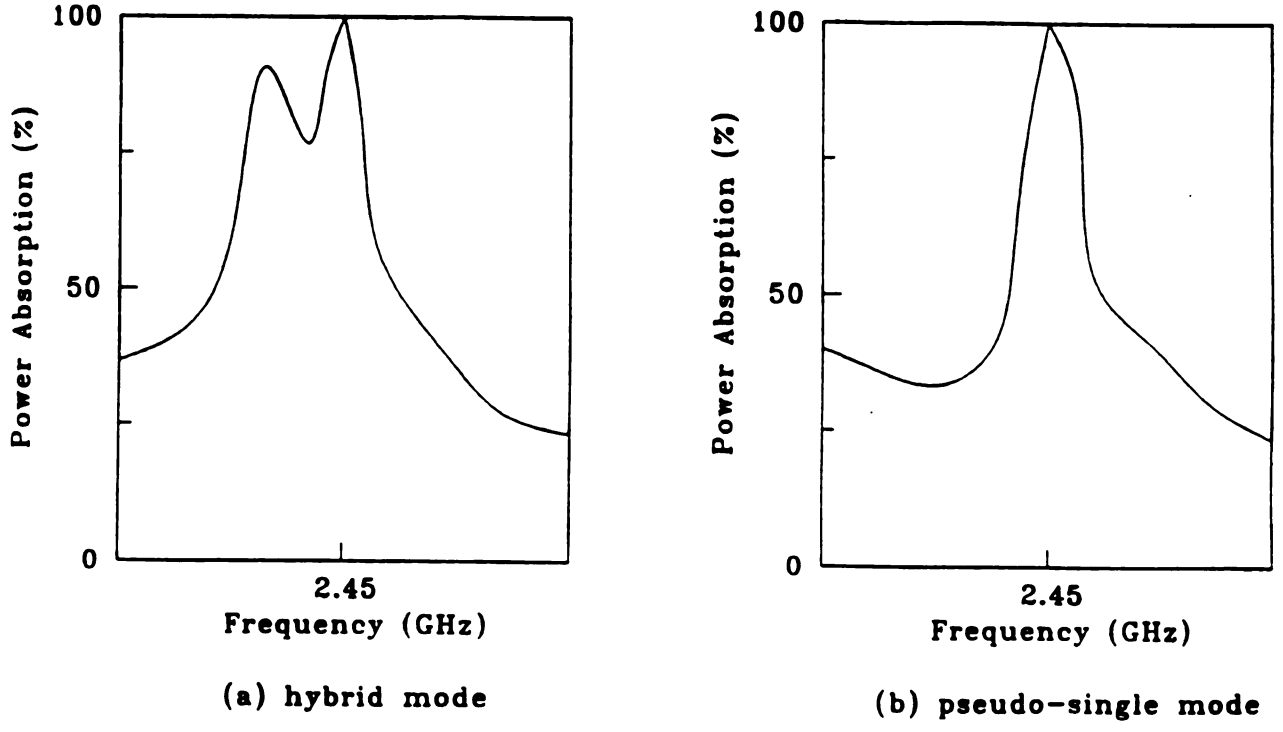

Figure 2.11 Definition of Pseudo-single, Controlled-hybrid, and Uncontrolled-hybrid Modes

CHAPTER 3
MICROWAVE CURE OF EPOXY

3.1 Introduction

The general advantages of microwave heating over thermal heating were discussed in Chapter 1. Chapter 2 summarized the interactions between microwave radiation and materials, microwave processing systems, and other fundamental principles relating to microwave heating. This chapter discuses how microwave radiation affects the curing of one of the most widely used thermoset, epoxy resin.

Microwave processing of polymers and polymer composites has been studied as an alternative to conventional thermal processing. In general, the unique microwave heating mechanism[3,7] allows selective, global, faster and more controllable heating than is possible with thermal heating. To determine whether microwave energy is superior to thermal energy in the processing of thermoset and composites, some fundamental questions must be studied. They include: 1) whether microwave radiation enhances the polymerization reaction rates 2) does the microwave radiation induced reaction follow the same reaction path 3) whether these two types of processing will result in the same polymer network structure 4) do microwave processed polymers have different physical properties (such as density), mechanical properties (such as strength and modulus), and thermal properties (such as thermal expansion coefficient and glass transition temperature) compared to those of thermally processed samples.

In order to understand the effect of microwave radiation on polymer reaction kinetics, epoxy resins have been microwave cured using single-mode cavities[10,16,20,22,25], commercial multimode ovens[20,66], and waveguides[18,19,28,29]. However, literature reports disagree on whether microwave heating accelerates or

decelerates the reaction rate compared to thermal heating. This discrepancy may be due to effects of the temperature gradient within the material during microwave cure, caused by the low thermal conductivity, heat transfer area of curing epoxy resin, and non uniformity of power absorption inside the sample.

To elucidate the microwave radiation effects on the reaction kinetics, efforts have been made to develop a novel thin film technique to ensure spatial uniformity of the temperature and the extent of cure[16,25] inside the samples. A parallel isothermal microwave and thermal cure of DGEBA/mPDA epoxy resin has been done using this novel technique, and only a slight increase in reaction rate was observed in the case of microwave cure[25]. This increase may be due to a change in the microwave radiation excited reaction kinetics and/or localized "hot spots" on a molecular level by rotational excitation resulting from the dipolar response to the electromagnetic fields[26]. A similar study was carried out using DGEBA/DDS epoxy resin[16], and significant increase in reaction rate was observed in microwave cure. An increased glass transition temperature (Tg) was found in the microwave cured samples as compared to the thermally cured samples at a high extent of cure. Similar Tg values were obtained for microwave and thermal cured samples at a low extent of cure[16]. However, Mijovic et. al[18,19] used DSC to determine both extent of cure and Tg, and decreased reaction rates and Tg in the microwave cure of DGEBA/DDS were observed as compared to those of thermal cure.

This chapter reports the results of a study of the reaction kinetics and the glass transition temperature of microwave and thermally cured epoxy resins. Isothermal cure of DGEBA/DDS and DGEBA/mPDA epoxy resins was done at three different temperatures in a single mode resonant cavity and a thermal oven. A cavity resonated in the TE_{111} mode was used in microwave cure. Thin film samples were used in this study and FTIR was used to measure the extent of cure. TMA was used to determine the glass transition temperatures of the cured thermoset.

3.2 Thermal Cure of Epoxy Resins

In modelling Tg and the reaction kinetics of microwave cured epoxy resins, models based on the thermal cure kinetics can be used and parallel parameters calculated and compared. To elucidate the critical parameters in the analysis of the microwave cure of epoxy resins, a general literature review of the Tg and reaction kinetics of the thermal cure of epoxy resins is necessary. A complete review should address cure kinetics, reaction mechanism, reaction by-products, crosslinked network structure, glass transition temperature, mechanical properties and other physical properties of the cured epoxy resin, effects of the stoichiometry, diluents, fillers, and cure conditions on the reaction kinetics and the thermal properties of the curing epoxy resins. While general reviews are available elsewhere[67,68,69], a review of the reaction kinetics model and glass transition temperature of cured epoxy is provided here.

3.2.1. Cure Kinetics

Two different types of models for thermal cure kinetics have been proposed, an n^{th} order reaction kinetics model[70,71] and an autocatalytic reaction model[72,73,74,75].

3.2.1.1 The n^{th} order kinetics model

For the n^{th} order assumption, the reaction kinetics can be expressed as

$$\frac{d\alpha}{dt} = k(T)\, f(\alpha) \qquad (3-1)$$

where α is the extent of cure, t is the time, the function $f(\alpha)$ is expressed as $(1-\alpha)^n$,

and k(T) is the overall reaction rate constant and obeys an Arrhenius relation.

$$k(T) = A \exp\left(-\frac{E/R}{T}\right)$$

where A is the pre-exponential constant (min^{-1}), E is the overall activation energy (cal/mole), R is the gas constant (1.987 cal/mole/°K), and T is cure temperature (°K). Substituting the Arrhenius relation into Equation (3-1) and rearranging produces

$$\ln\left(\int_o^{\alpha} \frac{1}{f(\alpha)}\, d\alpha\right) = \ln k(T) + \ln(t) \qquad (3\text{-}2)$$

The left hand side is only a function of α, or equivalently, only a function of the glass transition temperature, Tg, as there is a unique relationship between α and Tg. Equation (3-2) can be rewritten as

$$f(Tg) = -\frac{E/R}{T} + \ln(A) + \ln(t) \qquad (3\text{-}3)$$

The left hand side of Equation (3-3) has the same value for different cure temperatures at a given α or Tg. Therefore, the activation energy can be obtained by relating the cure time to cure temperature at the same α or Tg.

$$\ln\left(\frac{t}{t_{ref}}\right) = \frac{E}{R}\left(\frac{1}{T} - \frac{1}{T_{ref}}\right) \qquad (3\text{-}4)$$

E/R is the slope of the $\ln(t/t_{ref})$ versus 1/T line. Equation (3-4) also suggests that the α or Tg versus ln(t) curve at various cure temperatures can be shifted to a single curve at a reference temperature T_{ref} using the shifting factor $SF=(E/R)(1/T-1/T_{ref})$. This single curve is generally referred to as the master curve[76]. Once E is determined, the value of A and n can be obtained from Equation (3-1) using experimental data at the reference temperature.

A and n can be determined from the intercept and slope of the $\ln(d\alpha/dt)+(E/R)/T$ versus $\ln(1-\alpha)$ line.

$$\ln\left(\frac{d\alpha}{dt}\right) + \frac{E/R}{T} = \ln(A) + n\ln(1-\alpha) \qquad (3\text{-}5)$$

3.2.1.2 Autocatalytic Kinetics Model

The n^{th} order reaction kinetics has the advantage of simplicity. However, the maximum reaction rate should occur at the beginning of the reaction according to the n^{th} order assumption. In reality, the maximum rate usually happens at an extent of cure, $\alpha = 0.3 \sim 0.4$. This phenomenon has been explained by an autocatalyzed reaction mechanism and the phenomenological cure kinetics expression for a stoichiometric epoxy-resin has been given as[72,74,75]

$$\frac{d\alpha}{dt} = (k_1 + k_2\alpha^m)(1-\alpha)^n \qquad (3\text{-}6)$$

where

k_2 is the autocatalytic polymerization reaction rate constant,

$$k_2 = A_2 \exp(-E_2 / RT)$$

k_1 is the non-catalytic polymerization reaction rate constant,

$$k_1 = A_1 \exp(-E_1 / RT)$$

m is the autocatalyzed polymerization reaction order, and

n is the non-catalyzed polymerization reaction order,

Based on the reaction mechanism for epoxy resin, a general cure kinetics expression was derived as follows[77]

$$\frac{d\alpha}{dt} = (k_1 + k_2\alpha)(1-\alpha)(B-\alpha) \qquad (3\text{-}7)$$

where B is the ratio of initial hardener equivalents to epoxide equivalents. For a stoichiometric mixture, B = 1. The proposed reaction kinetic mechanism is[78]

$$a_1 + e \underset{K_1'}{\overset{K_1}{\rightleftharpoons}} a_2 + OH \qquad (3\text{-}8)$$

$$a_2 + e \underset{K_2'}{\overset{K_2}{\rightleftharpoons}} a_3 + OH \qquad (3\text{-}9)$$

$$OH + e \underset{K_3'}{\overset{K_3}{\rightleftharpoons}} et + OH \qquad (3\text{-}10)$$

where a_1, a_2, a_3, e, and et are primary amine, secondary amine, tertiary amine, epoxide, and ether group, respectively. K_i and K_i', i=1,2,3, are specific reaction rate constants for the catalytic and noncatalytic reactions, respectively. The experimental evidence shows that for a stoichiometric mixture of epoxide and amine, the etherification reaction can be ignored[78,79,80,81,82,83,84] at low cure temperatures. Equation (3-7) for a stoichiometric mixture can be easily derived from the proposed mechanism and the following assumptions.

1) There are no substitution effects, i.e. the reaction rate constant is the same for primary and secondary amine.

2) No OH impurity, ie. initial OH concentration equals zero.

3) Extent of cure is defined as $\alpha=(e_o-e)/e_o$, where e_o is the initial epoxide concentration.

Most of the derivation is straightforward except the kinetics equation for a_1:

$$\frac{da_1}{dt} = 2\,a_1\,e\,[K_1' + K_1\,(OH)] \qquad (3\text{-}11)$$

The factor 2 is due to the fact that the neighboring amine hydrogen becomes a secondary amine hydrogen as the primary amine hydrogen is reacted.

If k_1/k_2 in Equation (3-7) is independent of temperature, the approach to generate the master curve used for n^{th} order reaction kinetics can be applied here. The Tg data can be represented by a single master curve at a reference temperature using the Tg versus ln(t) curve. The Tg versus ln(t) curves of all other temperatures can be obtained simply by shifting the master curve horizontally using a shifting factor $SF = (1/T - 1/T_{ref}) E/R$. As α has a single relationship with Tg, the α versus ln(t) curve at the reference temperature can also be used as the master curve for reaction rate. The reaction kinetics at all other temperatures can be obtained simply by shifting the curve using the same SF used for shifting Tg master curves.

Equation (3-7) is no longer applicable if there is an etherification reaction and/or OH impurity, or the reaction rate constants for primary and secondary amine are not the same. For epoxy/amine systems, the reaction rate constant ratio between the secondary amine-epoxy and primary amine-epoxy, defined as $n=K_2/K_1=K_2'/K_1'$, is not always equal to unity and is system dependent. For example, n for thermal cure of diglycidyl ether of bisphenol A (DGEBA)/ ethylenediamine (EDA) is equal to 1 while n for thermal cure of diglycidyl ether of bisphenol A (DGEBA)/ diaminodiphenyl sulfone (DDS) is equal to 0.4[85]. Further more, for an epoxy/aromatic system curing at high temperatures or having excess epoxy, the etherification reaction can no longer be neglected. The reaction rate constant ratio between etherification reaction and primary epoxy-amine reaction is defined as $L=K_3/K_1=K_3'/K_1'$. For a stoichiometric epoxy/amine system having an OH impurity, a non-unity reaction rate constant ratio between secondary amine-epoxy and primary amine-epoxy, and an etherification reaction, the cure kinetics can be derived from the fundamental reaction steps, Equations (3-8) to (3-10).

$$\frac{d\alpha}{dt} = \left(\frac{2(1-n)\phi + n\phi^{n/2}}{2-n} + LF(\phi)\right)(1-\alpha)\,[k_1 + k_2 F(\phi)] \qquad (3\text{-}12)$$

$$F(\phi) = 1 + [OH]_o/e_o - [(1-n)\phi + \phi^{n/2}]/(2-n) \qquad (3\text{-}13)$$

$$\alpha = \frac{1}{2(2-n)}\left((1-\phi)(1-n)(2-L) + 2(1-\phi^{n/2})(1-L/n) - (2-n)L(1+[OH]_o/e_o)\ln\phi\right) \qquad (3\text{-}14)$$

where $[OH]_o$ is initial OH concentration, ϕ is a_1/e_o, $k_1 = e_0 K_1'$, and $k_2 = e_0^2 K_1$. Equation (3-7) for a stoichiometric system can be easily obtained from Equations (3-12), (3-13), and (3-14) with $[OH]_0 = 0$, $L = 0$, and $n = 1$.

Equation (3-7) has been used to describe the reaction kinetics of Hercules 3501-6 epoxy resin. It holds very well for the early stages of cure, but it is not valid after the gelation point. To model the whole curing reaction, an equivalent first order reaction has been suggested to model the reaction kinetics after the gelation point[86,87]. The reaction kinetics are given by

$$\frac{d\alpha}{dt} = \begin{cases} (k_1 + k_2\alpha)(1-\alpha)(B-\alpha) & \alpha < \alpha_{gel} \\ k_3(1-\alpha) & \alpha > \alpha_{gel} \end{cases} \qquad (3\text{-}15)$$

where k_3 is the first order reaction rate constant and α_{gel} is the extent of cure at the gelation point. Two expressions have been proposed for k_3, they are

$k_3 = A_3 \exp(-E_3 / RT)$ in one reference[87], and

$k_3 = A_3 \exp(-1.9\alpha) \exp(-E_3 / RT)$ in the second reference[86].

Clearly, the above model has a lack of continuity at the gelation point. To couple the diffusion effect into the kinetics of the reaction, Havlicek and Dusek[88] suggested the Rabinowitch model[89] to calculate the overall reaction rate constant

$$\frac{1}{k_o(\alpha, T)} = \frac{1}{k_T(T)} + \frac{1}{k_d(\alpha, T)} \qquad (3\text{-}16)$$

where $k_o(\alpha,T)$ is the overall reaction rate constant, $k_T(T)$ is the kinetics rate constant, and $k_d(\alpha,T)$ is the diffusion rate constant. $k_o(\alpha,T)$ refers to the overall non-catalytic polymerization reaction rate constant. There are two extremes during the reaction. On one hand, $k_d >> k_T$ for the reaction prior to vitrification, especially at a low extent of cure. On the other hand, $k_T >> k_d$ for the reaction near and after vitrification, where the diffusion effect is significant. The diffusion rate constant, k_d, is controlled by the diffusion of chain segments and is expected to be proportional to the diffusion constant of the reactants. Equivalently, k_d is inversely proportional to the relaxation time of the polymer segments[90]. Based on the above assumption and the modified Williams-Landel-Ferry (WLF) equation for molecular relaxation time[91,92], the temperature dependence of k_d is suggested to be[93]

$$\ln[k_d(T)] = \ln(k_{do}) + \frac{\beta (T - Tg)}{51.6 + |T - Tg|} \qquad (3\text{-}17)$$

where k_{d0} is the diffusion rate constant at T_g and is assumed to be a constant and ß is a constant. Both k_{d0} and ß need to be determined from the experimental data. Equation (3-17) is identical to the modified WLF equation with the reference temperature taken to be Tg. The Arrhenius relation can be also used to relate the relaxation time of the polymer segments to the temperature.

From Equation (3-7), the overall reaction rate constant k_o can be calculated from α and $d\alpha/dt$ by assuming k_2/k_1 remains the same.

$$k_o = \frac{d\alpha/dt}{(1-\alpha)(B-\alpha)(k_2/k_1+\alpha)} \qquad (3\text{-}18)$$

As the kinetics rate constant remains the same, $k_d(\alpha,T)$ can be obtained by rearranging equation (3-16).

$$k_d = \frac{k_o k_T}{k_T - k_o} \tag{3-19}$$

A brief review of the general nature of curing will be helpful to fully describe the curing characteristics. Several distinct steps are observed during the complex curing process. The polymerization starts off with formation and linear growth of the polymer chains. At this stage, there is no hindrance for the reacting molecules and the effective reactant concentration is equal to the existing reactant concentration. The chains begin to branch and then to crosslink as the reaction proceeds. A sudden and irreversible transformation from a viscous liquid to an elastic gel will occur when the crosslinks develop into a network of infinite molecular weight. This phenomenon is called gelation. The extent of cure at gelation, α_{gel}, is only a function of the epoxy system. For a system containing a mixture of A1, A2, ... Ai moles of monomer with a functionality of f1, f2, ... fi, and B1, B2, ... Bj with a functionality of g1, g2, ... gj, Macosko and Miller have proposed an equation to calculate α_{gel} by assuming A's can only react with B's[94]

$$\alpha_{gel} = \frac{1}{\sqrt{(f_e - 1)(g_e - 1)}}$$

$$\text{where} \quad f_e = \frac{\sum_i f_i^2 A_i}{\sum_i f_i A_i} \tag{3-20}$$

$$g_e = \frac{\sum_j g_j^2 B_j}{\sum_j g_j B_j}$$

For a difunctional monomer reacting with a tetrafunctional monomer (e.g. DGEBA/DDS), Flory proposed a simple equation for α_{gel} prediction[95]

$$\alpha_{gel} = \sqrt{\frac{B}{3}} \tag{3-21}$$

Again, B is the ratio of initial hardener equivalents to epoxide equivalents.

There are two types of material in the post-gel reactants, soluble material and gelled material[96]. Usually these two materials are mixed together in a macro-uniform fashion. Because of this, the number of reactants available for reaction will be less than the number of reactants that exist in the mixture. Therefore, an effective reactant concentration should be used instead of the existing reactant concentration in order to properly model the reaction kinetics. For a difunctional epoxide and tetrafunctional amine system, the weight fraction of solubles, w_s, has been calculated theoretically by assuming a single rate constant[96].

$$w_s = w_A p^4 + w_E (\alpha_{exp}^2 p^3 + 1 - \alpha_{exp})^2 \qquad (3\text{-}22)$$

$$p = \left(\frac{1}{\alpha_{exp}^2} - \frac{3}{4}\right)^{1/2} - \frac{1}{2}$$

where w_A and w_E are the weight fractions of amine and epoxy molecules, respectively. w_A is 0.135 and 0.264 for the DGEBA/mPDA and DGEBA/DDS systems, respectively. P is the probability of finding a finite chain when looking out from a randomly chosen amine molecule. α_{exp} is the experimentally determined extent of cure.

Another distinct step during cure is the onset of vitrification. Vitrification occurs when the Tg of the thermoset reaches the cure temperature which transforms the elastic gel into a glassy solid. The curing may enter vitrification without passing through gelation if the cure temperature is less than ${}^{gel}T_g$. ${}^{gel}T_g$ is the temperature at which gelation and vitrification occur simultaneously. The onset of vitrification switches the reaction from chemical control to diffusion control which brings an abrupt halt to curing. Vitrification is a reversible transformation and the cure can be resumed by heating to devitrify the partially cured thermoset. The effects of vitrification on the kinetics can be modelled by using an overall rate constant instead of a reaction rate constant as described in Equation (3-16).

3.2.2 Glass Transition Temperature

The glass transition temperature, Tg, is the temperature of transition between a glassy state and a liquid or rubbery state. Because of the dramatic change in the physical properties of the polymer at this transition, Tg is an important material parameter in polymer applications. Physical properties useful in determining Tg include; polymer density, specific heat, mechanical strength and modulus, stiffness, dielectric properties, and rate of gas or liquid diffusion through the polymer. Glass transition is a complicated phenomenon and a significant amount of uncertainty exists in Tg measurement. Many factors affect Tg, including the structure, crystallinity and the molecular weight of the polymer, diluents in the polymer, thermal history and the method of measurement. Many physical and chemical properties will change at the glass transition. However, only the sensitive ones will change significantly and can be used for Tg measurement and process monitoring. The sensitive properties at the glass transition also vary with the polymer system. Therefore, the measurement conditions and methods should be reported with Tg data. To obtain a reliable Tg value, the choice of the right measurement method is very important[97]. TMA (thermal mechanical analysis, which traces changes in polymer dimensions) and DSC (differential scanning calorimetry, which traces changes in polymer enthalpy) are two classical methods for Tg measurement. Figures 3.1 and 3.2 show the DSC and TMA thermographies for both microwave and thermally cured DGEBA/DDS samples[10]. The interpretation of Tg in the DSC thermograph is rather arbitrary, especially in the case of the microwave cured sample. On the other hand, the TMA thermographies reveal well-defined transitions at Tg. For this reason, TMA was chosen to measure the Tg of both microwave and thermal cured samples.

The glass transition temperature of epoxy resins has been intensively studied due to its importance in industrial applications[67]. These studies include the effects of the extent of cure and crosslinking density, polymer structure, impurity, and annealing on the Tg. Different experimental methods have been investigated to

determine Tg according to the magnitude of change of different physical properties of cured epoxy matrix in the glass transition region. Glass transition temperature effects on physical properties have also been studied. Tg in epoxy matrix-based composites were measured and found to be different from pure epoxy. Generally speaking, Tg increases with extent of cure until reaching an ultimate value corresponding to the ultimate conversion at a given temperature. This is the so called vitrification point. In general, vitrification is defined as the point where Tg equals the cure temperature, Tc. Experimental results show that Tg at the ultimate extent of cure actually equals Tc+C, where C is a constant. For the DGEBA/mPDA system, C is 10-13°C[77]. Impurities present in the epoxy matrix usually lower Tg. For partially cured epoxy resin, Tg may also depend on the thermal history. Because Tg is very sensitive to small changes in conversion when the diffusion effect is important and when the reactant concentration is low, Tg has been used to monitor the cure process[98]. Two stages of Tg behavior have been proposed with cure temperature as the dividing point. Tg has been found to be a function of the extent of cure, cure temperature and cure stage[99].

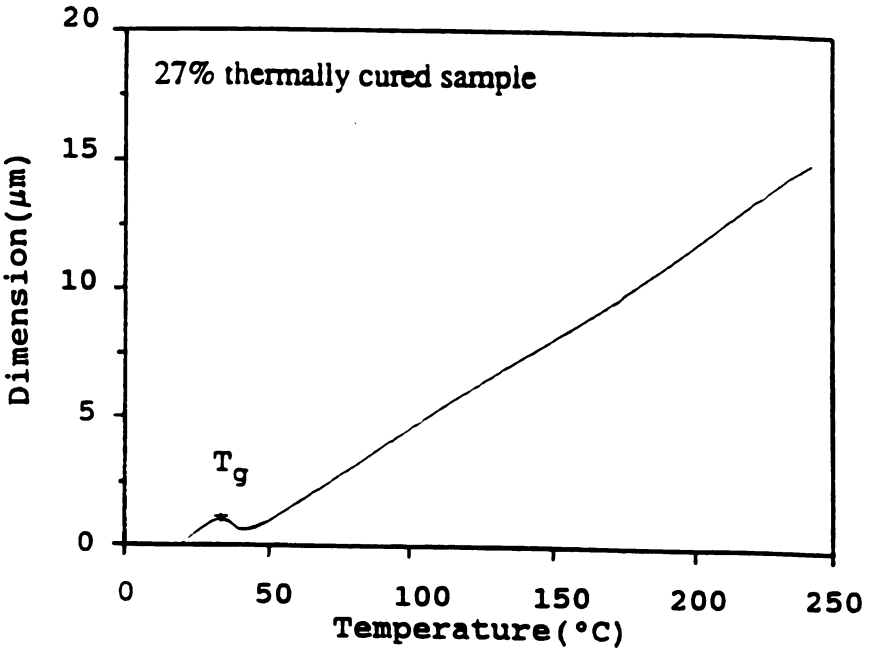

TMA Thermograph

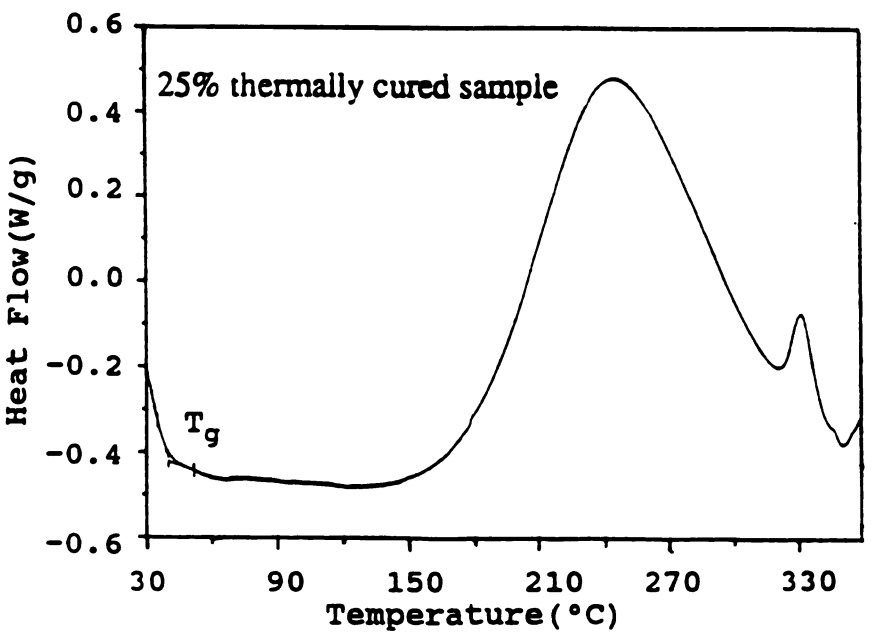

DSC Thermograph

Figure 3.1 Comparison of Tg Determination for Thermally Cured DGEBA/DDS

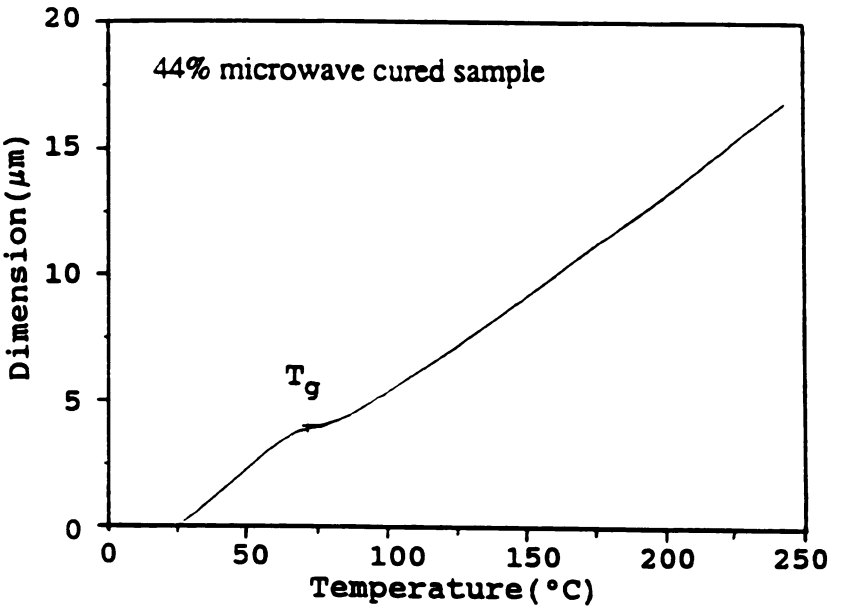

TMA Thermograph

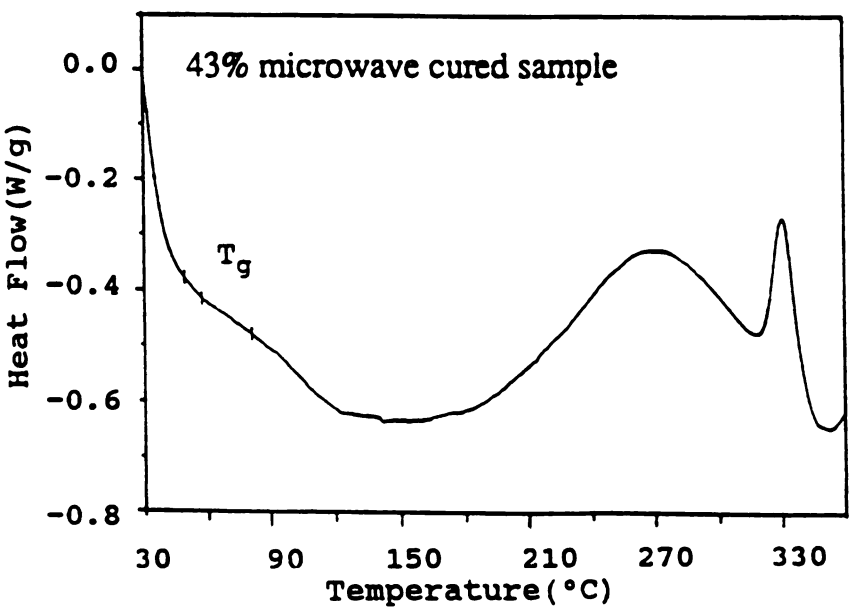

DSC Thermograph

Figure 3.2 Comparison of Tg Determination for Microwave Cured DGEBA/DDS

In the study of physical aging effects on the thermal and mechanical properties of cured epoxy polymers, Jo and Ko found that both properties are strong functions of the extent of cure and the thermal history[100]. In aged samples, where the free volume is low, the major factor which determines the properties of the cured epoxy polymer is the packing density rather than the extent of cure. However, in the quenched samples where sufficient free volume exists, the major factor which determines the properties of the cured samples is the extent of cure. The thermal history effects on Tg have not been fully explored yet. Several predictive models for Tg have been proposed[101,102,103]. The most widely accepted one is the DiBenedetto model, derived from the lattice energy of the polymer:

$$\frac{T_g - T_{go}}{T_{go}} = \frac{\left(\frac{E_x}{E_m} - \frac{F_x}{F_m}\right)\alpha}{1 - \left(1 - \frac{F_x}{F_m}\right)\alpha} \qquad (3\text{-}24)$$

where

T_{go} is the glass transition temperature of the unreacted sample,

E_m is the unreacted epoxy-monomer lattice energy,

E_x is the full-cure epoxy-monomer lattice energy,

F_m is the unreacted epoxy-monomer segmental mobility,

F_x is the full-cure epoxy-monomer segmental mobility, and

α is the extent of cure.

3.3 Experiments

Stoichiometric epoxy/amine mixtures were isothermally cured in a 15.24 cm inner diameter single-mode resonant cylindrical microwave cavity and in a conventional thermal oven. The epoxide used was DGEBA (diglycidyl ether of bisphenol A, Dow Chemical DER 332) with an epoxy equivalent weight of 173. The crosslinking amines used were DDS (diaminodiphenyl sulfone, Aldrich Chemical) with an amine

equivalent weight of 62 and mPDA (meta phenylene diamine, Aldrich Chemical) with an amine equivalent weight of 27. Figure 3.3 shows the chemical structures of DER 332, DDS, and mPDA. To ensure spatial uniformity of the temperature and the extent of cure in the sample during the cure, thin films were used. The stoichiometric mixtures were dissolved in a solvent, acetone for DGEBA/DDS system and diethyl ether for DGEBA/mPDA system. Ether was used as the solvent for DGEBA/mPDA because of its higher volatility, which is required for mPDA. Samples were prepared by casting several drops of solution onto a 13 mm diameter, 1mm thick potassium bromide (KBr) disk. The recipe used for the solution in this study was 5g of mixture in 80cc of solvent and casting six drops of this solution onto a KBr disk to form a thin film sample. An approximately 10 micron thick film remained on the KBr disk after the evaporation of solvent at room temperature. Time periods of 1 hour and 15 minutes were allowed for the evaporation of acetone and ether, respectively. KBr was chosen because of its transparency to infrared and microwave radiation (dielectric constant measured in our lab is $\epsilon^* = \epsilon^o$ (2.71 - j 0.002) at 2.45 GHz). The detailed procedure of thin film sample preparation is available elsewhere[25]. Another KBr disk was placed on the top to protect the sample after the solvent evaporated. Fresh samples were scanned using a Fourier Transform Infrared(FTIR) spectrometer (Perkin-Elmer 1850) for later reference in the extent of cure determination.

The 2.45GHz system was used with a 15.24cm inner diameter cylindrical cavity for microwave curing. The detailed description of the system was provided in Chapter 2. The TE_{111} resonant heating mode was used to isothermally cure the thin film samples at three different temperatures. Figure 3.4 shows the electromagnetic field pattern of the TE_{111} mode in the cylindrical resonant cavity. The line density represents the magnitude of E-field strength. The thin film samples were placed in the center of the cavity where electric field is strongest. As the sample size is very small relative to the cavity size, the electric field pattern inside the thin film loaded cavity is almost the same as that of the empty cavity. The electric field is fairly

uniform across the sample. Therefore, the temperature is fairly uniform across the sample. The center temperature was measured by placing the Luxtron fluoroptic probe directly on the top of the thin epoxy film through a hole in the top BKr disk. An initial heating rate was obtained with a typical value of 2°C per second. The reaction was quenched after each sample had been heated for a given time. Quenching the cured samples was necessary to ensure that the T_g is determined mainly by the extent of cure[100]. Parallel thermal cures with the same sample configurations were run in a conventional thermal oven. The experimental temperatures used are listed in Table 3.1.

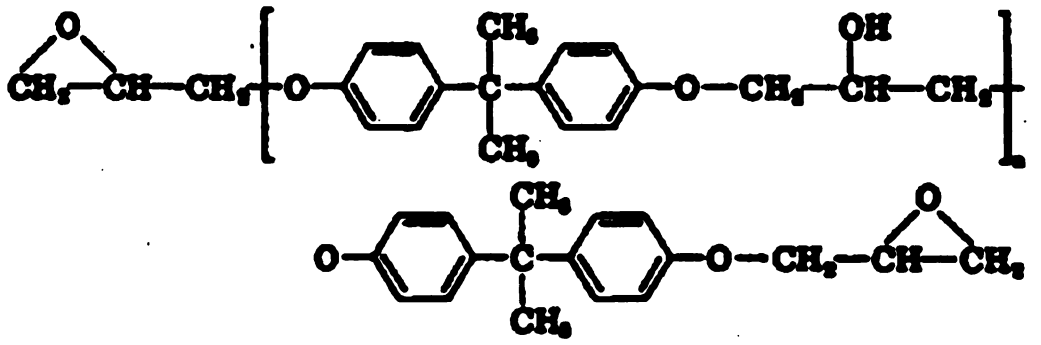

DGEBA

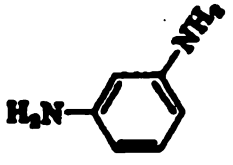

mPDA

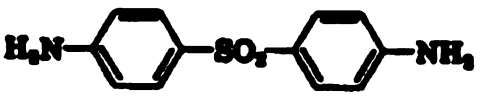

DDS

Figure 3.3. Chemical Structure of DGEBA, DDS, and mPDA

Each cured sample was scanned in the FTIR and the transmission infrared spectra of the cured sample was used to determine the extent of cure. As the concentration of the absorbing species is linearly related to the area under absorbance peak, the extent of cure (conversion of epoxy) can be calculated as

$$\alpha = 1 - \frac{\left[\frac{A_{915}}{A_{2962}}\right]_{cured}}{\left[\frac{A_{915}}{A_{2962}}\right]_{unreacted}} \qquad (3\text{-}25)$$

where A_{915} and A_{2962} are the areas under the analyte absorbance peak and the reference absorbance peak, corresponding to the infrared absorption of an epoxy ring vibration at wavenumber 915 cm^{-1} (891-927 cm^{-1}) and non-reactive aromatic vibration at wavelength 2962 cm^{-1} (2778-2992 cm^{-1}), respectively. Normalized analyte absorbance peak areas were used to compensate for the possible difference in the film thickness from experiment to experiment.

Table 3.1. Temperatures Used for Microwave and Thermal Cure

		Cure Temp. (°C)		
DGEBA/DDS	microwave	125	135	145
	thermal	135	145	165
DGEBA/mPDA	microwave	80	100	120
	thermal	80	100	120

FTIR has been used to determine the reaction extent of epoxy/amine systems previously[16,25,104,105,106]. Although the analyte peak used was always 915 cm^{-1}, several reference peaks have been used in the literature. In the analysis of the DGEBA/mPDA system, the 1034 cm^{-1} peak that was declared to be due to an out-of-plane CH deformation of the aromatic ring was used as the reference peak[105]. The 1184 cm^{-1} peak[106] and the 1508 cm^{-1} peak[25] were also used as reference peaks to

analyze the same system. In the analysis of the DGEBA/DDS system, the 2962 cm^{-1} peak was used as the reference peak[16]. However, according to the SPECTRA-STRUCTURE CORRELATIONS released by Stamford Research Labs of the American Cyanamid Co., which describes the possible positions of characteristic infrared absorption bands, the 2962 cm^{-1} peak seems to be the most reasonable reference peak. The NH band, which decreases as the reaction proceeds, may also appear at 1508 cm^{-1}. The C-N stretching, which increases with reaction, may appear at 1034 cm^{-1} and 1184 cm^{-1}. For this reason, the 2962 cm^{-1} peak, which is due to an aromatic vibration, was chosen as the reference peak in this study.

The thin film disk was cut into five pieces after being scanned in the FTIR. The small pieces of the sample were used to measure the dimensional change in the thickness when it was heated from room temperature to 350°C in a TMA furnace. A small tin ball was loaded on the top of the probe to ensure the proper contact between the probe tip and the sample surface. A temperature ramping rate of 10 °C per minute was used in the experiments. The glass transition temperature was determined from the TMA thermograph.

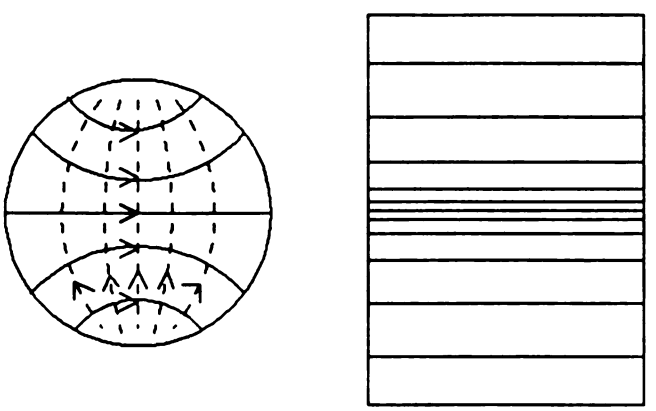

Figure 3.4. Electromagnetic Field Patterns for TE_{111} Mode in the Cylindrical Cavity

3.4 Results and Discussion

3.4.1 Reaction Kinetics

Infrared spectra of microwave and thermal cured DGEBA/DDS were compared to those of fresh samples, as shown in Figure 3.5. Figure 3.6 shows the comparison for the DGEBA/mPDA system. The transmission spectra of microwave and thermal cured samples showed no significant difference for both systems.

The extent of cure of both microwave and thermally cured samples at various times for the DGEBA/DDS and DGEBA/mPDA systems are shown in Figure 3.7 and Figure 3.8, respectively. The symbols th and mw mean thermal and microwave, respectively. The numbers after th and mw are the curing temperatures. The solid lines are the least-squares fit of the experimental data using the equation α=b1 (b2-b3 * exp(-b4 * t)), where b1, b2, b3, b4 are the fitted parameters and t is the curing time. Table 3.2 lists the fitted values of b1, b2, b3, and b4 and the standard deviation of the fit, ϵ, for each curing experiment. Low standard deviation of fit indicates a good fit between the experimental data and fitted lines. With thin film FTIR technique, DGEBA/mPDA system has been previously cured using both microwave and thermal energy[25]. As listed in Table 3.2, the standard deviation of microwave and thermal cure experiment at 120°C for the DGEBA/mPDA system are 0.032 and 0.047 respectively in this research. With the fitted expression obtained in this research to analyze the experimental data reported in the literature 25, the calculated standard deviation of microwave and thermal cure experiment at 120°C are 0.038 and 0.053. The comparison between the curing results in this research and the results reported in the literature 25 suggests that the curing using thin film FTIR technique is experimentally reproducible.

Table 3.2. The values of b1, b2, b3, b4 and ϵ from the least-squares fit

	b1	b2	b3	b4	ϵ^*
DDS,mw125	0.6161	0.9476	0.9491	0.0582	0
DDS,mw135	0.4064	1.5292	1.5249	0.1211	0.063
DDS,mw145	0.4713	1.9592	2.0298	0.1302	0.079
DDS,th135	0.5731	1.0867	1.0916	0.0369	0
DDS,th145	0.5478	1.1798	1.1862	0.0673	0.016
DDS,th165	4.7102	0.2106	0.2140	0.0931	0.027
mPDA,mw80	1.4783	0.6574	0.6641	0.0346	0.024
mPDA,mw100	0.0761	12.522	12.596	0.1300	0.028
mPDA,mw120	0.8430	1.1292	1.1218	0.4285	0.047
mPDA,th80**					0.029
mPDA,th100	2.7330	0.3382	0.3410	0.1001	0.043
mPDA,th120	9.2797	0.1011	0.1021	0.1862	0.032

* $e=\sqrt{\frac{1}{N-3}\sum(\alpha_{exp}-\alpha_{fit})^2}$, where N is the number of the data points.

** A polynomial fit was used in this case. The fitted equation is $\alpha=2.302\text{x}10^{-3} + 1.158\ \text{x}10^{-2}\ t - 2.250\text{x}10^{-4}\ t^2 + 1.324\text{x}10^{-5}\ t^3 - 1.698\text{x}10^{-7}\ t^4$. The standard deviation for this fit is $e=\sqrt{\frac{1}{N-5}\sum(\alpha_{exp}-\alpha_{fit})^2}$.

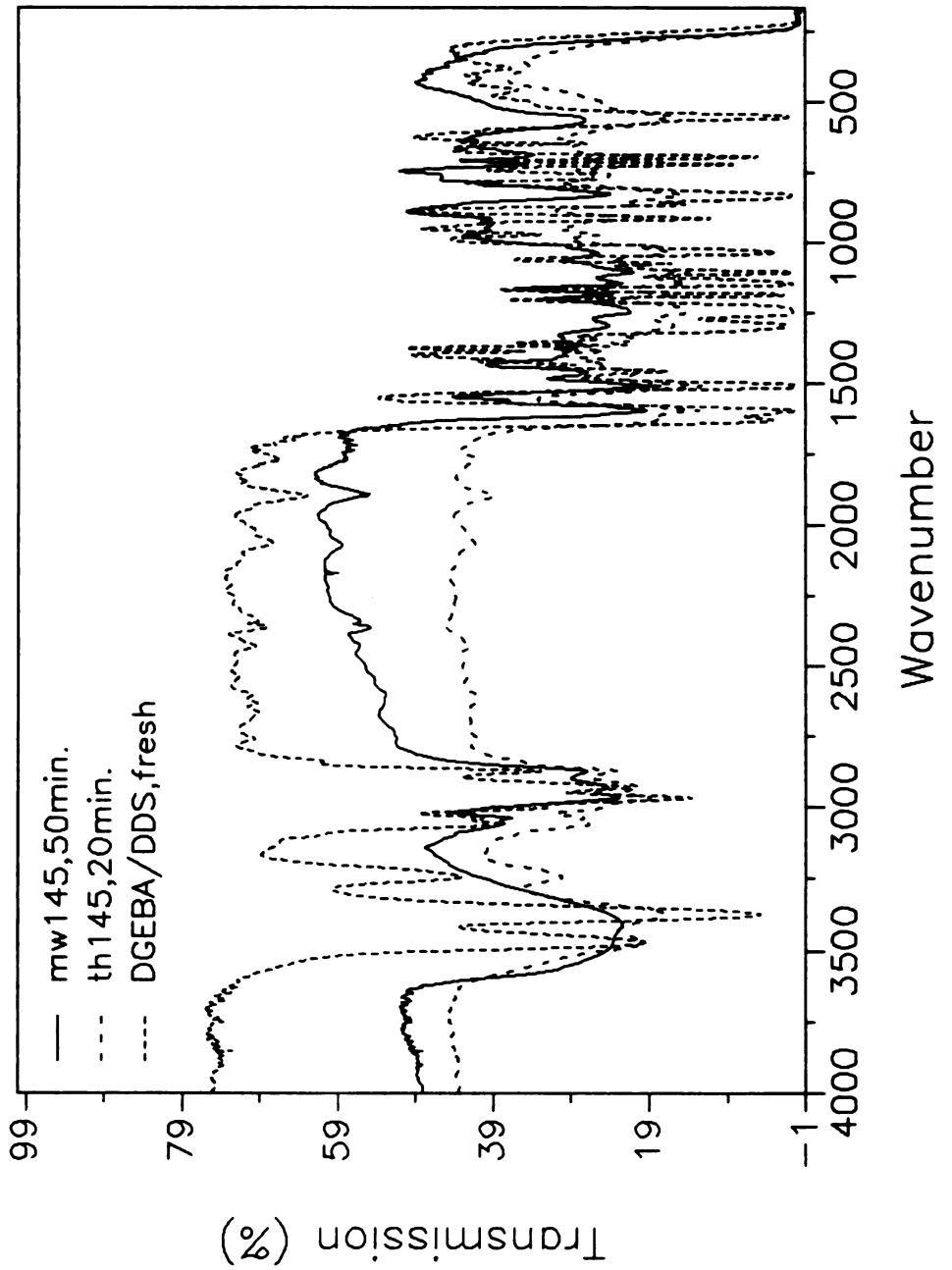

Figure 3.5. Comparison of FTIR Spectra of Microwave Cured, Thermal Cured, and Fresh DGEBA/DDS samples

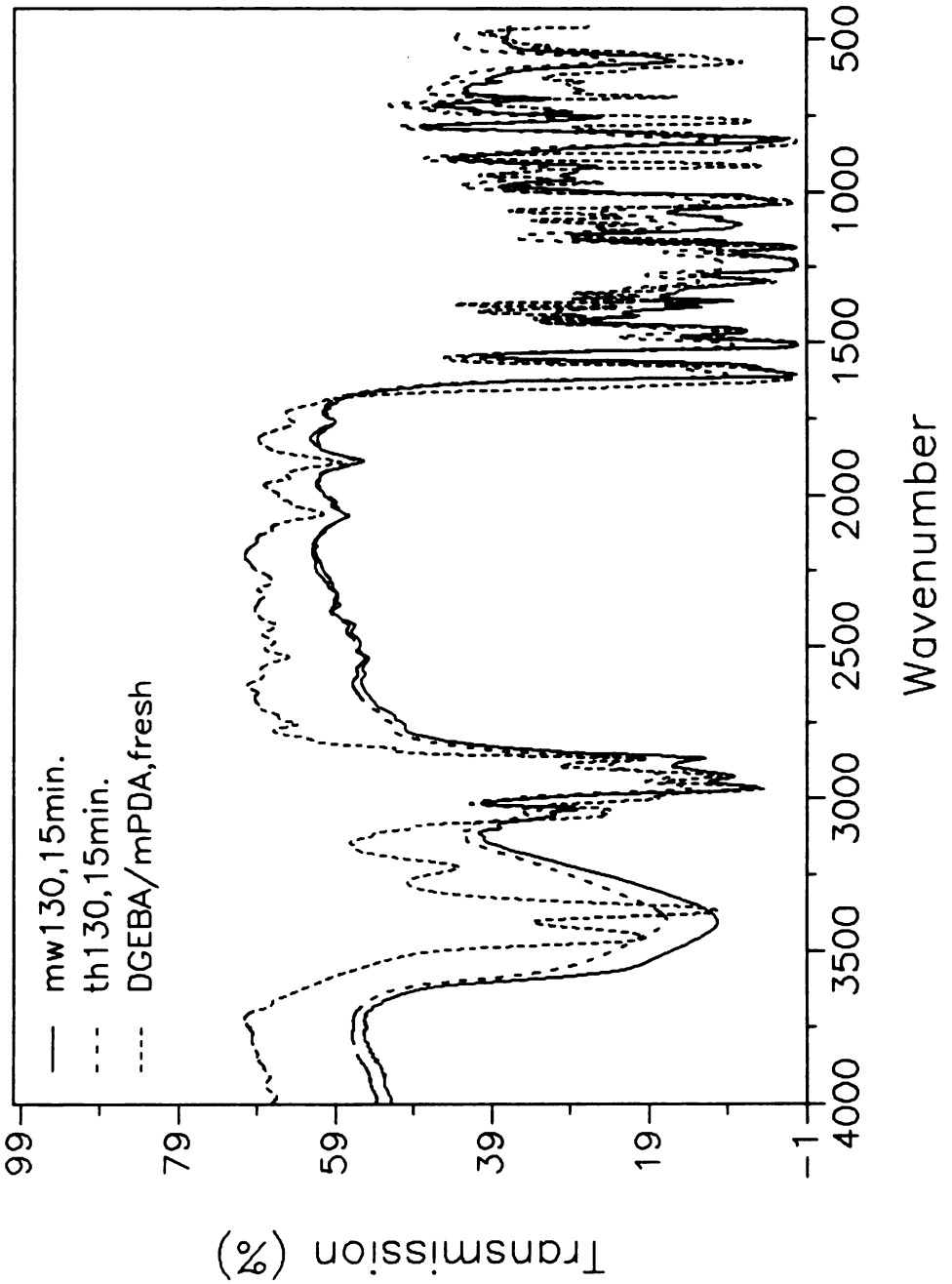

Figure 3.6. Comparison of FTIR Spectra of Microwave Cured, Thermal Cured, and Fresh DGEBA/mPDA samples

As seen in Figure 3.7 and Figure 3.8, instead of a decrease in the reaction rate in microwave cure as reported in some earlier work[18,19], microwave cure has a higher reaction rate when compared to that of thermal cure at the same cure temperature. This result agrees with results in most of the literatures[10,16,20,22,25].

Figure 3.7 shows the extent of cure versus time curves for the DGEBA/DDS system. Significant increases in the reaction rates for microwave curing were observed as compared to those for thermal curing at the same temperature. Figure 3.8 shows the extent of cure versus time curves for the DGEBA/mPDA system. Only slight increases in the reaction rates for the microwave curing were observed as compared to those for thermal curing at the same temperature. This may be due to the chemical structure difference in DDS and mPDA as shown in Figure 3.3. Apparently, the effects of microwave radiation on the cure of a thermosetting polymer depend on the particular curing agent used. The enhancement of the polymerization reaction rate of epoxy resins by microwave radiation is expected. Comparing the microwave and thermal heating mechanisms, microwave cure should have a faster reaction rate than thermal cure providing that the reaction pathway is the same for both microwave and thermal cure. For the same bulk cure temperature, the local molecular temperature will be higher in microwave heating than in the thermal heating due to the difference in microwave and thermal heating characteristics. In microwave cure, microwave radiation heats up polymer molecules directly due to the relaxation of the polarization of the polymer dipoles along the electric field. The measured bulk temperature therefore is less than the local molecular temperature which is the effective temperature for the polymerization reaction. On the other hand, the local molecular temperature is at most equal to the bulk temperature during the thermal cure.

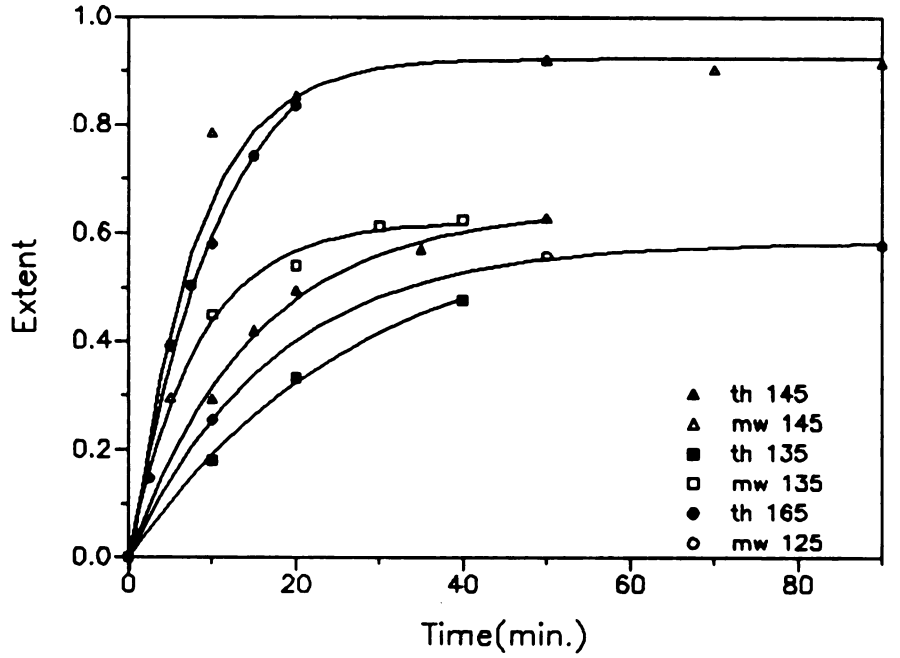

Figure 3.7. Reaction Rates of Microwave and Thermally Cured DGEBA/DDS

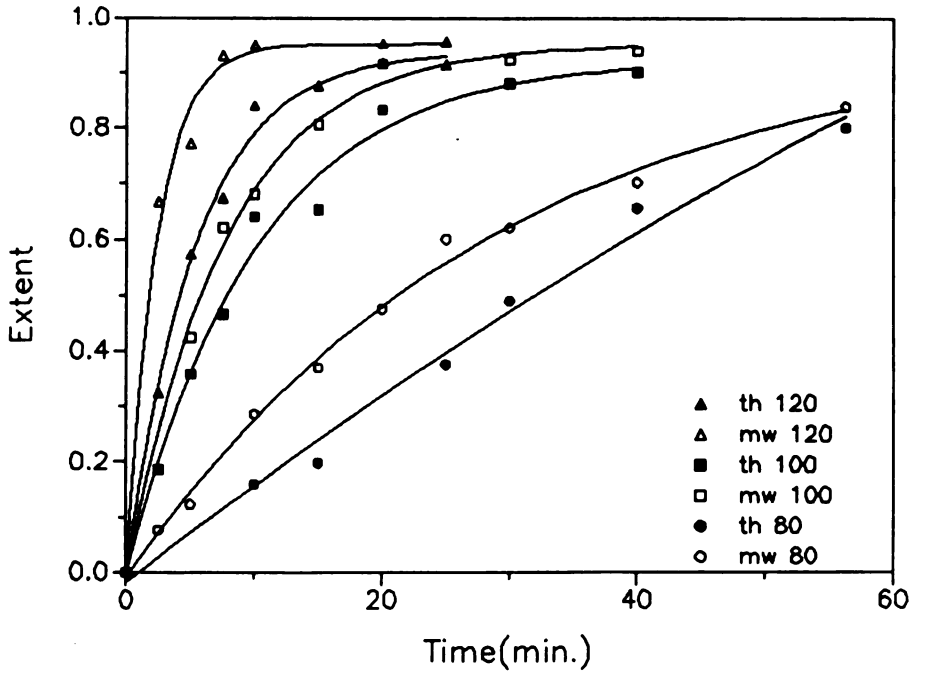

Figure 3.8. Reaction Rates of Microwave and Thermally Cured DGEBA/mPDA

The opposite results of Mijovic's work[18,19] may due to the following reasons:

a) Higher curing temperature in the thermal cure. Although the oven temperature is set equal to the microwave cure temperature, the sample temperature is higher than the oven temperature due to the heat released during exothermic reaction for the thermal cure, while the sample temperature can be controlled exactly at the desired cure temperature for microwave cure.

b) Due to a different reaction pathway for microwave and thermal cure. In the current work, the extent of cure is determined using FTIR and defined as one minus the ratio of residual amount of epoxide group to the initial amount of epoxide group. For Mijovic's work, the extent of cure is determined using DSC and defined as one minus the ratio of the residual exothermic heat to total exothermic heat of unreacted sample. One assumption in the DSC definition of the extent of cure is that there is no exothermic/endothermic reaction that does not involve epoxide. This may or may not be the case in both microwave and thermal cures. Clearly, the DSC measurements take into account of all reactions while the FTIR measurements only monitor the disappearance of epoxide group. If the Mijovic's DSC samples were taken from the area close to the temperature probe in microwave cured samples and from the surface in thermal cured samples, the opposite result of the extent of cure from FTIR and DSC suggests a different reaction pathway for microwave cure compared to thermal cure.

The fitted parameters in Table 3.2 are used to analyze the kinetics. Assuming that there is no steric hindrance and no etherification has occurred, that is $n=1$ and $L=0$, the reaction rate constants can be calculated from Equation (3-7) by plotting $d\alpha/dt/(1-\alpha)^2$ vs. α curves. The intercept is k_1 and the slope is k_2. Only the early portion of the $d\alpha/dt/(1-\alpha)^2$ vs. α curve is used because Equation (3-7) is not valid for systems having an etherification reaction, which may be significant when reacting systems reach high extent of cure, and because the diffusion effect becomes more

significant as the reaction proceeds. The activation energy E and pre-exponential constant A of k_1 and k_2 are obtained through a linear fit of ln(k) vs. 1/T.

Table 3.3 lists the calculated k_1 and k_2 for the DGEBA/DDS and the DGEBA/mPDA systems. The absolute values of k_1 and k_2 in the microwave cure were greater than those of thermal cure at the same cure temperature for both the DGEBA/DDS and the DGEBA/mPDA systems. Table 3.4 lists the activation energies and the pre-exponential constants for the DGEBA/DDS and DGEBA/mPDA systems calculated from Table 3.3. The α versus t curves were regenerated using parameters in Table 3.4. Figure 3.9 and 3.10 show the comparison between regenerated curves and the experimental data for the DGEBA/mPDA and the DGEBA/DDS systems respectively.

Table 3.3 Reaction Rate Constants for Both Thermal and Microwave Cure of DGEBA Reacting with DDS and mPDA With Assumption of n=1, L=0

	$k_1(min^{-1})$	$k_2(min^{-1})$	k_1/k_2
DDS, th135	0.0230	0.0090	2.56
DDS, th145	0.0435	0.0195	2.23
DDS, th165	0.0923	0.0972	0.95
DDS, mw125	0.0340	0.0087	3.91
DDS, mw135	0.0753	0.0258	2.92
DDS, mw145	0.120	0.116	1.04
mPDA, th80	0.00930	0.0941	0.0991
mPDA, th100	0.0341	0.383	0.0889
mPDA, th120	0.0640	0.721	0.0888
mPDA, mw80	0.0206	0.116	0.178
mPDA, mw100	0.0694	0.395	0.176
mPDA, mw120	0.133	1.97	0.0674

Table 3.4 Activation Energies and Pre-exponential constants

for DGEBA Reacting with DDS and mPDA With Assumption of n=1, L=0

	k_1 (min^{-1})		k_2 (min^{-1})	
	E(kcal/mol)	A	E(kcal/mol)	A
DDS, mw	21.0	9.745E+9	42.8	1.907E+21
DDS, th	16.1	1.085E+7	28.3	1.069E+13
mPDA,mw	12.9	2.185E+6	19.5	1.203E+11
mPDA,th	13.3	1.882E+6	14.1	5.768E+7

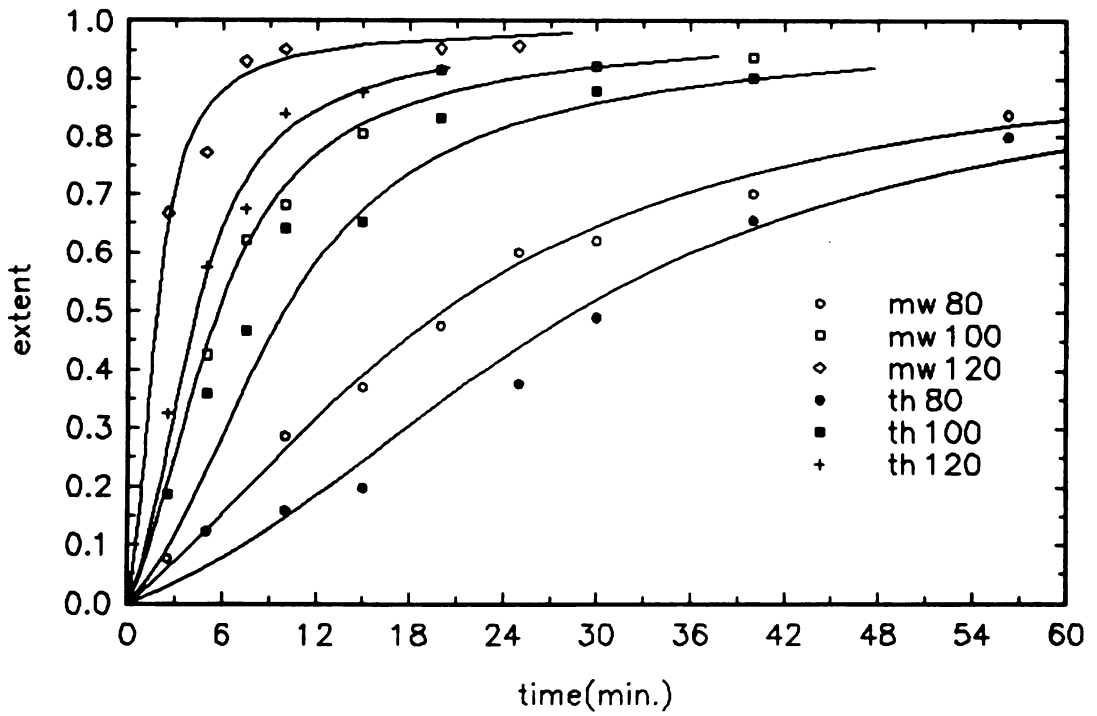

Figure 3.9 Regeneration of Reaction Rates for Microwave and Thermally Cure of DGEBA/mPDA From the Model Using n=1 and L=0

For the DGEBA/mPDA system, the reaction kinetics can be described well by Equation (3-7) for both microwave and thermal cure. This implies that for the stoichiometric DGEBA/mPDA system, the reaction rate constants of primary amine-epoxy are equal to secondary amine-epoxy and the etherification reaction can be neglected for both microwave and thermal cure in the temperature range studied. As listed in Table 3.3, the k_1/k_2 ratio of microwave cure is higher than that of thermal cure at low temperatures but lower than that of thermal cure at high temperatures. As listed in Table 3.4, the activation energy of k_2 is about the same for microwave and thermal cure while the activation energy of k_1 is larger for microwave cure than thermal cure for DGEBA/mPDA system. The reaction kinetics of thermal cure DGEBA/mPDA have been studied using DSC. The reported reaction rate constants are[77]

$$K_1 = 5.53 \times 10^8 \times \exp(-9763.5/T)$$

$$K_2 = 8.06 \times 10^5 \times \exp(-5737.3/T)$$

Comparing the above values of E to the values of E in Table 3.4, the activation energy of k_1 is lower in this study while E of k_2 is higher in this study. The difference may be due to the different definition of the extent of cure for DSC and FTIR.

Rewriting Equation (3-7) as

$$\frac{d\alpha}{dt} = k_2 \left(\frac{k_1}{k_2} + \alpha\right)(1-\alpha)(B-\alpha) \qquad (3\text{-}26)$$

For the DGEBA/mPDA system, the values of k_1/k_2 are small as compared one. Especially in the thermal cure of DGEBA/mPDA, k_1/k_2 is relatively independent of cure temperature and the value is about 0.09 as in Table 3.3. This means the reaction rate expression can be approximated by the product of two terms, one is a function of temperature and the other is a function of the extent of cure, α. The reaction can be described phenomologically by an n^{th} order kinetics model. Following the procedure described in section 3.2.1.1, the order of reaction and the parameters for the reaction

rate constants are calculated. Table 3.5 lists the calculation conditions and results. A master curve can be generated by combining n^{th} order reaction kinetics with the relationship between glass transition temperature and extent.

Table 3.5 Calculations based n^{th} order assumption for DGEBA/mPDA

	microwave cure	thermal cure
T_{ref} (°C)	100.0	100.0
α_{shift}	0.621	0.466
$(T_g)_{shift}$ (°C)	76.4	69.0
E (kcal/mole)	17.3	13.7
Correlation Coefficient for E	0.9995	0.9914
A ($min.^{-1}$)	2.42E+9	1.13E+7
Correlation Coefficient for A	0.9395	0.9672
n	1.6	1.5

For the DGEBA/DDS system, the reaction rates are not be described well by Equation (3-7) for both microwave and thermal cure as shown in Figure 3.10. At lower cure temperatures, Equation (3-7) overestimates the reaction rates. However, the overestimation was corrected at higher cure temperatures. This may be due to the fact that the reaction rate of primary amine-epoxy is larger than that of secondary amine-epoxy, that is $n<1$. At low cure temperatures, no etherification occurred and Equation (3-7) which assumes that $n=1$ overestimates the reaction rates. At higher cure temperatures, etherification reaction occurrs, i.e. L is not equal to 0. Since $n+L$ is closer to 1, the overestimation is partially corrected. To model the DGEBA/DDS system, Equations (3-12) to (3-14) should be used. For our system, $[OH]_o = 0$. Taking the derivative of Equation (3-14) with respect to time t, we obtain

$$\frac{d\alpha}{dt} = -\frac{(1-n)(2-L) + (n-L)\phi^{\frac{n-2}{2}} + (2-n)L\phi^{-1}}{2(2-n)}\frac{d\phi}{dt} \qquad (3\text{-}27)$$

combining Equation (3-27) with (3-12) and (3-13), we have $d\phi/dt = f(n,L,\phi)(k_1 + k_2F(\phi))$.

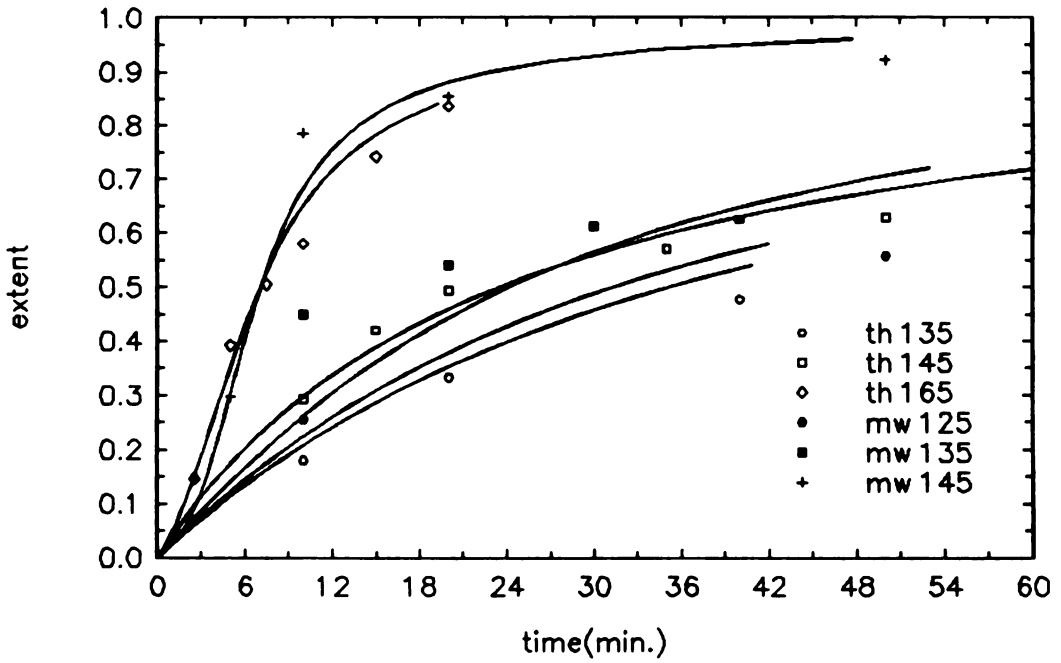

Figure 3.10 Regeneration of Reaction Rates for Microwave and Thermally Cure of DGEBA/DDS From the Model Using n=1 and L=0

At low cure temperatures, L=0 and $F(\phi)=\alpha$. n and L can be obtained by a least-squares fit of experimental data to Equation (3-12), (3-13) and (3-14). The procedure is

1) Assuming an n and L, an expression for $d\phi/dt$ as function of ϕ can be obtained from experimental data and Equation (3-27).

2) Obtain k_1 and k_2 values for all temperatures by plotting $d\phi/dt/f(n,L,\phi)$

versus $F(\phi)$ by varying ϕ from 1.0 to 0.0. Calculate the activation energies and pre-exponential constants of k_1 and k_2.

3) Regenerate the α vs. t curve by using assumed n,L and the calculated reaction constant parameters. Compare the regenerated values with experimental results.

4) Repeat the above procedures with new n and L until the regenerated values match the experimental data.

The reaction rate constants and the calculated parameters for DGEBA/DDS are listed in Table 3.6 and Table 3.7 respectively.

As listed in Table 3.6, the reaction rate constants of microwave cure were higher than those of thermal cure at the same cure temperature for the DGEBA/DDS the system. However, the values of k_1/k_2 were lower in microwave cure than in thermal cure. In other words, the microwave radiation enhances the catalytic reaction of DGEBA/DDS system more than the non catalytic reaction, just as for the DGEBA/mPDA system. The activation energies of microwave cure are higher than those of thermal cure, for both k_1 and k_2, as listed in Table 3.7. While microwave radiation increases the reaction rate constant of primary amine-epoxy reaction as listed in table 3.6, it decreases the reaction rate ratio of secondary amine-epoxy reaction to primary amine-epoxy reaction, n, and reaction rate ratio of etherification to primary amine-epoxy reaction, L, as listed in Table 3.7. The absolute value of the reaction rate constant for the secondary amine-epoxy reaction, nk_1, nk_2, and etherification reaction nL, are still larger in microwave cure than in thermal cure. Figure 3.11 shows the comparison of the calculated α vs. t curves based on the kinetics model with $n \neq 1$, $L \neq 0$ and the experimental data for both microwave and thermal cure of DGEBA/DDS systems. Good agreement is found between the two.

Table 3.6 Reaction rate constants for DGEBA/DDS system

	k_1 (min^{-1})	k_2 (min^{-1})	k_1/k_2
mw125	0.0338	0.0448	0.754
mw135	0.0749	0.1107	0.677
mw145	0.1190	0.2701	0.440
th135	0.0229	0.0251	0.912
th145	0.0434	0.0510	0.851
th165	0.0917	0.1793	0.511

Table 3.7 Calculated reaction kinetics parameters for DGEBA/DDS system

		microwave	thermal
n		0.15	0.4
L^*		0.6	0.8
k_1	E (kcal/mole)	20.9	16.1
	A (min^{-1})	1.001E+10	9.946E+6
k_2	E (kcal/mole)	29.7	23.2
	A (min^{-1})	9.156E+14	7.063E+10

* etherification reaction only occurred at high cure temperature, that is at 145°C for microwave and 165°C for thermal cure.

All of the reaction kinetic parameters for the DGEBA/DDS and DGEBA/mPDA systems are listed in Table 3.8 for easy comparison. For DGEBA/mPDA, both microwave and thermal cure have the same reaction rate for primary and secondary amine and a negligible etherification reaction. For this system, the activation energy E for k_1 is about the same for both microwave and thermal cure while the activation energy E for k_2 is higher in microwave cure than

thermal cure. The same values of n and L imply a similar network structure for microwave and thermally cured DGEBA/mPDA. Similar Tg versus α data is expected from microwave and thermally cured DGEBA/mPDA samples. For the DGEBA/DDS system, n and L of microwave cure are less than those of thermal cure. For this system, the activation energy E for both k_1 and k_2 are higher in microwave cure than in thermal cure. The different values of n and L may result in a different crosslinked network structure in microwave and thermal cured DGEBA/DDS. The lower values of n and L suggest that the primary amine-epoxy reaction is more dominant in microwave cure than in thermal cure as compared to secondary amine-epoxy and etherification reactions. This implies that the epoxy molecules have a better chance to form a long linear chain through reacting with primary amine at both ends before crosslinking in the microwave environment. The network structure will have higher T_g if the two crosslinks are one at each end rather than both at one end[84]. Also, the linear chains in the microwave cured epoxy are aligned with the applied electric field due to the effect of molecular polarization of both epoxide and amine molecules. This alignment creates an oriented crosslinking network structure which also increases the T_g of the cured epoxy. Therefore, higher T_g is expected for microwave cured DGEBA/DDS than thermally cured samples. Polarization of molecules under microwave radiation may also lead to a different reaction pathway from that of thermal cure.

Table 3.8 Reaction kinetic parameters for both DGEBA/DDS and DGEBA/mPDA systems

		DGEBA / mPDA		DGEBA / DDS	
		microwave	thermal	microwave	thermal
n		1.0	1.0	0.15	0.4
L		0	0	0.6	0.8
k_1	E (kcal/mole)	12.9	13.3	20.9	16.1
	A (min^{-1})	2.185E+6	1.882E+6	1.001E+10	8.975E+6
k_2	E (kcal/mole)	19.5	14.1	29.7	23.2
	A (min^{-1})	1.203E+11	5.768E+7	9.156E+14	7.063E+10

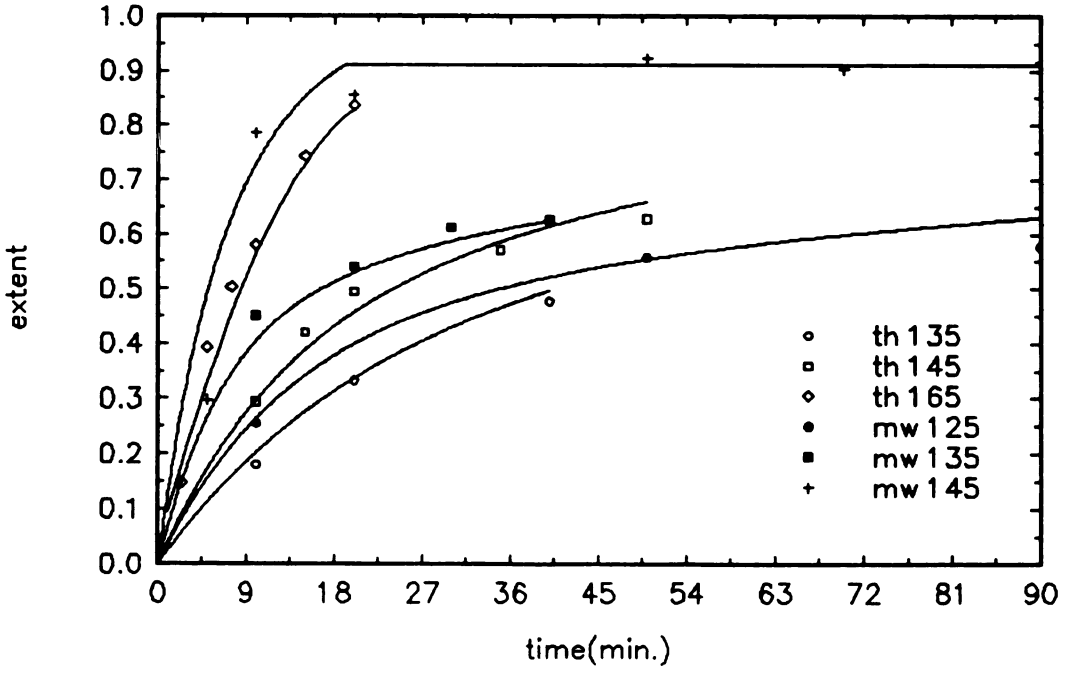

Figure 3.11 Regeneration of Reaction Rates for Microwave and Thermally Cure of DGEBA/DDS From the Model Using $n \neq 1$ and $L \neq 0$

3.4.2 Glass transition temperature

The glass transition temperature, T_g, is defined as the temperature where the step transition of the thermal expansion coefficient occurs on the TMA thermograph, as shown in Figure 3.1 and Figure 3.2. Figures 3.12 and Figure 3.13 show the Tg versus extent of cure for the DGEBA/DDS and DGEBA/mPDA system, respectively. While similar glass transition temperatures for microwave and thermally cured samples were obtained at low conversion, higher T_g's were observed in microwave cured samples at an extent of cure higher than α_{gel}, which occurs at α=0.58. The increase is significant in the DGEBA/DDS system but small in the DGEBA/mPDA system. The increase of T_g in the microwave cured epoxy at high extent may be due to the different polymer crosslinked network structures in the microwave cured samples as discussed earlier. A similar T_g at low extent of cure implies that the difference between microwave and thermal cured epoxy at this level is not significant enough to cause any difference in T_g. Apparently, the microwave radiation effect is stronger in DDS cured epoxy than in mPDA cured epoxy. The different effect of microwave radiation on T_g of DDS and mPDA cured epoxy may be due to the different network structure resulting from the microwave environment for the two systems as speculated in the kinetics analysis. Other techniques, such as a polarized infrared technique, wide-angle X-ray diffraction, or solid state Nuclear Magnetic Resonance (NMR) are required to detect these structure differences in the cured polymer samples.

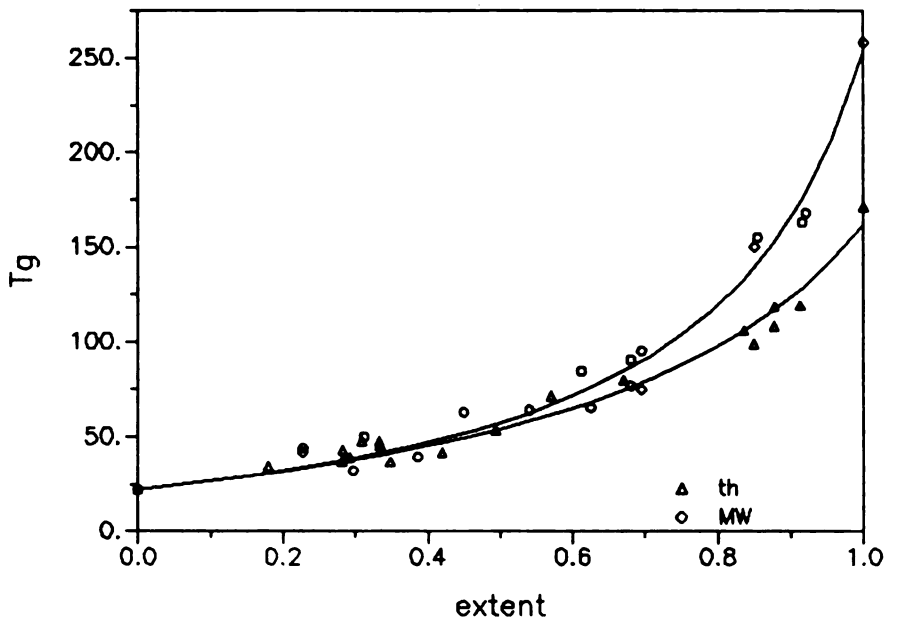

Figure 3.12. Comparison of Tg of Microwave and Thermally Cured DGEBA/DDS

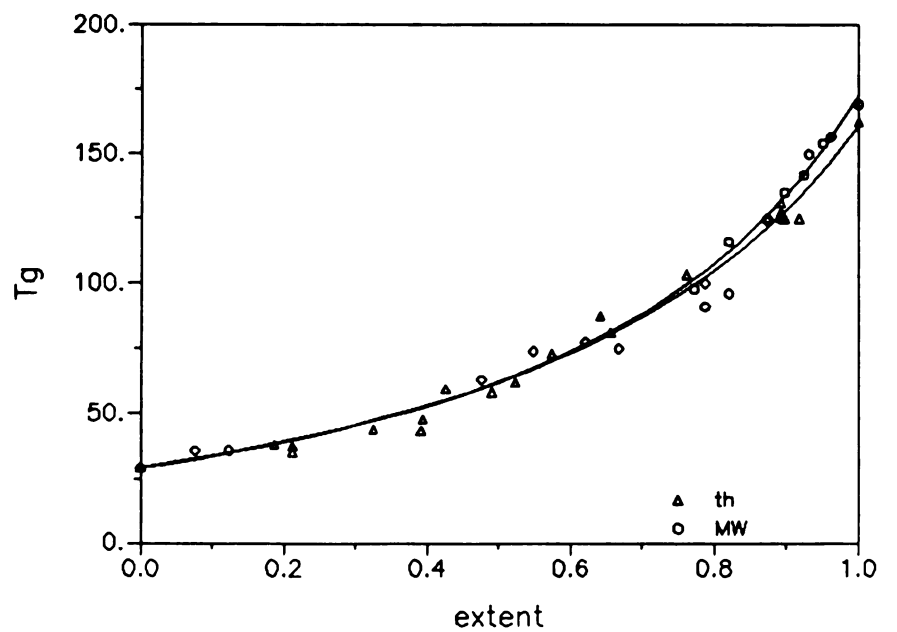

Figure 3.13. Comparison of Tg of Microwave and Thermally Cured DGEBA/mPDA

Another interesting phenomenon is that microwave radiation affects Tg in the same fashion as it does the reaction rates. The magnitude of increase in Tg by microwave radiation is much higher in the DDS cured epoxy than in mPDA cured epoxy, just like the microwave radiation effect on the reaction rate. DiBenedetto's model was used to fit the TMA- determined Tg data. Table 3.9 lists the experimentally determined Tg_o, Tg_∞, and the estimated values of Ex/Em, Fx/Fm, along with the values reported in the literaure. As listed in Table 3.9, the values of Ex/Em and Fx/Fm are lower in the microwave cured samples than in the thermally cured ones. As Em and Fm are the same for both microwave and thermal cure, the lattice energy and the segmental mobility of fully cured epoxy are lower in microwave cure than in thermal cure for both systems. The magnitude of decrease is more significant in the DGEBA/DDS system than in the DGEBA/mPDA system. The lower segmental mobility in the microwave cured sample may be due to a more rigid network as a result of an oriented network structure. The ratio of segmental mobility of the fully cured to unreacted epoxy resins, F_x/F_m, has been related to the ratio of the isobaric heat capacities of the fully cured to the initial systems, λ[95].

$$\lambda = \frac{\Delta C_{p\infty}}{\Delta C_{po}} = \frac{F_x}{F_m} \qquad (3\text{-}28)$$

Where $\Delta C_{p\infty}$ and ΔC_{po} are the isobaric heat capacities of the fully cured and the initial systems, respectively. λ is smaller for the microwave cured samples than for the thermally cured samples. This is a possible reason why the T_g transition in the DSC thermograph is more difficult to observe in the microwave cured epoxies than in the thermal cured samples.

Table 3.9. The Parameters for DiBenedetto Model

System	Tg_o(°C)	Tg_∞(°C)	method	E_x/E_m	F_x/F_m	ref.
DGEBA/DDS, MW	22.2	258.3	TMA	0.32	0.18	this
DGEBA/DDS, Th	22.2	171.4	TMA	0.44	0.30	this
DGEBA/DDS, Th	5		DSC	0.751	0.419	[34]
DGEBA/DDS, Th	11	189		1.21	0.74	[107]
DGEBA/DDS, Th	0	190	DSC			[14]
DGEBA/DDS, MW	0	190	DSC			[14]
DGEBA/DDS, Th		210	TBA*			[108]
DGEBA/DDS, Th		183	DSC			[109]
DGEBA/DDS, Th		184	**			[110]
DGEBA/DDS, Th	0		DSC	0.3	0.18	[111]
DGEBA/mPDA, Th		158	DSC			[27]
DGEBA/mPDA, Th		150	TBA			[50]
DGEBA/mPDA, Th		163	DSC			[51]
DGEBA/mPDA, MW	29	169.2	TMA	0.44	0.30	this
DGEBA/mPDA, Th	29	162.3	TMA	0.48	0.34	this

* Torsional Braid Analysis
** Dynamic Mechanical Test.

3.4.3 Master Curve and TTT diagrams

The master curve and the time-temperature-transformation (TTT) diagram are commonly used to interpret the curing process[76]. The master curve describes the relation between glass transition temperature (Tg) and cure time (t) at a reference temperature. The Tg versus t curves at other temperatures can be obtained from the master curve and the shifting factors which are calculated from the kinetics data. A master cure is only possible when the kinetics can be expressed in the form of Equation (3-1). Therefore, only master curves for microwave and thermal cure of DGEBA/mPDA were generated. From the kinetics expression, Equation (3-2), and the DiBenedetto model, the master curves at a reference temperature of 120°C were constructed for DGEBA/mPDA system.

Figure 3.14 shows the master curves for both microwave and thermal cure of DGEBA/mPDA at a reference temperature of 120°C. The data points are experimental results obtained from α versus t and Tg versus α relations. The solid lines are calculated from the modeling, Equations (3-2) and (3-24) and the kinetics parameters listed in Table 3.5. The modeling results were compared to the experimental data and a good agreement was found for both microwave and thermal cure. Clearly, microwave cure is faster than thermal cure. Using the vitrification point as a reference, for example, the time to reach vitrification is about 5 min. and 12 min. for microwave and thermal cure, respectively. Microwave cure is more than twice as fast as thermal cure at 120°C.

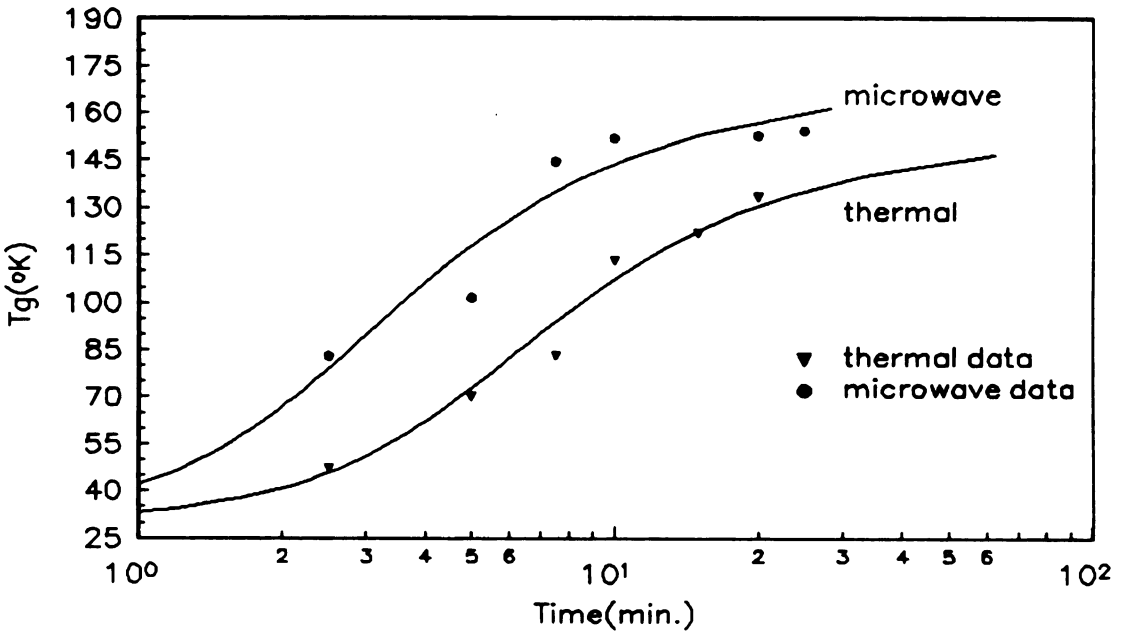

Figure 3.14. Master Curves for Microwave and Thermal Cure of DGEBA/mPDA at Reference Temperature of 120°C

Figure 3.15 shows the TTT diagrams for both microwave and thermal cure of DGEBA/mPDA. Again, the point data are experimental values. The solid lines are calculated based on Equation (3-7) and Equation (3-24). The vitrification time at a given cure temperature was calculated based on the definition that vitrification occurs when Tg equals the cure temperature. **mw vitrification curve 1 and th vitrification** are vitrification lines based on this definition for microwave and thermal cure. The calculated vitrification curves agree with the experiment data very well. Figure 3.15 shows that the time to gelation is shorter in microwave cure than in thermal cure, especially at high cure temperatures. The vitrification times in microwave cure are shorter than in thermal cure, and the time difference between the two increases with cure temperature. The cure temperatures which display the minimum vitrification times are about 152°C and 131°C for microwave and thermal cure, respectively. The corresponding vitrification times are 2.4 min. and 12.6 min. for microwave and thermal cure respectively. This implies that the processing time can be reduced by

approximately a factor of five when conventional thermal heating is replaced by microwave heating.

The decrease in the vitrification time in the microwave cure is due to the increase of reaction rate and Tg. The Tg of microwave cured samples are higher than those of thermally cured samples at the same extent of cure. The extent of cure at vitrification is, therefore, lower in the microwave cure than in the thermal cure. In consideration of this effect, the vitrification for microwave cure was redefined as the point when the extent of cure of microwave cure is equal to the vitrification extent of thermal cure at the same cure temperature. With this definition, the microwave vitrification curve only take into account the effect of faster reaction rates caused by microwaves. The curve, **mw vitrification curve 2**, was calculated based on the new definition of vitrification for microwave cure. Comparing this curve to the thermal vitrification curve, the minimum vitrification times for microwave and thermal cure are observed at approximately the same temperature. The new cure temperature which has minimum vitrification time for microwave cure is 137°C. The corresponding vitrification time is 4.7 min. Based on this definition of the vitrification for microwave cure, the processing time is reduced by approximately a factor of two when conventional thermal heating is replaced by microwave heating. Clearly, from curve **th. vitrification** to curve **mw vitrification 2**, the shortening of processing time is due to the increase of reaction rate by microwave radiation. From curve **mw. vitrification 2** to curve **mw vitrification 1**, the shortening of processing time is due to the increase of Tg by microwave radiation. Also the increase of reaction rate only shorten the processing time while the increase of Tg not only shorten the processing time, but also increase the cure temperature which display the minimum vitrification time.

Figure 3.16 shows the TTT diagram for microwave and thermal cure of the DGEBA/DDS system. The notation in Figure 3.16 is the same as in Figure 3.15. Only one experimental data point of vitrification can be obtained from Figure 3.7,

because the curing at the other temperature was not long enough to achieve vitrification. Again, the data points are experimental results. The solid lines are reconstructed from the kinetics expressions, Equations (3-12) to (3-14), the DiBenedetto model, Equation (3-24), and fitted parameters in Table 3.8 and Table 3.9.

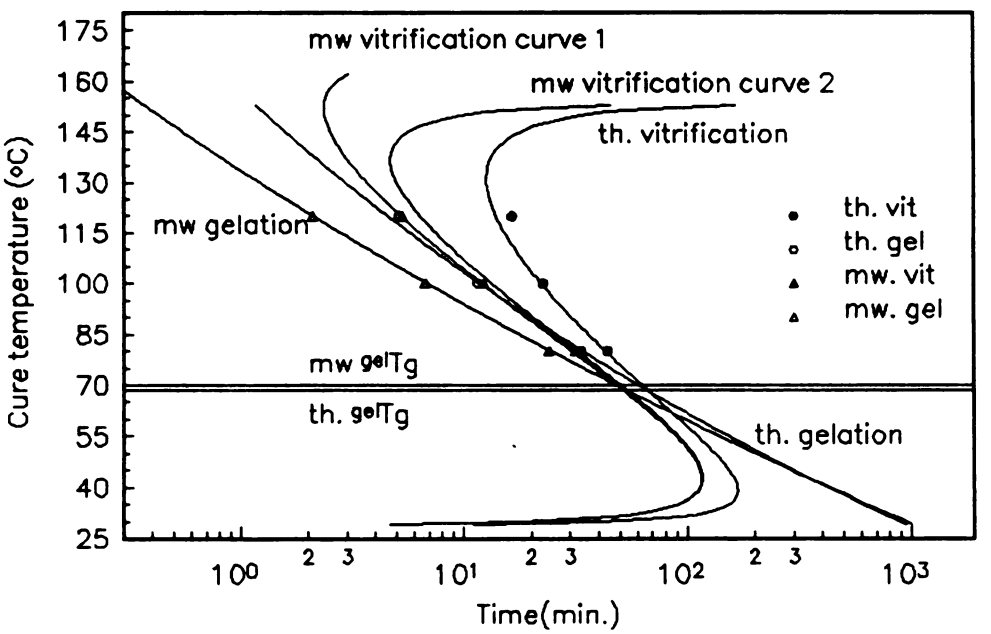

Figure 3.15. TTT Diagrams for Both Microwave and Thermal Cure of DGEBA/mPDA System

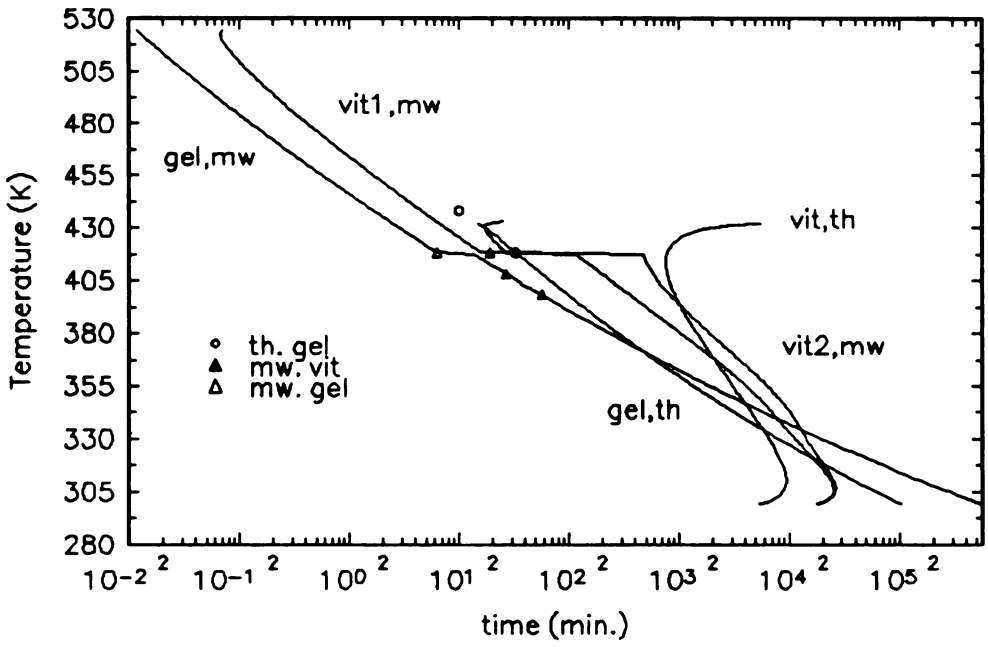

Figure 3.16. TTT Diagrams for Both Microwave and Thermal Cure of DGEBA/DDS System

No analytical expression can be derived in the calculation of vitrification and gelation curves for DGEBA/DDS system. Numerical methods have to be used in these calculations. The FORTRAN code for this calculation is listed in Appendix I. The calculating procedure is

1) Determine the extent of cure at vitrification for a given cure temperature using Equation (3-24).

2) Calculate the extent vs. time curve using Equations (3-12) to (3-14). The time required to reach gelation and vitrifications at that temperature are recorded.

3) Repeat for the next temperature.

In our experiments, the etherification reaction is only significant at high cure temperatures, that is, above 145°C for microwave cure and 165°C for thermal cure. In the generation of the TTT diagrams, the reaction rate constant ratio of etherification to primary amine-epoxy reaction, L, is considered to be zero for low temperatures. The jump of the gelation and vitrification curves for the microwave cure at 145°C is due to the introduction of a non zero L. In reality, L is a function of temperature and both gelation and vitrification curves are smooth curves. To observe this, more isothermal cures are needed above 135°C. A good agreement is found between experimental data and calculated curves based on the models.

The temperature for the simultaneous occurrence of gelation and vitrification, ${}^{gel}T_g$, can be determined using Equation (3-24) with $\alpha=\alpha_{gel}$. They are 67°C and 62°C for microwave and thermal cure of DGEBA/DDS respectively. Comparing the microwave vitrification curve, **vit1,mw**, and thermal vitrification curve, **vit,th**, the minimum vitrification time is much smaller in microwave cure than in thermal cure as shown in Figure 3.16. Also the cure temperature at minimum vitrification is much higher in microwave cure than in thermal cure. For thermal cure, the minimum

vitrification time is 758.9 min., occurring at the temperature 140°C and an extent of 0.951. For microwave cure, the minimum vitrification time is 0.067 min., occurring at the temperature 249°C and an extent of cure of 0.998. Once again, the processing time is reduced dramatically by using microwave energy. Microwave radiation increases both the reaction rate and T_g of cured epoxy. The **vit1,mw** curve includes both effects. The T_g effects on the vitrification curve can be eliminated by redefining the microwave vitrification as discussed earlier. The **vit2.mw** curve only includes the enhancement of reaction rate effect during microwave cure. Based on this definition, the minimum vitrification time is 17 min. occurring at 157°C. The processing time is reduced by 44.6 times only through the increase of the reaction rate by using microwave energy.

Both Figure 3.15 and Figure 3.16 show that microwave radiation shortens the minimum vitrification time in two ways. One is through the enhancement of the reaction rate. The other is through increasing T_g of the cured epoxy. Apparently, the effect of microwave radiation is much more significant in the DGEBA/DDS system than in the DGEBA/mPDA system. This may be due to the fact that DDS has a much higher dipole moment than mPDA. The dipole moment ratio of DDS:mPDA:DGEBA is 19.8E-30:4.95E-30:8.5E-30 C-m[112,113]. Other possibilities for stronger microwave effects in the DDS system are the activity of the SO_2 group in DDS and the inhibiting effect of the proximity of amines in mPDA. More research needs to be carried out to determine the key functional groups responsible for microwave radiation effects.

3.5 Conclusions

Stoichiometric mixtures of DGEBA/DDS and DGEBA/mPDA epoxy resins have been prepared using a thin film technique. Parallel samples were cured in a

cylindrical resonant cavity resonating in a TE_{111} mode and a conventional thermal oven. FTIR was used for measurement of the extent of cure and TMA was used for determination of T_g. Faster reaction rates were observed in the microwave cure when compared to those of thermal cure at the same cure temperature for both systems. Effects of microwave radiation on the cure of thermosetting polymers depends upon the curing agent used. Similar values of Tg were obtained for microwave and thermal cure at low extent of cure while higher Tg have been observed in microwave cure at extent of cure greater than α_{gel}. Microwave radiation has stronger effects in the DGEBA/DDS system than the DGEBA/mPDA system. Tg data of microwave cured samples were fitted by the DiBenedetto model. The full-cure epoxy-monomer lattice energy is lower in microwave cure than in thermal cure and the full-cure epoxy-monomer segmental mobility is lower in microwave cure than in thermal cure for both the DGEBA/DDS and DGEBA/mPDA systems.

It has been demonstrated that the cure kinetics of DGEBA/mPDA and DGEBA/DDS systems can be described by an autocatalytic kinetic model up to vitrification in both microwave cure and thermal cure. For the stoichiometric DGEBA/mPDA system, the reaction rate constants of primary amine-epoxy are equal to secondary amine-epoxy and the etherification reaction is negligible for both microwave and thermal cure. For the stoichiometric DGEBA/DDS system, the reaction rate constants of primary amine-epoxy are greater than those of secondary amine-epoxy and the etherification reaction is only negligible at low cure temperatures for both microwave and thermal cure. Microwave radiation decreases the reaction rate constant ratio of primary amine-epoxy to secondary amine-epoxy and the ratio of primary amine-epoxy to the etherification reaction. Microwave radiation increases the activation energies of both k_1 and k_2 in the DGEBA/DDS system while it only increases the activation energy of k_2 in DGEBA/mPDA system. The vitrification time is shorter in microwave cure than in thermal cure, especially at higher isothermal cure temperatures.

CHAPTER 4

MICROWAVE PROCESSING OF UNIDIRECTIONAL AND CROSSPLY CONTINUOUS GRAPHITE FIBER/EPOXY COMPOSITES

4.1 INTRODUCTION

The advantages of microwave curing over thermal curing of epoxy resins have been discussed in Chapter 3. This chapter discusses the feasibility of processing continuous graphite fiber/epoxy composite using microwave energy in a 17.78 cm resonant microwave cavity. The microwave radiation effects on the mechanical properties of the microwave processed composite are also discussed.

Based on their investigation using a waveguide and continuous graphite fiber/epoxy laminates, Lee and Springer[8] have reported that heating in a microwave environment is effective only for unidirectional composites exposed to linearly polarized TEM waves having a polarization angle of 90 degrees, and a laminate thickness limitation of about 32 plies. Lee has also studied the microwave processing of graphite/epoxy composites using a commercially available microwave oven[4] and has reported that the microwave curing of multidirectional graphite epoxy composites was not successful. Using a tunable resonant microwave cavity, Vogel[27] has reported that 7.62 x 7.62 cm, 24 ply unidirectional graphite fiber/epoxy composites can be successfully cured using microwaves with a relatively low input power. The heating rate and the cure uniformity of the composite are strongly dependent upon the electromagnetic processing mode.

For a given epoxy resin, the mechanical properties vary with the extent of cure. Theoretically, mechanical strength should increase with increasing extent of cure as the covalent bonds in a crosslinked network are much stronger than the Van

Der Waals forces in a non-crosslinked structure. In reality, however, the strengths of thermally cured resins increase with increasing extent of cure only to a certain point and then begin to fall off[114,115,116]. This is attributed to submicroscopic cracks induced by the internal thermal stresses resulting from resin shrinkage and non-uniform temperature distribution during cure[114]. A similar trend was also observed for thermally processed graphite fiber/epoxy composites[116]. The strengths of microwave cured epoxy resins, however, did not exhibit this trend, but rather showed consistently increasing strength with increasing extent of cure[115].

A tunable microwave resonant cavity operating at 2.45 GHz has been developed and successfully used to transfer microwave energy efficiently into loaded materials and control the heating process by maintaining a selected resonant electromagnetic field during cure[35,117,118,119]. To further demonstrate the feasibility of microwave processing of graphite fiber/epoxy composites in a tunable resonant cavity, this study focuses on the microwave cure of 24-ply unidirectional and crossply graphite fiber/epoxy composites and the effects of the resonant cavity mode on the mechanical properties of microwave cured composites. Parallel thermal processing was conducted for comparison of mechanical properties. The ability to cure relatively thick, 72 ply crossply and unidirectional laminates is also demonstrated.

4.2 EXPERIMENTS

Microwave curing experiments were performed using a 17.78 cm diameter tunable resonant microwave cavity. The microwave processing and diagnostic system used was the 2.45 GHz system described in Chapter 2. A coaxial switch (micronetics RSN-2D-I/12V) was used to turn microwave power on and off to maintain isothermal conditions. This switch was regulated by a dc power supply (Electronic Measurements HCR-30-8-111) that was controlled by an I/O interface board (Omega DAS-16) in a personal computer. Actuation of the on/off switch was

in response to a temperature feedback from a fluoroptic temperature sensing system (Luxtron 750).

Figure 4.1 shows the layup configuration of the composite laminates before microwave processing. Commercially available, continuous, graphite fiber/epoxy prepreg (Hercules AS4/3501-6) was used for this study. The physical and chemical properties of this material are available in the literature[120]. Unidirectional prepreg tape was cut into 7.62 x 7.62 cm square sheets (about 1.5 grams/ply in weight and 0.21 mm/ply in thickness) and stacked with either uni- or crossply fiber orientation. The composite laminate was then surrounded with an adhesive cork dam to prevent composite deformation by not allowing excess epoxy resin flow through the edges during cure. A porous teflon release film was placed on the top and bottom of the laminate and several layers of polyester bleeder cloth (one layer of bleeder cloth for every four plies of composite) were laid below the bottom porous film. A nonporous teflon release film was then placed on each side.

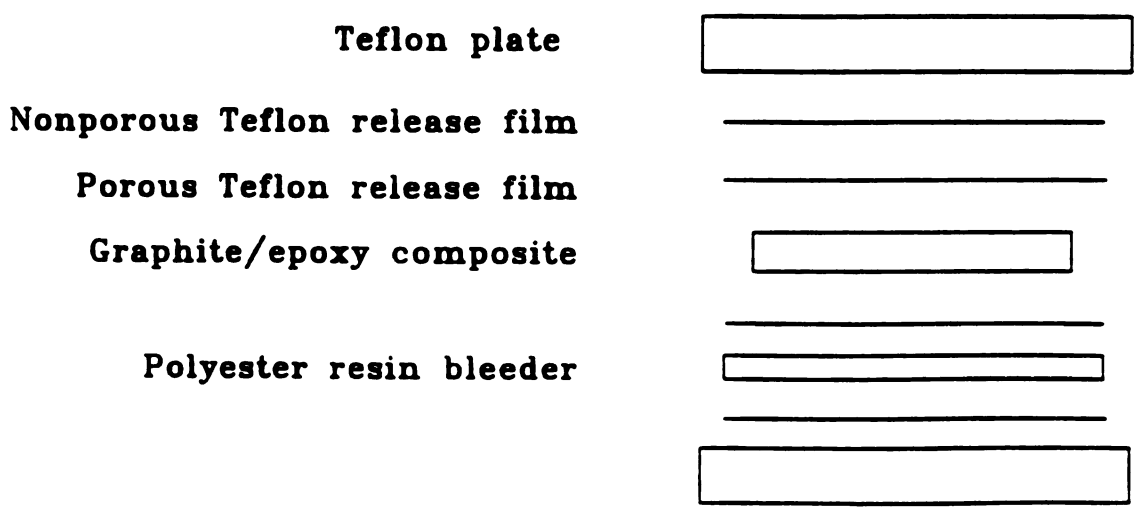

Figure 4.1 Composite Layup for Microwave Process

The whole composite panel was sealed in a polyamide vacuum bag under a vacuum pressure of 85 kPa (25.0 in Hg) and was packed between two teflon plates (1.5" in thickness and 5.0" in diameter) to reduce the heat loss during microwave processing. The bottom Teflon plate also lifted the composite laminate to a location having a stronger electric field strength since the tangential electric field strength at the bottom plate of the cavity is zero. The coupling probe was located slightly higher than the composite laminate. The fluoroptic temperature probes from the temperature sensing system were placed in contact with the top surface of the composite panel by insertion through the top teflon plate. Glass capillary tubes were used to protect the probe tips from encasement in the composite. The laminate assembly was then loaded into the bottom of the microwave cavity for processing. The configuration for comparative thermal processing was the same as in Figure 4.1 except that no Teflon plates were used.

4.2.1 Resonant Heating Mode Selection and Maintenance

Low power swept-frequency microwave energy was coupled into the loaded cavity and was used to locate the resonant heating mode. The swept-frequency power reflected from the loaded cavity was shown as a curve of power absorption versus frequency on an X-Y oscilloscope. The point of minimum reflected power was indicative of a resonant mode and therefore called a resonant peak. For an empty cavity, the point of zero power reflection was indicative of a critically coupled resonant mode, as shown in Figure 4.2. Both over and under coupling resulted in a non-resonant field pattern inside the cavity and exhibited a certain amount of reflected power. When either a unidirectional or crossply composite was loaded into the cavity, a non-resonant power absorption curve was usually observed on the oscilloscope as shown in Figure 4.3 at the critical cavity length and coupling probe depth of an empty cavity mode. However, a resonant power absorption curve with several resonant peaks could be generated by adjusting the cavity length and coupling

probe depth. Most of the resonant heating modes at 2.45 GHz found in the cavity length range of 9 to 15 cm in the 17.78 cm cavity have been used to process 24 ply unidirectional and crossply composites. Once the resonant heating mode, either PS, or CH, or UH, was selected, the low power swept-frequency source was replaced by a high power, 2.45 GHz single frequency source.

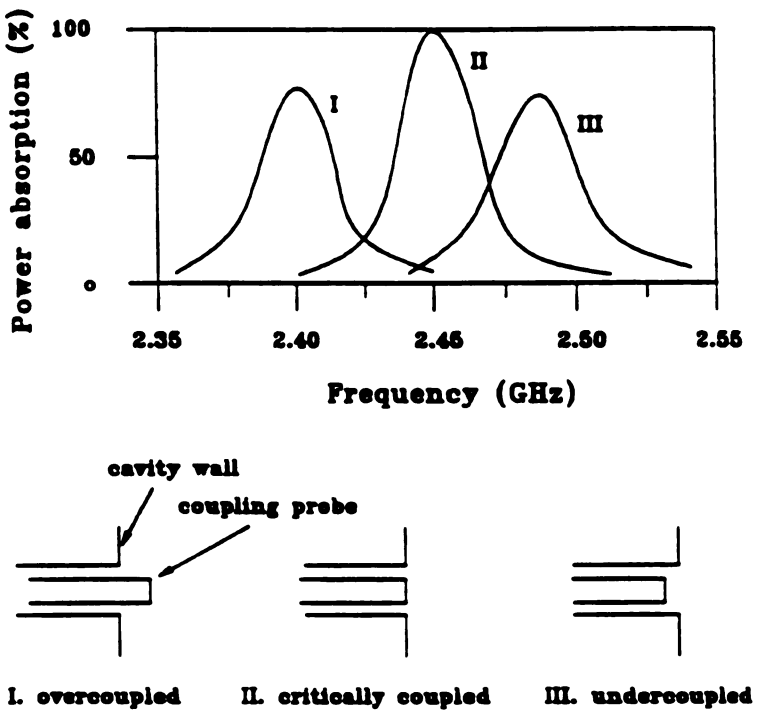

Figure 4.2 Power Absorption Curve of Empty Cavity under Various Coupling Situation

4.2.2 Microwave Processing and Mechanical Properties Test

The microwave processing and diagnostic system operating at 2.45 GHz was connected to the loaded cavity after the resonant heating mode was selected. For

crossply composite processing, the composite was oriented with the top ply fiber direction perpendicular to the coaxial coupling probe. For unidirectional composite processing, the composite was oriented with fiber direction either perpendicular, parallel, or 45° to the coupling probe. Four top surface temperatures, one at the center and three evenly distributed at the edges, were measured during the processing. The distance from edge to center probe, b, is 3 cm. The locations of the temperature probes and the meaning of the fiber orientations are shown in Figure 4.4.

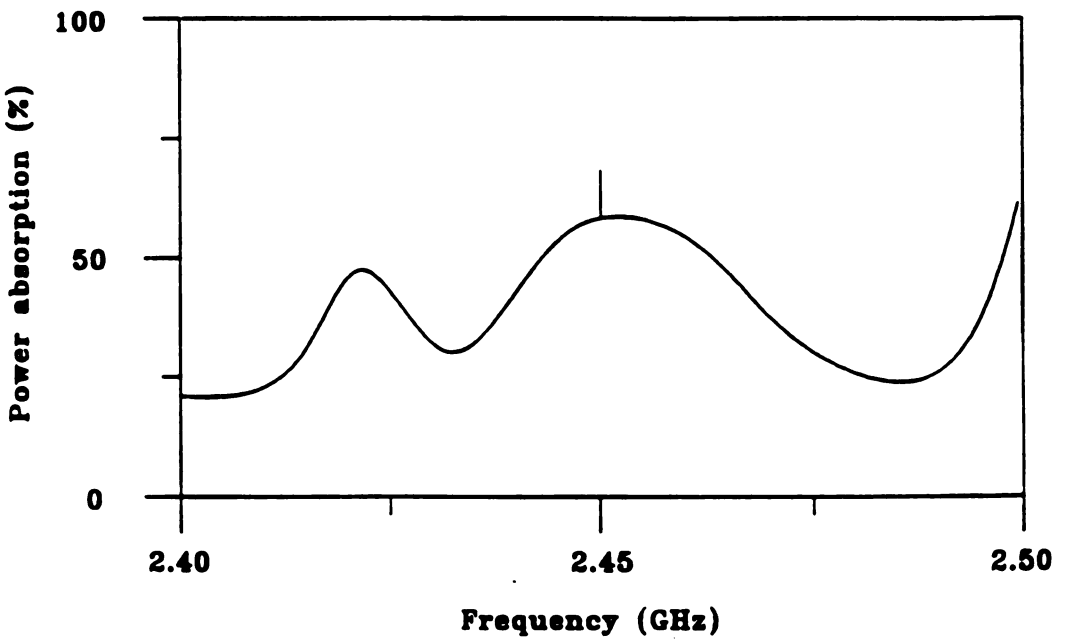

Figure 4.3 Typical Non-resonant Power Absorption Curve in the Composite Loaded Cavity

24-ply crossply composite laminates (about 30 grams each) were processed in nine different resonant modes. Each composite was processed with an input power of 60 W, corresponding to a power density of 2 W/g, for 90 minutes at a control temperature of 160°C. No pressure was applied during the process. The 24-ply unidirectional composites were processed in the same cavity under the same process conditions except with a lower input power of 42 W, corresponding to a power density of 1.5 W/g.

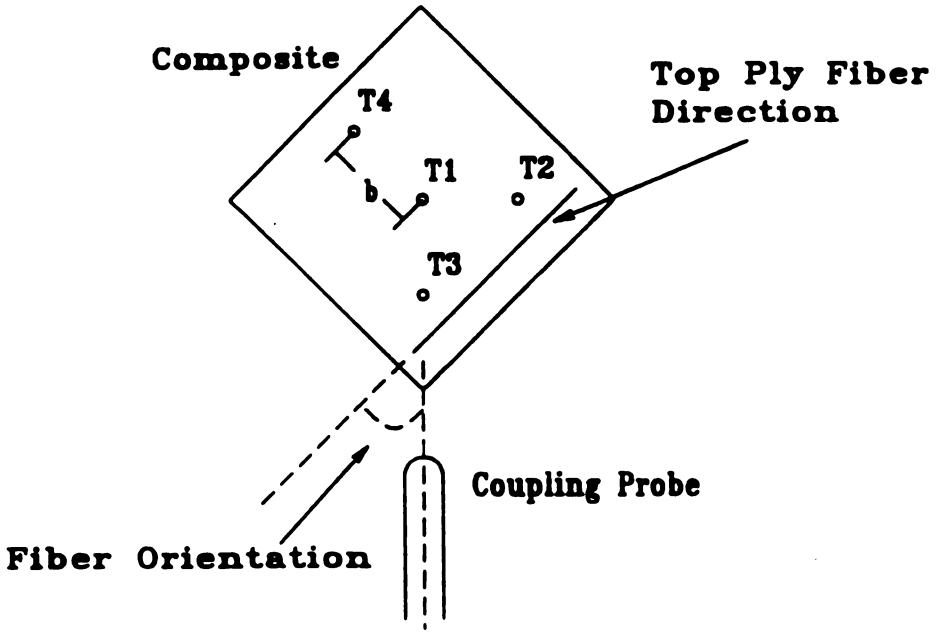

Figure 4.4 The Locations of Four Temperature Probes and Meaning of Fiber Orientations

As the complex dielectric properties of the composites were functions of temperature, extent of cure, and fiber volume fraction, the resonant conditions for the selected mode changed continuously during the cure. The selected resonant heating mode was maintained during cure by slightly tuning the cavity length and coupling probe depth to compensate for these changes.

Once the measured temperature reached the control temperature during cure, the input power was pulsed to maintain isothermal conditions at the control temperature. Figure 4.5 shows the temperature/location/time profiles during microwave processing of 24-crossply composite in various modes. The uniformity and completeness of cure achieved during heating was strongly dependent upon the resonant mode used for processing. In some cases, the samples were partially cured in one region and burned in another. Uniform cure of the sample was achieved using modes giving uniform temperature/location/time profiles. The radial electric

field pattern of the resonant heating mode along the cavity wall in the axial direction was also measured during the processing. Figure 4.6 shows a typical field pattern obtained during processing of 24-ply crossply composite when a uniform heating profile presented. The strongest radial electric field is at the laminate height. Similar behavior was observed during microwave processing of unidirectional laminate.

In preparation for measuring the mechanical properties of the final product, all microwave cured composite samples were cut into four pieces, each about 15 mm wide and 72 mm long. The flexural strength and modulus of each testing coupon were determined (ASTM D790 3-point flexural test) using an MTS testing machine with a support span of 64.22 mm, a crosshead rate of 0.06 in/min, and a support-to-depth ratio of 16. The maximum flexural strength and modulus were calculated using

$$FS_{max} = \frac{3PL}{2bd^2} \tag{4-1}$$

$$FM_{max} = \frac{L^3 m}{4bd^3} \tag{4-2}$$

where FS_{max} and FM_{max} = maximum flexural strength at midspan and modulus of elasticity

in bending, respectively, N/m^2 (psi),

P = maximum load on the load-deflection curve, N (lbf),

L = support span, m (in.),

b and d = width and depth of the coupon tested, m (in.), and

m = slop of the initial straight-line of the load-deflection curve, N/m (lbs/in.).

Figure 4.7 shows the typical load-deflection curves obtained during MTS testing for the microwave cured crossply composite at L_c=9.95 cm. The load increased with the displacement linearly at first. The coupon usually experienced some local failures before the final failure.

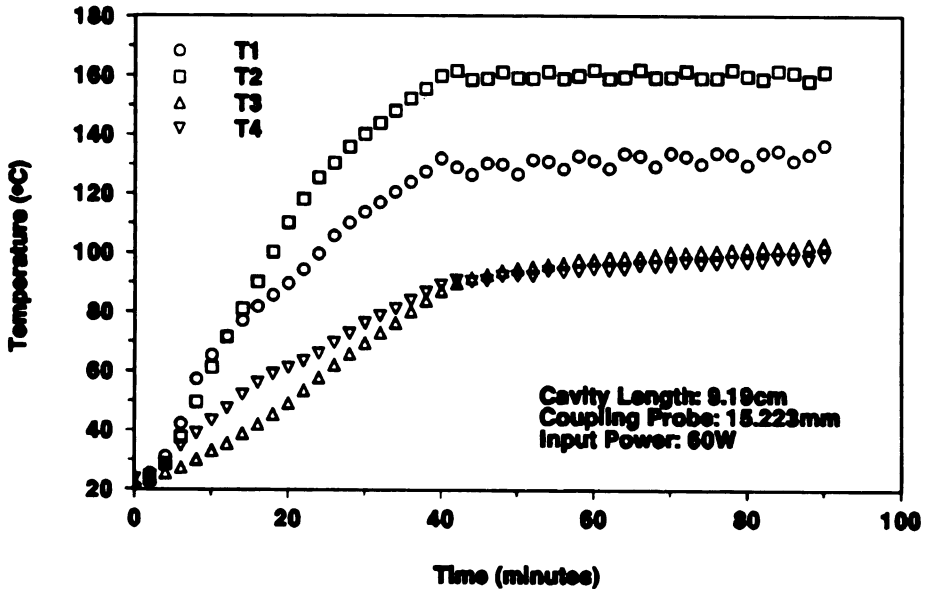

Figure 4.5(a) PS mode at L_c=9.19 cm

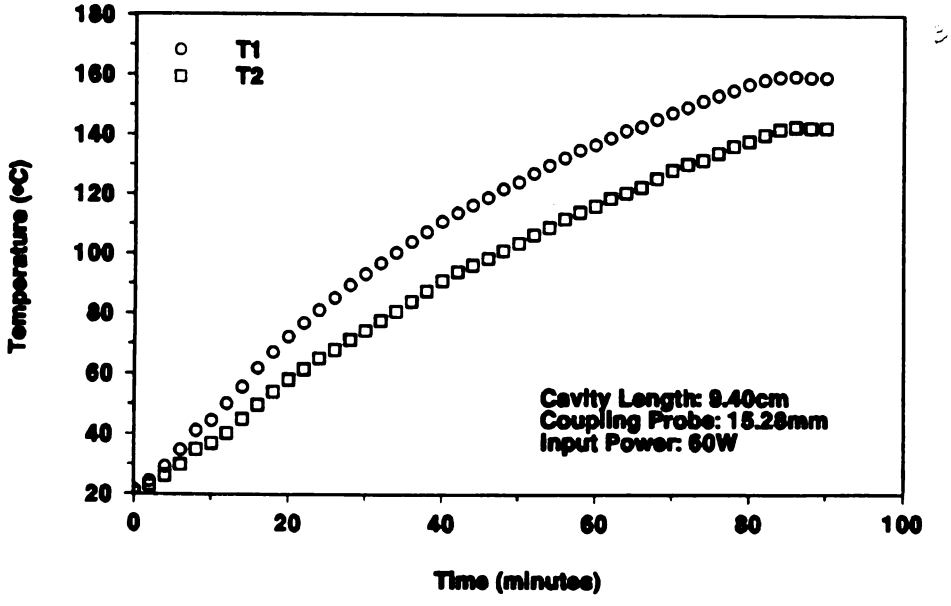

Figure 4.5(b) UH mode at L_c=9.40 cm

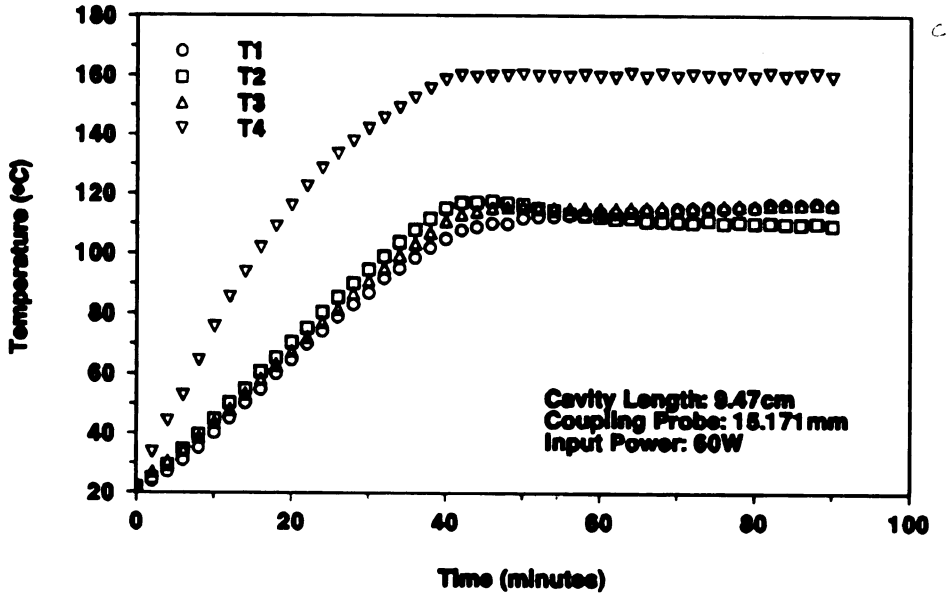

Figure 4.5(c) PS mode at L_c=9.47 cm

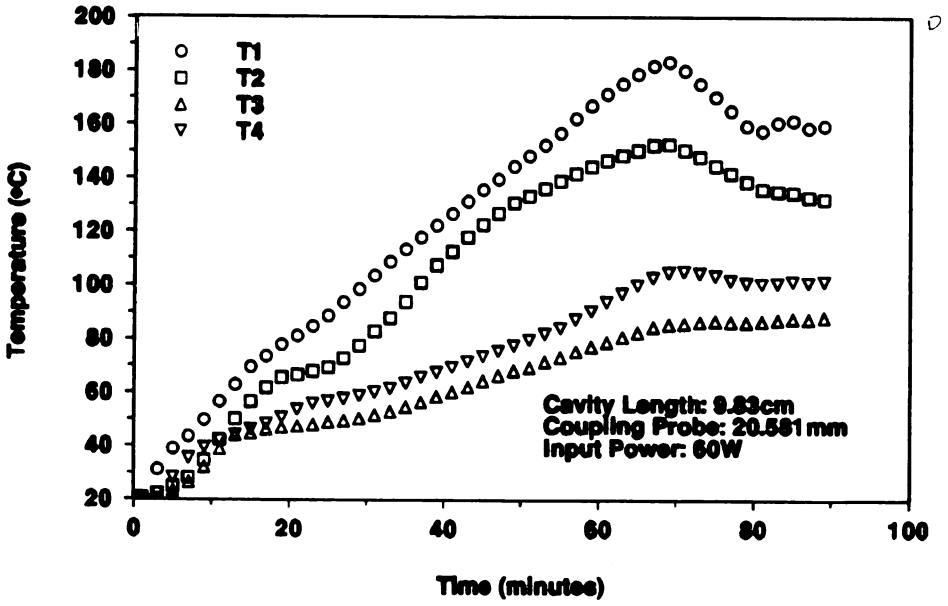

Figure 4.5(d) CH mode at L_c=9.83 cm

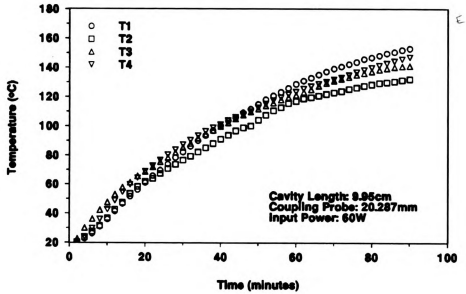

Figure 4.5(e) CH-PM mode at L_c=9.95 cm

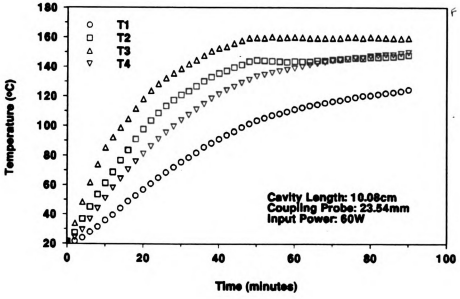

Figure 4.5(f) CH mode at L_c=10.08 cm

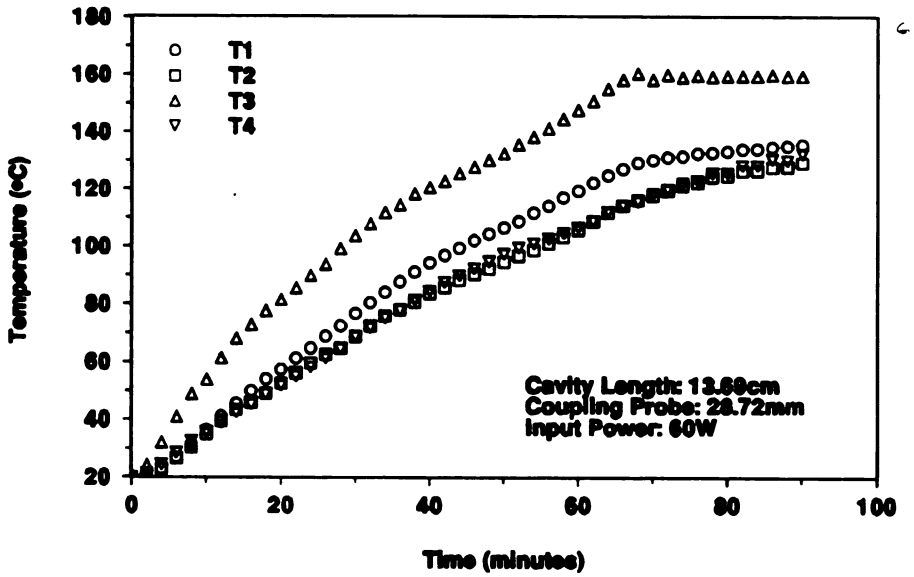

Figure 4.5(g) CH mode at $L_c = 13.69$ cm

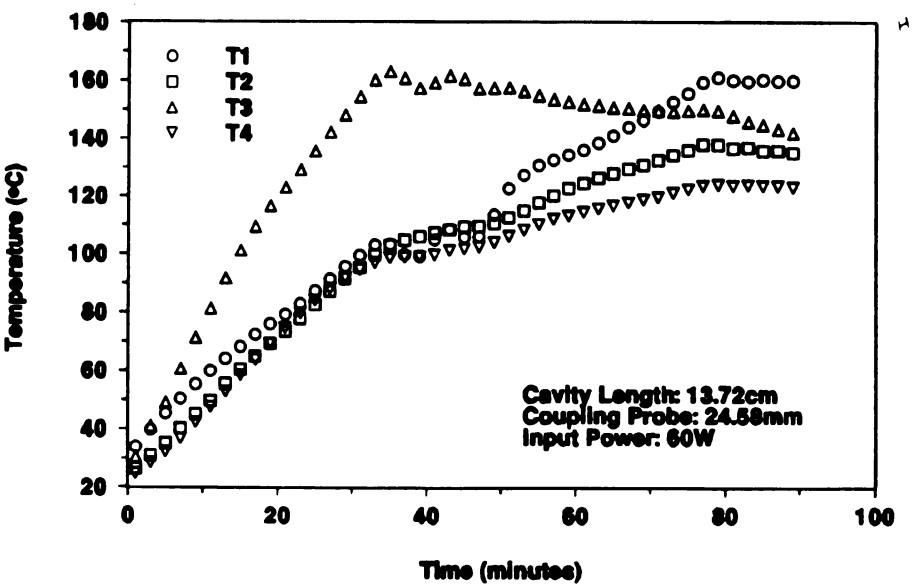

Figure 4.5(h) CH mode at $L_c = 13.72$ cm

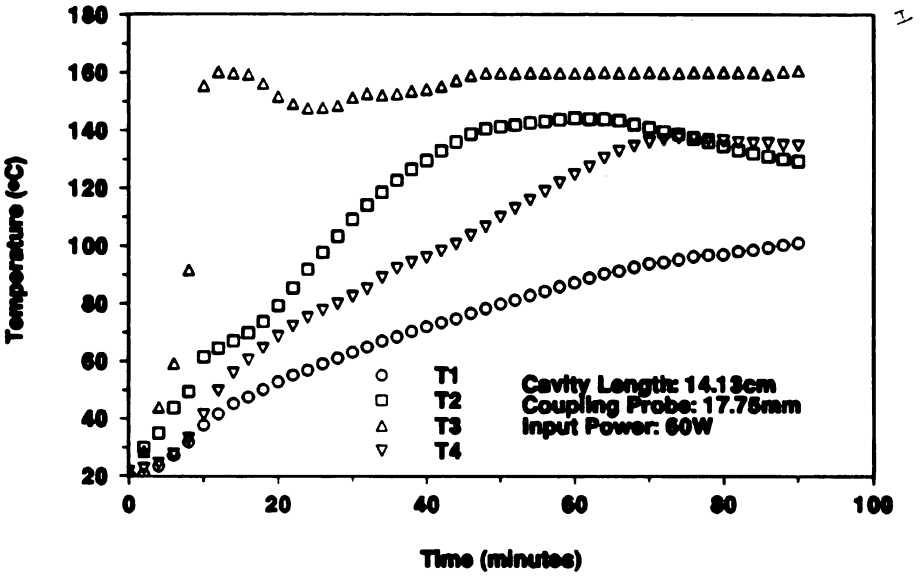

Figure 4.5(i) PS mode at $L_c = 14.13$ cm

Figure 4.5 Temperature/position/time Profile during Microwave Processing of 24 Crossply AS4/3501-6 Composites at Various Heating Modes.

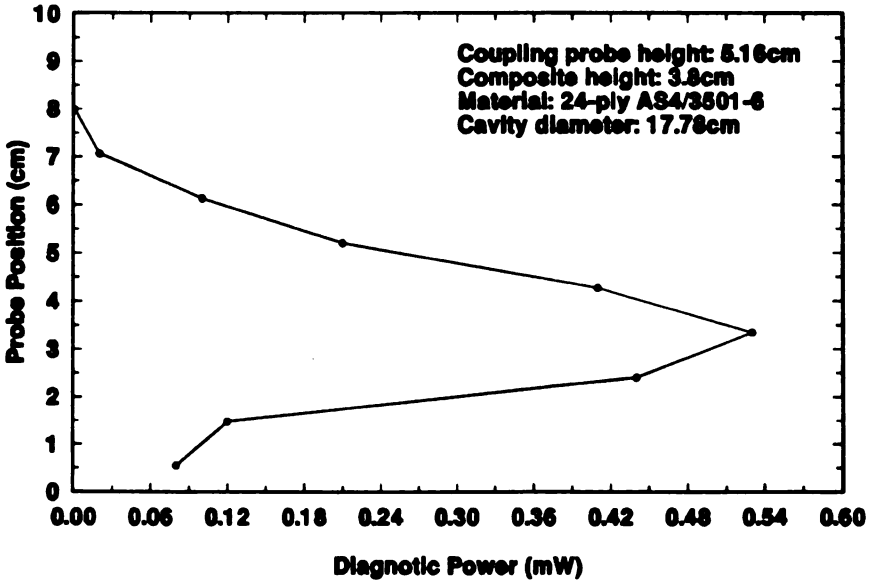

Figure 4.6 Typical Radial Electric Field Strength Distribution Along Axial Position

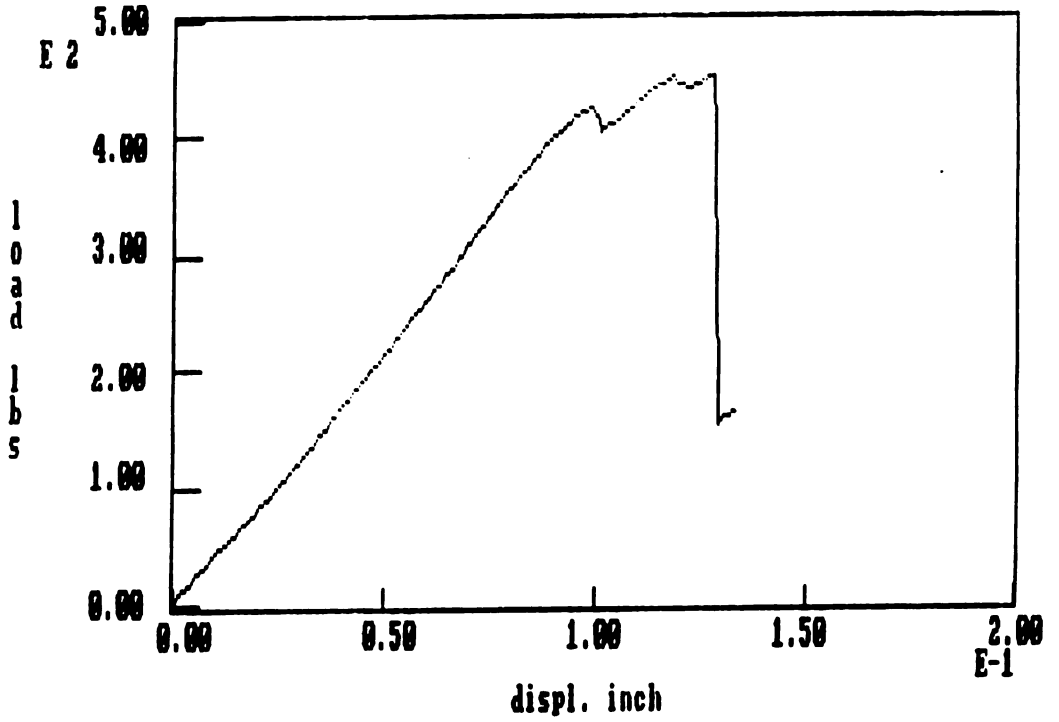

Figure 4.7 Load Versus Deflection Curves for 3-point Bending Test

For the purpose of comparison, 24-ply unidirectional and crossply laminates were processed thermally. Because we were not able to apply pressure during microwave processing, unpressurized thermal cures in the thermal oven (Fisher, 200 Series) were carried out for comparison. The oven temperature was dynamically controlled so that a similar sample temperature profile was obtained as compared to that of microwave cure with final temperatures of 160°C and 180°C at the end of 90 minutes. To compare our unpressurized microwave processed composites with the thermally processed composite used in industry, the autoclave (United McGill) was also used to process 24 ply unidirectional and crossply AS4/3501-6 composite using the manufacturer's suggested curing cycle. The mechanical properties of thermally processed composite were determined using the same method as used for the microwave processed samples.

In order to examine the bonding between the matrix and the fiber as function of the extent of cure for microwave processed composite, 24-ply unidirectional

composite was processed under various conditions to obtain composites of various levels of cure. Each processed sample was cut into a coupon with a length to thickness ratio of 6 and width of 0.64 cm for short-beam interlaminar shear testing (ASTM D2344-84). A support span to thickness ratio of 4 and a crosshead rate of 1.3 mm/min. were used in each test. The samples were subjected to 3-point bending until delamination occurred. A small amount (10-20 mg) of each coupon was removed from the delamination surface and tested for extent of cure in a differential scanning calorimeter (DSC, DuPont 9900). The same test for an autoclave processed composite using manufacture's cure cycle was also conducted for comparison. The failure surfaces of those samples, both thermally and microwave processed, were photographed using a scanning electron microscope (SEM, JEOL JSM T330).

To demonstrate the ability to cure a relatively thick section graphite fiber/epoxy composite laminate in the tunable resonant cavity, 72-ply, 7.62 x 7.62 cm unidirectional and crossply composite laminates were processed. The modes were selected using the criteria established based on the experimental results from microwave processing of 24-ply laminates. The samples were heated for about 75 minutes with at input power of 75 W. Top surface and midplane temperatures were measured during cure. Figure 4.8 shows the temperature/time profiles during microwave processing of 72-ply unidirectional composite. The cured samples appeared solid and uniform. No mechanical properties of the thick composites were measured due to the size restriction. However, the extent of cure distribution across the thickness of the composite was determined using DSC. As shown in Figure 4.9, the microwave processed composite was uniform in cure extent across the sample. Using the heating profile obtained during microwave processing of 72-ply unidirectional composite as oven temperature, a 72-ply unidirectional composite was processed thermally. The heating cycle was a ramp to 170°C in 45 minutes then hold at 170°C for 30 minutes. Both surface and midplane temperatures were measured and the results are shown in Figure 4.10.

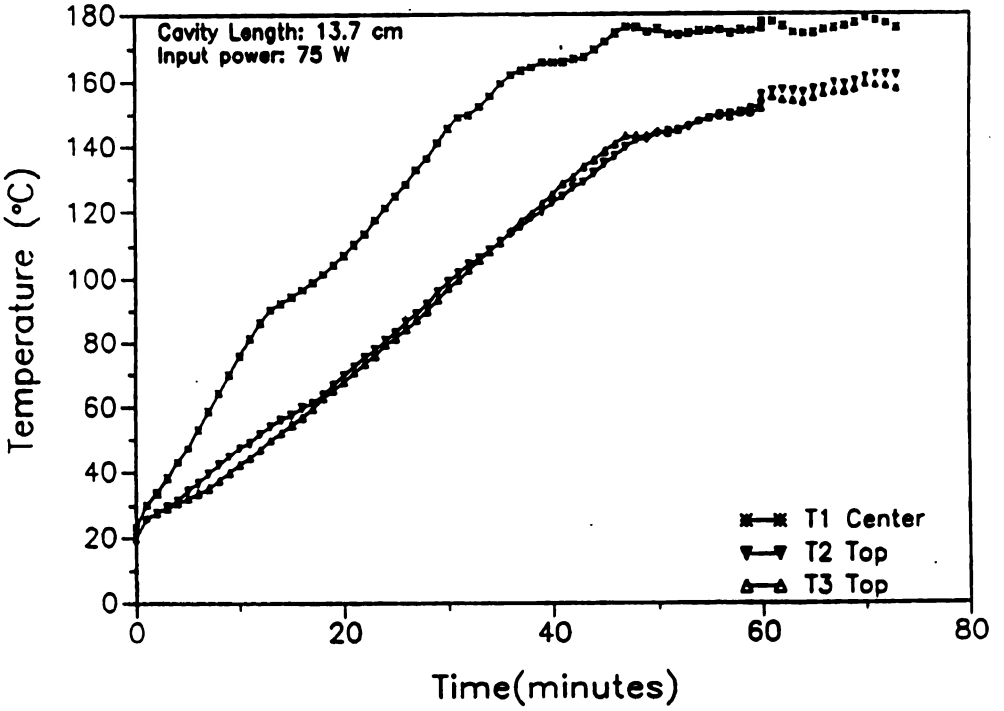

Figure 4.8 Temperature/time Profiles during Microwave Processing of 72-ply Unidirectional AS4/3501-6 Composite at a PM Mode.

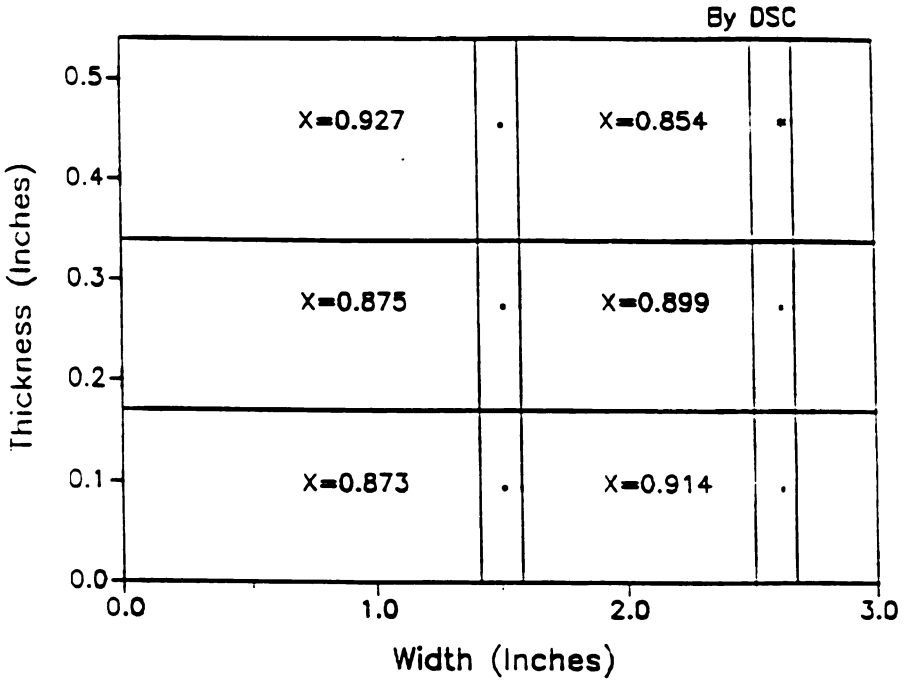

Figure 4.9 Spatial Distribution of the Extent of Cure in the Cross Section of the Microwave Cured 72-ply Unidirectional Composite.

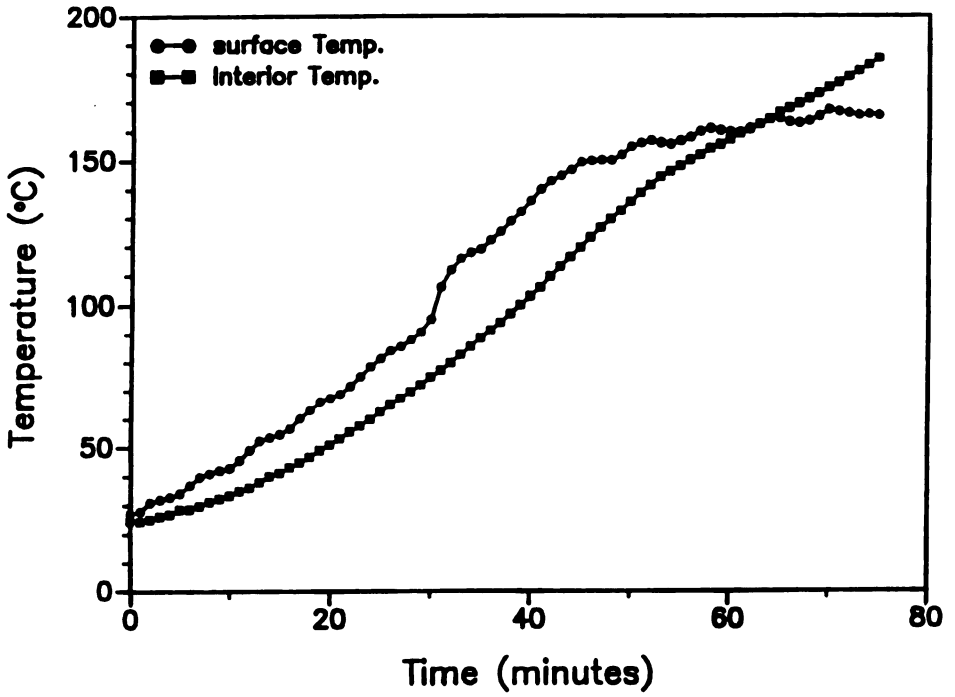

Figure 4.10 Temperature/time Profiles during Thermal Processing of 72-ply Unidirectional AS4/3501-6 Composite

4.3 Results and Discussion

24-ply crossply AS4/3501-6 composites have been cured in nine different resonant heating modes using 2.45 GHz radiation. Each resonant heating mode has its own electric field strength and pattern with a corresponding cavity length and coupling probe insertion length. As shown in Figure 4.5, the temperature uniformity is a strong function of the resonant heating mode. The temperature profiles in all PS modes (a,c,i) are not uniform. Most temperature profiles in CH modes are not uniform either except 4.6(b) and (e). Flexural properties of these microwave cured crossply coupons are listed in Table 4.1. Table 4.1 listed the location of the electromagnetic heating mode, thickness, flexural strength and modulus of microwave processed composites. In column 2 to 4, the number in front of the sign $\pm$ is the

average value obtained from four coupons which were cut from the same composite sample. The number after the sign $\pm$ is the maximum deviation from the averaged value. The composite thickness is ranging from 3.6 to 4.4 mm. The processed composites is fairly uniform in thickness among the four coupons as the maximum deviation is within 0.23mm.

As listed in Table 4.1, composites cured in a PS resonant heating mode (such as resonant cavity lengths of 9.19 cm and 14.13 cm) had relatively low flexural properties due to non-uniform curing. Although samples showing the highest flexural properties were cured in CH modes, not all crossply composites cured in CH modes had high flexural properties. The highest flexural properties were measured for samples cured in CH modes at 9.95 and 9.40 cm cavity lengths, while the lowest measured values were recorded for a sample cured in a CH mode at 9.83 cm. Given the fact that successful cure of crossply composites depends strongly on the mode chosen, and that selection of a CH mode does not always result in a successful cure, the CH modes resulting in high flexural properties are designated as process modes (PM) and the CH modes resulting in low flexural properties are designated as non-process modes (NPM). For example, the composite cured in the CH mode with a resonant cavity length of L_c=9.95 cm has relatively high flexural properties and therefore this mode is called a PM. The composite cured in the CH mode with resonant cavity length of L_c=9.83 cm has relatively low flexural properties so this mode is called a NPM.

Figures 4.5(b) and 4.5(d-h) show the temperature/location/time profiles on the surface of samples during cure in CH modes. Based on the above definition of PM and NPM and flexural properties listed in Table 4.1, Figure 4.5(b) and (d) show profiles corresponding to PM and the others show profiles corresponding to NPM. Clearly, the surface temperatures are more uniform in the PM than in the NPM. This may due to a more uniform electric field inside the composite in a PM than in a NPM. The experimental measurement of electric field during processing shows that

the identification of PM and NPM can be made from the radial electric field strength distribution along the axial direction. If the radial electric field strength distribution along the axial position of the CH mode has the shape of Figure 4.6 and the maximum radial electric field strength is located at the axial position of the composite, then the controlled-hybrid mode is a PM. Figure 4.5(a,c,i) show the temperature/location/time profiles on the surface of samples during cure in the three PS modes. The temperature is nonuniform on the surface in all cases. The more uniform temperature distribution during cure, the higher the flexural properties as shown by relating Figure 4.5 to Table 4.1.

The rheology of the epoxy matrix and void formation mechanism during microwave processing are very complicated. These complexity lead to a nonuniform distribution of void, therefore, the flexural strength of microwave processed composites, even in the composites processed in the PM modes. The max. variation/averaged value ratios of flexural strength for composite processed in the PM modes at L_c=9.40 cm and L_c=9.95 cm are 15% and 20%, respectively. To process composites with a uniform mechanical property, a fully understanding of rheology during microwave processing is required.

Table 4.1 Flexural Properties of Microwave Processed 24-crossply AS4/3501-6 Composite

Cavity Length (cm)	Composite Thickness (mm)	Flexural Strength (MPa)	Flexural Modulus (GPa)
9.19(PS)	4.09 ± 0.04	125.34 ± 18.08	33.93 ± 1.75
9.40(CH-PM)	3.99 ± 0.02	685.60 ± 103.90	44.51 ± 1.14
9.47(PS)	4.18 ± 0.11	127.92 ± 70.39	26.23 ± 11.05
9.83(CH-NPM)	4.43 ± 0.14	87.42 ± 52.48	13.96 ± 7.68
9.95(CH-PM)	4.35 ± 0.18	724.91 ± 143.73	40.46 ± 4.29
10.08(CH-NPM)	3.64 ± 0.03	269.30 ± 239.06	43.85 ± 5.04
13.69(CH-NPM)	4.23 ± 0.17	228.21 ± 50.91	35.74 ± 5.36
13.72(CH-NPM)	4.39 ± 0.11	189.33 ± 27.15	29.46 ± 5.01
14.13(PS)	4.09 ± 0.23	135.54 ± 15.34	31.80 ± 7.43

Unidirectional AS4/3501-6 composites of 24 plies were processed in the same cavity at three fiber orientations, namely 0, 45, and 90 degrees, with respect to the coupling probe. Figures 4.11, 4.12 and 4.13 show the temperature profiles of the three orientations in their processing modes. Apparently, the rate of heating depended on sample fiber orientation with respect to the coupling probe. Samples oriented parallel to the probe heated the slowest, as shown in Figure 4.11. Parallel oriented samples reached the set point temperature at times greater than 90 minutes. Samples oriented 45 degrees with respect to the probe reached the set point within 45 minutes, as shown in Figure 4.12. Samples oriented perpendicular to the probe heated the fastest, reaching the set point within 15 minutes, as shown in Figure 4.13. A maximum curing rate for samples oriented perpendicular to the probe agrees with previous studies. Lee and Springer[4,8] have found that unidirectional samples cured fastest when oriented perpendicular to a plane polarized wave in a waveguide. Chen and Lee[37] have shown that heating rates in a resonant cavity for cured unidirectional

carbon fiber/epoxy samples were faster for samples heated perpendicular to the coupling probe than for those oriented parallel. Temperature uniformity upon reaching the set-point temperature also depended on the sample orientation. The 45 degree-oriented sample maintained the most uniform thermal profile across the specimen, as shown in Figure 4.12. The dependence of heating rate and temperature uniformity on fiber orientation confirms that the coupling of electromagnetic energy into a carbon fiber composite is affected by the fiber orientation as reported previously[4,8,37]. Coupling of microwave energy into the anisotropic composite is dependent upon the relative orientations of the fiber axes and electromagnetic field, as reflected by heating rate. No attempt was made to optimize the curing and to maximize the heating rate. The objective of this study was to identify the important parameters for the processing of graphite fiber/epoxy composites in a microwave cavity.

Table 4.2 lists the mechanical properties of microwave processed 24 ply unidirectional composites oriented at 0, 45, and 90 degrees with respect to the coupling probe. The highest flexural strength was obtained when the composite was oriented at 45 degrees. The experimental results listed in Table 4.1 and 4.2 clearly show that 24-ply unidirectional and crossply graphite fiber/epoxy composites can be processed using resonant standing microwaves in a tunable resonant cavity. The flexural properties of the cured sample are strongly dependent on the processing mode and higher flexural properties were achieved using a PM. The highest flexural properties measured for microwave cured 24-ply crossply composite are compared with those of 24-ply unidirectional composites cured with fiber direction either perpendicular or parallel to the coaxial coupling probe for the same heating time at a lower input power density of 1.5 W/g, as listed in Table 4.3. Table 4.3 shows that the flexural properties of the microwave cured crossply sample fall between those of the best unidirectional samples cured perpendicular and parallel to the probe. A comparison of temperature/time profiles at the surface of unidirectional and crossply composites during processing in their PM is shown in Figure 4.14. Figure 4.14

indicates that crossply composites require a higher input power density than unidirectional composites to obtain a similar temperature/time profile.

Table 4.2. Flexural Properties of Microwave Cured 24-ply Unidirectional AS4/3501-6 Composites at Various Orientations and Modes

Sample Orientation	Cavity Length (cm)	Cured Laminate Thickness (mm)	Flexural Strength (MPa)	Flexural Modulus (GPa)
0°	9.46	4.58 ± 0.09	615.47 ± 72.10	30.37 ± 3.71
	9.61	3.87 ± 0.21	415.73 ± 169.16	34.92 ± 11.15
	14.60	4.82 ± 0.14	389.75 ± 44.68	33.64 ± 4.69
45°	14.05	3.65 ± 0.07	1316.79 ± 67.58	100.73 ± 2.44
	14.41	3.84 ± 0.18	857.63 ± 215.92	86.98 ± 10.69
	17.77	3.74 ± 0.07	411.65 ± 91.15	71.26 ± 26.60
	17.16	4.05 ± 0.41	970.50 ± 342.19	83.47 ± 19.48
	17.10	3.83 ± 0.12	763.14 ± 158.48	83.30 ± 10.16
	17.08	3.61 ± 0.08	1136.07 ± 123.81	99.97 ± 6.04
90°	8.66	3.42 ± 0.14	851.28 ± 208.78	59.30 ± 3.93
	9.01	3.17 ± 0.04	944.56 ± 183.14	74.53 ± 11.97
	13.60	3.30 ± 0.13	769.72 ± 76.22	60.89 ± 10.57
	9.03	4.31 ± 0.10	838.64 ± 173.03	58.24 ± 7.05
	9.17	5.05 ± 0.49	389.11 ± 142.07	33.07 ± 12.76

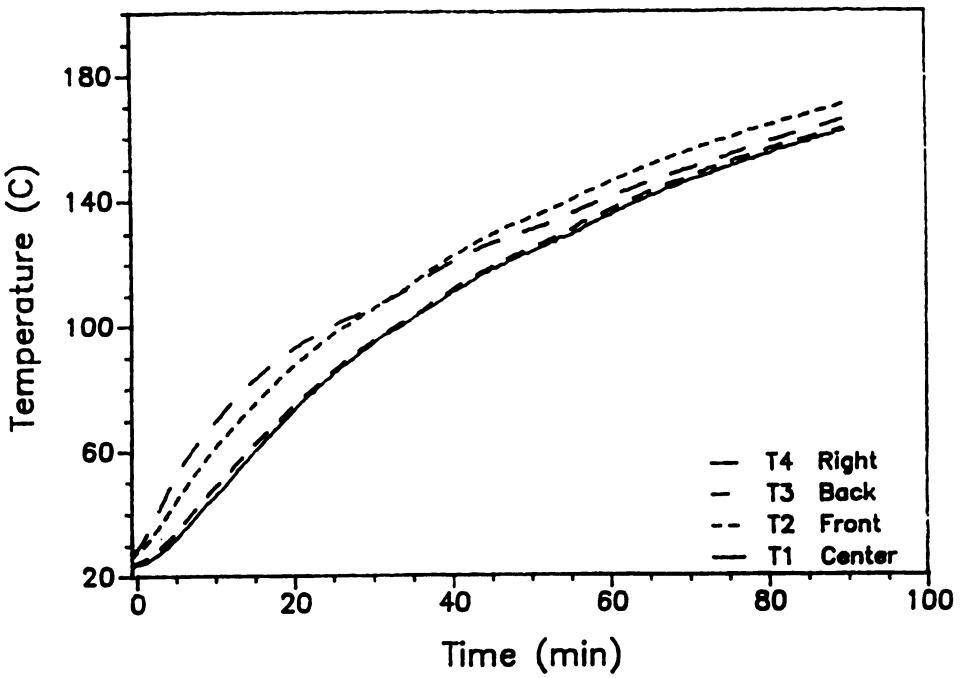

Figure 4.11 Temperature/time Profile During Microwave Cure of 24 ply Unidirectional AS4/3501-6 Composite at Fiber Orientation of 0° with respect to the Coupling Probe

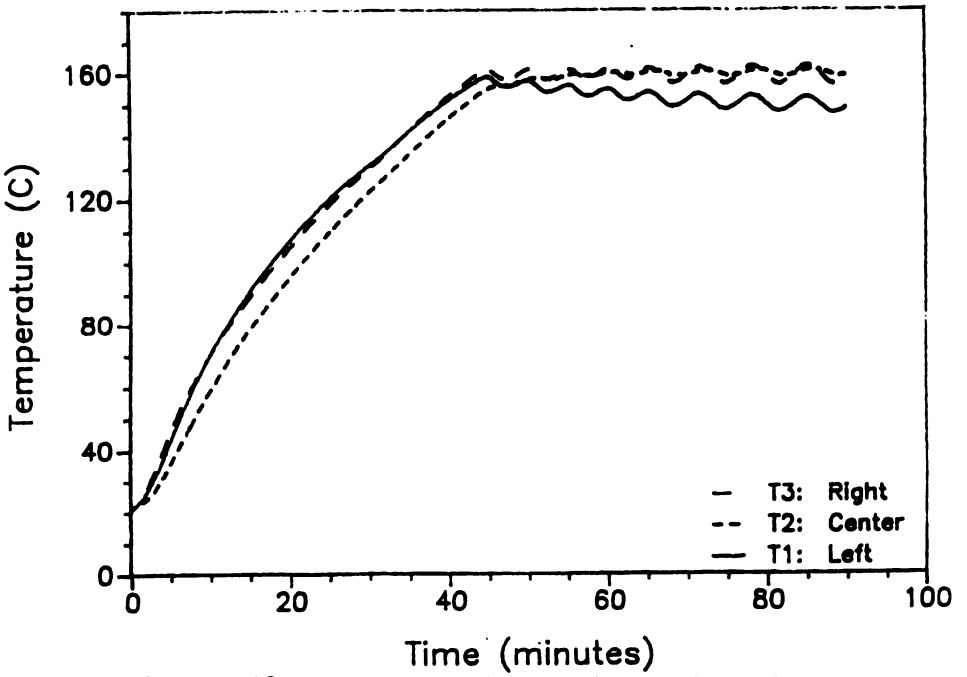

Figure 4.12 Temperature/time Profile During Microwave Cure of 24 ply Unidirectional AS4/3501-6 Composite at Fiber Orientation of 45° with respect to the Coupling Probe

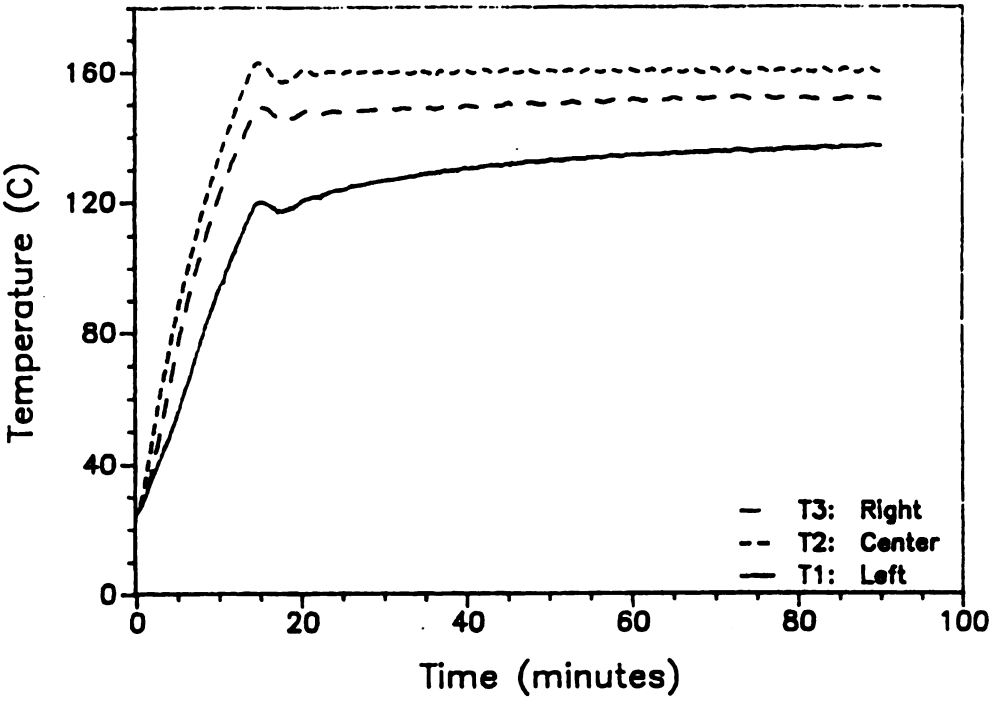

Figure 4.13 Temperature/time Profile During Microwave Cure of 24 ply Unidirectional AS4/3501-6 Composite at Fiber Orientation of 90° with respect to the Coupling Probe

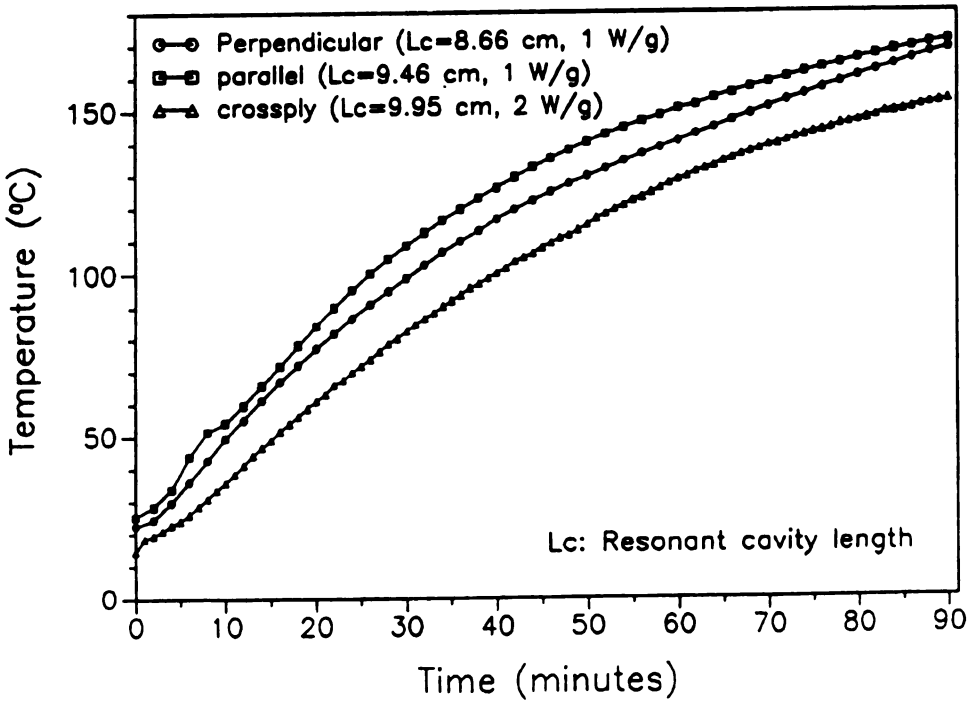

Figure 4.14 Comparison of the Temperature/time Profiles During Microwave Cure of 24-ply AS4/3501-6 Composites

Table 4.3: Comparison of Flexural Properties between Microwave and Thermally Cured 24-ply AS4/3501-6 Composites

Composites	Lc (cm) for mw cure /Final Temp.(°C) for th cure	Thickness (mm)	Strength (MPa)	Modulus (GPa)
Crossply				
Microwave	9.40	3.99 ± 0.02	685.6 ± 103.9	44.51 ± 1.14
	9.95	4.35 ± 0.18	724.9 ± 143.73	40.46 ± 4.29
Thermal*	160	----	-----	-----
	180	3.53 ± 0.05	313.7 ± 55.37	40.51 ± 3.70
Autoclave**		2.99 ± 0.03	817.4 ± 70.3	62.17 ± 1.36
Unidirectional				
Microwave				
Parallel	9.46	4.58 ± 0.10	615.5 ± 72.1	30.37 ± 3.71
	9.61	3.87 ± 0.21	415.7 ± 169.2	34.92 ± 11.14
Perpendicular				
	8.66	3.42 ± 0.14	851.3 ± 208.8	59.30 ± 3.92
	9.01	3.17 ± 0.04	944.6 ± 183.1	74.52 ± 11.97
45 degree				
	14.05	3.65 ± 0.07	1316.8 ± 67.58	100.73 ± 2.44
	17.08	3.61 ± 0.08	1136.1 ± 123.81	99.97 ± 6.04
Thermal*	160	3.33 ± 0.08	165.6 ± 27.8	39.8 ± 20.23
	180	3.74 ± 0.33	789.6 ± 107.57	63.3 ± 15.69
Autoclave**		2.80 ± 0.05	1320.9 ± 25.58	123.49 ± 3.03

** Using manufacture suggested cure cycle (4 hours and pressure of 100 psig).
* Dynamic heating to the final temperature in 90 minutes.

The unpressurized thermal processing of both unidirectional and crossply 24-ply Hercules AS4/3501-6 composite was also conducted for comparison. Table 4.3

listed the flexural properties of both microwave and thermal processed composites. With a final temperature of 160°C, the unpressurized thermally cured crossply composites were too soft to test, the flexural strengths of thermally cured unidirectional composites were much lower than those of microwave cured samples (3-8 times); and the flexural moduli of thermally cured unidirectional composites were comparable to those of parallel (with respect to coupling probe) microwave cured unidirectional samples but lower than the other two fiber orientations. This may be due to the low extent of cure in the thermally cured composite. This result indirectly implies that the polymerization rate of Hercules 3501-6 resin is faster during microwave cure than thermal cure. In order to obtain a testable crossply composite, the experiment was repeated with a final temperature of 180°C instead of 160°C. With a final temperature of 180°C, the flexural strength of thermally cured crossply samples was about half of the value for the microwave cured samples and the flexural moduli were comparable to those of microwave cured crossply samples. The flexural strengths of thermally cured unidirectional composites were between parallel and perpendicular oriented microwave cured unidirectional samples and the flexural moduli were comparable to those of perpendicular microwave cured samples. The flexural properties of the microwave cured samples (without pressure) are also compared to those of autoclave cured (with 100 psig pressure) samples. The flexural moduli of unpressurized microwave processed crossply and unidirectional composites (0,45, and 90 degrees) are lower than those of pressurized autoclave cured samples. The flexural strengths of unpressurized microwave cured 24 ply crossply, parallel oriented, and perpendicular oriented unidirectional composites were lower than those of autoclave cured samples. The unpressurized microwave cured unidirectional 24 ply composites had a comparable flexural strength as pressurized autoclave cured samples when they were cured at 45 degrees to the coupling probe. The lower flexural properties of microwave cured samples may be due to the higher void content in the unpressured microwave cured samples than pressured thermally cured samples.

Figure 4.15 shows the extent of cure effects on the apparent interlaminar shear strength (ISS) of the microwave processed 24-ply unidirectional AS4/3501-6 composites. ISS increases with increasing extent of cure, the same trend as for the microwave cured pure epoxy resins[115]. The ISS of fully cured microwave processed unidirectional composites is slightly lower than that of autoclave processed samples because a significant amount of voids existed in the microwave processed composites due to the lack of pressure during processing.

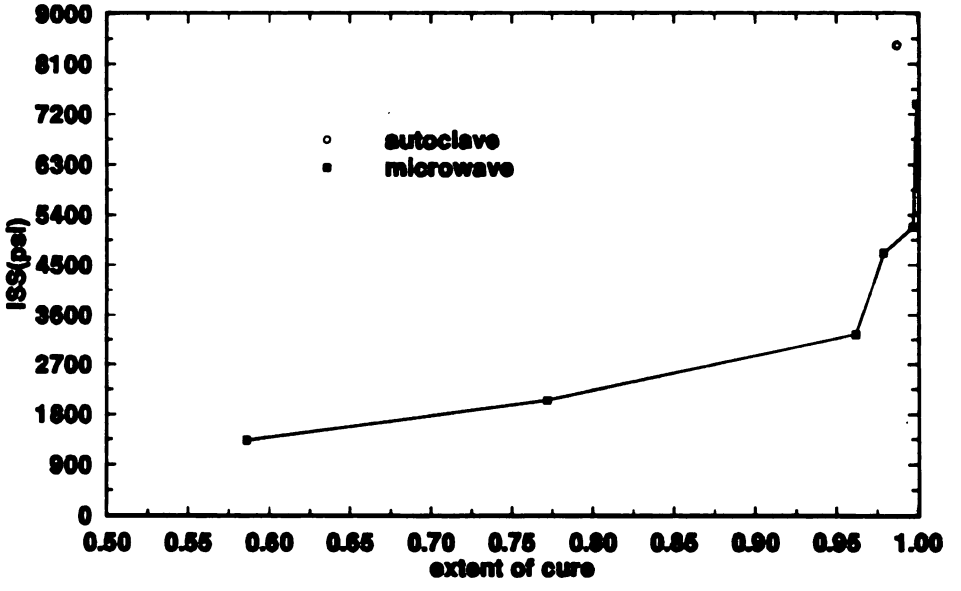

Figure 4.15 Interlaminar Shear Strength of Microwave Processed 24-ply Unidirectional AS4/3501-6 Composites at Various Extent of Cure

Figure 4.16 shows SEM photographs of the delaminated surfaces from the short-beam shear test of both microwave and autoclave processed 24-ply unidirectional AS4/3501-6 composites. Figures 4.16(a) and 4.16(b) are the SEM photographs of the delaminated surface for microwave processed samples having high and low extents of cure. For the sample having a high extent of cure, the delamination was mainly due to matrix failure, as shown in Figure 4.16(a). A close look at the surface of the failed fibers of this sample revealed that the pulled fiber was coated by a layer of matrix about 2 microns thick as shown in Figure 4.16(c). The

shear failure modes for microwave processed samples of lower extent of cure were a combination of both matrix failure and interfacial failure as revealed by Figure 4.16(b). For the autoclaved processed sample, the sample failed in a combination of interfacial and matrix failure mode as indicated by matrix debris in Figure 4.16(d). This result agrees with previous result[6] that a better bonding between graphite fiber and epoxy can be achieved in microwave processing than in thermal processing. Further more, the failure mode in the microwave processed samples of low extent of cure is similar to that of thermally processed samples.

As a further demonstration of the feasibility of microwave processing of graphite fiber/epoxy composite in a resonant cavity, 72-ply unidirectional and crossply laminates were successfully processed in their PM. The PM was located using selection criteria established based on the experimental results during microwave processing of 24-ply laminates. The crossply sample was processed with the top ply fiber direction perpendicular to the coupling probe at a resonant cavity length of 13.7 cm and the unidirectional sample was processed with its fiber direction perpendicular to coupling probe at a resonant cavity length of 10.1 cm. It is interesting to note that the midplane temperature T1 is always higher than the surface temperatures T2 and T3 during microwave processing as shown in Figure 4.8. The uniform surface temperature shown in Figure 4.8 strongly suggests a uniform power absorption rate around the surface area. The higher center temperature as compared to the surface temperatures may be due to the surface heat loss or the combination of surface heat loss and a higher power absorption rate in the center. Figure 4.8 suggests that a significant electromagnetic field exists in the interior of the composite. As shown in Figure 4.9, the cure distribution was quite uniform across the thickness of the composite. Comparing Figure 4.10 to Figure 4.8, the advantage of microwave processing of thermoset composites over thermal processing is quite clear. The temperature excursion was eliminated during microwave processing by using pulsed microwave power input and the temperature was maintained at the desired value. The heat up time can be shortened by using higher input power if it is necessary.

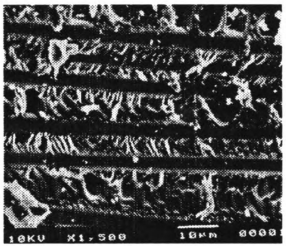

(a) Fully cured

Microwave processed, ISS=7379 PSI

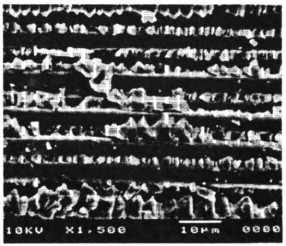

(b) 58% cured

Microwave processed, ISS=1329 PSI

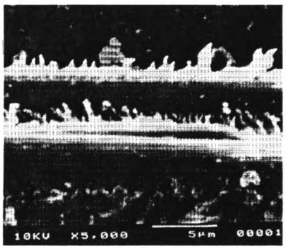

(c)

Close look of pull-out fiber of (a)

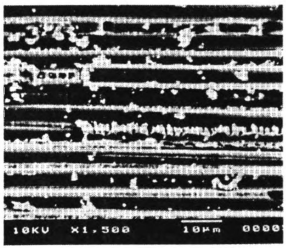

(d) Fully cured

Autoclave processed, ISS=8430 PSI

Figure 4.16. SEM Pictures of Delaminated Surface from SBS Test for Microwave and Autoclave Processed Unidirectional AS4/3501-6 Composites.

The advantages of tunable resonant cavity over other microwave applicator were fully demonstrated in the processing of graphite fiber composites. While only unidirectional graphite fiber/epoxy composite of 32 plies or less can be processed in waveguide or multimode microwave oven, both unidirectional and crossply 72-ply composites can be processed in the tunable cavity. When a graphite fiber/epoxy composite is processed in a commercial microwave oven, a fixed field pattern and strength distribution are obtained as the location of the composite inside the oven and the processing frequency are selected. Usually the input power can not be transferred into the composite efficiently due to impedance mismatch and the composite can not be uniformly cured due to the nonuniform field inside the composite. Compared to commercial untunable microwave ovens, the tunable resonant cavity offers several advantages in processing of composites, including (1) the ability to obtain a resonant standing electromagnetic field for unidirectional and crossply graphite fiber/epoxy composite to transfer input energy efficiently into the composite, (2) the ability to select an appropriate resonant heating mode to heat the composite uniformly, and (3) the ability to maintain the selected resonant heating mode to prevent loss of resonance as the material permittivity changes during the heating.

4.4 Conclusion

This study demonstrates that it is feasible to process continuous graphite fiber/epoxy composite materials in a tunable resonant microwave cavity. Unidirectional and crossply graphite fiber/epoxy composite laminates consisting of 24 plies have been processed in a 17.78 cm tunable electromagnetic resonant cavity using 2.45 GHz microwave radiation. No pressure was applied during microwave processing. Temperature distributions in the composite were measured during processing using fluoroptic sensors. The flexural properties of the processed composites were determined using a 3-point bending test. Temperature uniformity,

cure uniformity, and the flexural properties of the processed samples were shown to be strong functions of the processing mode. The flexural properties of the microwave processed unidirectional composites were also affected by the fiber orientation of the composites with respect to the coupling probe. The maximum flexural properties of unidirectional composites were observed when the sample was processed at an orientation of 45 degrees to the coupling probe. The flexural properties of microwave processed crossply samples have been found to be between those values measured for microwave processed unidirectional laminates cured with fiber orientations perpendicular and parallel to the coaxial coupling probe. Unpressurized thermal cure in an ordinary thermal oven and pressurized thermal cure in an autoclave of 24-ply composites have been carried out for comparison. The flexural strengths of the unpressurized thermally cured unidirectional and crossply composites were much lower than those of unpressurized microwave cured samples under similar heating conditions. The microwave processed 24-ply unidirectional composites have comparable flexural strength but lower flexural modulus when compared to that of thermally processed samples (with pressure) in the autoclave with manufacturer's suggested cure cycle. Both flexural strength and flexural modulus of microwave processed 24 ply crossply samples were lower than those of autoclave processed samples. The processing results show only a small decrease in flexural properties for unpressurized microwave cured composites as compared to those of pressurized thermally cured samples although a short processing time (90 minutes) and no pressure was applied in microwave cure while a long processing time (4 hours) and a pressure of 100 psig were applied during thermal processing in the autoclave. Selection of the proper resonant mode, however, has been shown to be a critical factor in achieving high flexural properties of microwave processed composite. The concept of a processing mode (PM) is defined based on the flexural properties of the processed composites. The criteria defining a processing mode were obtained from a database of types of processing modes, radial field patterns during processing, and the flexural properties of processed composites. Using modes selected based on

the above criteria, 72-ply unidirectional and crossply composites have been successfully cured with a uniform spatial distribution of the extent of cure.

The extent of cure effects on the mechanical properties of microwave processed graphite fiber/epoxy composite were also studied using 24-ply unidirectional AS4/3501-6 composite. Apparent interlaminar shear strengths (ISS) of microwave processed samples were determined using a short-beam method (ASTM D2344-84). ISS of microwave processed composite increased with increasing extent of cure. Scanning electron microscope analysis of the fracture surfaces of both microwave and thermally processed composites revealed that graphite fiber/epoxy bonding was higher in microwave processed composites than in thermally processed samples. Microwave processed composites failed in the matrix failure mode for samples of high extent of cure and in a combination of interfacial and matrix failure modes for samples of low extent of cure. The autoclave processed samples failed in a combination of interfacial and matrix failure modes.

CHAPTER 5
FIBER ORIENTATION EFFECTS ON THE MICROWAVE HEATING OF CONTINUOUS GRAPHITE FIBER/EPOXY COMPOSITES

5.1. Introduction

Chapter 4 demonstrated the feasibility of processing thin-section unidirectional and crossply graphite fiber/epoxy composites using microwave energy in a tunable resonant cavity. The results in chapter 4 showed that temperature uniformity is the key parameter to obtain uniformly cured composites and therefore a composite of high mechanical strength. This chapter discusses the microwave heating characteristics of a fully cured thick-section crossply graphite fiber/epoxy composite at various fiber orientations.

In the microwave processing of composites, the heating profile and distribution depend upon the electromagnetic field pattern inside the sample. A uniform electric field inside the composite will result in a uniform temperature distribution and a high electric field strength will lead to a fast heating rate during processing. For a given composite size and input microwave power of a given frequency, the electromagnetic field pattern depends on the cavity length, coupling probe length, fiber orientation, and sample location. The key objective in the microwave processing of graphite fiber/epoxy composite is, therefore, to experimentally find a proper cavity length, coupling probe length, composite location, and fiber orientation such that a uniform electric field pattern will be resulted inside the composite and all the input power will be focused on the composite. In this study, a fully cured 3.8cm thick crossply graphite fiber/epoxy composite was heated in a 17.8cm tunable resonant cavity at five fiber orientations. The effects of fiber orientation on microwave heating profiles were studied.

5.2. Experiments

Microwave heating experiments were performed using a thermally cured 7.6x7.6 x3.8cm crossply graphite fiber/epoxy composite (Hercules AS4/3501-6). A teflon disk, 10.2cm in diameter and 3.8cm thick, was placed on both on the top and bottom of the sample to prevent heat loss and to lift the sample from the bottom of the cavity. The whole setup was placed at the center of the bottom plate in a 17.8cm tunable microwave resonant cavity. A series of runs was conducted with top fiber orientations of 0, 15, 45, 75, and 90 degrees with respect to the coupling probe. The microwave applicator and accompanying diagnostic and control system were the same as used in Chapter 4. Four surface and four midplane temperatures were measured. The probe locations were the same for midplane and surface temperature measurement, as shown in Figure 4.4. Five resonant heating modes were found for each fiber orientation and each mode was used to heat the sample using an input power of 60W. The type of each resonant heating mode was determined based on the power absorption curve on the oscilloscope as discussed in Chapter 2. The heating was allowed to continue at constant input power until one temperature, either on the surface or in the midplane, reached 160°C. In addition, a fresh 7.6x7.6cm 200-ply crossply sample was processed in the microwave cavity with a 15° fiber orientation at a cavity length of 13.22cm and a coupling probe depth of 21.98mm.

5.3. Results and Discussion

A fully cured 3.8 cm thick crossply AS4/3501-6 composite was microwave heated at five fiber orientations. Figures 5.1 to 5.5 show the temperature profiles in various modes for each fiber orientation.

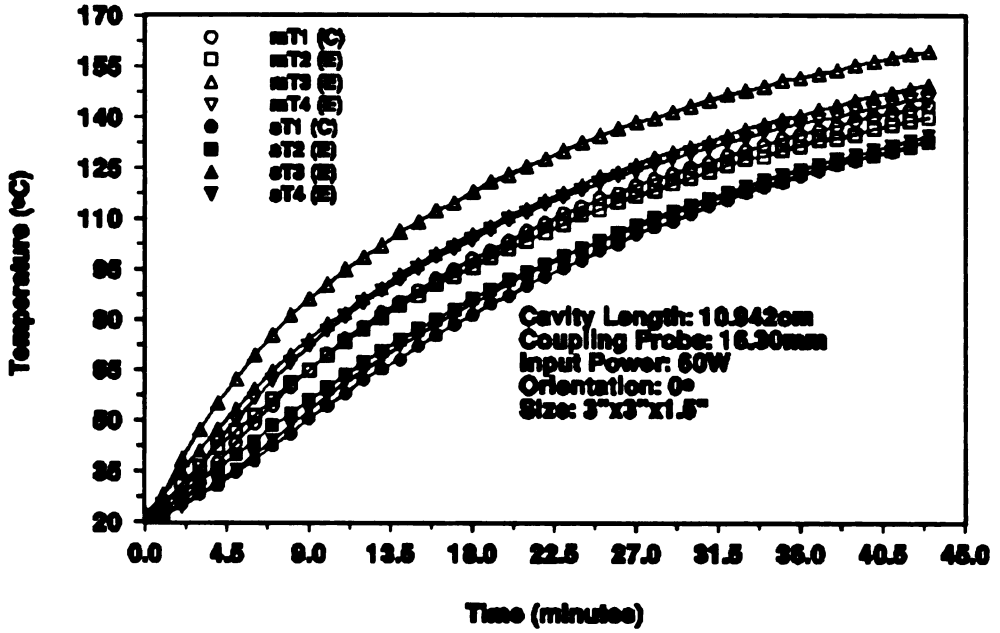

5.1(a) UH at L_c=10.94 cm & L_p=16.30 mm

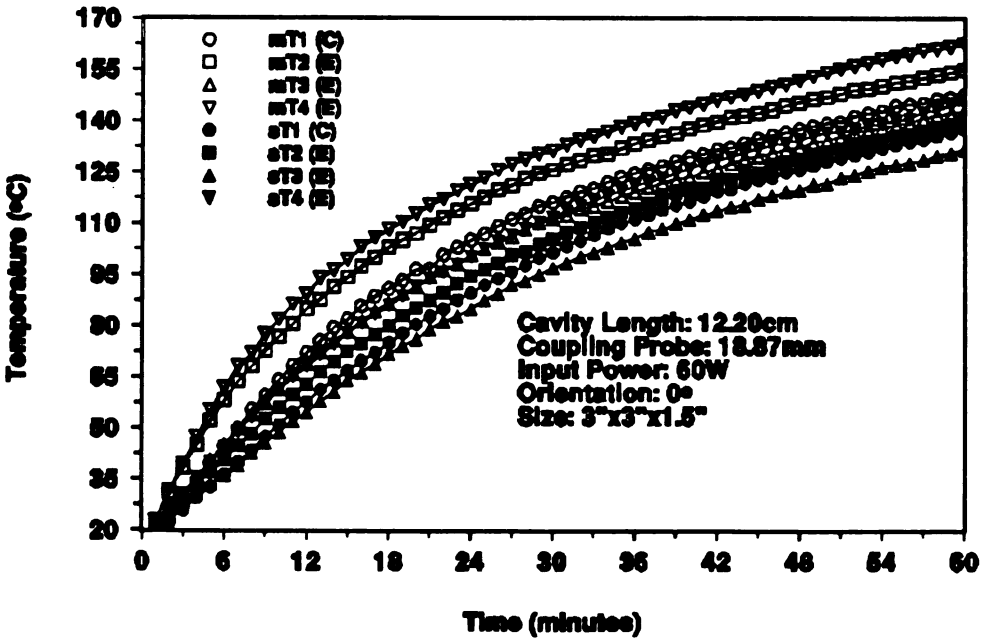

5.1(b) UH at L_c=12.20 cm & L_p=18.87 mm

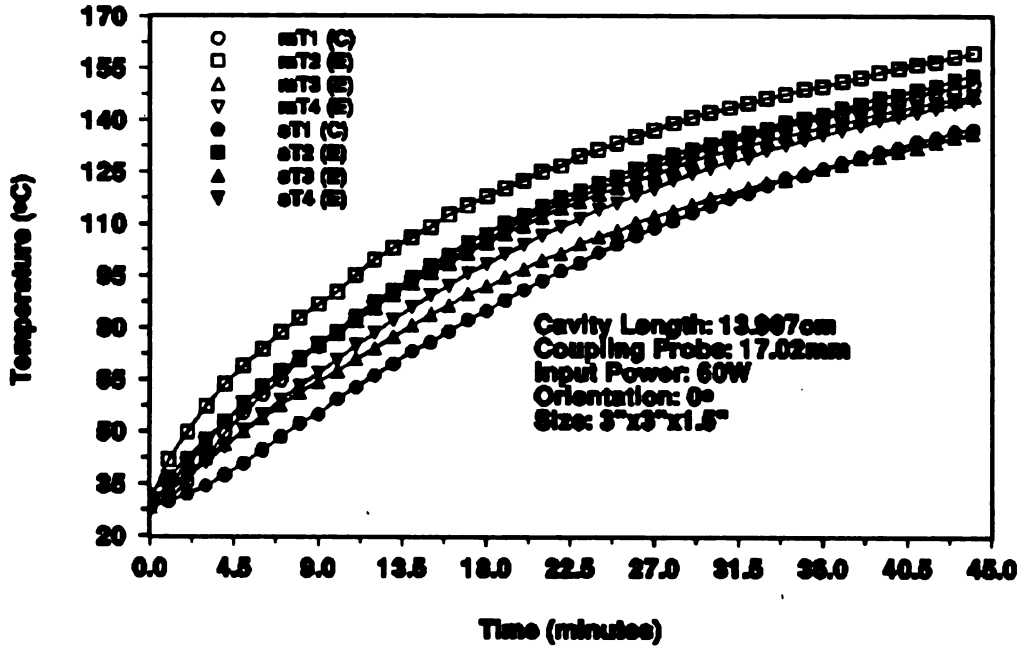

5.1(c) CH at L_c=13.91 cm & L_p=17.02 mm

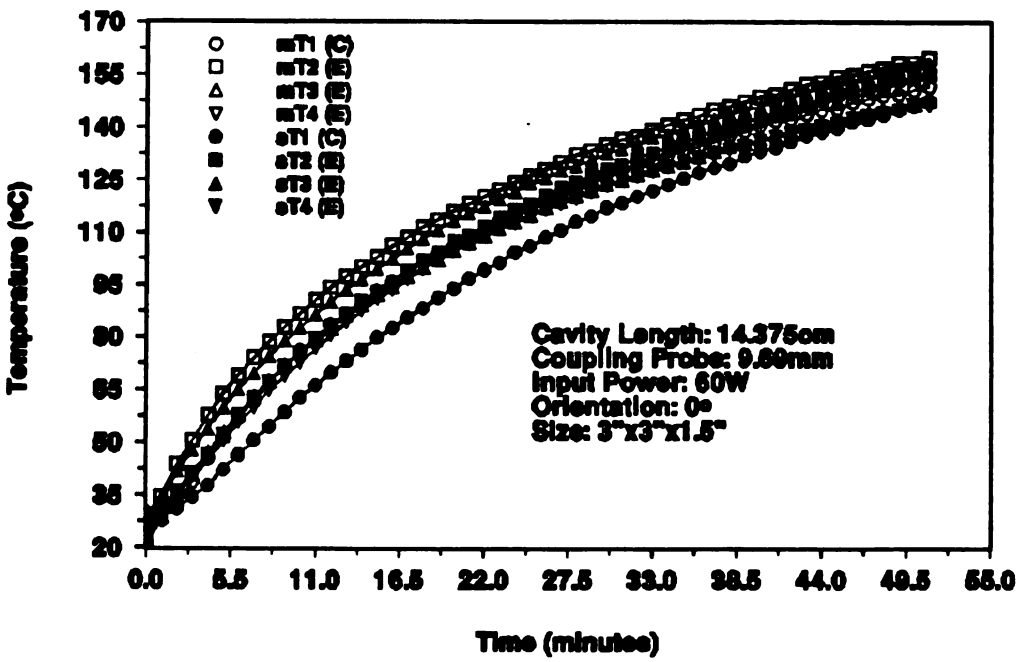

5.1(d) CH at L_c=14.38 cm & L_p=9.69 mm

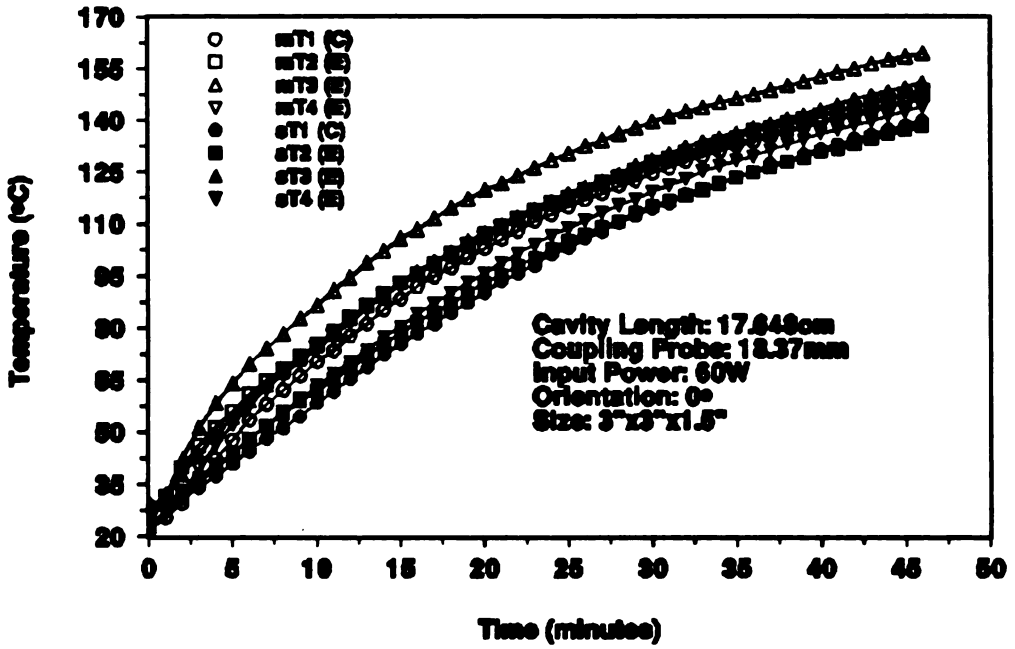

5.1(e) PS at L_c=17.65 cm & L_p=18.37 mm

Figure 5.1 Temperature/position/time Profiles during Microwave Heating of 3.8 cm Thick Crossply AS4/3501-6 Composite at 0° Fiber Orientation

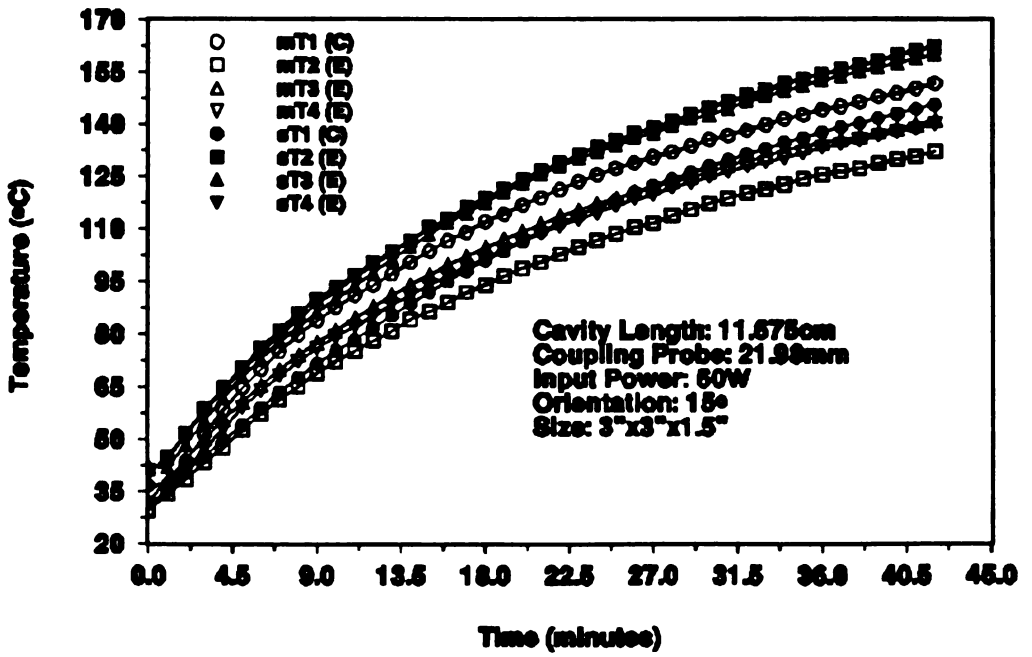

5.2(a) UH at L_c=11.68 cm & L_p=21.89 mm

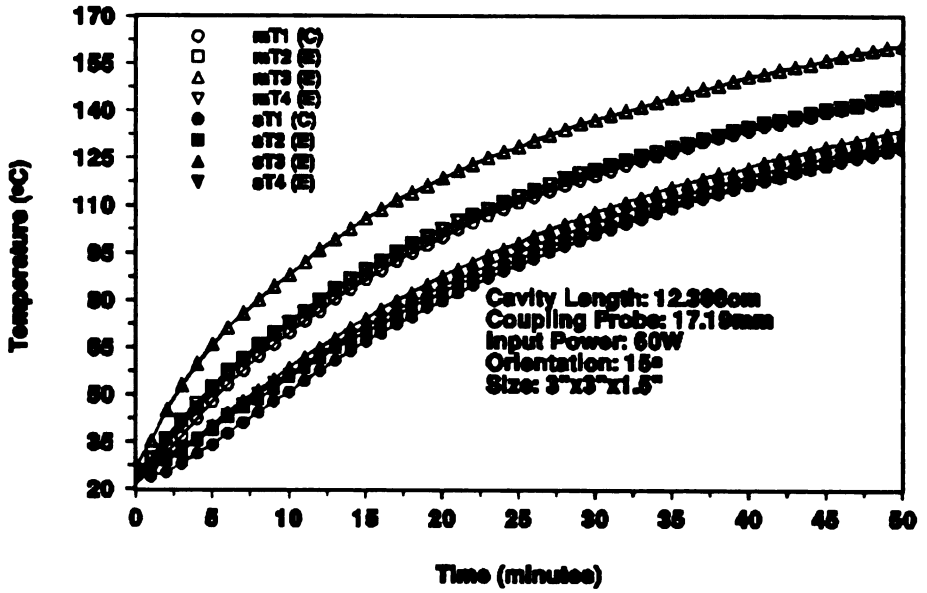

5.2(b) UH at L_c=12.31 cm & L_p=17.19 mm

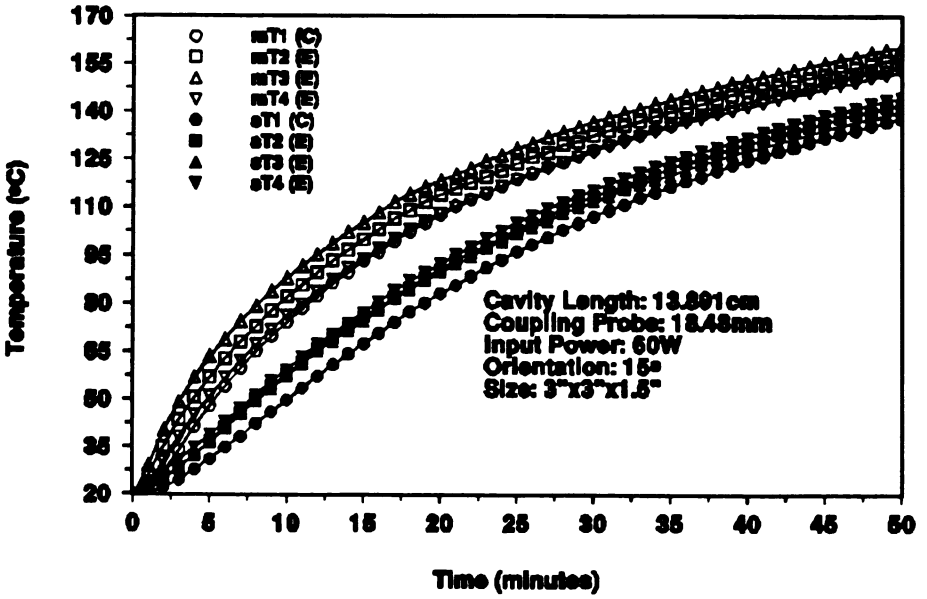

5.2(c) CH at L_c=13.89 cm & L_p=18.48 mm

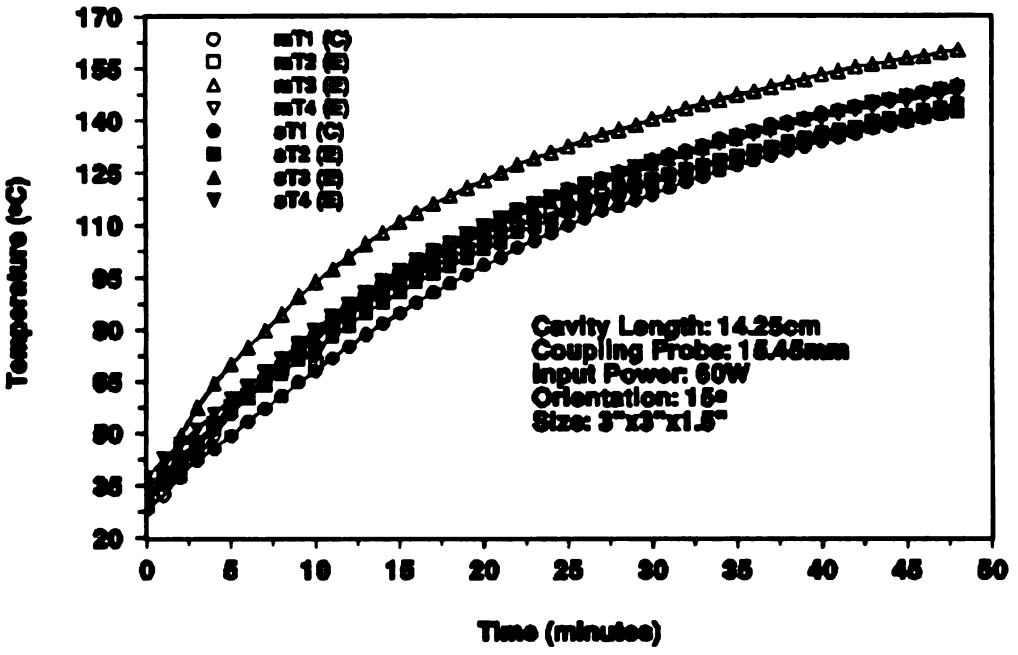

5.2(d) CH at L_c=14.25 cm & L_p=15.45 mm

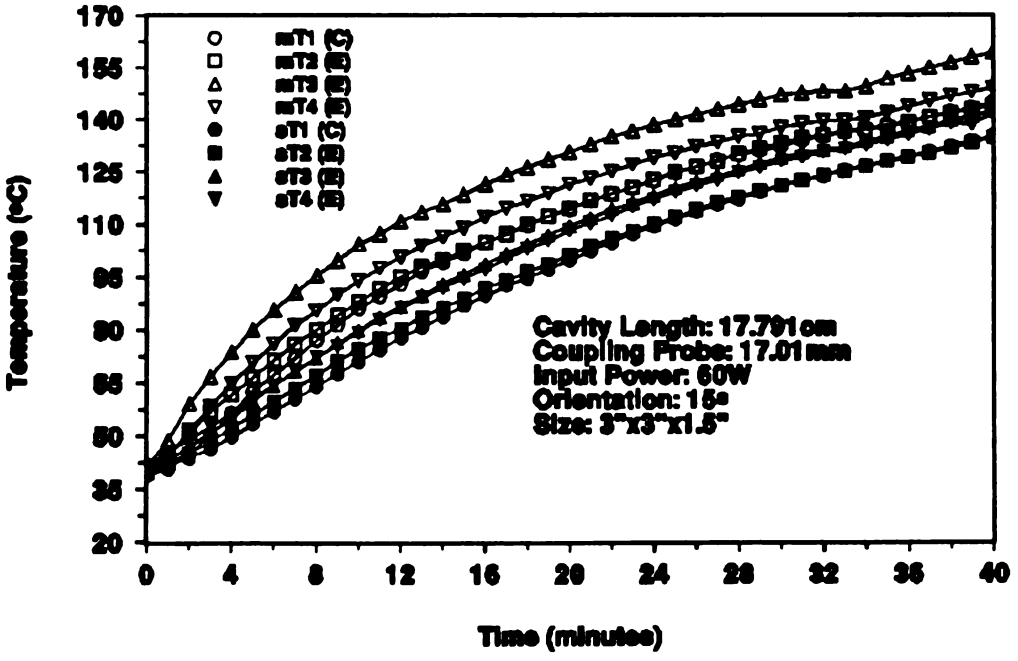

5.2(e) PS at L_c=17.79 cm & L_p=17.01 mm

Figure 5.2 Temperature/position/time Profiles during Microwave Heating of 3.8 cm Thick Crossply AS4/3501-6 Composite at 15° Fiber Orientation

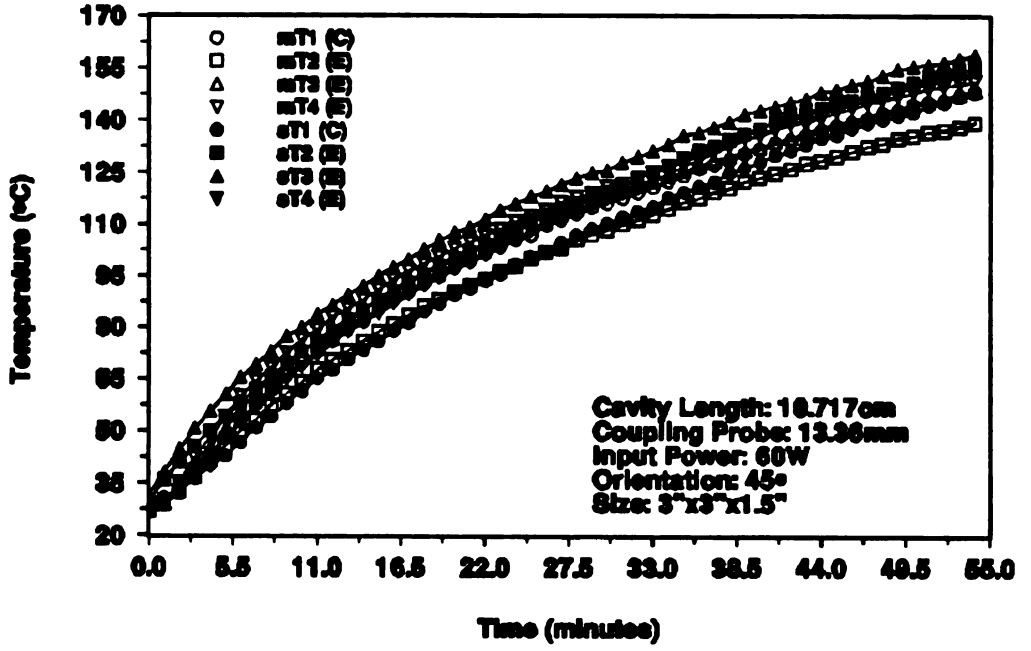

5.3(a) PS at L_c=10.71 cm & L_p=13.36 mm

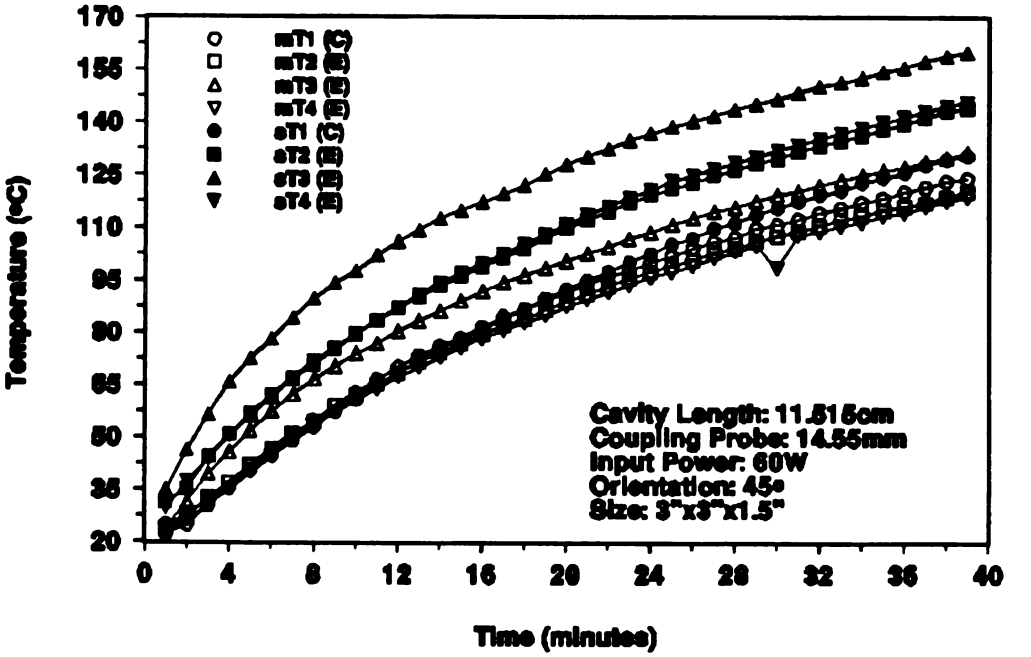

5.3(b) CH at L_c=11.52 cm & L_p=14.55 mm

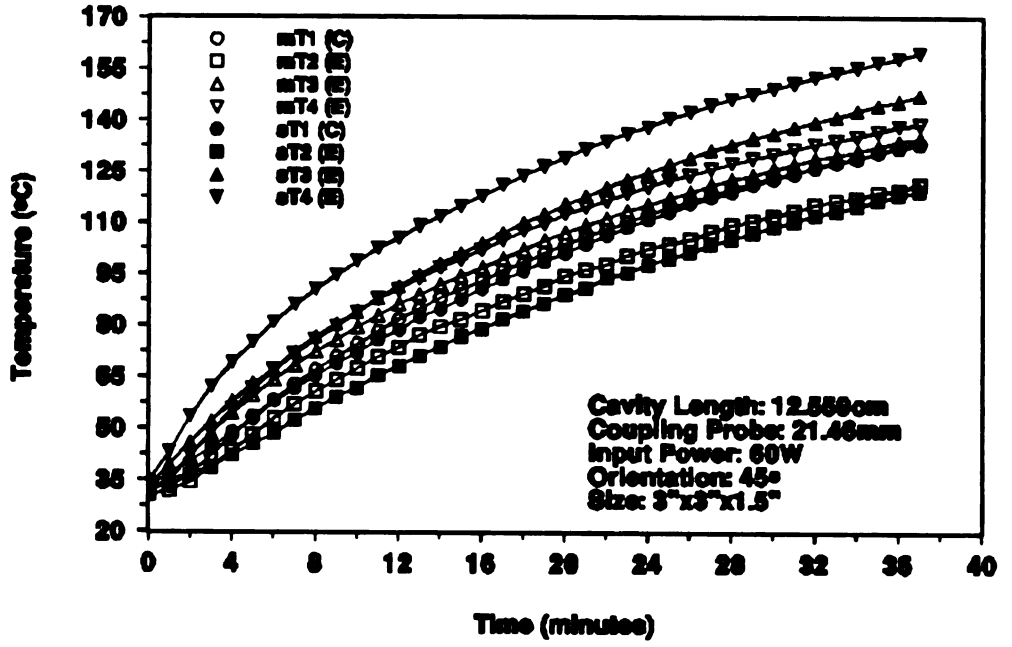

5.3(c) CH at L_c=12.56 cm & L_p=21.46 mm

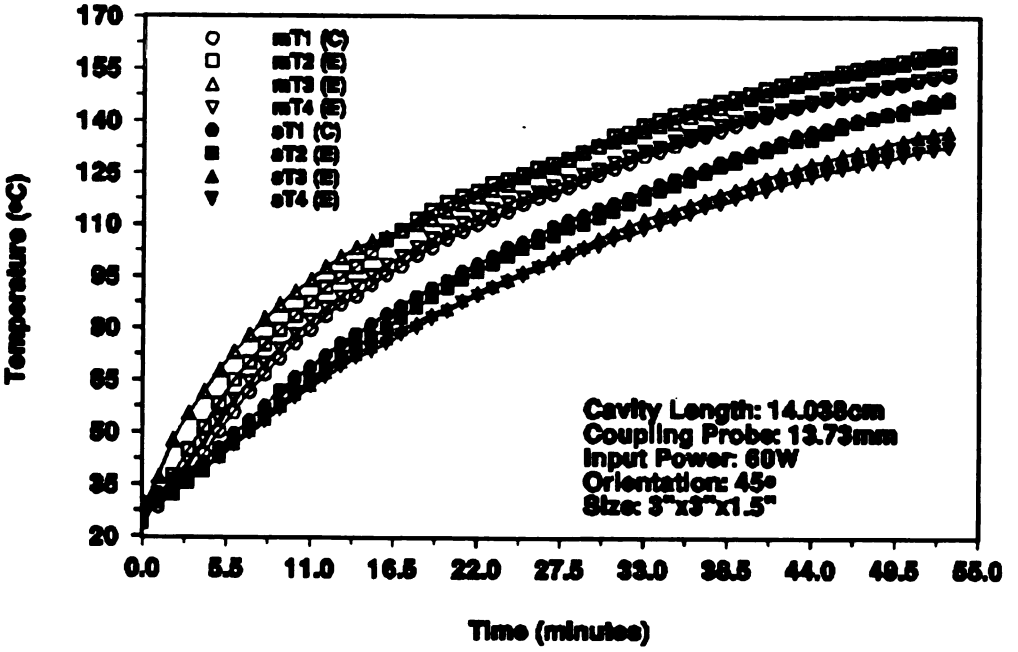

5.3(d) UH at L_c=14.04 cm & L_p=13.73 mm

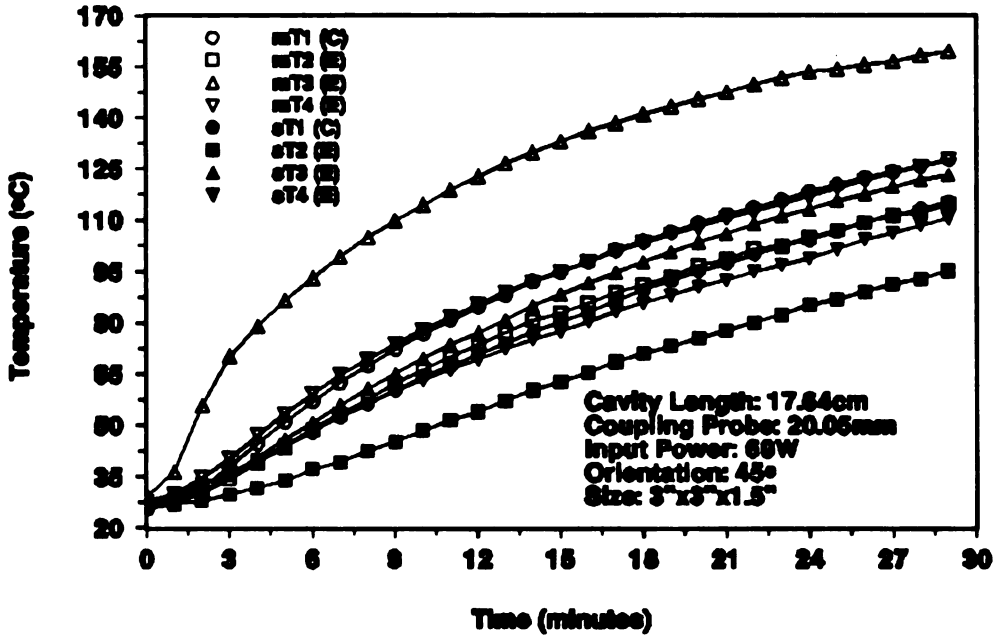

5.3(e) PS at L_c=17.64 cm & L_p=20.05 mm

Figure 5.3 Temperature/position/time Profiles during Microwave Heating of 3.8 cm Thick Crossply AS4/3501-6 Composite at 45° Fiber Orientation

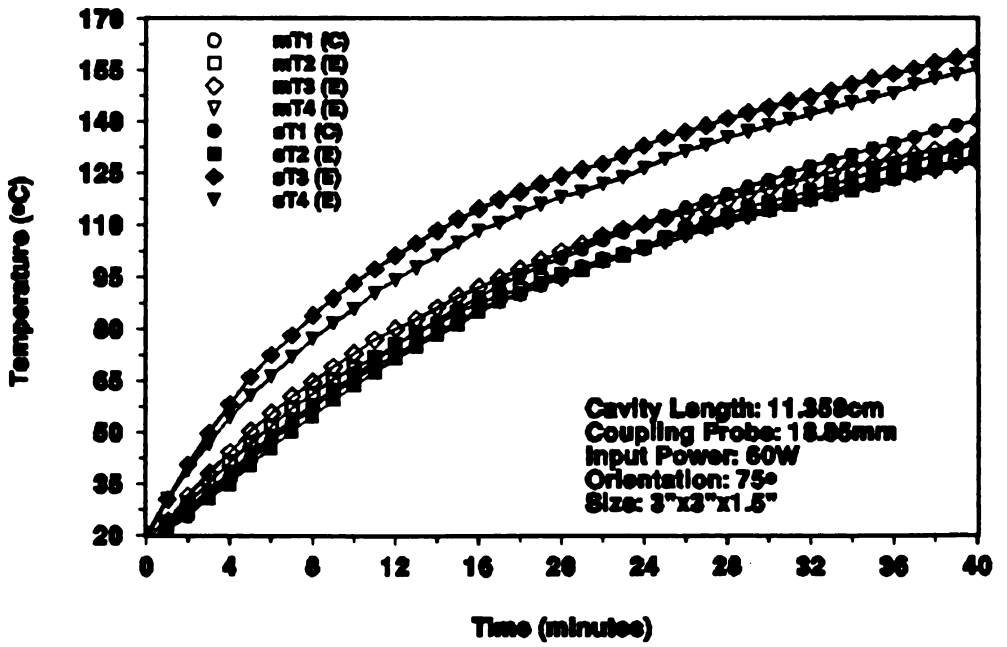

5.4(a) UH at L_c=11.36 cm & L_p=18.85 mm

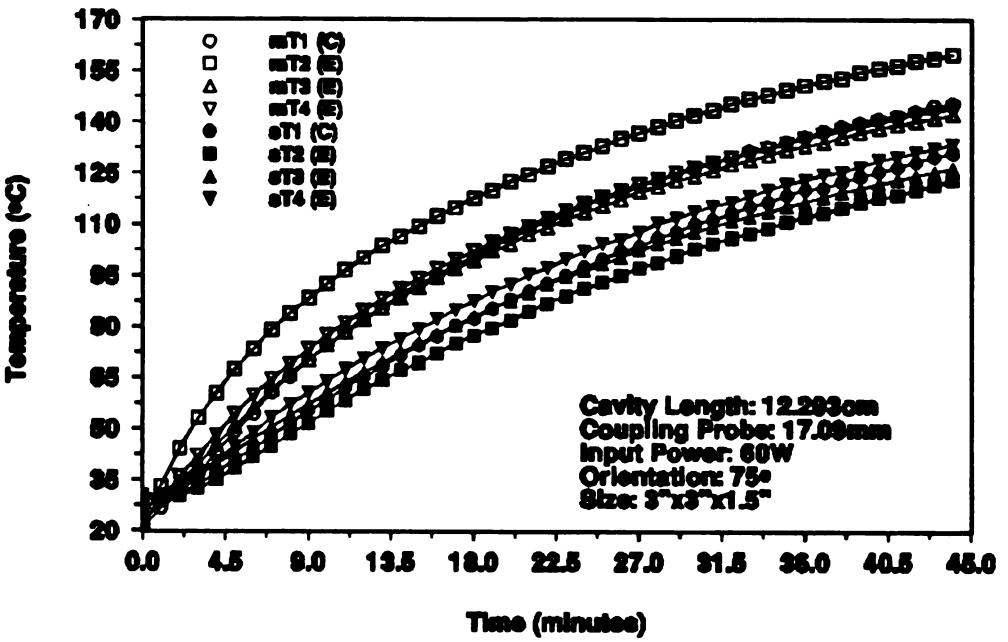

5.4(b) UH at $L_c = 12.29$ cm & $L_p = 17.09$ mm

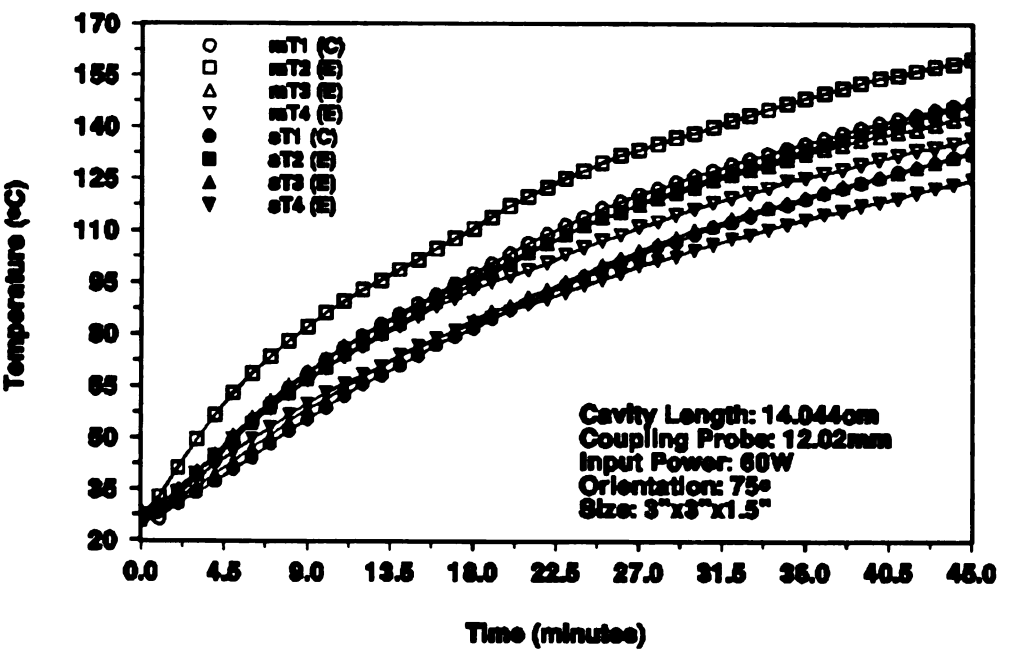

5.4(c) CH at $L_c = 14.04$ cm & $L_p = 12.02$ mm

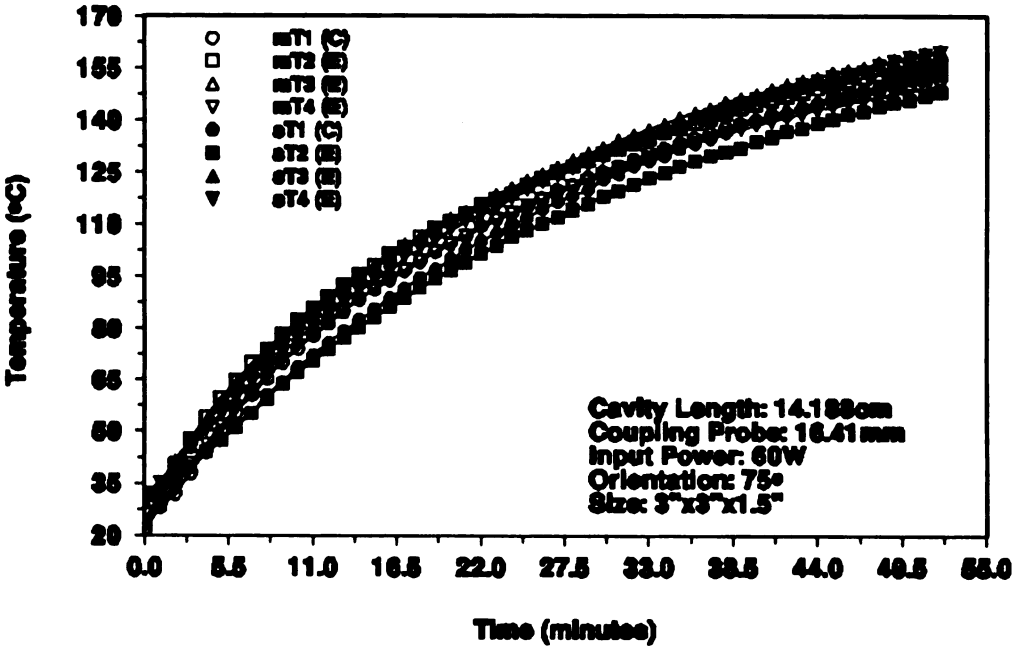

5.4(d) CH at L_c=14.19 cm & L_p=16.41 mm

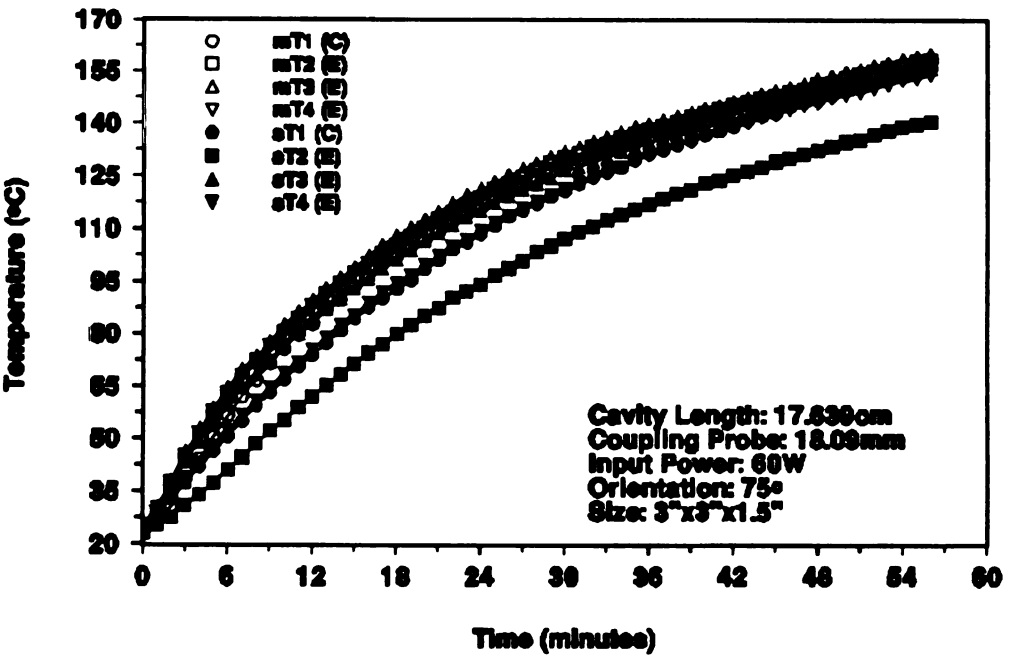

5.4(e) PS at L_c=17.64 cm & L_p=18.09 mm

Figure 5.4 Temperature/position/time Profiles during Microwave Heating of 3.8 cm Thick Crossply AS4/3501-6 Composite at 75° Fiber Orientation

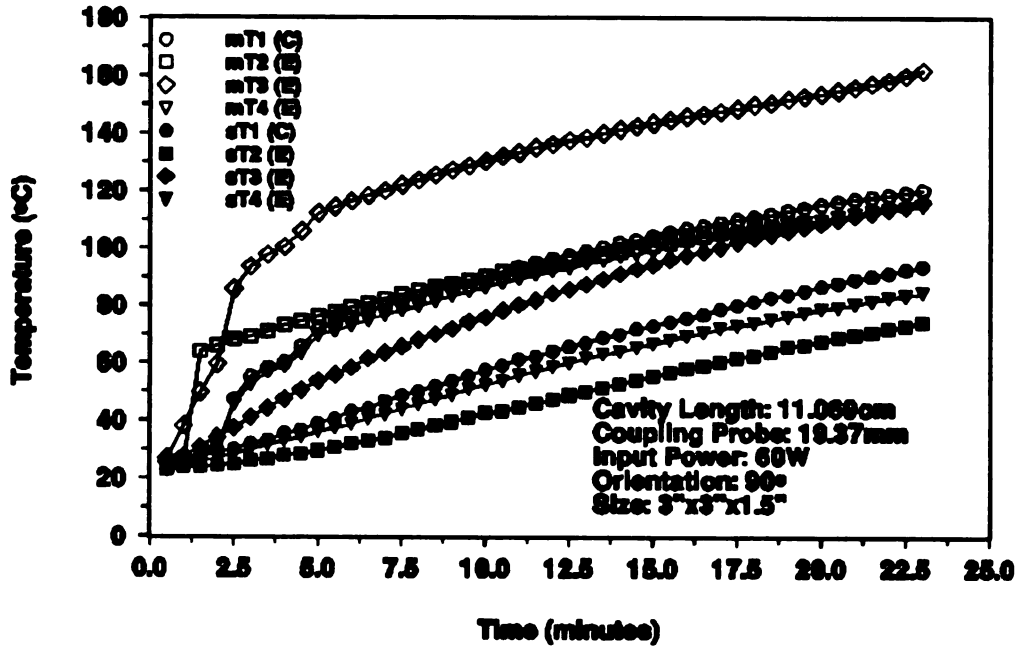

5.5(a) UH at L_c=11.07 cm & L_p=19.37 mm

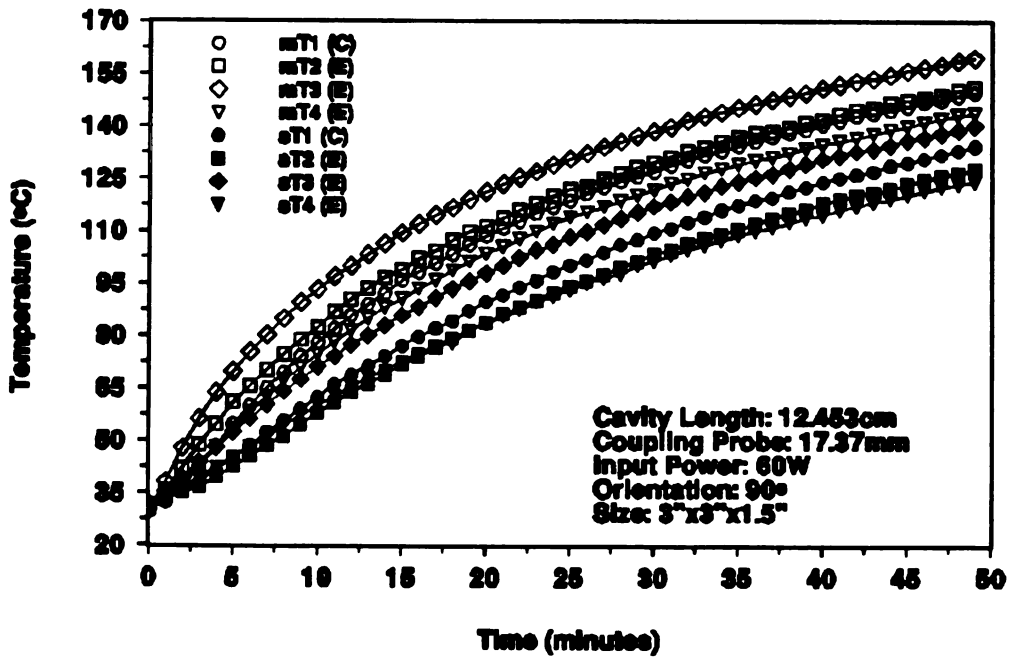

5.5(b) UH at L_c=12.45 cm & L_p=17.37 mm

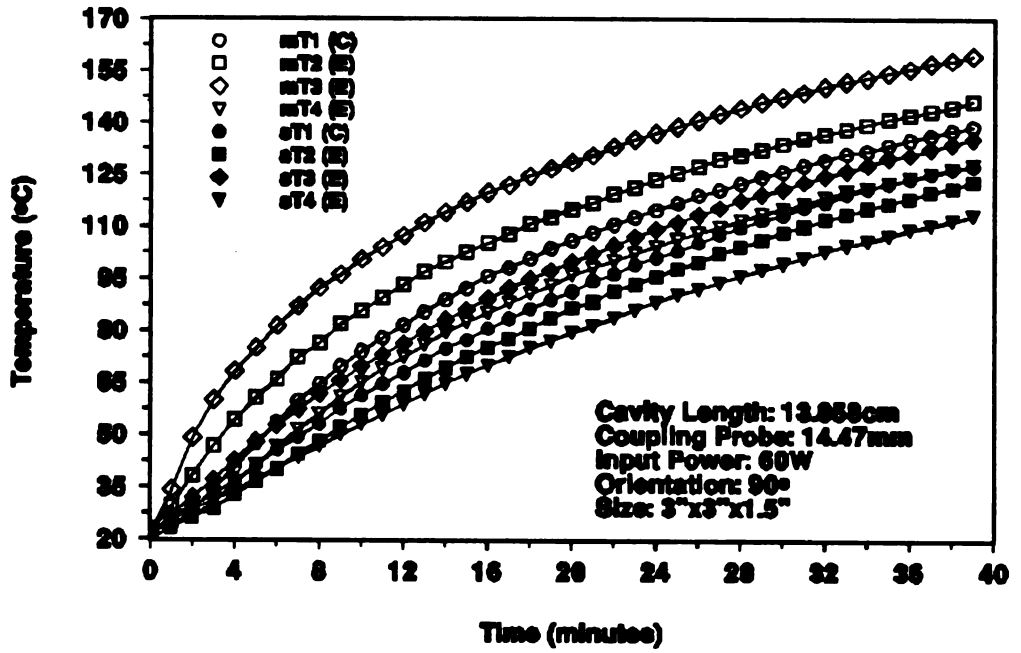

5.5(c) CH at L_c=13.86 cm & L_p=14.47mm

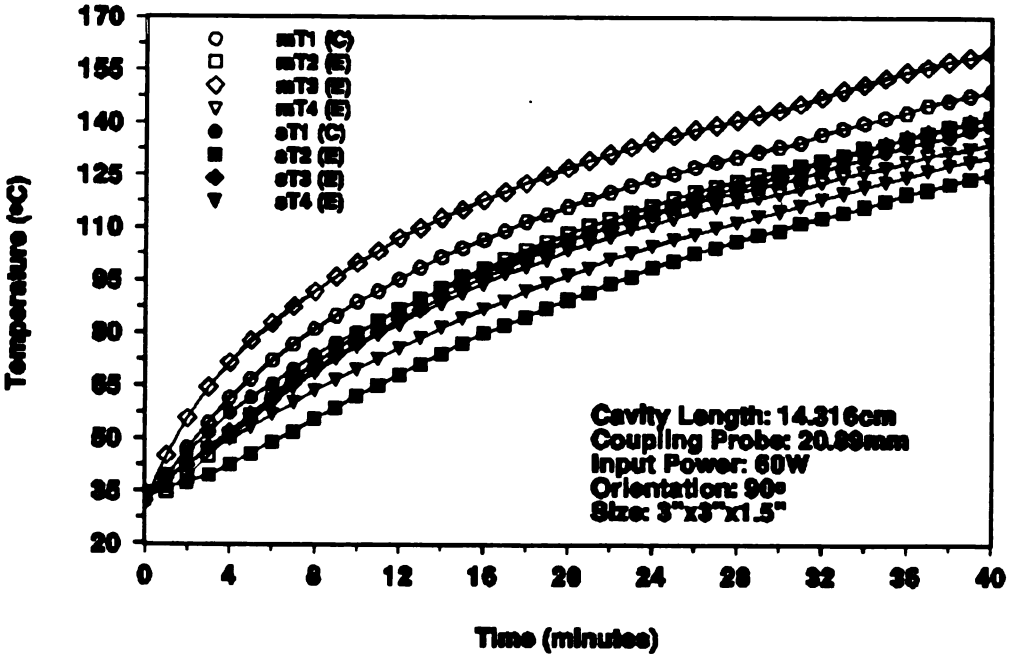

5.5(d) CH at L_c=14.32 cm & L_p=20.89 mm

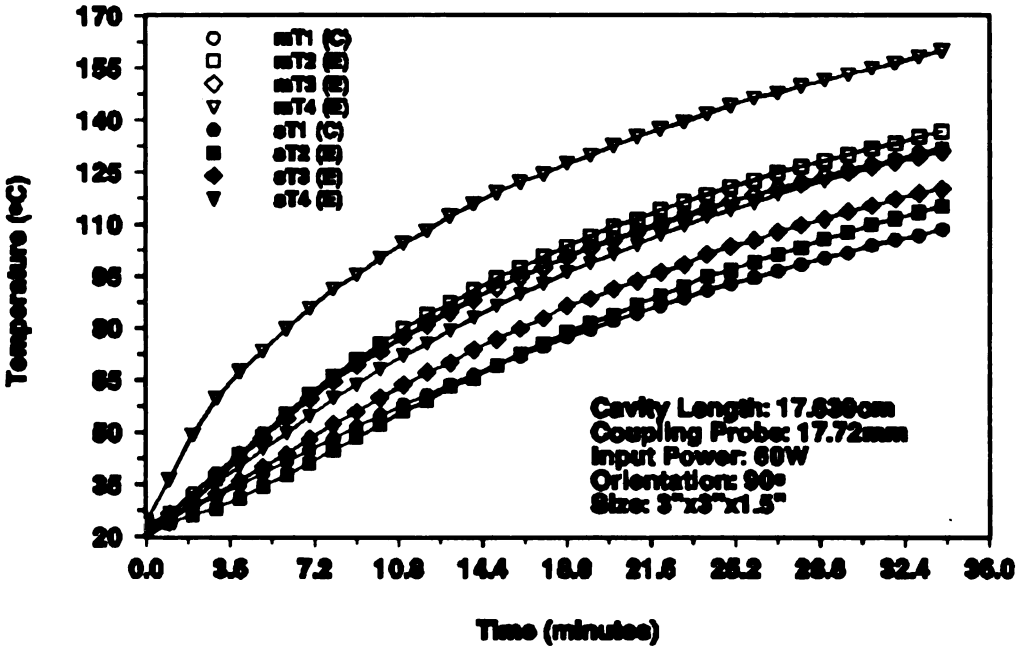

5.5(e) PS at L_c=17.64 cm & L_p=17.72 mm

Figure 5.5 Temperature/position/time Profiles during Microwave Heating of 3.8 cm Thick Crossply AS4/3501-6 Composite at 90° Fiber Orientation

For processing purposes, the more uniform the spatial temperature distribution and the smaller temperature gradient across the thickness of the composite, the better the mode. Therefore, the preference of processing mode selection can be based on the temperature uniformity. From Figure 5.1, the sequence of preference for the 0° fiber orientation was the CH mode at L_c=14.38 cm, PS mode at L_c=17.65 cm, CH mode at L_c=13.91 cm, UH mode at L_c=12.20 cm, and UH mode at L_c=12.20 cm. From Figure 5.2, the sequence of preference for the 15° fiber orientation was the CH mode at L_c=13.89 cm, UH mode at L_c=12.31 cm, CH mode at L_c=14.25 cm, PS mode at L_c=17.79 cm, and UH mode at L_c=11.68 cm. From Figure 5.3, the sequence of preference for the 45° fiber orientation was the PS mode at L_c=10.71 cm, UH mode at L_c=14.04 cm, CH mode at L_c=11.52 cm, CH mode at L_c=12.56 cm, and PS mode at L_c=17.64 cm. From Figure 5.4, the sequence of preference for

the 75° fiber orientation was the CH mode at L_c=14.19 cm, PS mode at L_c=17.64 cm, UH mode at L_c=12.29 cm, UH mode at L_c=11.36 cm, and CH mode at L_c=14.04 cm. From Figure 5.5, the sequence of preference for the 90° fiber orientation was the UH mode at L_c=12.45 cm, CH mode at L_c=14.32 cm, PS mode at L_c=17.64 cm, CH mode at L_c=13.86 cm, and UH mode at L_c=11.07 cm. If the allowable temperature gradient is 30°C, all of the heating modes at the 0° and 15° fiber orientations could be used for processing while none of the modes at the 90° orientation were qualified for processing. There were two modes having overall temperature gradient less than 30°C for the 45° and 75° orientations. The mode having the most uniform spatial temperature distribution was the CH mode with L_c=13.89 cm at the 15° fiber orientation with ΔT=10°C. The mode having the most uniform overall temperature distribution was the CH mode at L_c=14.19 cm at the 75° orientation with ΔT=10°C.

For easy comparison, the results in Figures 5.1 to 5.5 were converted into a tabular form. Tables 5.1 to 5.5 list the conditions and results of the microwave heating of a 3.8cm thick fully thermally cured crossply graphite fiber/epoxy composite at five fiber orientations. The first column in the tables shows the mode type along with the cavity length L_c and the coupling probe depth L_p. Comparing Table 5.1 to Table 5.5, the types of resonant heating modes are ordered in the same way for 0° and 90° fiber orientations. The sequence is two uncontrolled-hybrid modes (UH), followed by two coupled controlled-hybrid modes (CH), and a pseudo-single mode (PS). The corresponding modes are also located at similar cavity lengths for both orientations. Comparing Table 5.2 to Table 5.4, the same similarity of modes (type, sequence, and L_c) is found between the 15° and 75° orientations. The sequence is again two UH, two CH, and a PS. The mode sequence and locations for the 45° fiber orientation are unique as listed in Table 5.3. The mode sequence is a PS, two CH, a UH, and a PS. These results suggest that a symmetry of mode characteristics (mode type and L_c) exists with regard to fiber orientation. The existence of a symmetry of mode type do not necessarily imply the symmetry of

electric field pattern. The symmetry of electric field pattern can be determined from the comparison of the temperature/time/position profiles of corresponding modes. Comparing Figure 5.1, heating results at the 0° fiber orientation, to Figure 5.5, heating results at the 90° fiber orientation, only one similar heating pattern, case (b), was found. This may be because these two modes not only share the same mode type (UH) and cavity length, but also similar coupling probe depth. However, the symmetry of heating pattern is not found for PS modes even though they share the same mode type, cavity length, and coupling probe depth, such as case (e). The same symmetry phenomenon of heating pattern was observed for 15° and 75°. Comparing Figure 5.2 to Figure 5.4, the (b)'s shared the same mode type (UH), L_c, and L_p and the heating patterns were the same. Though the PS mode in the (e)'s shared the same L_c and L_p, the heating pattern was different for the 15° and 75° fiber orientations.

Table 5.1. Conditions and Results for Microwave Heating of 7.8 X 7.8 X 3.8cm Fully Thermally Cured Crossply AS4/3 501-6 Composite in a 17.8cm Cylindrical Cavity for 0° Fiber Orientation.

Mode Type & Lc(cm) Lp(mm)	Time* to reach 160 °C (min.)	ΔT_s (°C)	ΔT_m (°C)	Overall ΔT (°C)	Overall Processing Index
UH Lc=10.94 Lp=16.30	42-M	21	22	30	8.1
UH Lc=12.20 Lp=18.87	60-M	15	17	30	7.6
CH Lc=13.91 Lp=17.02	44-M	17	14	25	6.5
CH Lc=14.38 Lp= 9.69	51-M	10	16	17 2(Ts>Tm)	5.1
PS Lc=17.65 Lp=18.37	46-M	13	15	22	5.9

Table 5.2. Conditions and Results for Microwave Heating of 7.8 X 7.8 X 3.8cm Fully Thermally Cured Crossply AS4/3 501-6 Composite in a 17.8cm Cylindrical Cavity for 15° Fiber Orientation.

Mode Type & Lc(cm) Lp(mm)	Time* to reach 160 °C (min.)	ΔT_s (°C)	ΔT_m (°C)	Overall ΔT (°C)	Overall Processing Index
UH Lc=11.68 Lp=21.89	42-S	18	20	30 3(Ts>Tm)	7.6
UH Lc=12.31 Lp=17.19	49-M	6	16	22	5.4
CH Lc=13.89 Lp=18.48	49-M	5	10	23	4.8
CH Lc=14.25 Lp=15.45	47-M	8	19	19	5.5
PS Lc=17.79 Lp=17.01	39-M	8	18	25	5.9

Table 5.3. Conditions and Results for Microwave Heating of 7.8 X 7.8 X 3.8cm Fully Thermally Cured Crossply AS4/3 501-6 Composite in a 17.8cm Cylindrical Cavity for 45° Fiber Orientation.

Mode Type & Lc(cm) Lp(mm)	Time* to reach 160 °C (min.)	ΔT_s (°C)	ΔT_m (°C)	Overall ΔT (°C)	Overall Processing Index
PS Lc=10.71 Lp=13.36	55-S	10	12	20 3(Ts>Tm)	5.3
CH Lc=11.52 Lp=14.55	39-S	30	12	45 4(Ts>Tm)	9.5
CH Lc=12.56 Lp=21.46	37-S	43	16	43 2(Ts>Tm)	10.9
UH Lc=14.04 Lp=13.73	54-M	13	10	30	6.6
PS Lc=17.64 Lp=20.05	29-M	26	48	65	14.5

Table 5.4. Conditions and Results for Microwave Heating of 7.8 X 7.8 X 3.8cm Fully Thermally Cured Crossply AS4/3 501-6 Composite in a 17.8cm Cylindrical Cavity for 75° Fiber Orientation.

Mode Type & Lc(cm) Lp(mm)	Time* to reach 160 °C (min.)	ΔT_s (°C)	ΔT_m (°C)	Overall ΔT (°C)	Overall Processing Index
UH Lc=11.36 Lp=18.85	40-S	30	4	32 4(Ts>Tm)	7.4
UH Lc=12.29 Lp=17.09	44-M	10	19	38	7.5
CH Lc=14.04 Lp=12.02	44-M	21	23	35	8.8
CH Lc=14.19 Lp=16.41	52-S	15	6	15 2(Ts>Tm)	4.4
PS Lc=17.64 Lp=18.09	55-M	13	4	20	4.8

Table 5.5. Conditions and Results for Microwave Heating of 7.8 X 7.8 X 3.8cm Fully Thermally Cured Crossply AS4/3 501-6 Composite in a 17.8cm Cylindrical Cavity for 90° Fiber Orientation.

Mode Type & Lc(cm) Lp(mm)	Time* to reach 160 °C (min.)	ΔT_s (°C)	ΔT_m (°C)	Overall ΔT (°C)	Overall Processing Index
UH Lc=11.07 Lp=19.37	23-M	43	53	88	18.9
UH Lc=12.45 Lp=17.37	49-M	15	17	39	8.1
CH Lc=13.86 Lp=14.47	39-M	35	25	50	8.8
CH Lc=14.32 Lp=20.89	40-M	15	26	35	8.4
PS Lc=17.64 Lp=17.72	34-M	22	29	51	10.9

* The time required to reach the control temperature 160°C. The M or S indicate that the location of the temperature probe that reached 160°C was at midplane or surface.

In Table 5.1 to 5.5, the value in column 2 is a qualitative index of the heating rate for the modes. Columns 3, 4, and 5 list the maximum surface, midplane, and overall temperature differences respectively. As shown in Figures 5.1 to 5.5, the midplane temperatures were usually higher than the corresponding surface temperatures. The number of locations was listed using $T_s > T_m$ as indicator in Column 5 when the surface temperature was higher than the corresponding midplane temperature.

Columns 2-5 in Tables 5.1 to 5.5 show that the microwave heating rates and temperature uniformity vary with fiber orientation and cavity length of the resonant heating mode. Figure 5.6 shows the heating time as function of cavity length (i.e. mode) for various fiber orientations. The time ranges from 20 minutes to 60 minutes. Figure 5.7 shows the overall temperature difference as function of cavity length (i.e. mode) for various fiber orientations. From Figures 5.6 and 5.7, it is clear that time and the temperature difference are related. If the temperature difference was low, the microwave energy was evenly distributed inside the composite and it took a longer time to heat the whole composite to the control temperature. If the temperature difference was large, the microwave energy was focused on one spot and the time required to heat one spot to the control temperature was short.

To quantify the quality of each heating mode, the overall processing index (I) was introduced. The I is a dimensionless value and was calculated by:

$$I = \frac{a\Delta T_s + b\Delta T_m + \Delta T + dt}{10} \qquad (5\text{-}1)$$

where a,b,c,d are relative weight factors. a,b, and c have units of 1/°C while d has units of 1/min. The smaller the value of I, the higher the quality of the heating mode. In the processing of composites, the temperature uniformity, ΔT_s, ΔT_m, and ΔT_{tot}, is critical to the final mechanical properties. The time, t, required to reach control-temperature can be reduced, however, by increasing input power. Therefore, the weight factors a, b, and c are much more important than d. For the calculation in Tables 5.1 to 5.5, a, b, and c were set equal to 1, and d was set equal to 0.2.

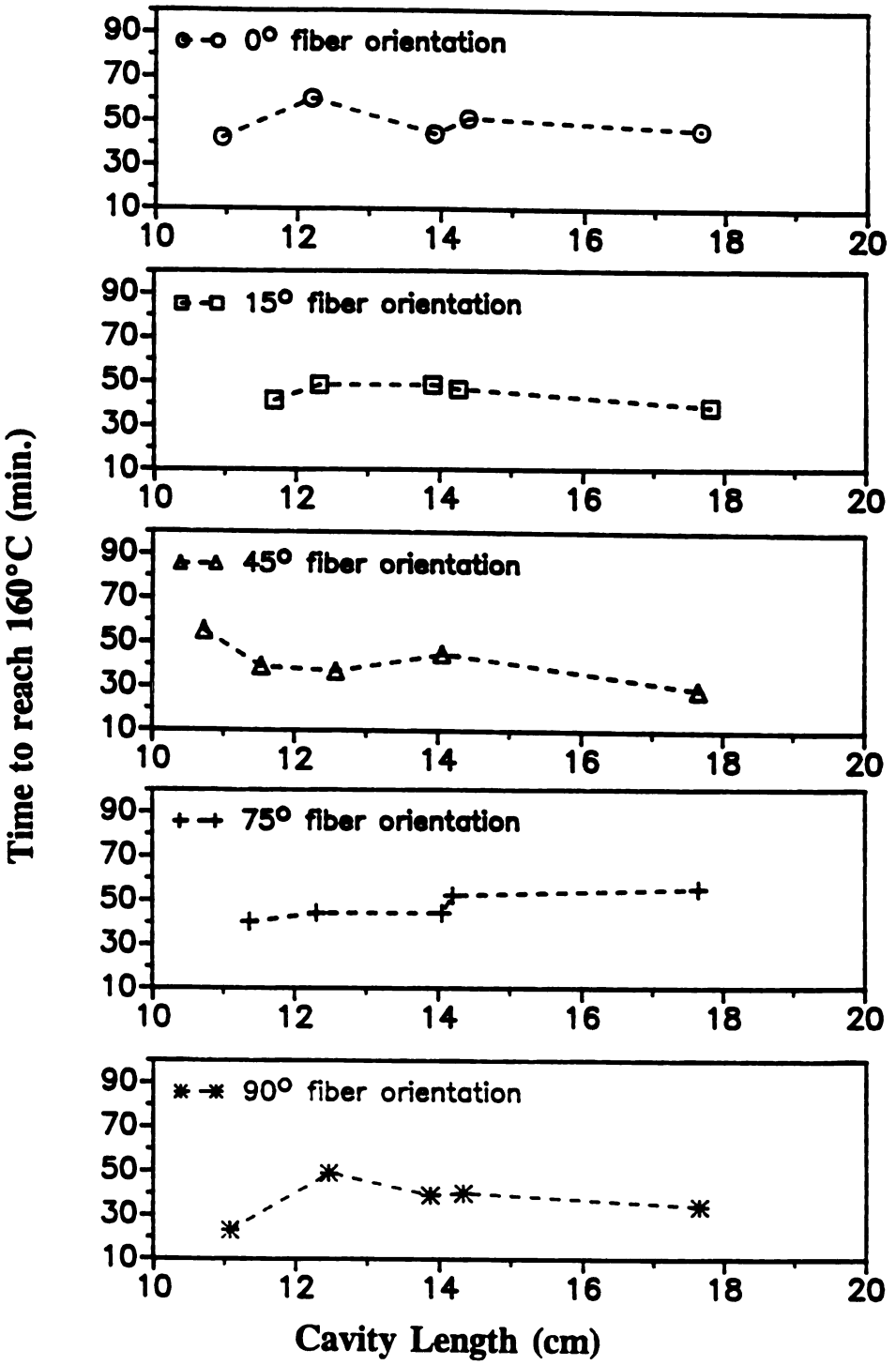

Figure 5.6 Heating Time for Various Resonant Heating Mode at Various Fiber Orientation

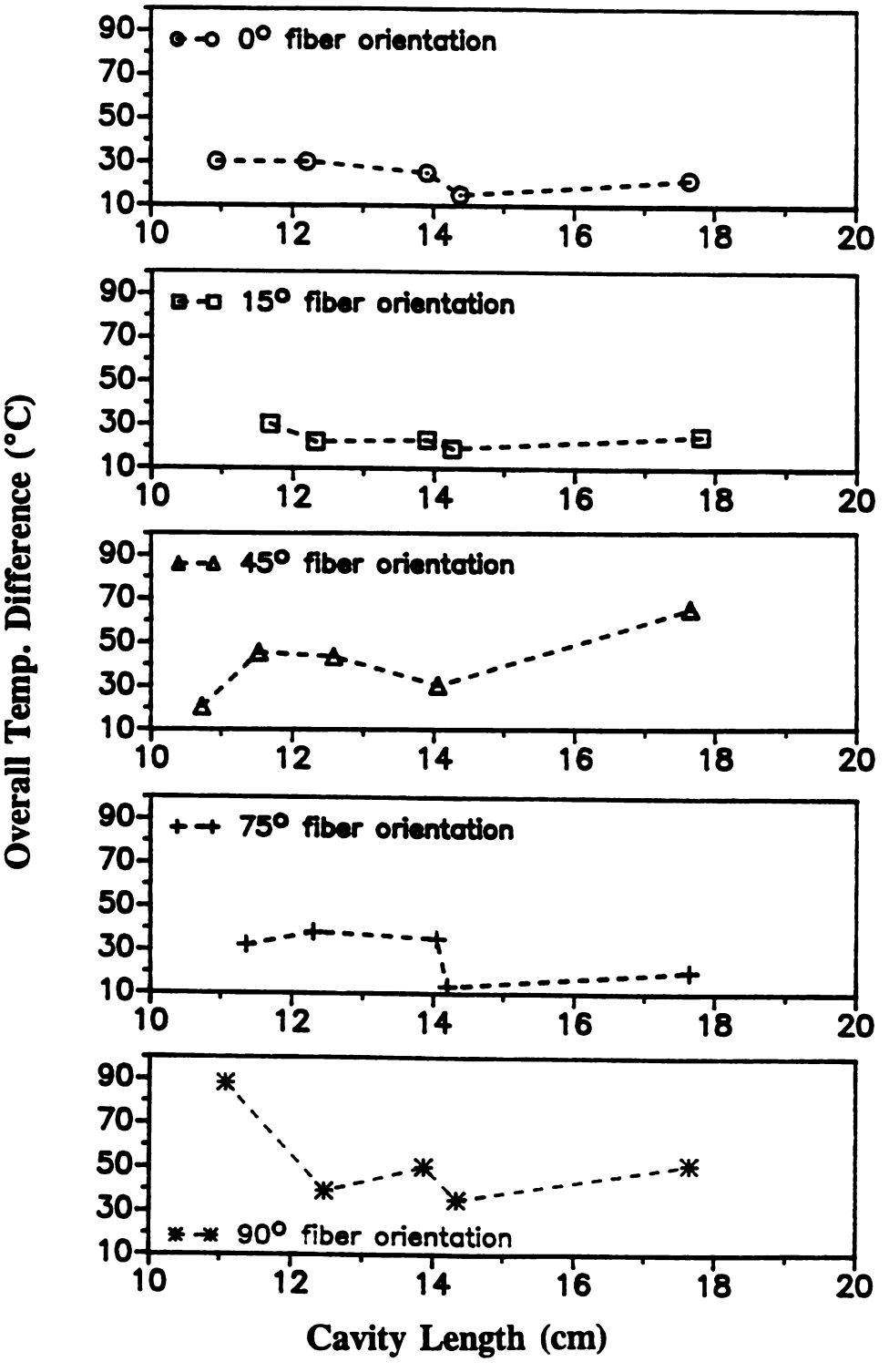

Figure 5.7 Temperature Difference for Various Resonant Heating Mode at Various Fiber Orientation

Figure 5.8 shows the overall processing index I versus cavity length for various fiber orientations. The cavity length of each heating mode is similar for 0°, 15°, 75°, and 90° fiber orientations. The similarity increases with cavity length. For the resonant heating modes between L_c =17cm and L_c =18cm, the cavity length is essentially the same, L_c =17.6cm, even for 45° fiber orientation. The overall processing index I is, however, very different and is a strong function of fiber orientation and cavity length. If the maximum allowable index value is set equal to 6, (the maximum temperature difference is 25°c), the number of allowable resonant heating modes for 15°, 75°, 0°, 45°, and 90° fiber orientations were found to be 4, 2, 2, 1, and 0, respectively. The best fiber orientation for microwave processing of 3.8cm thick crossply composite is 15°. As listed in Tables 5.1 to 5.5, there are 3 modes having I lower than 5. They are the CH mode of 75° fiber orientation at L_c = 14.19cm, L_p = 16.41 mm, the PS mode of 75° fiber orientation at L_c = 17.64cm, L_p =18.09mm, and the CH mode of 15° fiber orientation at L_c =13.89cm, L_p=18.48mm. The temperature differences listed in columns 3, 4, and 5 of Tables 5.1 to 5.5 indicate that the temperature profiles are the most uniform in these modes.

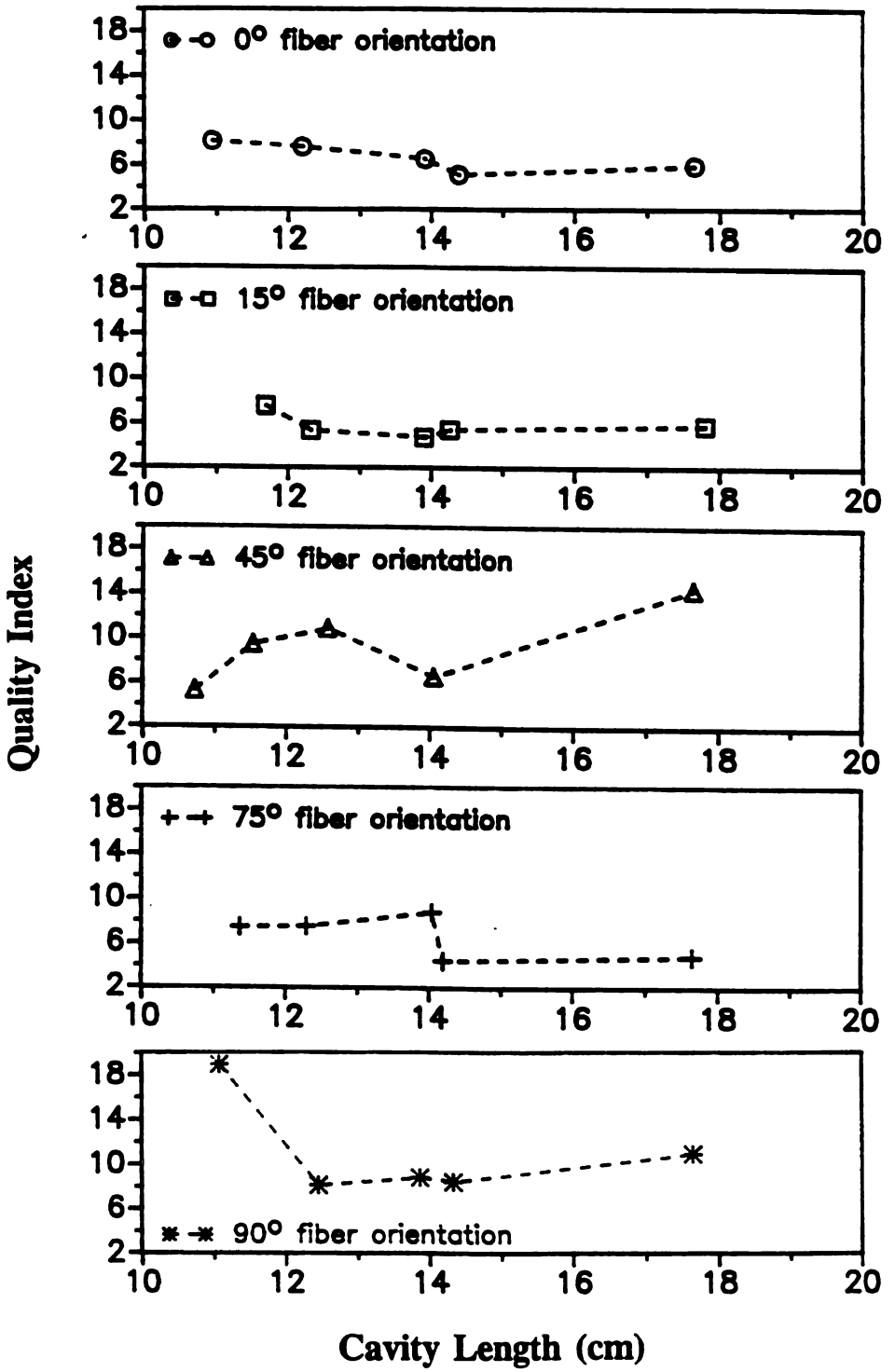

Figure 5.8 Quality Index for Various Resonant Heating Mode at Various Fiber Orientation

Column 5 in Table 5.1 to Table 5.5 also shows that there were only two cases where all surface temperatures were higher than the corresponding midplane temperatures. This result implies that there is a significant amount of the electric field at the midplane. According to the skin depth theory, the electric field along the fiber direction of AS4/3501-6 composite has a skin depth of 9.8mm. The low skin depth implies that the electric field in this direction will not contribute to the heating in the midplane. The skin depth for the electric field perpendicular to the fiber direction of AS4/3501-6 composite, however, has a value of 3.2m. The qualitative description of penetration depth for various configurations between electric field and fiber directions for individual fibers, unidirectional composites, and crossply composites are shown in Figures 5.9, 5.10, and 5.11 respectively. For individual fibers and unidirectional composites, there are three directions of the incident electric field which will have a large penetration depth. They are electric fields perpendicular to the fibers, one from the top and two from the sides, as shown in Figure 5.9 and 5.10. For crossply composites, only the electric field from the side has a large penetration depth as shown in Figure 5.11. Therefore, the high midplane temperatures suggest that the electric field inside the composite was from the side for the majority of the heating modes. The data in Tables 5.1 to 5.5 reveal that a 3.8cm thick crossply graphite fiber/epoxy composite can be uniformly heated in a 17.8cm resonant cavity by 2.45GHz microwave radiation.

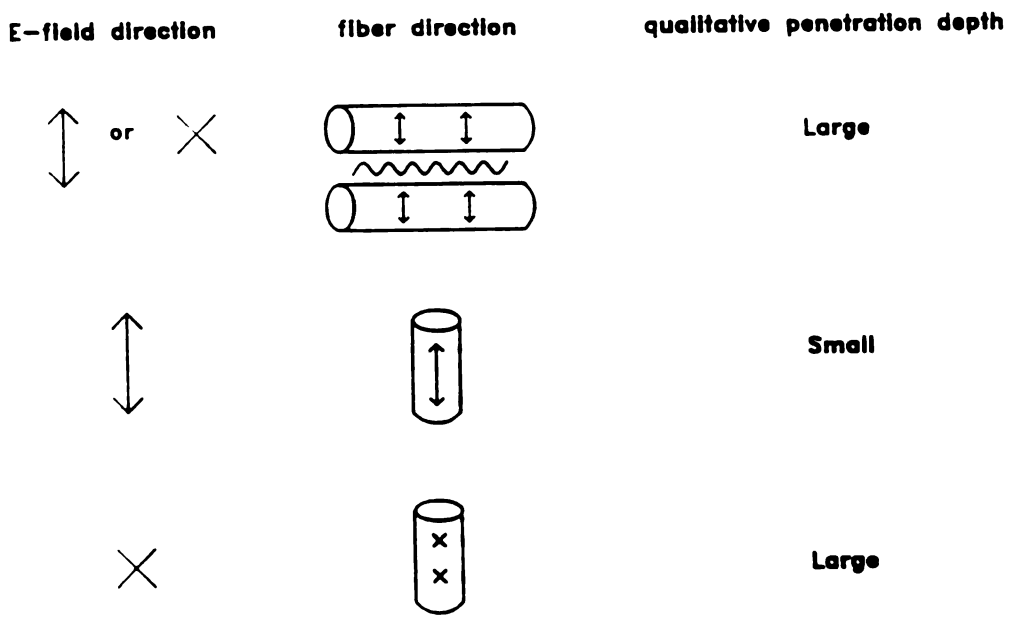

Figure 5.9 Qualitative Description of Penetration Depth for Individual Fibers

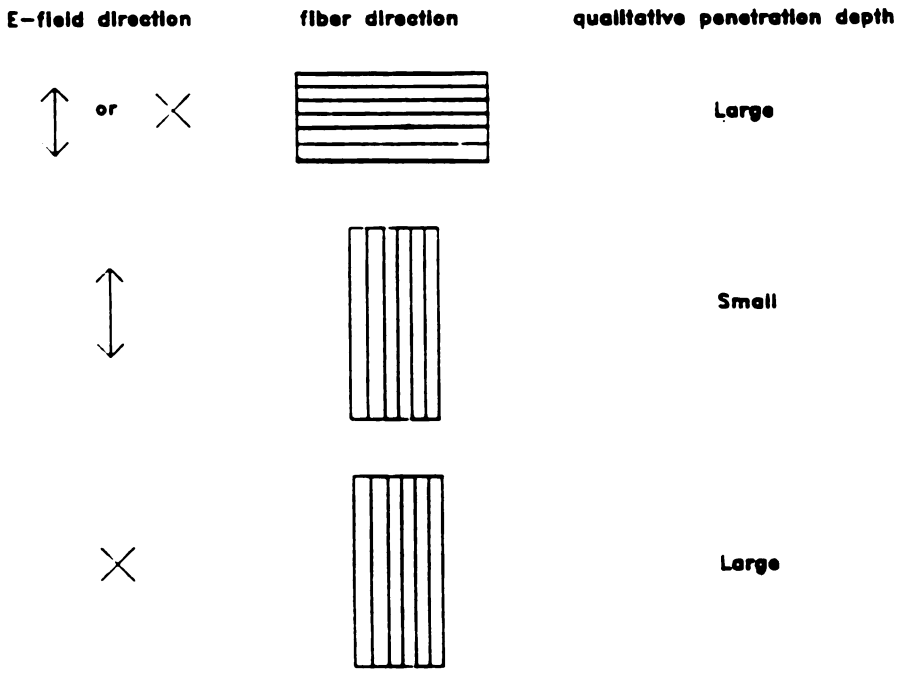

Figure 5.10 Qualitative Description of Penetration Depth for Unidirectional Composites

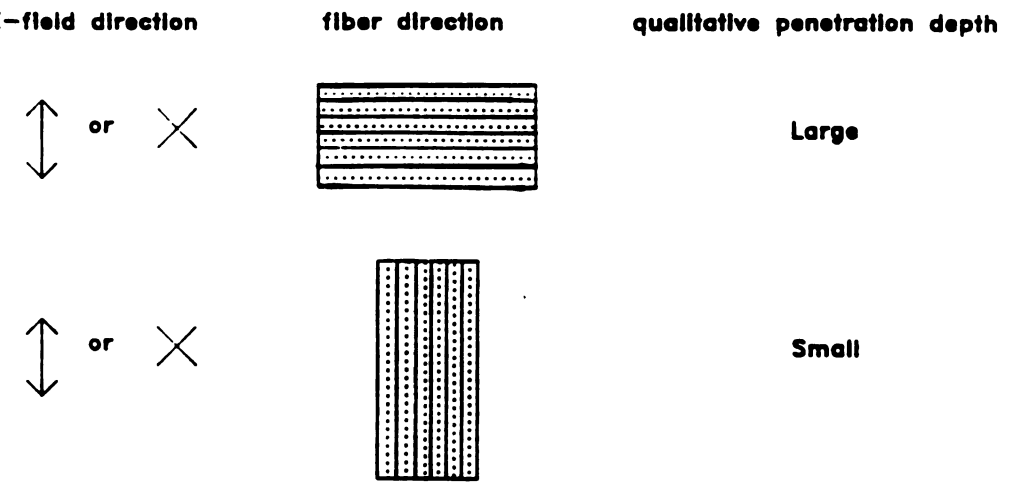

Figure 5.11 Qualitative Description of Penetration Depth for Crossply Composites

Based on the microwave heating experiments of thick-section graphite fiber composite, a fresh 7.6x7.6x3.3 cm crossply AS4/3501-6 laminate (200 plies) was microwave processed using a resonant mode at the 15° fiber orientation with L_c = 13.22cm and L_p = 21.98mm. This mode is the analog to the best heating mode for the fully thermally cured 3.8cm thick crossply sample. The difference in the cavity length is due to the difference of thickness and loss factor between the fresh and fully cured samples. Figure 5.13 shows the temperature/position/time profiles for the fresh sample. As shown in Figure 5.13, both surface and midplane temperatures in the fresh composite are uniform by themselves during microwave processing, similar to those of the fully cured composite. Comparing Figure 5.13 and Figure 5.3(c), the temperature difference between surface and midplane of the fresh sample is 50°C higher than that of the fully cured composite at the time when the midplane reached controlled temperature. The heating rate of the midplane in the fresh sample is, however, twice as fast as in the fully cured sample. Both differences are due to the

exothermic reaction in the fresh sample. With the midplane temperature controlled at 160°C, the surface/midplane temperature difference in the fresh composite decreased with time, and reached 40°C after 65 minutes. To reduce the temperature difference between the surface and midplane, a resonant heating mode with uniform planar temperature profiles but a higher surface heating rate should used for the processing of fresh composite. The best candidate for achieving uniform temperature distribution across thick-section composites during microwave processing is the CH mode at the 75° fiber orientation at L_c = 14.19cm as shown in Figure 5.4(d).

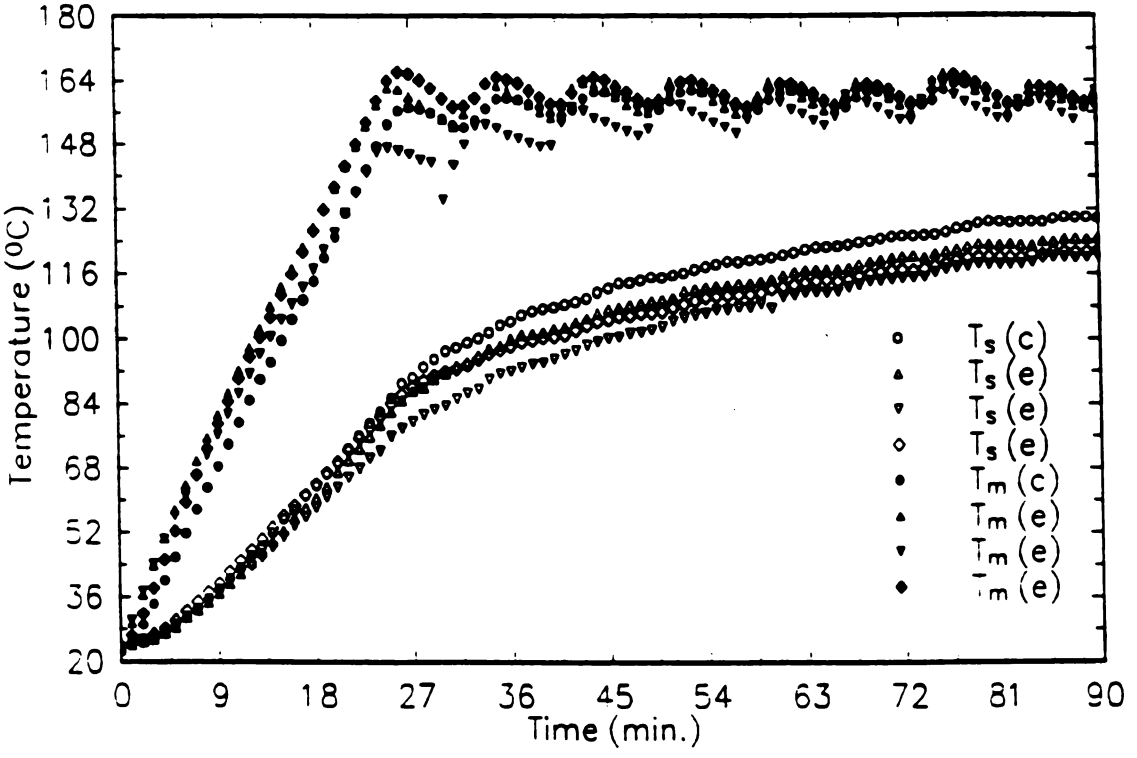

Figure 5.13 Temperature/position/time Profiles during Microwave Processing of 200-crossply Fresh AS4/3501-6 Composite.

5.4. Conclusion

Fiber orientation effects in the microwave processing of graphite fiber/epoxy composite were studied in a 17.8cm cylindrical tunable resonant cavity using 2.45

GHz microwave radiations. A thick-section fully autoclave cured crossply (7.8x7.8x3.8 cm) AS4/3501-6 composite, supported by a 3.8 cm thick teflon disk, was located at center of the bottom plate and heated at five fiber orientations. Five resonant heating modes were found for each fiber orientation. The heating rate and the temperature uniformity were strong functions of the fiber orientation and the cavity length. The composite can be uniformly heated in several resonant heating modes at 0°, 15°, 45°, and 75° fiber orientations. All the modes at 0° and 15° fiber orientations have overall temperature differences of less than 30°C during microwave heating. Among all the modes, the planar temperature uniformity is the highest in the CH mode at the 15° fiber orientation at L_c = 13.89 cm. The most uniform overall temperature distribution was found in the CH mode at the 75° fiber orientation at L_c = 14.19 cm. To quantify the processing qualities of the heating modes, a concept of processing index (I) was introduced. It was a function of the heating rate and temperature uniformity, and was a strong function of the fiber orientation. The processing quality was the highest in 15° and 75° fiber orientations.

A fresh 200-crossply AS4/3501-6 composite (7.8x7.8x3.8 cm) was processed at a 15° fiber orientation with L_c = 13.22cm, L_p = 21.98 mm. The temperature profiles of both surface and midplane were uniform with themselves. The temperature difference between surface and midplane in the fresh composite was higher than that in fully cured sample.

CHAPTER 6
SCALE-UP STUDY OF MICROWAVE HEATING IN TUNABLE CAVITIES

6.1. Introduction

Microwave heating of graphite fiber/epoxy composite was discussed in Chapters 4 and 5. However, all the previous experiments were conducted in the small cavities, such as 15.24cm and 17.78 cm. In order to process large composites, the scale-up of microwave heating needs to be studied. This Chapter investigates the scale-up effects by comparison of temperature profiles in fully cured epoxy and graphite fiber/epoxy squares heated in a 17.78cm cylindrical cavity using 2.45GHz microwave radiation and a 45.72cm inner diameter cavity using 915MHz microwave radiation.

6.2. Scale-up Frequency

The heating of a material by microwave radiation depends not only on the complex permittivity and permeability, but also on the microwave frequency and electromagnetic (EM) field strength incident on the material. Since polymers and composites are non-magnetic materials, it is the electric field strength rather than the magnetic field strength that determines the heating of these materials. A resonant EM field pattern or mode must be established inside a cavity to confine microwave power inside the cavity and to heat a lossy material in the cavity. For an empty cavity, the EM field of each mode can be obtained analytically through Maxwell's equations and the application of the proper boundary conditions. In order to obtain a resonance condition in a circular cylindrical cavity, the source frequency must be higher than a specific cutoff frequency. The specific cutoff frequency, f_c, is the lowest frequency required for establishing the resonance mode. The f_c for TM and TE modes respectively is given by[42]

$$(f_c)_{TM_{np}} = \frac{x_{np}}{2\pi r\sqrt{\epsilon_o \mu_o}} \tag{6-1}$$

$$(f_c)_{TE_{np}} = \frac{x'_{np}}{2\pi r\sqrt{\epsilon_o \mu_o}} \tag{6-2}$$

where r is the radius of the cavity, x_{np} and x_{np}' are the ordered zeros of the Bessel function $J_n(x)$ and its derivative $J_n'(x')$, and ϵ_o and μ_o are the permittivity and permeability of free space.

Two commercial frequencies are being investigated, 2.45GHz and 915MHz. A cavity of 17.78cm (7") inner diameter was used for 2.45GHz system. The corresponding cavity size for 915MHz system is 45.72cm (18") as determined from Equations (6-1) and (6-2).

6.3. Experiments

Two microwave systems, one operating at 2.45GHz with a 17.78cm inner diameter cavity and one operating at 915MHz with a 45.72cm inner diameter cavity, were used in this study. The microwave circuit setup was described in Chapter 2.

Parallel experiments in the 17.78cm and 45.72cm cavities were carried out for two materials, thermally cured diglycidyl ether of bisphenol-A (DGEBA)/diaminodiphenyl sulfone (DDS) epoxy and thermally cured unidirectional Hercules AS4/3501-6 graphite fiber/epoxy composite squares. The midplane of the epoxy squares was located 2.94 cm and 7.29 cm above the bottom plate in the 17.78cm and the 45.72cm cavities, respectively. The midplane of composite squares was located 2.80 cm and 6.91 cm above the bottom plate in the 17.78cm and the

45.72cm cavities, respectively. The empty cavities were used for mode reference. For the empty cavities, each resonant mode was located by the power absorption curve on the oscilloscope. Two additional measurements were made for mode name assignment - the existence of axial E-field was determined from the top of the cavity for differentiation between TE and TM modes and the radial E-field pattern in the axial direction was measured for determination of q, the number of half waves in the axial direction. For the epoxy loaded cavities, modes were located with the swept frequency microwave sources and samples were heated in each mode using the single frequency microwave energy at an input power density of 0.327 W/cm^3. Four midplane temperatures were measured during microwave heating of the epoxy squares. The probe locations are shown in Figure 6.1(a). T1 was located at the center of the epoxy square, T2 was aligned with coupling probe, and T3 and T4 were on the diagonals opposite the coupling probe. T2, T3, and T4 were located the same distance (b) away from T1. This distance was 2.5 cm and 6.4 cm for samples heated in the 17.78cm and the 45.72cm cavities, respectively. For the composite loaded cavities, modes were located with the swept frequency microwave sources and samples were heated in each mode using the single frequency microwave energy at an input power density of 0.423 W/cm^3. Eight surface temperatures were measured during microwave heating of the composite squares. The probe locations are shown in Figure 6.1(b). T1 was located at the center of the square, T2, T3, and T4 were evenly distributed around T1 at radius b1, and T5 to T8 were located at the four corners of the square with the same distance (b2) away from T1. b1 and b2 were 2.54 cm and 5.08 cm for the sample heated in the 17.78cm cavity. For the sample heated in the 45.72cm cavity, b1 and b2 were 6.35 cm and 12.7 cm. Table 6.1 summarizes the sample size and operating conditions for the heating experiments in both 17.78cm and 45.72cm cavities.

Table 1. Heating Conditions for Scale-up Experiments

Material	Cavity Radius(cm)	Source Frequency	Sample Dimensions (cm)	Input Power (W)
Cured	8.89	2.45 GHz	6.92x6.92x0.56	8.8
Epoxy	22.86	915 MHz	17.78x17.78x1.45	150
Graphite/epoxy	8.89	2.45 GHz	10.16x10.16x0.28(24-ply)	12
Composite	22.86	915 MHz	25.4x25.4x0.68(60-ply)	185

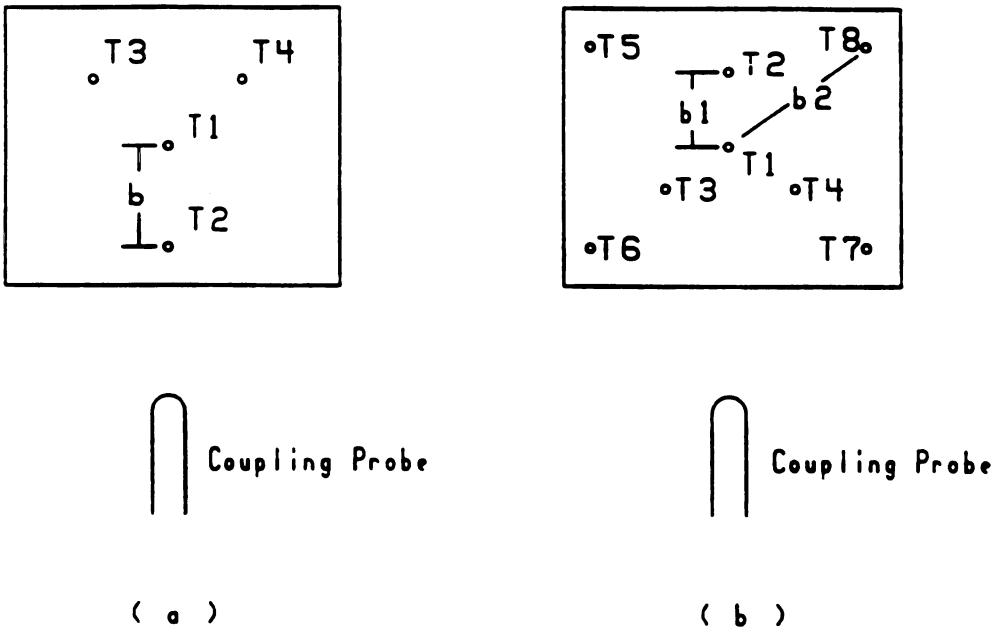

Figure 6.1 Location of the temperature probes

6.4. Results and Discussion

The resonance conditions of an empty cavity can be calculated from Maxwell's equations and the boundary conditions for the circular cylindrical cavity[12]. Equations 6-3 and 6-4 are used to calculate the cavity length of resonant modes for a given cavity radius and operating frequency. Table 6.2 lists the theoretically calculated and

measured cavity length of a given resonant mode for both cavities and the scale-up factor for various modes. The scale-up factor is defined as the ratio of the cavity length of the 45.72cm cavity to that of the 17.78cm cavity for the same resonant mode. The calculations of Lc assume a perfect cavity. The measured cavity lengths of the resonant modes in the empty cavity are very close to the theoretical values in every case. The measured scale-up factors are fairly close to the calculated values at each mode. With a constant ratio of cavity radii (2.57), the scale-up factor for cavity length is different for each resonant mode, ranging from 2.7 to 3.7.

Table 6.2. Theoretical and Measured Results of Modes for Empty Cavity

Mode	L_c in small cavity* (cm)		L_c in large cavity** (cm)		Scale-up Factor	
	measured	theoretical	measured	theoretical	measured	theoretical
TE_{111}	6.73	6.69	18.10	18.07	2.69	2.70
TM_{011}	7.31	7.20	19.20	19.62	2.63	2.72
TE_{211}	8.33	8.24	22.50	22.88	2.70	2.78
TM_{111}	11.35	11.28	33.70	33.87	2.97	3.00
TE_{112}	13.43	13.38	35.70	36.14	2.66	2.70
TM_{012}	14.52	14.41	39.00	39.23	2.69	2.72
TE_{311}	15.83	15.71	----	58.13	----	3.70
TE_{212}	16.58	16.48	45.60	45.75	2.75	2.78

* Inner diameter 17.78cm
** Inner diameter 45.72cm

6.4.1. Scale-up of Epoxy Loaded Cavities

Table 6.3 summarizes the Lc of the resonant modes and the heating results for the cavities loaded with epoxy. Modes are named based on the radial E-field strength

pattern along the axial direction, the existence of axial E-field, and the heating profiles. Although the same names were used for the loaded cavities as for the empty cavities, the electric field patterns were not the exactly same as those of the empty cavity. Since the cavity was loaded with a lossy material, the actual EM fields inside the cavity were disturbed and not exactly the same as those of the theoretical modes. The naming procedures of modes are described as follows. A resonant mode was found at Lc = 9.24cm in 17.78cm cavity. The epoxy square was heated in this mode and the resulting temperature profiles are shown in Figure 6.2(a). The radial E-field strength was also measured along the axial direction during the heating as shown in Figure 6.2(b). The axial E-field strength at the center point was measured through an opening at the top of the sliding short of the cavity. The existence of axial E-field implies that the resonant mode at Lc = 9.24cm is a TM mode. The radial E-field pattern shown in Figure 6.2(b) suggests that the number of the half waves in the axial direction, q, is 1. The possible names for this resonant mode are TM_{011}, TM_{111}, and TM_{211} and so on. The temperature profiles in Figure 6.2(a) shows that the heating is strongest in the center, T1, while the edges, T2, T3, and T4 are lower. As the local heating rate reflects the E-field strength at that location, TM_{111} is the only possible TM mode that will result this heating pattern[12]. Figures 6.2 and 6.3 show the typical temperature profiles and the electric field pattern distributions in the axial direction during microwave heating of epoxy squares in both cavities for TM_{111} and TE_{112} modes respectively.

For the 45.72cm inner diameter cavity, the corresponding TM_{111} mode was found at Lc = 26.4cm using the same procedure as described for the 17.78cm cavity. Figure 6.2(c) shows the temperature profiles of the scaled-up epoxy square during microwave heating in 45.72cm cavity in the TM_{111} mode. Figure 6.2(d) shows the radial E-field strength along the axial direction.

Similar radial E-field patterns are observed for TM_{111} mode for both cavities as shown in Figures 6.2(b) and 6.2(d). With the same input power density, the heating

rate in the epoxy square is similar in the 17.78cm cavity operating 2.45GHz to the 45.72cm cavity operating at 915 MHz. The microwave heating of epoxy in the TM_{111} mode in a 17.78cm cavity can be scaled up in three dimensions to a 45.72cm cavity. The scale-up factor of the TM_{111} mode in epoxy loaded cavities is 2.86, which is similar to that of the empty cavities, 2.97.

Figure 6.3 shows the comparison of the TE_{112} mode in both cavities. The non-existence of axial E-field in both cavities proved both resonant modes were TE. From Figure 6.3(b) and Figure 6.3(d), it was determined that q equaled 2 in both modes. Both the radial E-field along axial direction and the temperature profiles in the samples are similar. TE_{11} is the only field pattern[12] which will cause the temperature profiles seen in Figure 6.3(a) and 6.3(c). From Figure 6.3, it is apparent that the microwave heating of epoxy at TE_{112} mode in a 17.78cm cavity operating at 2.45GHz can be also scaled up in three dimensions to the 45.72cm cavity operating at 915MHz. The scale-up factor of the TE_{112} mode in epoxy loaded cavities is 2.76, which is similar to that of the empty cavities, 2.66.

The Lc of various modes, the scale-up factors, and the comparison of the heating patterns in 17.78cm and 45.72cm cavities are listed in Table 6.3. All the heating patterns are similar for the two cavities using the same modes. This suggests that the results of the microwave heating of epoxy squares or other low to medium loss materials can be scaled up from the 17.78cm cavity to the 45.72cm cavity. Similar heating patterns can be achieved for the same resonant mode regardless of the cavity size if the same sample/cavity size geometry is maintained. A scale-up rule for scale up in three dimensions can be applied to the microwave processing of low to medium loss materials.

Table 6.3. Scale-up Results for Epoxy Loaded Cavity

Mode Name	Cavity Length Small Cavity	Cavity Length Large Cavity	Scale-up Factor	Temperature Profile* in Small Cavity	Temperature Profile* in Large Cavity
TE_{211}	6.67	20.2	3.03	T2=T3=T4>T1	T2=T4=T3>T1
TM_{111}	9.24	26.4	2.86	T1>T3≥T4=T2	T1>T2≥T3=T4
TE_{112}	11.83	32.7	2.76	T1≥T3=T2=T4	T1≥T2=T4≥T3
TM_{012}	13.38	37.2	2.78	T4=T2=T3>T1	T4=T3=T2>T1
TE_{311}	14.45	---**	----	T2=T4>T2=T1	----------
TE_{212}	15.06	43.2	2.87	T3≥T4=T2>T1	T4=T3=T2>T1

* The symbols =, ≥, and > are used to represent temperature difference ΔT at a heating time of 2 minutes. = means ΔT less than 5°C, ≥ means between 6-10°C, and > means 11-20°C of difference.

** The TE_{311} mode can not be located in the large cavity because of the limit of the cavity length.

Figure 6.4 shows the scale-up factors of various modes for the cases of empty cavity (calculated and measured) and cavity loaded with epoxy. The measured scale-up factors of the empty cavities are slightly lower than those of the calculated values. The scale-up factors of the epoxy loaded cavities are very close to those of the calculated values for empty cavities. This suggests that the processing of epoxy samples or other materials with similar dielectric properties follows the empty cavity scale-up rule.

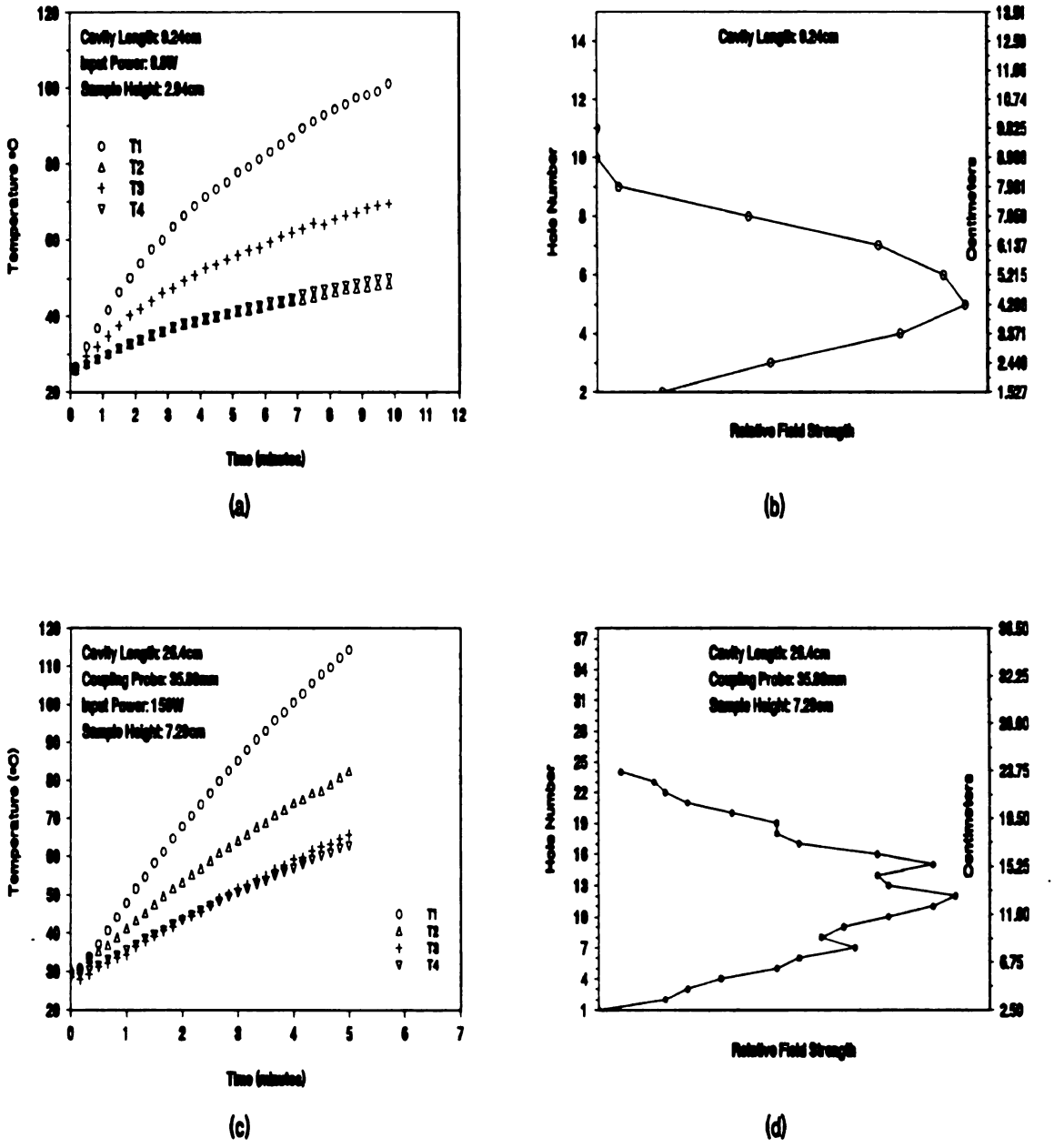

Figure 6.2 Temperature Profiles and Radial Electric Field Pattern Along Axial Direction during Microwave Heating of Epoxy Squares at TM_{111} Mode

(a) Temperature profiles in 17.78 cm cavity

(b) Radial electric field pattern in 17.78 cm cavity

(c) Temperature profiles in 45.72 cm cavity

(d) Radial electric field pattern in 45.72 cm cavity

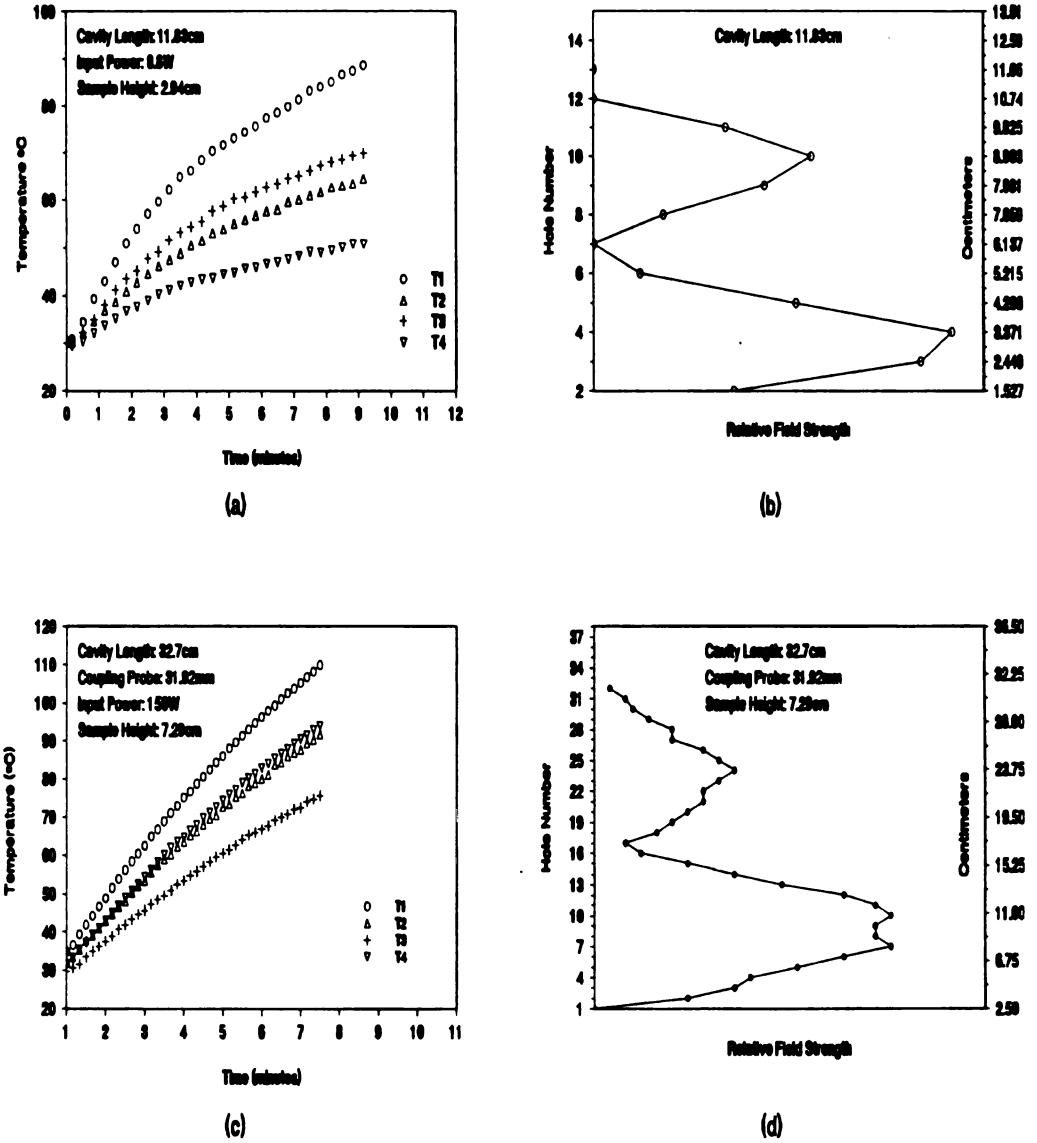

Figure 6.3 Temperature Profiles and Radial Electric Field Pattern Along Axial Direction during Microwave Heating of Epoxy Squares at TE_{112} Mode

(a) Temperature profiles in 17.78 cm cavity

(b) Radial electric field pattern in 17.78 cm cavity

(c) Temperature profiles in 45.72 cm cavity

(d) Radial electric field pattern in 45.72 cm cavity

Figures 6.5 and 6.6 show the shift of cavity length of each resonant mode for the empty cavities (calculated and measured) and cavities loaded with epoxy squares. The cavity length of the epoxy loaded cavities shifted down from that of the empty cavities for all resonant modes. For the 45.72cm cavity, the shifts of the cavity length are similar for all the modes (1.8 to 3cm) except the TM_{111} mode which shifted down 7.3cm. The same shift pattern of the cavity length was observed for 17.78 cm cavity. The shifts of the cavity length are similar for all modes (1.1 to 1.7cm) except for the TM_{111} mode which shifted down 2.11cm. The percentage of cavity length shift for all the heating mode is within 20% in the range studied.

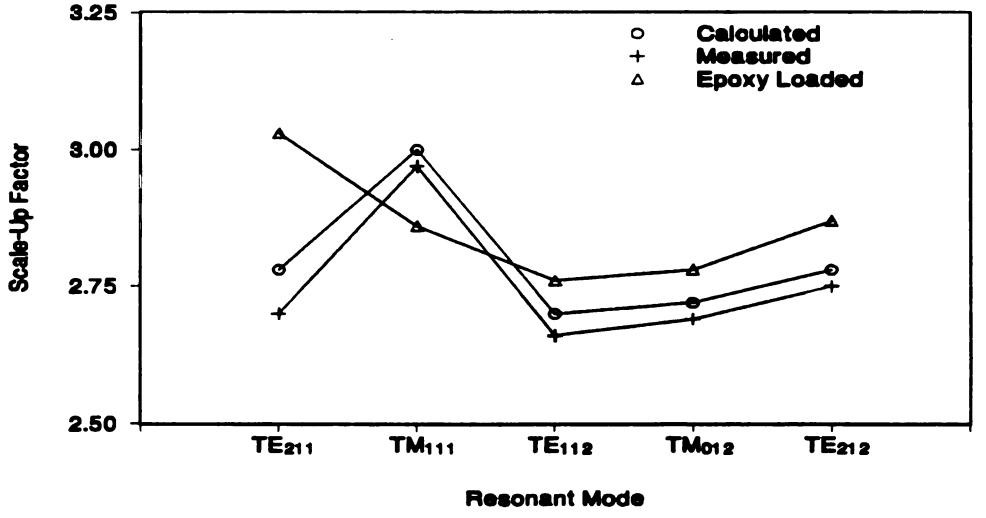

Figure 6.4 Shift of the Scale-up Factor during Microwave Heating of Epoxy Squares

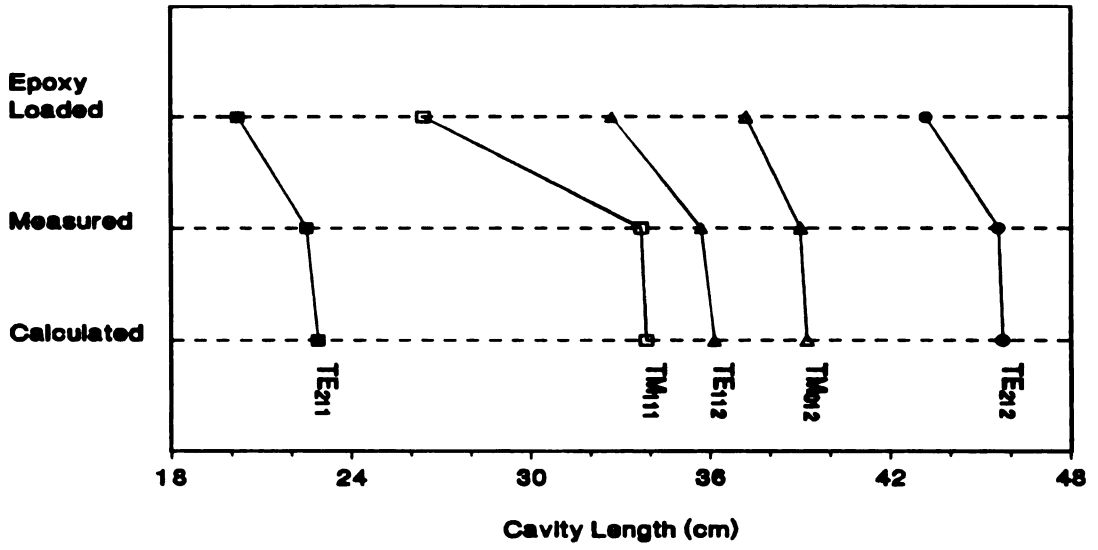

Figure 6.5 Shift of Cavity Length during Microwave Heating of Epoxy Square in a 45.72 cm Cavity

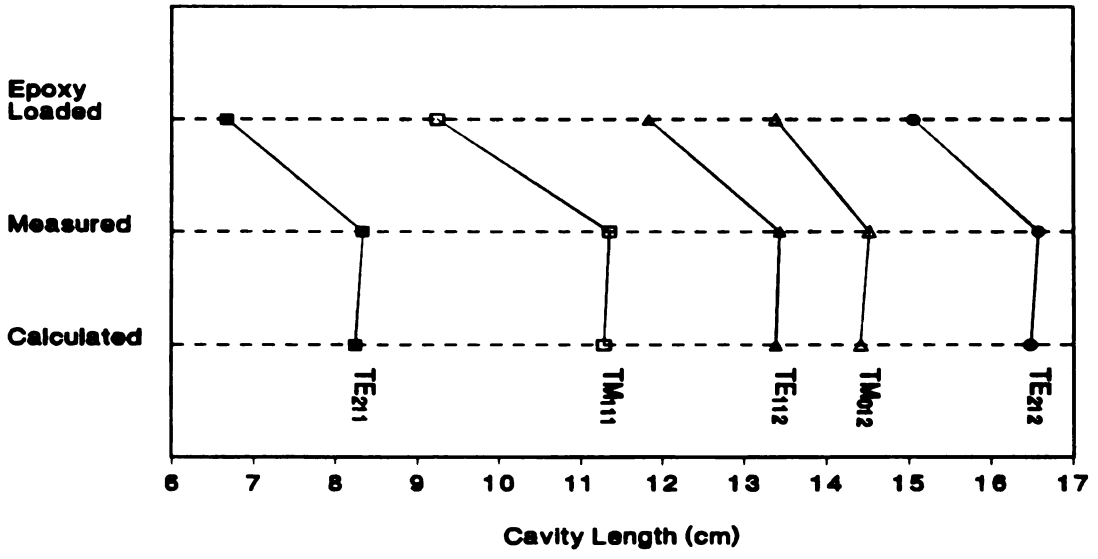

Figure 6.6 Shift of Cavity Length during Microwave Heating of Epoxy Square in a 17.78 cm Cavity

6.4.2 Scale-up Study of Graphite Fiber Composite Loaded Cavities

For unidirectional graphite fiber/epoxy composite loaded cavities, the electromagnetic field is greatly disturbed and the single-mode nomenclature is no longer applicable. However, the electric field pattern along axial direction and the existence of z direction field can still be measured. Tables 6.4 and 6.5 list the heating modes and the results for microwave heating of a 10.16 cm x 10.16 cm 24-ply unidirectional composite square in the 17.78 cm cavity and a 25.40 cm x 25.40 cm 60-ply unidirectional composite square in the 45.72 cm cavity, respectively.

Table 6.4 Heating Modes and Results for 60-ply Unidirectional Composite in a 45.72 cm Cavity

Mode location	q	z field	ΔT_{max}	T_{max}	Temperature distribution
L_c=17.2 cm L_p=50.0 mm	1	No	54	90	T5=T7=T6=T8 >>>T4=T2=T3=T1
L_c=22.5 cm L_p=25.3 mm	1	No	49	92	T5=T7=T6=T8>>>T4=T2=T3=T1
L_c=29.4 cm L_p=39.8 mm	2	Yes	32	80	T7=T6=T4=T2=T5=T8>T3=T1
L_c=32.4 cm L_p=27.0 mm	2	Yes	53	97	T7=T6=T5=T8>>>T4=T2=T3=T1
L_c=52.8 cm L_p=43.2 mm	2	No	35	84	T2=T4=T7≥T5=T8=T6>>T3=T1
L_c=57.7 cm L_p=11.8 mm	1	Yes	18	65	T5=T7=T6=T8=T1=T2=T4=T3
L_c=65.7 cm L_p=19.0 mm	1	Yes	22	70	T5=T7=T6=T8≥T4=T2=T1≥T3

* The meaning of the symbols =, ≥, and > are the same as in Table 6.3. Each additional > represents additional 10°C in temperature difference.

Table 6.5 Heating Modes and Results for 24-ply Unidirectional Composite in a 17.78 cm Cavity

Mode location	q	z field	ΔT_{max}	T_{max}	Temperature distribution
L_c= 7.56 cm L_p= 4.24 mm	1	No	18	63	T8=T7≥T6=T2=T4= T3=T5=T1
L_c= 7.91 cm L_p=11.62 mm	1	Yes	10	52	T8=T6=T5=T7=T2= T4=T3=T1
L_c=10.60 cm L_p= 8.11 mm	2	Yes	26	68	T6>T5=T8=T7=T2= T3=T1=T4
L_c=15.24 cm L_p=15.83 mm	2	No	28	66	T2>T4≥T1=T8=T5= T6=T3=T7
L_c=15.83 cm L_p=10.90 mm	2	Yes	9	51	T3=T6=T8=T2=T5= T1=T4=T7
L_c=16.39 cm L_p= 8.41 mm	2	Yes	14	60	T2=T6=T8=T4=T7= T5≥T3=T1

* The meaning of the symbols =, ≥, and > are the same as in Table 6.3.

In Tables 6.4 and 6.5, the first column lists the cavity length, L_c, and the coupling probe length, L_p, for the various resonant heating modes. The second column lists the measured number of half waves in the axial direction. The third column lists the measured results for the existence of z-field in the center of the top of the cavity. The fourth column lists the maximum temperature difference at the composite surface at the end of nine minutes heating. The fifth and sixth columns list the maximum temperature and the temperature distribution in the composite in descending order for various heating modes after 9 minutes heating. As shown in columns 4 to 6 of Tables 6.4 and 6.5, the heating patterns are strong functions of the resonant heating modes for both cavities. With the same input power density, the temperature difference during microwave heating of graphite fiber/epoxy composite is, in general, lower in the 10.16 cm square sample in the 17.78 cm cavity with 2.45

GHz radiation than in the 45.4 cm square sample in the 45.78 cm cavity with 915 MHz radiation. This may be due to non-uniform electric field inside the composite and the finite thermal conductivity of the graphite fiber composite. Heat is more easily transferred from hot spots to cold spots across the composite in the small sample than in the large sample. Comparing the composite heating results between the small sample in 2.45 GHz system and the large sample in 915 MHz system, no one-to-one correspondence can be found as in the epoxy heating results.

The maximum temperature, T_{max}, is closely related to the maximum temperature difference, ΔT_{max} during microwave heating, as shown in columns four and five of Tables 6.4 and 6.5. With the same input power density, the higher the maximum temperature, the higher the temperature difference was regardless the sample size. Figure 6.7 shows the relationship between ΔT_{max} and T_{max} for microwave heating of graphite fiber/epoxy composite in both the 915 MHz and 2.45 GHz systems. A linear relationship is found between the ΔT_{max} and T_{max}. Extrapolating to $\Delta T_{max}=0$, T_{max} is 44.6°C at the end of 9 minutes heating. From the energy balance,

$$P_m = sh(T-Ta) + v\rho C_p \frac{dT}{dt} \tag{6-3}$$

the energy required to heat the composite uniformly up to T in t minutes is

$$P_m = \frac{sh(T-T_a)}{1-e^{-\frac{sht}{v\rho C_p}}} \tag{6-4}$$

where s and v are the surface area and volume of the composite, ρ and C_p are the density and the heat capacity of the composite, h is the heat transfer coefficient at the surface, T, T_a, t are the composite temperature, environment temperature, and time, and P_m is the microwave power dissipated in the composite. With the parameters in Chapter 9, the microwave power required to heat a 10.16 x 10.16 x 0.28 cm and a

25.4 x 25.4 x 0.68 cm composite to 44.6°C in 9 minutes are 7.14 W and 89.7 W respectively. As the input powers used for composite heating are 12 and 185 W for the 17.78 cm and 45.72 cm cavities, the percentage of input power dissipated in the composite is 59.5 and 48.5 for the 17.78 cm and the 45.72 cm cavity respectively.

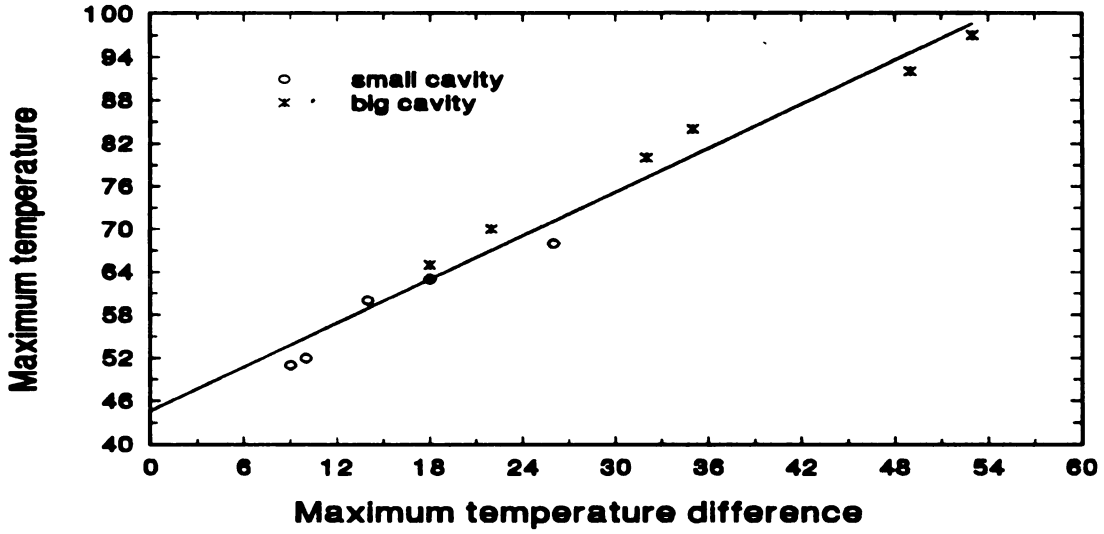

Figure 6.7 Heating Rate and Heating Uniformity Relationship for Microwave Heating of Graphite Fiber/epoxy Composite

6.5. Conclusions

The microwave heating of DGEBA/DDS epoxy and Hercules AS4/3501-6 composite squares in various resonant heating modes was studied in 17.78cm inner diameter and 45.72cm inner diameter tuneable cylindrical resonant cavities. A microwave source operating at 2.45GHz was used for the 17.78cm cavity and 915MHz was used for the 45.72cm cavity in order to reproduce the same empty cavity resonant mode for the same cavity geometry ratio. The scale-up factor is defined as the ratio of the cavity length in the 45.72cm cavity to that in the 17.78cm cavity at the same resonant mode. For a given ratio of the cavity radii, the scale-up

factor varies with resonant mode. For microwave heating of epoxy squares, the electromagnetic modes were identified using the empty cavities as a reference. The same heating profiles were observed for the same resonant modes in the 17.78 cm and 45.72 cm cavities with the same cavity geometry ratios, the same sample/cavity size ratios, and the same power densities. The scale-up of microwave heating of low to medium loss materials, such as an epoxy square, can be approximated by the scale-up of the empty cavities. For the microwave heating of graphite fiber/epoxy composites, no similar heating profiles were found when the samples were scale-up in three dimensions according to the scale-up of the cavity. The maximum temperature was linearly related to the maximum temperature difference during microwave heating of graphite fiber/epoxy composite. This relationship was the same for both 2.45 GHz system and 915 MHz system. The power absorption efficiencies for the composite loaded cavity are 59.5% and 48.5% in the 17.78 cm and 45.72 cm cavity, respectively.

CHAPTER 7
CONTINUOUS PROCESSING OF GRAPHITE FIBER/EPOXY TAPE IN A MICROWAVE APPLICATOR

7.1 Introduction

Microwave radiation effects on the kinetics of epoxy polymerization and the glass transition temperature of cured epoxy resins were discussed in Chapter 3. Chapters 4 and 5 discussed batch microwave processing of epoxy based graphite fiber composite in a 17.78 cm cavity. Chapter 6 discussed the scale up of microwave heating from a 17.78 cm cavity to a 45.72 cm cavity. This chapter addresses the feasibility of continuous processing of graphite fiber/epoxy prepreg tape using microwave energy.

A critical problem in continuous processing of materials using microwave energy is control of the microwave leakage through the entry and exit ports of the cavity. The threshold limit value (TLV) at 2.45GHz is 10 mW/cm^2 [121]. The TLV refers to the maximum radiation level to which workers may be repeatedly exposed without adverse health effects. The quoted TLV value is based on an average whole body specific absorption rate of 0.4 W/kg in a six-minute period.

Doubly corrugated reactive chokes have been studied and used for reducing the microwave leakage at the entry points during the continuous processing of polystyrene[122]. Many rubbers, polar and non-polar, have been processed continuously using microwave heating systems[123,124]. Non-polar rubbers, such as natural rubber, were usually mixed with carbon black or blended with polar rubbers for better heating during microwave processing. Continuous processing of rubbers in the microwave environment is, however, fundamentally different from the continuous processing of graphite fiber/epoxy composites. The continuous conductor in the latter case would cause tremendous microwave leakage in microwave heating systems

designed for the continuous processing of rubber. With proper modification of the batch tunable resonant applicator, continuous processing of graphite fiber/epoxy prepreg tapes using microwave energy has been demonstrated[36]. The preliminary results of the continuous processing of graphite fiber/epoxy prepreg tape in a microwave applicator are reported here.

7.2 Experiments

The microwave circuit of the continuous processing system is similar to that of the batch processing system as described in Chapter 2. A swept frequency oscillator was used to locate resonant modes. A single frequency (2.45 GHz) power source was used for heating. The input power and reflected power were measured on-line during processing. The microwave applicator and the temperature measurement system for the continuous system are, however, different from those of the batch processing system. The 17.78cm inner diameter tunable cylindrical batch microwave cavity was modified for continuous processing of conductor reinforced materials. Figure 7.1(a) shows the modification of the cavity. Two rectangular slots were cut in opposite sides of the cavity wall perpendicular to the coupling probe. A jacket was put around each slot to protect against microwave leakage. The input and output ports of the cavity and the jackets were specifically designed to eliminate leakage due to both the opening and the conducting graphite fibers. Figures 7.1(b) and (c) show the design of the cavity wall and the jacket dies. As shown in Figure 7.1(b), the fins are movable along the cavity wall and their distance from the material can be adjusted. As these fins are grounded to the cavity wall, the majority of the induced current in the conducting fiber will be shorted by these fins if the distance between the conducting material and the fin is properly adjusted. This design ensures that the induced current in the conducting fiber will not be significant outside the cavity. Also these fins reflect some of the microwave leakage back into the cavity. Figure 7.1(c) shows the details of the design of the jacket dies. The dies are designed to be

adjustable so that prepregs of different thickness and width can be processed. The finger stock touches the material to eliminate the remaining induced current in the conducting fiber and confine the microwaves inside the jacket.

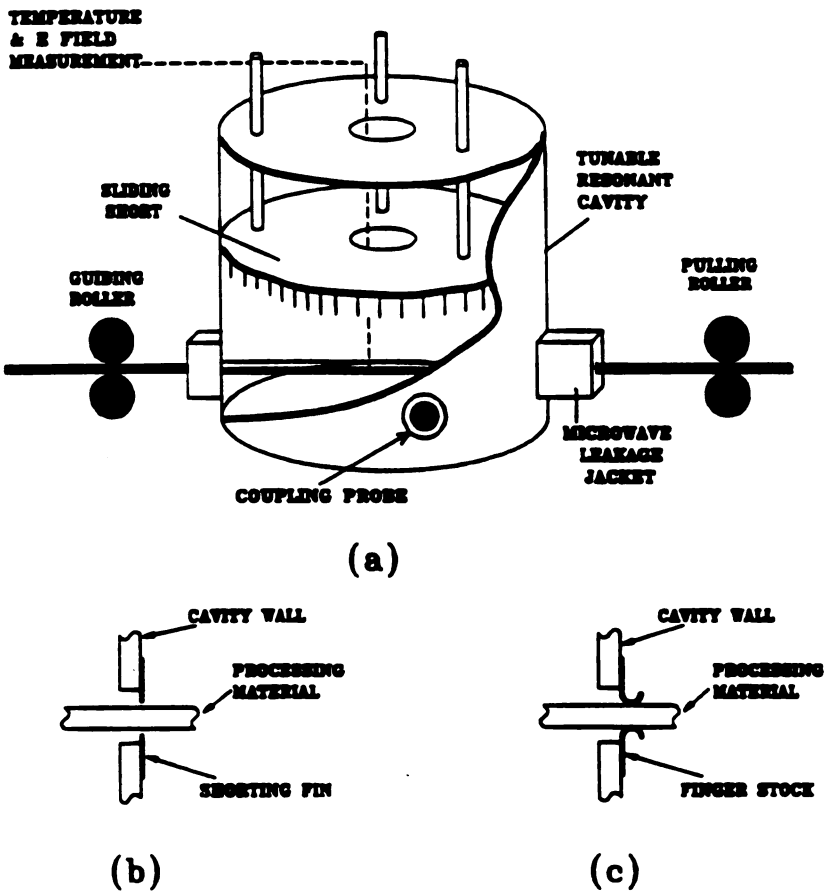

Figure 7.1 Modified 17.78 cm Tunable Cavity for Continuous Processing

The material used in this study was continuous graphite fiber/epoxy prepreg (Hercules AS4/3501-6). The microwave circuit for the continuous processing system is the 2.45 GHz system described in Chapter 2, except that no feed-back temperature control mechanism is present. Figure 7.2 shows the continuous processing system. The modified applicator allowed the material to pass through the applicator continuously and controlled microwave leakage to well below the TLV.

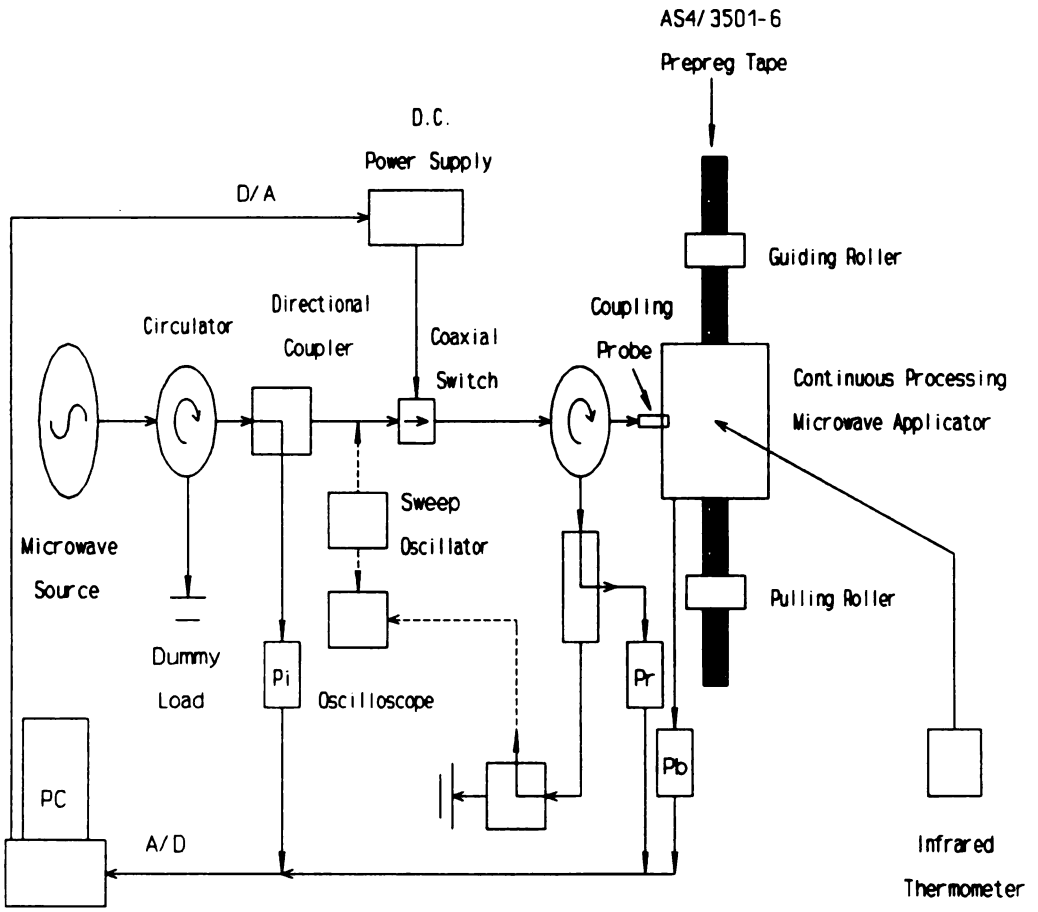

Figure 7.2 Microwave System for Continuous Processing

An infrared thermometer (Omega OS1100) was used to measure the surface temperature on the center line of the prepreg tape during processing. The temperature measurement was accomplished through an opening in the top of the cavity. The temperature is taken at fixed spot, the center point of the tape inside the cavity, while the continuous tape is pulling through the cavity. The pulling roller was controlled by a variable speed stepper motor which controlled the speed of transportation. The prepreg tapes, 3.81cm wide and 0.68mm thick, were processed continuously in all available resonant modes using a single frequency source at an input power of 60W. The prepreg feed rate was 0.508 cm/min. and the maximum

microwave leakage was controlled to within 0.3 mW/cm^2. The reflected power was minimized to be less than 0.1 W during the process by continuous fine tuning of the cavity length and coupling probe length. Differential Scanning Calorimetry (DSC) was used to determine the extent of cure of the precessed tape.

7.3 Results and Conclusion

There were five resonant heating modes available in the loaded cylindrical tunable cavity in this study, two controlled-hybrid (CH) modes and three pseudo-single (PS) modes. Table 7.1 lists the heating conditions and results for the various modes. Both CH modes were able to heat the prepreg tape up to 200°C while the PS modes could not heat the samples higher than 130°C with the same input power.

Table 7.1. Heating Conditions and Results

Mode No.	Mode Type	Cavity Length(cm)	Maximum Temp. (°C)
1	PS	7.41	126
2	CH	10.45	202
3	CH	12.45	212
4	PS	14.77	110
5	PS	15.85	50

Figure 7.3 shows the center surface temperature versus residence time during continuous processing of prepreg tapes in four resonant modes. The temperature reached steady state in 20 seconds for both CH modes. In the PS modes, it took one and three minutes to establish steady state for mode 1 and mode 5, respectively. Clearly, the center line surface temperatures of the prepregs in the CH modes are much higher than in the PS modes.

Figure 7.4 shows the extent of cure distribution along the edge of the microwave processed composite tapes at various residence times for the two CH modes and one PS mode. In both CH modes, the prepreg achieved 90 percent cure in 15 minutes. In the PS mode, the prepreg achieved 90 percent cure in 35 minutes. The faster curing on the edge of the prepreg tape in the CH mode than that in the PS mode implies a higher cure temperature at the prepreg edge in the CH mode.

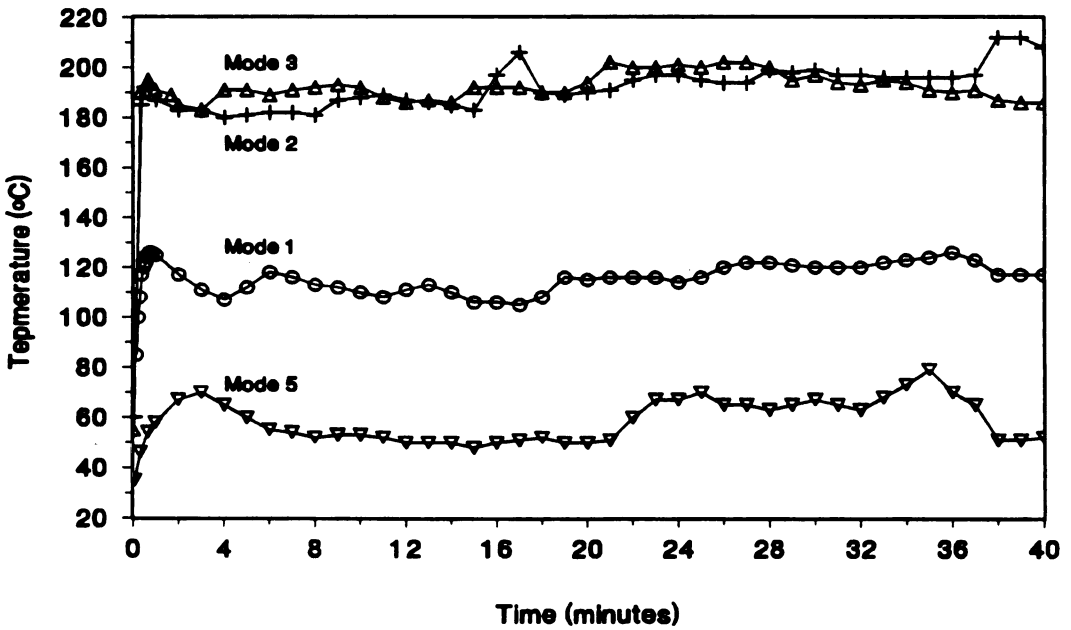

Figure 7.3 Center Surface Temperature during Continuous Processing of Hercules AS4/3501-6 Prepreg using Microwave Energy

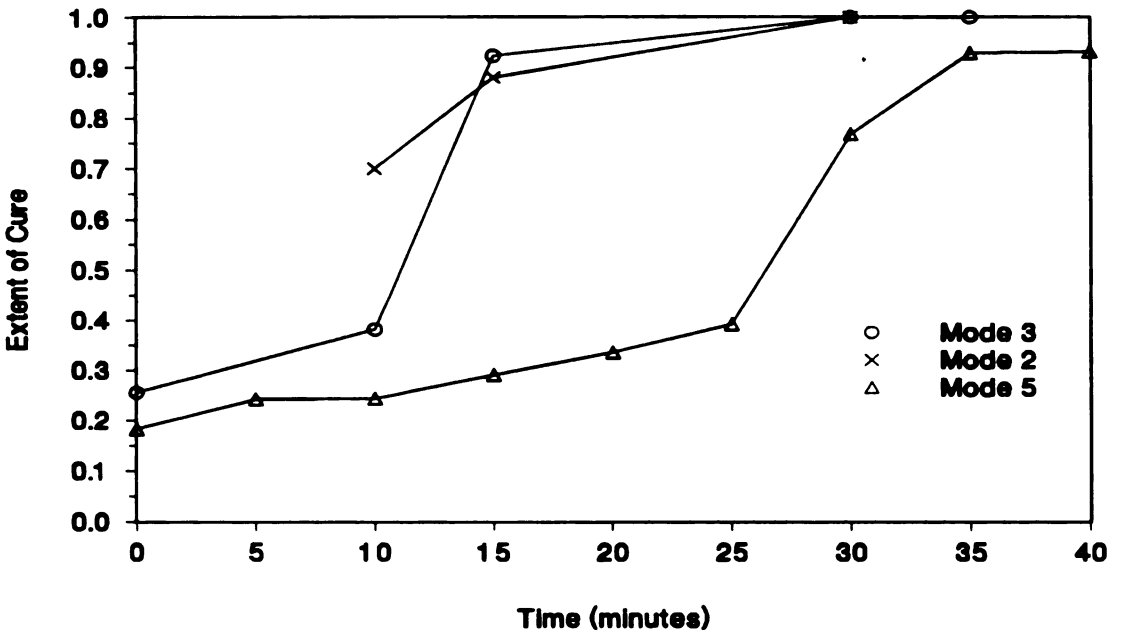

Figure 7.4 Extent of Cure at Various Resident Time in Three Modes

Figures 7.5 and 7.6 show the extent of cure distribution across the processed composite tape at various residence times for the CH mode at Lc=12.45cm and the PS mode at Lc=15.85cm respectively. Although the extent of cure is higher in the center than the edge at the beginning of the processing in the CH mode, the prepreg reached almost full cure across the tape in 15 minutes. Figure 7.5 also implies that the cure temperature is higher in the center than at the edge. Since the prepreg was uniformly fully cured in 20 minutes, the prepreg feed rate can be increased to 0.89 cm per minute if the input power and applicator size remain the same. For the PS mode, the extent of cure is higher at the edge than in the center as shown in Figure 7.6. This implies that the cure temperature must be higher at the edges than in the center in this PS mode. The laminate was also not fully cured at the end of 30 minutes residence time. Higher input power is therefore required in order to fully cure the composite in this PS mode.

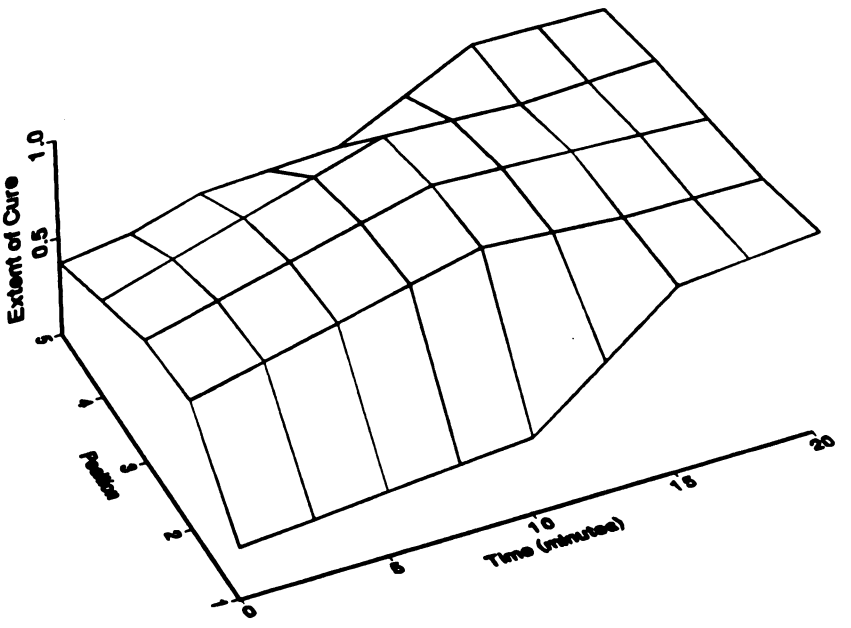

Figure 7.5 Extent of Cure Distribution Across the Tape as Function of Resident Time for a CH mode at 12.45 cm

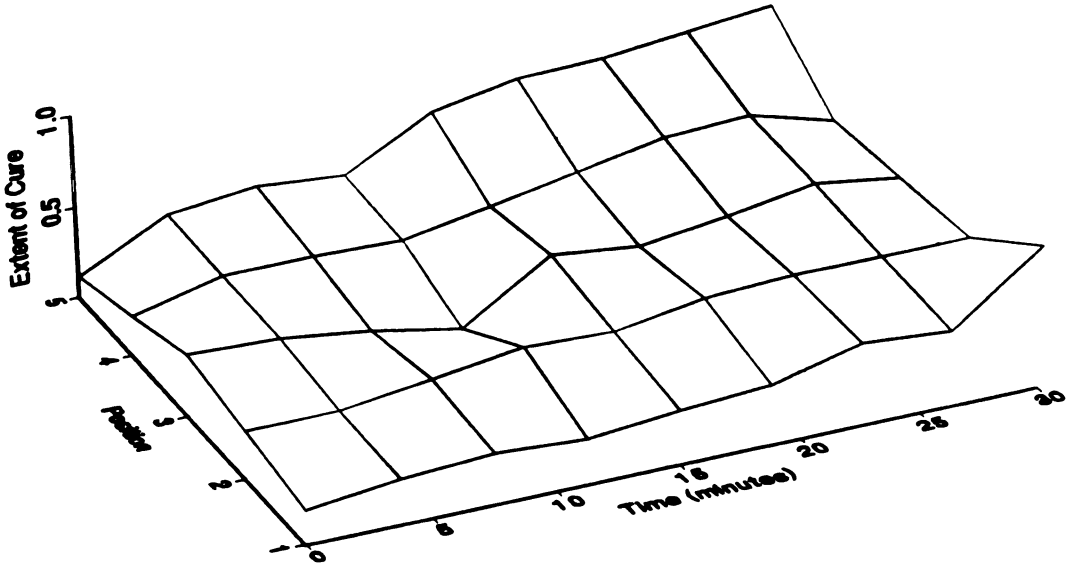

Figure 7.6 Extent of Cure Distribution Across the Tape as Function of Resident Time for a PS mode at 15.85 cm

Comparing Figure 7.5 to 7.6, the curing was much faster and more uniform in the CH mode than in the PS mode across the prepreg tape during continuous processing. As the curing rate is controlled by heating efficiency which, in turn, depends on the energy coupling efficiency of the resonant mode, the coupling of microwave energy was more effective in the CH modes than in the PS modes. Clearly, it is more efficient to select CH modes for the continuous processing of graphite fiber/epoxy prepreg in the microwave environment under the current conditions. The microwave heating is not only a function of the electromagnetic resonant modes, but also a function of the dielectric properties and the location of the load in the cavity. The PS modes may also be able to heat the prepreg efficiently and fully cure the prepreg in other sample locations. More detailed studies of sample location effects on the continuous processing of graphite fiber/epoxy prepreg in the microwave environment are required for optimum heating results. Other experimental modifications may be required to fully explore the advantages of continuous processing in the microwave environment.

With the modified microwave cavity, continuous processing of graphite fiber/epoxy composite was realized using microwave energy. This breakthrough brings the microwave processing technique to a new stage of commercialization potential. The success of this study will enable us to process high performance composite parts, such as long pipes, cost-effectively. This technique also makes possible many other continuous processes for conducting materials using microwave energy, such as pultrusion, filament winding, and production of carbon/graphite fibers.

7.4 Conclusion

It was demonstrated that graphite fiber reinforced epoxy prepreg tapes can be processed continuously using 2.45GHz microwave radiation in a modified 17.78 cm

tunable resonant applicator. The microwave radiation leakage was controlled to under 0.3 mW/cm^2 during processing, which is much lower than the safety threshold limit value (10 mW/cm^2). The absorption and distribution of the input power in the prepreg tapes were a strong function of the resonant heating mode. The continuous prepreg tape effectively absorbed the input power and was fully cured in the controlled-hybrid modes. The prepreg tapes were not fully cured in the pseudo-single modes. The CH modes heat more effectively than the PS modes during continuous processing of the graphite fiber/epoxy prepreg under these experimental conditions.

CHAPTER 8
POWER ABSORPTION MODEL FOR MICROWAVE PROCESSING OF COMPOSITES IN A TUNABLE RESONANT CAVITY

8.1 Introduction

Graphite fiber/epoxy composites have been processed using microwave energy in tunable resonant cavities. The temperature uniformity and heating rate during processing were controlled by the electric field pattern and strength inside the composite. In order to take full advantage of microwave processing, the interaction between microwave radiation and composites needs to be understood. For an empty cavity, the electric field inside the cavity can be calculated based on Maxwell's equations and the boundary conditions. For a cavity loaded with a small object which only perturbs the resonant frequency by a few percent, a cavity perturbation technique is usually used to calculate the electric field inside the cavity[42]. This technique has been used to measure the dielectric properties of polymers in the TM_{012} mode[7]. For a coaxially loaded cavity with a homogeneous, isotropic lossy rod, the electric field inside cavity was calculated using a mode-matching technique[65,125]. However, the electric field inside an anisotropic composite plate loaded cavity is very complicated. In order to approximate the microwave power absorption rate during processing, a simplified five-parameter model is presented in this chapter.

8.2 Problem Simplification

The electromagnetic field inside a cavity loaded with an anisotropic composite, especially a graphite fiber reinforced composite, is rather complicated. Figure 8.1 shows the configuration of the composite loaded cavity and interactions between the composite and the electromagnetic standing waves inside the cavity. As shown in

Figure 8.1(a), the composite is lifted up from the bottom where the electric field is very small. The electric waves interact with the composite in every surface as shown in Figure 8.1(b). As a first approximation, the incident wave on each composite surface was considered to be a linearly polarized transverse electromagnetic (TEM) wave. The arrow in the Figure 8.1(b) represents the direction of the propagating TEM wave. The interaction between travelling TEM waves and graphite fiber/epoxy composites have been studied previously in the areas of material science[8,126,127,128] and aerospace[129,130].

Since the incident TEM waves from the four edges are perpendicular to the incident TEM waves from the top and bottom, the power dissipated in the composite, P_c, can be decomposed into two terms, P_1 and P_2. P_1 is the power dissipated due to the incident TEM waves from the edges while P_2 is the power dissipated due to the incident TEM waves from the top and the bottom. To further simplify the problem, P_1 is considered to be constant through the thickness of the composite.

Based on the above assumptions, the electric field distribution across the thickness of the composite only depends upon the propagating behavior of the incident TEM waves from the top and bottom. Once $\vec{E}$ is known through the thickness, the power dissipation due to TEM waves from top and bottom can be calculated from Poynting's theorem.

$$P_2 = \frac{1}{2}\omega \vec{E} \cdot \bar{\bar{\varepsilon}}_c'' \cdot \vec{E}^* \tag{8-1}$$

where P_2 is time average power dissipated in the composite due to electric field of the incident TEM waves from the top and bottom of the composite ($\vec{E}_T$ and $\vec{E}_B$ in W/m^3), $\vec{E}$ and $\vec{E}^*$ are the electric field vector and its conjugate in V/m, and $\bar{\bar{\varepsilon}}_c''$ is the effective dyadic loss factor of the composite in F/m.

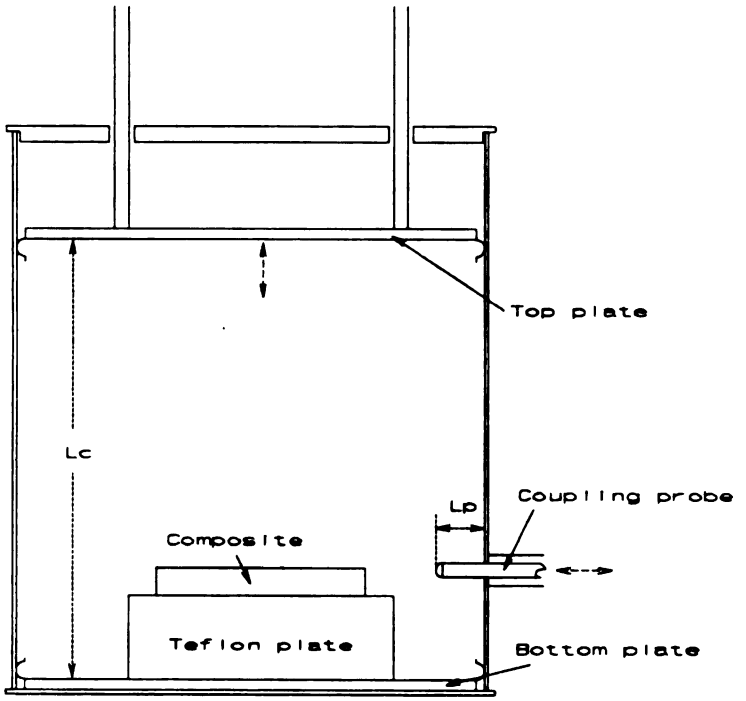

(a) Configuration of the Composite Loaded Cavity

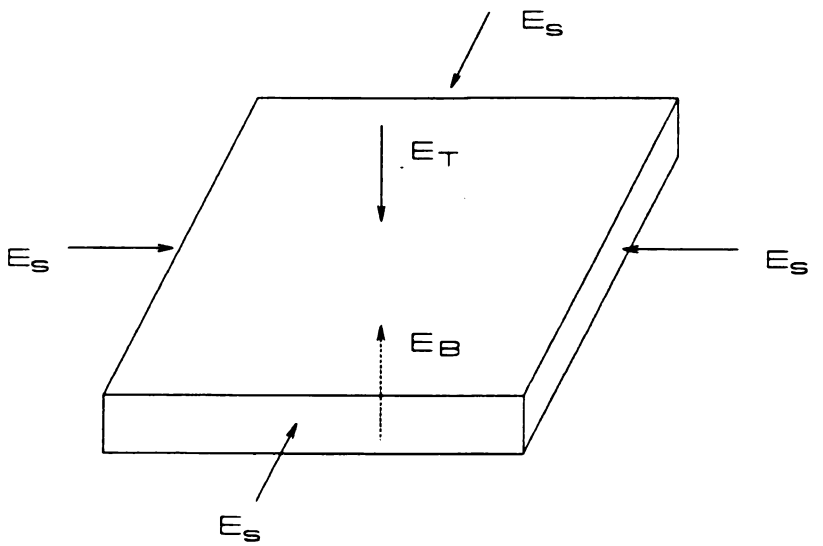

(b) Interaction Between Composite and EM Waves

(The Arrow Shows the Propagating Direction of the TEM Waves.)

Figure 8.1 Incident Waves on the Composites During Processing.

8.3 Electromagnetic Model

Figure 8.2 shows the configuration for the simplified electromagnetic model. The composite, consisting of N laminate plies, is exposed to top and bottom incident TEM waves. To calculate the power absorption rate due to the top and bottom TEM waves in each ply, the wave behavior at each interface must be derived first.

Let's consider +z travelling waves at the n^{th} interface. As shown in Figure 8.3, part of the incident wave, $\vec{E}_i$, will reflect back as a reflected wave, $\vec{E}_r$, and the rest of the incident wave will go through the interface as a transmitted wave, $\vec{E}_t$. The $\vec{E}_i$ can be decomposed into two parts, E_x and E_y. Using new coordinates p and q to represent the composite's principle direction, the angle from the x-y coordinate to the p-q coordinate is δ as shown in Figure 8.4. We assume that the fiber direction is the principle direction of the complex permittivity tensor for the composite and let p and q be parallel and perpendicular to the fiber direction, respectively. Therefore, the dyadic complex permittivity in p-q-z coordinates is a diagonal tensor.

$$\bar{\bar{\varepsilon}}_c = \begin{pmatrix} \varepsilon_p^* & 0 & 0 \\ 0 & \varepsilon_q^* & 0 \\ 0 & 0 & \varepsilon_z^* \end{pmatrix} \tag{8-2}$$

Since there are no off-diagonal terms, the calculation in this coordinate system will be much easier than in x-y-z coordinates where off-diagonal terms exist. Once E_p and E_q are known, E_x and E_y can be easily obtained by projection of E_p and E_q in x-y coordinates.

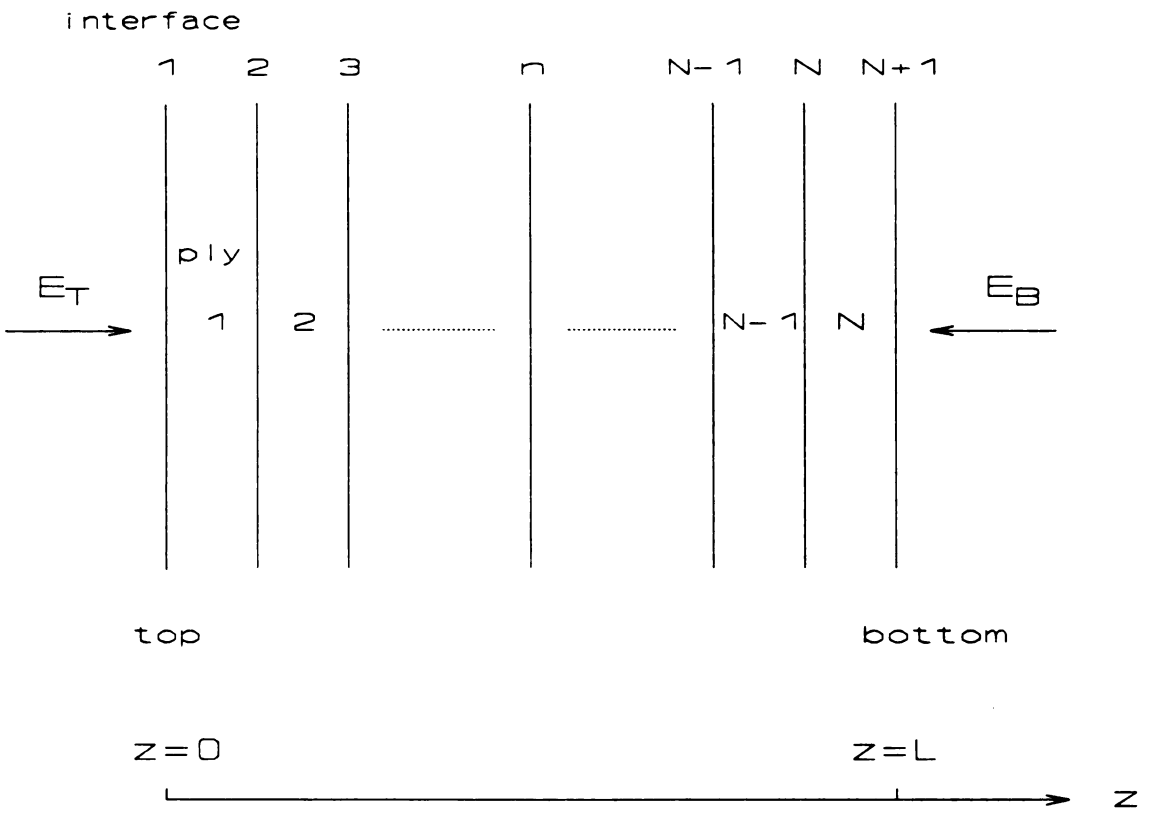

Figure 8.2. One Dimensional Configuration for Power Absorption Model

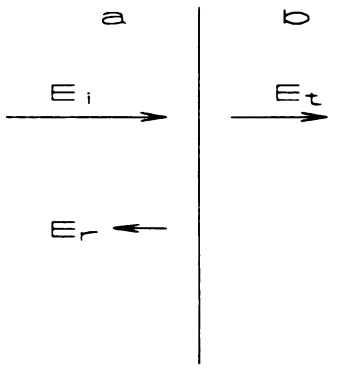

Figure 8.3. TEM Wave at Two Isotropic Media a and b

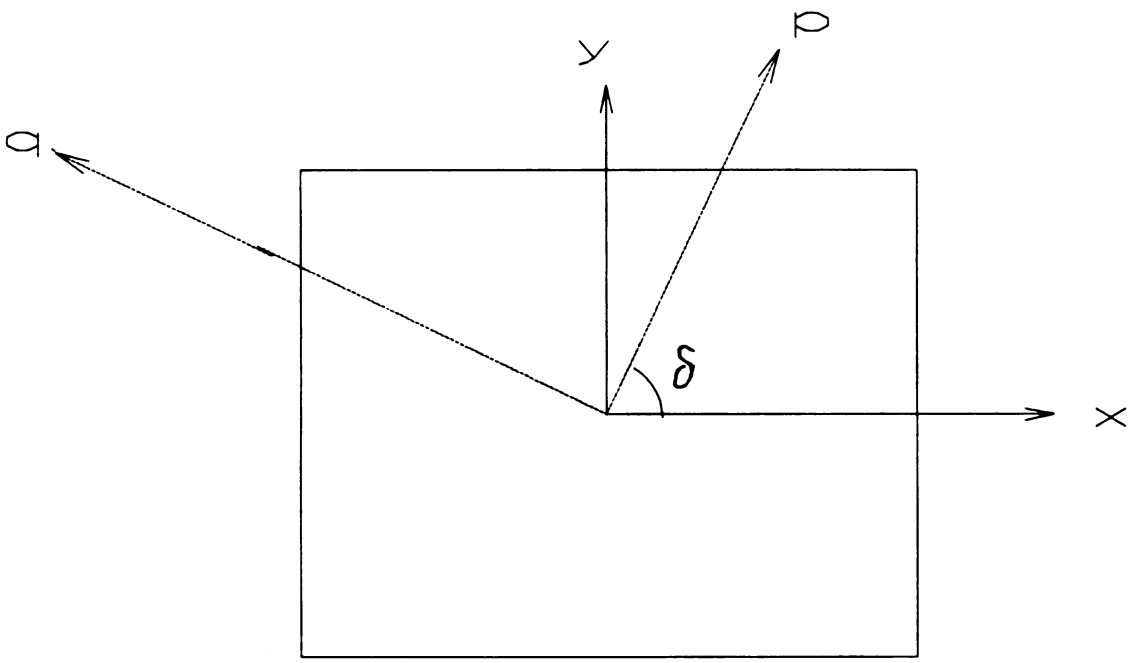

Figure 8.4. Base and Principle Coordinates

Maxwell's equations are used to relate the electric field vector to the magnetic field vector[64]. Maxwell's equations in an anisotropic, non-magnetic composite are

$$\nabla \times \vec{E} = -j\omega\mu\vec{H} \tag{8-3}$$

$$\nabla \times \vec{H} = j\omega\vec{\varepsilon}_e \cdot \vec{E} \tag{8-4}$$

Taking the curl of Equation (8-3), we have

$$\nabla \times \nabla \times \vec{E} = -j\omega\mu\nabla \times \vec{H} \tag{8-5}$$

Combining Equations (8-4) and (8-5), we obtain

$$\nabla(\nabla \cdot \vec{E}) - \nabla^2\vec{E} = -j\omega\mu(j\omega\vec{\varepsilon}_e \cdot \vec{E}) \tag{8-6}$$

As $\vec{E}$ is a linearly polarized TEM wave propagating in the z direction, we have

$$\nabla \cdot \vec{E} = 0 \tag{8-7}$$

Put Equation (8-7) into (8-6), the wave equation in the anisotropic medium becomes

As $\vec{E}$ is a planar TEM wave travelling in z direction, we obtain

$$\nabla^2 \vec{E} + \omega^2 \mu \bar{\bar{\epsilon}}_c \cdot \vec{E} = 0 \tag{8-8}$$

$$\vec{E} = E_p \varrho_p + E_q \varrho_q \tag{8-9}$$

$$\nabla^2 \vec{E} = \frac{d^2 \vec{E}}{dz^2} \tag{8-10}$$

Substituting Equations (8-9) and (8-10) into (8-8), we obtain

$$\begin{aligned} \frac{d^2 E_p}{dz^2} + k_p^2 E_p &= 0 \\ \frac{d^2 E_q}{dz^2} + k_q^2 E_q &= 0 \end{aligned} \tag{8-11}$$

where $k_p^2 = \omega^2 \mu \epsilon_p^*$ and $k_q^2 = \omega^2 \mu \epsilon_q^*$, μ is the permeability of free space, and ϵ_p^* and ϵ_q^* are the absolute complex permittivity of the composite in the p and q principle directions, respectively.

The solutions for E_p and E_q are

$$\begin{aligned} E_p &= E_p^+ e^{-jk_p z} + E_p^- e^{+jk_p z} \\ E_q &= E_q^+ e^{-jk_q z} + E_q^- e^{+jk_q z} \end{aligned} \tag{8-12}$$

where superscript + and - represent +z and -z propagating waves, respectively, and k_p and k_q are the wave numbers in the p-axis and q-axis directions respectively. Rewriting Equation (8-3) and combining with Equation (8-9), we obtain

$$\begin{aligned} \vec{H} &= \frac{j}{\omega \mu} \nabla \times \vec{E} \\ &= \frac{j}{\omega \mu} \left[-\frac{\partial E_q}{\partial z} \varrho_p + \frac{\partial E_p}{\partial z} \varrho_q \right] \end{aligned} \tag{8-13}$$

Defining

$$H_p = -\frac{j}{\omega\mu}\frac{\partial E_q}{\partial z}$$
$$H_q = \frac{j}{\omega\mu}\frac{\partial E_p}{\partial z} \tag{8-14}$$

and putting Equation (8-12) into (8-14), we obtain

$$H_p = \frac{k_q}{\omega\mu}[-E_q^+ e^{-jk_q z} + E_q^- e^{+jk_q z}]$$
$$H_q = \frac{k_p}{\omega\mu}[E_p^+ e^{-jk_p z} - E_p^- e^{+jk_p z}] \tag{8-15}$$

Defining

$$\begin{pmatrix} H_p^+ \\ H_q^+ \end{pmatrix} = \frac{1}{\sqrt{\mu}}\begin{pmatrix} -\sqrt{e_q^*} & 0 \\ 0 & \sqrt{e_p^*} \end{pmatrix}\begin{pmatrix} E_q^+ \\ E_p^+ \end{pmatrix} \tag{8-16}$$

and

$$\begin{pmatrix} H_p^- \\ H_q^- \end{pmatrix} = -\frac{1}{\sqrt{\mu}}\begin{pmatrix} -\sqrt{e_q^*} & 0 \\ 0 & \sqrt{e_p^*} \end{pmatrix}\begin{pmatrix} E_q^- \\ E_p^- \end{pmatrix} \tag{8-17}$$

and combining Equations (8-15), (8-16), and (8-17), we obtain

$$H_p = H_p^+ e^{-jk_q z} + H_p^- e^{+jk_q z}$$
$$H_q = H_q^+ e^{-jk_p z} + H_q^- e^{+jk_p z} \tag{8-18}$$

The $\vec{E}$ and $\vec{H}$ of the incident TEM waves in the x-y coordinates can be expressed in the p-q coordinates by

$$\begin{pmatrix} E_x^i \\ E_y^i \end{pmatrix} = \begin{pmatrix} \cos\delta & -\sin\delta \\ \sin\delta & \cos\delta \end{pmatrix}\begin{pmatrix} E_p^i \\ E_q^i \end{pmatrix} \tag{8-19}$$

and

$$\begin{pmatrix} H_x^i \\ H_y^i \end{pmatrix} = \begin{pmatrix} \cos\delta & -\sin\delta \\ \sin\delta & \cos\delta \end{pmatrix} \begin{pmatrix} H_p^i \\ H_q^i \end{pmatrix} \tag{8-20}$$

For incident waves, the relationship between $\vec{E}$ and $\vec{H}$ in the x-y coordinates can be obtained from Equations (8-16), (8-19), and (8-20).

$$\begin{pmatrix} H_x^i \\ H_y^i \end{pmatrix} = M_a \begin{pmatrix} E_x^i \\ E_y^i \end{pmatrix} \tag{8-21}$$

where i represents the incident wave, M_a is the characteristic matrix for an anisotropic homogeneous medium a, and δ is the angle from the x-y coordinate to the p-q coordinate in medium a.

$$M_a = \frac{1}{\sqrt{\mu}} \begin{pmatrix} \cos\delta & -\sin\delta \\ \sin\delta & \cos\delta \end{pmatrix} \begin{pmatrix} 0 & -\sqrt{\epsilon_q^*} \\ \sqrt{\epsilon_p^*} & 0 \end{pmatrix} \begin{pmatrix} \cos\delta & \sin\delta \\ -\sin\delta & \cos\delta \end{pmatrix} \tag{8-22}$$

For reflected waves, the relationship between $\vec{E}$ and $\vec{H}$ in the x-y coordinate can be obtained from Equations (8-17), (8-19), and (8-20).

$$\begin{pmatrix} H_x^r \\ H_y^r \end{pmatrix} = -M_a \begin{pmatrix} E_x^r \\ E_y^r \end{pmatrix} \tag{8-23}$$

where r represents the reflected wave.

Similarly, the relationship for a transmitted wave is

$$\begin{pmatrix} H_x^t \\ H_y^t \end{pmatrix} = M_b \begin{pmatrix} E_x^t \\ E_y^t \end{pmatrix} \tag{8-24}$$

where t represents the transmitted wave, and M_b is the characteristic matrix for an anisotropic homogeneous medium b.

$$M_b = \frac{1}{\sqrt{\mu}}\begin{pmatrix}\cos\delta' & -\sin\delta' \\ \sin\delta' & \cos\delta'\end{pmatrix}\begin{pmatrix}0 & -\sqrt{\epsilon_q^*} \\ \sqrt{\epsilon_p^*} & 0\end{pmatrix}\begin{pmatrix}\cos\delta' & \sin\delta' \\ -\sin\delta' & \cos\delta'\end{pmatrix} \tag{8-25}$$

where δ' is the angle from the x-y coordinate to the p-q coordinate in medium b.

At the interface, the continuity of the tangential component of the electric and magnetic field leads to

$$\begin{aligned}\vec{E}^t &= \vec{E}^i + \vec{E}^r \\ \vec{H}^t &= \vec{H}^i + \vec{H}^r\end{aligned} \tag{8-26}$$

Writing out each component in Equation (8-26), we obtain

$$\begin{pmatrix}E_x^t \\ E_y^t\end{pmatrix} = \begin{pmatrix}E_x^i \\ E_y^i\end{pmatrix} + \begin{pmatrix}E_x^r \\ E_y^r\end{pmatrix} \tag{8-27}$$

$$\begin{pmatrix}H_x^t \\ H_y^t\end{pmatrix} = \begin{pmatrix}H_x^i \\ H_y^i\end{pmatrix} + \begin{pmatrix}H_x^r \\ H_y^r\end{pmatrix} \tag{8-28}$$

Putting Equations (8-21), (8-23), and (8-24) into Equation (8-28), we obtain

$$M_b\begin{pmatrix}E_x^t \\ E_y^t\end{pmatrix} = M_a\begin{pmatrix}E_x^i \\ E_y^i\end{pmatrix} - M_a\begin{pmatrix}E_x^r \\ E_y^r\end{pmatrix} \tag{8-29}$$

Solving Equations (8-27) and (8-29), we obtain

$$\begin{pmatrix}E_x^t \\ E_y^t\end{pmatrix} = \ddot{T}\begin{pmatrix}E_x^i \\ E_y^i\end{pmatrix} \tag{8-30}$$

and

$$\begin{pmatrix}E_x^r \\ E_y^r\end{pmatrix} = \ddot{R}\begin{pmatrix}E_x^i \\ E_y^i\end{pmatrix} \tag{8-31}$$

where $\ddot{T}$ and $\ddot{R}$ are the transmission and reflection coefficients at the interface respectively.

$$\begin{aligned} \ddot{T} &= 2(M_a + M_b)^{-1} M_a \\ \ddot{R} &= (M_a + M_b)^{-1}(M_a - M_b) \end{aligned} \tag{8-32}$$

The above derivation is for incident TEM waves propagating in the +z direction only. If incident TEM waves come from both sides, as shown in Figure 8.5, the continuity condition at the interface becomes

$$\begin{aligned} \vec{E}_t^{\,+} &= \vec{E}_i^{\,+} + \vec{E}_r^{\,+} \\ \vec{E}_t^{\,-} &= \vec{E}_i^{\,-} + \vec{E}_r^{\,-} \end{aligned} \tag{8-33}$$

with

$$\begin{aligned} \vec{E}_r^{\,+} &= \ddot{R}\,\vec{E}_i^{\,+} \\ \vec{E}_r^{\,-} &= -\ddot{R}\,\vec{E}_i^{\,-} \end{aligned} \tag{8-34}$$

where $\ddot{R}$ is the reflection coefficient when the TEM wave is travelling from medium a to medium b as defined previously.

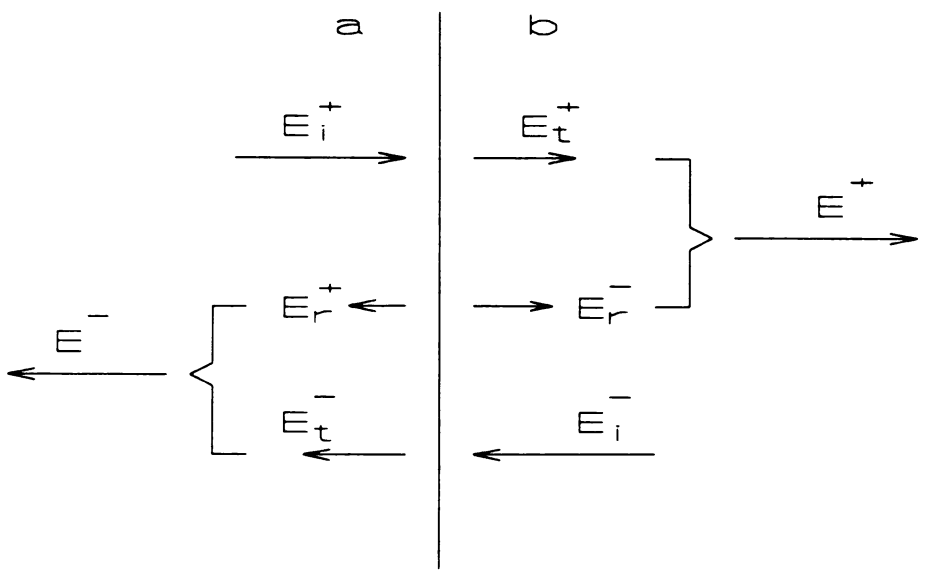

Figure 8.5. Waves at Interface with TEM Waves Propagating at Both Directions

Defining the +z and -z direction effective transmitted waves at the interface as

$$\vec{E}^{+} = \vec{E}_t^{+} + \vec{E}_r^{-}$$
$$\vec{E}^{-} = \vec{E}_r^{+} + \vec{E}_t^{-} \tag{8-35}$$

and putting Equations (8-33) and (8-34) into (8-35), we obtain

$$\vec{E}^{+} = (\vec{\vec{I}} + \vec{\vec{R}})\vec{E}_i^{+} - \vec{\vec{R}}\vec{E}_i^{-}$$
$$\vec{E}^{-} = (\vec{\vec{I}} - \vec{\vec{R}})\vec{E}_i^{-} + \vec{\vec{R}}\vec{E}_i^{+} \tag{8-36}$$

For a multi-ply composite, each interface, 1,2,...N+1, can be treated in the same way as above. From the wave behavior at each interface, the electric field inside each ply can be derived. Consider the electric field inside the n^{th} ply as shown in Figure 8.6. The electric field inside the n^{th} ply can be obtained from the +z effective transmitted waves at the n^{th} interface, the -z effective transmitted waves at the $(n+1)^{th}$ interface, and the attenuation tensor of the n^{th} ply, $\vec{\vec{A}}_n$. The -z incident travelling wave at the n^{th} interface, $(\vec{E}_i^{-})_n$, and the +z incident travelling wave at the $(n+1)^{th}$ interface, $(\vec{E}_i^{+})_{n+1}$, can be calculated as

$$(\vec{E}_i^{+})_{n+1} = \vec{\vec{A}}_n \vec{E}_n^{+}$$
$$(\vec{E}_i^{-})_n = \vec{\vec{A}}_n \vec{E}_{n+1}^{-} \tag{8-37}$$

If $\vec{\vec{A}}_n$, $\vec{E}_n^{+}$, and $\vec{E}_{n+1}^{-}$ are known, the average electric field in the n^{th} ply can be approximated by

$$(\vec{E})_n = \frac{1}{2}(\vec{E}_n^{+} + \vec{\vec{A}}_n\vec{E}_n^{+} + \vec{E}_{n+1}^{-} + \vec{\vec{A}}_n\vec{E}_{n+1}^{-}) \tag{8-38}$$

For TEM waves in a homogeneous isotropic material with permittivity ϵ^*, the electric field is attenuated according to following equation.

$$\vec{E}(z) = \vec{E}(0)\exp(-\gamma z) \tag{8-39}$$

where $\vec{E}(0)$ is the electric field vector entering material, z is the propagating

direction, and γ is the propagating constant:

$$\gamma = jk = j\omega\sqrt{\epsilon^* \mu} \tag{8-40}$$

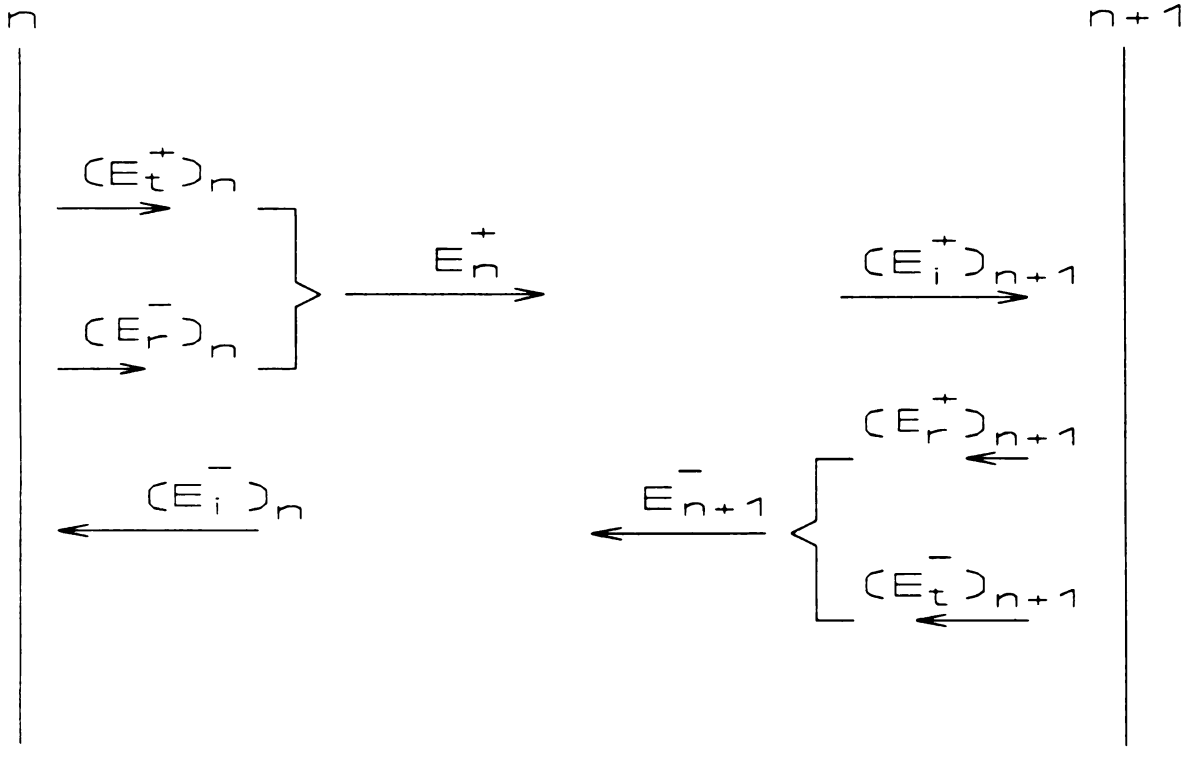

Figure 8.6. Electric Field Inside n^{th} Ply

For TEM waves in the composite material, the electric field can be decomposed into its principle direction, parallel and perpendicular to the fiber. The attenuation of the electric field in each direction can then be treated separately.

$$\begin{aligned} E_p(z) &= E_p(0)\exp(-\gamma_p z) \\ E_q(z) &= E_q(0)\exp(-\gamma_q z) \end{aligned} \tag{8-41}$$

where

$$\begin{aligned} \gamma_p &= jk_p \\ \gamma_q &= jk_q \end{aligned}$$

Rewriting Equation (8-41) in matrix form

$$\begin{pmatrix} E_p(z) \\ E_q(z) \end{pmatrix} = \begin{pmatrix} \exp(-\gamma_p z) & 0 \\ 0 & \exp(-\gamma_q z) \end{pmatrix} \begin{pmatrix} E_p(0) \\ E_q(0) \end{pmatrix} \tag{8-42}$$

From Equation (8-19)

$$\begin{pmatrix} E_p(0) \\ E_q(0) \end{pmatrix} = \begin{pmatrix} \cos\delta & \sin\delta \\ -\sin\delta & \cos\delta \end{pmatrix} \begin{pmatrix} E_x(0) \\ E_y(0) \end{pmatrix} \tag{8-43}$$

$$\begin{pmatrix} E_p(z) \\ E_q(z) \end{pmatrix} = \begin{pmatrix} \cos\delta & \sin\delta \\ -\sin\delta & \cos\delta \end{pmatrix} \begin{pmatrix} E_x(z) \\ E_y(z) \end{pmatrix} \tag{8-44}$$

From Equations (8-42), (8-43), and (8-44)

$$\begin{pmatrix} E_x(z) \\ E_y(z) \end{pmatrix} = \tilde{A}_n \begin{pmatrix} E_x(0) \\ E_y(0) \end{pmatrix} \tag{8-45}$$

where

$$\tilde{A}_n = \begin{pmatrix} \cos\delta & -\sin\delta \\ \sin\delta & \cos\delta \end{pmatrix} \begin{pmatrix} \exp(-\gamma_p z) & 0 \\ 0 & \exp(-\gamma_q z) \end{pmatrix} \begin{pmatrix} \cos\delta & \sin\delta \\ -\sin\delta & \cos\delta \end{pmatrix} \tag{8-46}$$

The effective transmitted +z travelling wave at the n^{th} interface, $\vec{E}_n^{\,+}$, can be expressed by the effective transmitted +z travelling wave at the $(n-1)^{th}$ interface, $\vec{E}_{n-1}^{\,+}$, and the effective transmitted -z travelling wave at the $(n+1)^{th}$ interface, $\vec{E}_{n+1}^{\,-}$, using Equations (8-36) and (8-37). Similar relations can be obtained for the effective transmitted -z travelling wave at n^{th} interface, $\vec{E}_n^{\,-}$.

$$\begin{aligned} \vec{E}_n^{\,+} &= (\tilde{I} + \tilde{R}_n)\tilde{A}_{n-1}\vec{E}^{+}_{n-1} - \tilde{R}_n\tilde{A}_n\vec{E}^{-}_{n+1} \\ \vec{E}_n^{\,-} &= (\tilde{I} - \tilde{R}_n)\tilde{A}_n\vec{E}^{-}_{n+1} + \tilde{R}_n\tilde{A}_{n-1}\vec{E}^{+}_{n-1} \end{aligned} \tag{8-47}$$

In addition, we look at two special interfaces, the top and bottom interfaces where n=1 and N+1. As shown in Figure 8.7, the incident TEM waves are assumed to be known.

$$(\vec{E}_i^{+})_1 = \vec{E}_T$$
$$(\vec{E}_i^{-})_{N+1} = \vec{E}_B \tag{8-48}$$

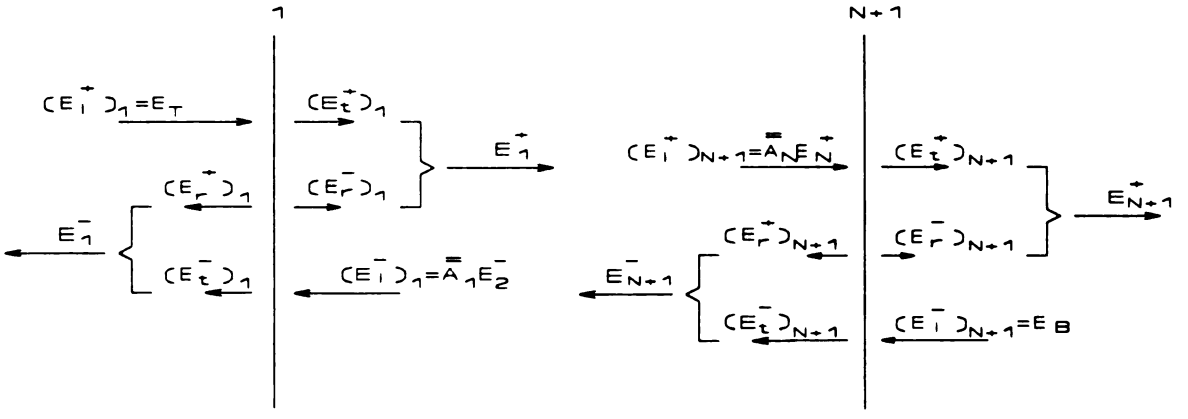

Figure 8.7 TEM Waves at Top and Bottom Plies

Rearranging Equation (8-47), the general equations for travelling waves become

$$(\ddot{I}+\ddot{R}_n)\ddot{A}_{n-1}\vec{E}_{n-1}^{\,+}-\vec{E}_n^{\,+}-\ddot{R}_n\ddot{A}_n\vec{E}_{n+1}^{\,-}=0$$
$$\ddot{R}_n\ddot{A}_{n-1}\vec{E}_{n-1}^{\,+}-\vec{E}_n^{\,-}+(\ddot{I}-\ddot{R}_n)\ddot{A}_n\vec{E}_{n+1}^{\,-}=0 \tag{8-49}$$

For n=1, Equation (8-49) becomes

$$-\vec{E}_1^{\,+}-\ddot{R}_1\ddot{A}_1\vec{E}_2^{\,-}=-(\ddot{I}+\ddot{R}_1)\vec{E}_T$$
$$-\vec{E}_1^{\,-}+(\ddot{I}-\ddot{R}_1)\ddot{A}_1\vec{E}_2^{\,-}=-\ddot{R}_1\vec{E}_T \tag{8-50}$$

For n=N+1, Equation (8-49) becomes

$$(\ddot{I}+\ddot{R}_{N+1})\ddot{A}_N\vec{E}_N^{\,+}-\vec{E}_{N+1}^{\,+}=\ddot{R}_{N+1}\vec{E}_B$$
$$\ddot{R}_{N+1}\ddot{A}_N\vec{E}_N^{\,+}-\vec{E}_{N+1}^{\,-}=-(\ddot{I}-\ddot{R}_{N+1})\vec{E}_B \tag{8-51}$$

Therefore, 2N+2 equations can be generated from (N+1) interfaces to solve for

2N+2 unknowns, $\vec{E}_i^{+}$ and $\vec{E}_i^{-}$, i=1,2,...N+1. Based on the above derivation, $\vec{A}_n$ and $\vec{R}$ depend upon the properties of the composite, incident wavelength, and the angles from x-y coordinate to fiber orientation (δ) of each laminate.

Putting 2N+2 equations generated based on Equations (8-49), (8-50), and (8-51) into a matrix form,

$$\vec{Q}\,\vec{E} = \vec{E}_0 \tag{8-52}$$

and

$$\vec{Q} = \begin{pmatrix} \vec{Q}_1 & \vec{Q}_2 \\ \vec{Q}_3 & \vec{Q}_4 \end{pmatrix} \tag{8-53}$$

where $\vec{Q}$ is a (2N+2) by (2N+2) matrix. The $\vec{Q}_i$'s are (N+1) by (N+1) matrices with i=1,2,3,4. $\vec{E}$ and $\vec{E}_0$ are (2N+2) by 1 matrices. The expressions for the $\vec{Q}_i$'s, $\vec{E}$, and $\vec{E}_0$ are

$$\vec{Q}_1 = \begin{pmatrix} -\vec{I} & 0 & 0 & 0 & 0 & 0 \\ (\vec{I}+\vec{R}_2)\vec{A}_1 & -\vec{I} & 0 & 0 & 0 & 0 \\ 0 & \ddots & \ddots & 0 & 0 & 0 \\ 0 & 0 & (\vec{I}+\vec{R}_n)\vec{A}_{n-1} & -\vec{I} & 0 & 0 \\ 0 & 0 & 0 & \ddots & \ddots & 0 \\ 0 & 0 & 0 & 0 & (\vec{I}+\vec{R}_{N+1})\vec{A}_N & -\vec{I} \end{pmatrix}_{(N+1)\times(N+1)} \tag{8-54}$$

$$\ddot{Q}_2 = \begin{pmatrix} 0 & -\ddot{R}_1\ddot{A}_1 & 0 & 0 & 0 & 0 & 0 \\ 0 & 0 & -\ddot{R}_2\ddot{A}_2 & 0 & 0 & 0 & 0 \\ 0 & 0 & 0 & \ddots & 0 & 0 & 0 \\ 0 & 0 & 0 & 0 & -\ddot{R}_n\ddot{A}_n & 0 & 0 \\ 0 & 0 & 0 & 0 & 0 & \ddots & 0 \\ 0 & 0 & 0 & 0 & 0 & 0 & -\ddot{R}_N\ddot{A}_N \\ 0 & 0 & 0 & 0 & 0 & 0 & 0 \end{pmatrix}_{(N+1)\times(N+1)} \tag{8-55}$$

$$\ddot{Q}_3 = \begin{pmatrix} 0 & 0 & 0 & 0 & 0 & 0 \\ \ddot{R}_2\ddot{A}_1 & 0 & 0 & 0 & 0 & 0 \\ 0 & \ddots & \ddots & 0 & 0 & 0 \\ 0 & 0 & \ddot{R}_n\ddot{A}_{n-1} & 0 & 0 & 0 \\ 0 & 0 & 0 & \ddots & \ddots & 0 \\ 0 & 0 & 0 & 0 & \ddot{R}_{N+1}\ddot{A}_N & 0 \end{pmatrix}_{(N+1)\times(N+1)} \tag{8-56}$$

$$\ddot{Q}_4 = \begin{pmatrix} -\ddot{I} & (\ddot{I}-\ddot{R}_1)\ddot{A}_1 & 0 & 0 & 0 & 0 & 0 \\ 0 & -\ddot{I} & (\ddot{I}_1-\ddot{R}_2)\ddot{A}_2 & 0 & 0 & 0 & 0 \\ 0 & 0 & \ddots & \ddots & 0 & 0 & 0 \\ 0 & 0 & 0 & -\ddot{I} & (\ddot{I}-\ddot{R}_n)\ddot{A}_n & 0 & 0 \\ 0 & 0 & 0 & 0 & \ddots & \ddots & 0 \\ 0 & 0 & 0 & 0 & 0 & -\ddot{I} & (\ddot{I}-\ddot{R}_N)\ddot{A}_N \\ 0 & 0 & 0 & 0 & 0 & 0 & -\ddot{I} \end{pmatrix}_{(N+1)\times(N+1)} \tag{8-57}$$

$$\vec{E} = \begin{pmatrix} \vec{E}_1^+ \\ \vec{E}_2^+ \\ \vdots \\ \vec{E}_n^+ \\ \vdots \\ \vec{E}_{N+1}^+ \\ \vec{E}_1^- \\ \vec{E}_2^- \\ \vdots \\ \vec{E}_n^- \\ \vdots \\ \vec{E}_{N+1}^- \end{pmatrix}_{(2N+2)\times 1} \tag{8-58}$$

$$\vec{E}_0 = \begin{pmatrix} -(\vec{\vec{I}} + \vec{\vec{R}}_1)\vec{E}_T \\ 0 \\ \vdots \\ 0 \\ \vdots \\ \vec{\vec{R}}_{N+1}\vec{E}_B \\ -\vec{\vec{R}}_1\vec{E}_T \\ 0 \\ \vdots \\ 0 \\ \vdots \\ -(\vec{\vec{I}} - \vec{\vec{R}}_{N+1})\vec{E}_B \end{pmatrix}_{(2N+2)\times 1} \tag{8-59}$$

$\vec{E}_i^-$ and $\vec{E}_i^+$ in the x-y coordinates are

$$\vec{\vec{E}} = \vec{\vec{Q}}^{-1}\vec{\vec{E}}_0 \tag{8-60}$$

where

$$\vec{\vec{Q}}^{-1} = \begin{pmatrix} \vec{\vec{Q}}_1' & \vec{\vec{Q}}_2' \\ \vec{\vec{Q}}_3' & \vec{\vec{Q}}_4' \end{pmatrix} \tag{8-61}$$

and

$$\begin{aligned} \vec{\vec{Q}}_1' &= (\vec{\vec{Q}}_1 - \vec{\vec{Q}}_2\vec{\vec{Q}}_4^{-1}\vec{\vec{Q}}_3)^{-1} \\ \vec{\vec{Q}}_4' &= (\vec{\vec{Q}}_4 - \vec{\vec{Q}}_3\vec{\vec{Q}}_1^{-1}\vec{\vec{Q}}_2)^{-1} \\ \vec{\vec{Q}}_2' &= -\vec{\vec{Q}}_1^{-1}\vec{\vec{Q}}_2\vec{\vec{Q}}_4' \\ \vec{\vec{Q}}_3' &= -\vec{\vec{Q}}_4^{-1}\vec{\vec{Q}}_3\vec{\vec{Q}}_1' \end{aligned} \tag{8-62}$$

Once $\vec{E}_i^-$ and $\vec{E}_i^+$, i=1,2,...N+1, are known, the electric field inside each ply can be estimated using Equation (8-38). For unidirectional composites, there are only two interfaces, n=1 and N+1. The only parameters that need to be calculated are $\vec{E}_1^+$, $\vec{E}_{N+1}^+$, $\vec{E}_1^-$, and $\vec{E}_{N+1}^-$. The reflection coefficients at the n=1 and N+1 interfaces have the following relationship

$$\vec{\vec{R}}_{N+1} = -\vec{\vec{R}}_1$$

For a unidirectional composite, Equation (8-52) can be simplified to

$$\begin{pmatrix} -\vec{\vec{I}} & 0 & 0 & -\vec{\vec{R}}_1\vec{\vec{A}}_1 \\ (\vec{\vec{I}} - \vec{\vec{R}}_1)\vec{\vec{A}}_1 & -\vec{\vec{I}} & 0 & 0 \\ 0 & 0 & -\vec{\vec{I}} & (\vec{\vec{I}} - \vec{\vec{R}}_1)\vec{\vec{A}}_1 \\ -\vec{\vec{R}}_1\vec{\vec{A}}_1 & 0 & 0 & -\vec{\vec{I}} \end{pmatrix} \begin{pmatrix} \vec{E}_1^+ \\ \vec{E}_{N+1}^+ \\ \vec{E}_1^- \\ \vec{E}_{N+1}^- \end{pmatrix} = \begin{pmatrix} -(\vec{\vec{I}} + \vec{\vec{R}}_1)\vec{E}_T \\ -\vec{\vec{R}}_1\vec{E}_B \\ -\vec{\vec{R}}_1\vec{E}_T \\ -(\vec{\vec{I}} + \vec{\vec{R}}_1)\vec{E}_B \end{pmatrix} \tag{8-63}$$

Once $\vec{E}_1^{\,+}$, $\vec{E}_{N+1}^{\,+}$, $\vec{E}_1^{\,-}$, and $\vec{E}_{N+1}^{\,-}$ are known, the electric field strength at any location inside the composite can be calculated based on the attenuation of the field. To simplify the calculation, the x-y coordinate is taken to be the same as the p-q coordinate with the fiber direction along the x or p axis.

$$E_x(z) = (E_1^+)_x \exp(-\gamma_p z) + (E_{N+1}^-)_x \exp(\gamma_p (z-L))$$
$$E_y(z) = (E_1^+)_y \exp(-\gamma_q z) + (E_{N+1}^-)_y \exp(\gamma_q (z-L)) \tag{8-64}$$

To simplify the calculation of the microwave power absorption inside the composite, i.e. to eliminate the off-diagonal terms in ϵ_c', the electric field strengths are needed in p-q coordinates. The electric field in p-q coordinates can be calculated from the in x-y coordinates.

$$(E_p)_n = (E_x)_n \cos\delta_n + (E_y)_n \sin\delta_n$$
$$(E_q)_n = -(E_x)_n \sin\delta_n + (E_y)_n \cos\delta_n \tag{8-65}$$

δ_n in Equation (8-65) for unidirectional composite equals zero. The microwave power dissipation rate due to top and bottom incident waves in the n^{th} ply, P_2, can be determined using Equations (8-1) and (8-2).

$$P_2 = \pi f(\epsilon_p'' |(E_p)_n|^2 + \epsilon_q'' |(E_q)_n|^2) \tag{8-66}$$

The total time-average microwave power dissipated in the composite due to the TEM waves from the top, bottom, and sides is

$$P = s\sum_{n=1}^{N} h_n (P_c)_n \tag{8-67}$$

where s is the area of the composite surface, h_n is the thickness of the n^{th} ply, and $P_c = P_1 + P_2$.

8.4 Parameter Estimation

In Equation (8-60), the 2N+2 unknowns are $\vec{E}_i^-$ and $\vec{E}_i^+$, i=1,2,...N+1. For a given composite, $\tilde{\tilde{A}}_n$ and $\tilde{\tilde{R}}$ are fixed. Therefore, $\vec{E}_i^-$ and $\vec{E}_i^+$ are only functions of $\vec{E}_T$ and $\vec{E}_B$. During microwave processing, the cavity is in a resonant condition and the microwave energy is confined inside the cavity and coupled to the composite. For a fixed composite location, $\vec{E}_T$ and $\vec{E}_B$ are only functions of the resonant mode and the input power level. $\vec{E}_T$ and $\vec{E}_B$ can be expressed as

$$\vec{E}_B = A_B(\cos\theta_B \underline{e}_x + \sin\theta_B \underline{e}_y)\exp(j\omega t + \gamma z)$$
$$\vec{E}_T = A_T(\cos\theta_T \underline{e}_x + \sin\theta_T \underline{e}_y)\exp(j\omega t - \gamma z) \tag{8-68}$$

where A_T and A_B are the magnitudes of the incident TEM waves at top and bottom, respectively and θ_T and θ_B are the polarization angles of the incident TEM waves at the top and bottom, respectively.

The total microwave power dissipated in the composite per unit volume per time, P_c, is a function of P_1, $\vec{E}_T$, and $\vec{E}_B$. From Equation (8-68), P_c can be expressed as

$$P_c = P_1 + P_2(A_T, A_B, \theta_T, \theta_B) \tag{8-69}$$

The values of P_1, A_T, A_B, θ_T, and θ_B for a given mode in microwave processing of composites can be obtained from the temperature measurement of fully cured composites in that mode.

8.4.1 Energy Balance

Assuming that the temperature is uniform across each laminate, the one-dimensional energy balance for a fully cured composite during microwave cure is

$$\rho c \frac{\partial T}{\partial t} = k_z \frac{\partial^2 T}{\partial z^2} + P_c(p_1, A_T, \theta_T, A_B, \theta_B) \tag{8-70}$$

with the initial condition

$$T(z,0) = T_0$$

and the boundary conditions

$$\frac{\partial T}{\partial z}\Big|_{z=L} = 0$$

$$-k_z \frac{\partial T}{\partial z}\Big|_{z=0} = h(T_s - T(0,t))$$

The heat loss occurs at the top, z=0, with free convection while the other side, z=L, is insulated. Once P_1, A_T, A_B, θ_T, and θ_B are known, $T(z,t,P_1,A_T,A_B,\theta_T,\theta_B)$ can be calculated numerically From Equation (8-70). To simplify the notation, β_1, β_2, β_3, β_4, and β_5 are used to represent P_1, A_T, A_B, θ_T, and θ_B, respectively.

8.4.2 Optimization of Parameters

Ordinary least squares minimization is used to optimize $\beta_{1\text{-}5}$. The optimization scheme is

$$S = \sum_i \sum_j^J (Y_{ij} - T_{ij}(\beta_{1\text{-}5}))^2 \tag{8-71}$$

where i represents time, j represents the measurement point, J is the number of points measured, Y_{ij} is the measured temperature at point j and time i, and $T_{ij}(\beta_{1\text{-}5})$ is the calculated temperature using Equation (8-70) at point j and time i.

To estimate ß's, we first need to calculate the sensitivity coefficients, X_{jn}. The sensitivity coefficient is defined as the first derivative of a dependent variable, the temperature in this case, with respect to an unknown parameter, ß1 to ß5.

$$X_{jn}(z_j,t_i) \equiv \frac{\partial T(z_j,t_i)}{\partial \beta_n}, \qquad n=1,2,...,5 \tag{8-72}$$

If the sensitivity coefficients are either small or correlated with one another, the estimation problem is difficult and very sensitive to measurement errors, and the solution will not be unique. Therefore, the X_{jn}'s are required to be large and uncorrelated. X_{jn} is considered to be large if $\beta_n X_{jn}$ is on the order of the temperature rise. X_{jn}'s are uncorrelated (linearly independent) if $\beta_n X_{jn}$ versus time curves have different shapes for different n. Furthermore, the estimation problem is linear if the sensitivity coefficients are not functions of the parameters.

One way to calculate the sensitivity coefficients is using a finite difference method[131]

$$\begin{aligned} X_{jn} &= \frac{\partial T(z_j,t,\beta_{1-5})}{\partial \beta_n} \\ &= \frac{T(z_j,t,\beta_m,\beta_n+\delta\beta_n) - T(z_j,t,\beta_{1-5})}{\delta\beta_n} \end{aligned} \tag{8-73}$$

where n=1,2,...,5, m=1,2,...,5, but $m \neq n$, and $\delta\beta_n = 0.0001\beta_n$.

Taking derivatives of Equation (8-71) with respect to ß's, we obtain

$$\frac{\partial S}{\partial \beta_n} = \sum_i \sum_j^J 2(Y_{ij} - T_{ij})(-\frac{\partial T_{ij}}{\partial \beta_n}), \qquad n=1,2,...,5 \tag{8-74}$$

Minimizing S with respect to β_n, we obtain

$$\sum_i \sum_j^J (Y_{ij} - \hat{T}_{ij})(\frac{\partial \hat{T}_{ij}}{\partial \beta_n}) = 0, \qquad n=1,2,...,5 \tag{8-75}$$

As T is a function of the ßs, the temperature of the $(k+1)^{th}$ iteration can be related to the temperature of k^{th} iteration.

$$T_{ij}^{(k+1)} = T_{ij}^{(k)} + \frac{\partial T_{ij}^{(k)}}{\partial \beta_1}\Delta\beta_1 + \frac{\partial T_{ij}^{(k)}}{\partial \beta_2}\Delta\beta_2 + \ldots + \frac{\partial T_{ij}^{(k)}}{\partial \beta_5}\Delta\beta_5$$
$$= T_{ij}^{(k)} + X_{j1}^{(k)}(i)\Delta\beta_1 + X_{j2}^{(k)}(i)\Delta\beta_2 + \ldots + X_{j5}^{(k)}(i)\Delta\beta_5 \qquad (8\text{-}76)$$

Putting Equation (8-76) into (8-75), we obtain

$$B_{n1}^{(k)}\Delta\beta_1 + B_{n2}^{(k)}\Delta\beta_2 + B_{n3}^{(k)}\Delta\beta_3 + B_{n4}^{(k)}\Delta\beta_4 + B_{n5}^{(k)}\Delta\beta_5 = A_n^{(k)} \qquad (8\text{-}77)$$
$$n = 1,2,\ldots,5.$$

where

$$A_n^{(k)} = \sum_i \sum_j^J (Y_{ij} - T_{ij}^{(k)}) X_{jn}^{(k)}(i)$$

and

$$B_{nq}^{(k)} = \sum_i \sum_j^J X_{jq}^{(k)}(i)\, X_{jn}^{(k)}(i), \qquad q = 1,2,\ldots,5.$$

Putting Equation (8-77) into matrix form, we obtain

$$\tilde{\tilde{B}}^{(k)}\tilde{\beta} = \tilde{A}^{(k)} \qquad (8\text{-}78)$$

where

$$\tilde{\tilde{B}}^{(k)} = \begin{pmatrix} B_{11}^{(k)} & B_{12}^{(k)} & B_{13}^{(k)} & B_{14}^{(k)} & B_{15}^{(k)} \\ B_{21}^{(k)} & B_{22}^{(k)} & B_{23}^{(k)} & B_{24}^{(k)} & B_{25}^{(k)} \\ B_{31}^{(k)} & B_{32}^{(k)} & B_{33}^{(k)} & B_{34}^{(k)} & B_{35}^{(k)} \\ B_{41}^{(k)} & B_{42}^{(k)} & B_{43}^{(k)} & B_{44}^{(k)} & B_{45}^{(k)} \\ B_{51}^{(k)} & B_{52}^{(k)} & B_{53}^{(k)} & B_{54}^{(k)} & B_{55}^{(k)} \end{pmatrix}_{5\times5}$$

$$\tilde{\beta} = \begin{pmatrix} \Delta\beta_1 \\ \Delta\beta_2 \\ \Delta\beta_3 \\ \Delta\beta_4 \\ \Delta\beta_5 \end{pmatrix}_{5\times1}$$

and

$$\vec{A}^{(k)} = \begin{pmatrix} A_1^{(k)} \\ A_2^{(k)} \\ A_3^{(k)} \\ A_4^{(k)} \\ A_5^{(k)} \end{pmatrix}_{5\times 1}$$

Clearly, $\vec{B}^{(k)}$ is a symmetric matrix since $B_{pq}^{(k)}$ equals $B_{qp}^{(k)}$. The increment of $\beta_{1\text{-}5}$ between the k^{th} and $(k+1)^{th}$ iteration can be obtained by solving Equation (8-78).

The next set of ß's is the values of previous set plus the difference calculated based on the least squares optimization, $\vec{\beta}$. The iteration is terminated when change in S is within 0.1 percent and the $\beta_{1\text{-}5}$ values of the last iteration are the five parameters for the electromagnetic heating mode. The electric field inside the composite can be generated based on these five parameters.

8.5 Measurement of Five Parameters for Microwave Power Absorption Model

A five-parameter microwave power absorption model has been developed in section 8.3. The five parameters are P_1 (the power dissipated due to the TEM waves from sides), A_T and θ_T (the magnitude and the polarization angle with respect to the fiber direction of the top TEM wave), and A_B and θ_B (the magnitude and the polarization angle with respect to the fiber direction of the bottom TEM wave). The methodology to generate the five parameters based on the temperature profiles obtained from microwave heating of a fully cured composite were described in section 8.4. The microwave power absorption model and the optimization methodology were applied to the microwave heating of a fully cured 72-ply unidirectional Hercules

AS4/3501-6 composite in a resonant mode at Lc=16.03 cm and a 0° fiber orientation. The dielectric properties of the unidirectional AS4/3501-6 composite is available elsewhere [8]. The computer code for the optimization is attached in Appendix II.

The experiments were conducted at three input power levels, 70W, 80W, and 150W. Temperatures were measured at five locations with T1, T2, T3, T4, and T5 locating at z=0, 0.177, 0.278, 0.532, and 0.785 cm respectively. The temperature profiles across the thickness during microwave heating at 70W, 80W, and 150W are shown in Figures 8.8 to 8.10, respectively. The points are experimental values and the lines are the calculated values from the optimization. In general, the two are in good agreement. The slightly higher calculated values than the experimental data at the beginning are due to the lack of critical coupling at the beginning of the microwave heating. Figure 8.11 shows the five parameters versus input power for the resonant mode at L_c=16.03 cm. Clearly, P_1, A_T, and A_B are functions of input power and the electromagnetic mode while θ_T and θ_B are only functions of mode for a given composite. θ_T and θ_B are equal to 1.556 and 0.0201 radian respectively for the given mode. A_T and A_B increase linearly with the square root of input power as shown in Figure 8.12 and Figure 8.13. Their relations are $A_T=9.75\times10^{-2}\ P^{1/2}$ and $A_B=5.867\ P^{1/2}$. P_1 increases linearly with $P^{0.3}$ as shown in Figure 8.14 with $P_1=0.104\ P^{0.3}$. With the relationship of the five parameters as a function of input power for the given mode, the temperature profiles during microwave cure can be readily simulated.

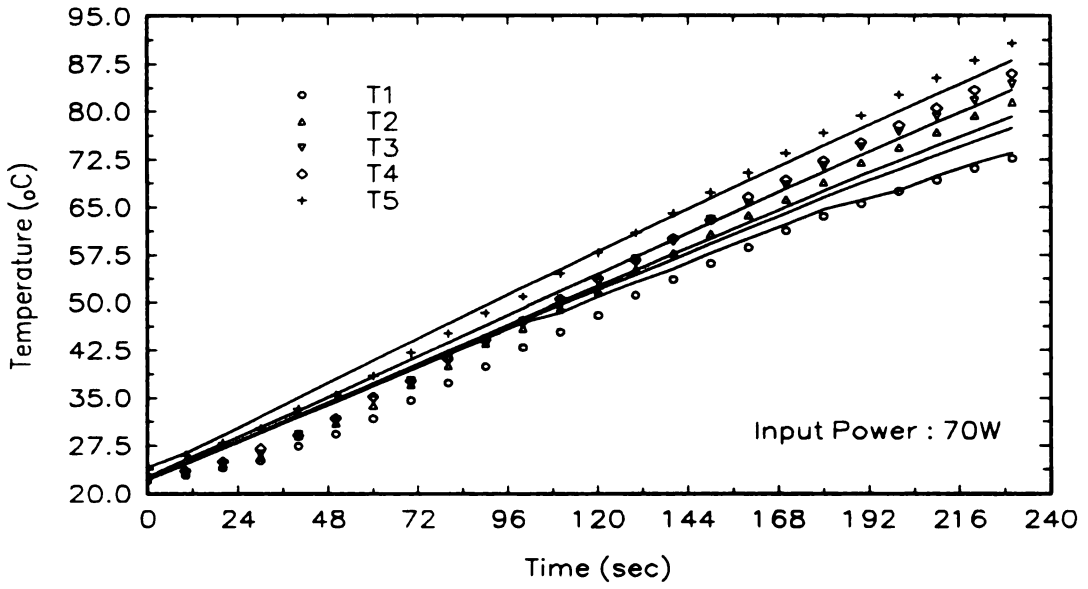

Figure 8.8 Temperature Distribution Across the Fully Cured 72-ply Unidirectional Hercules AS4/3501-6 Composite during Microwave Heating at L_c=16.03 cm with 70W Input Power

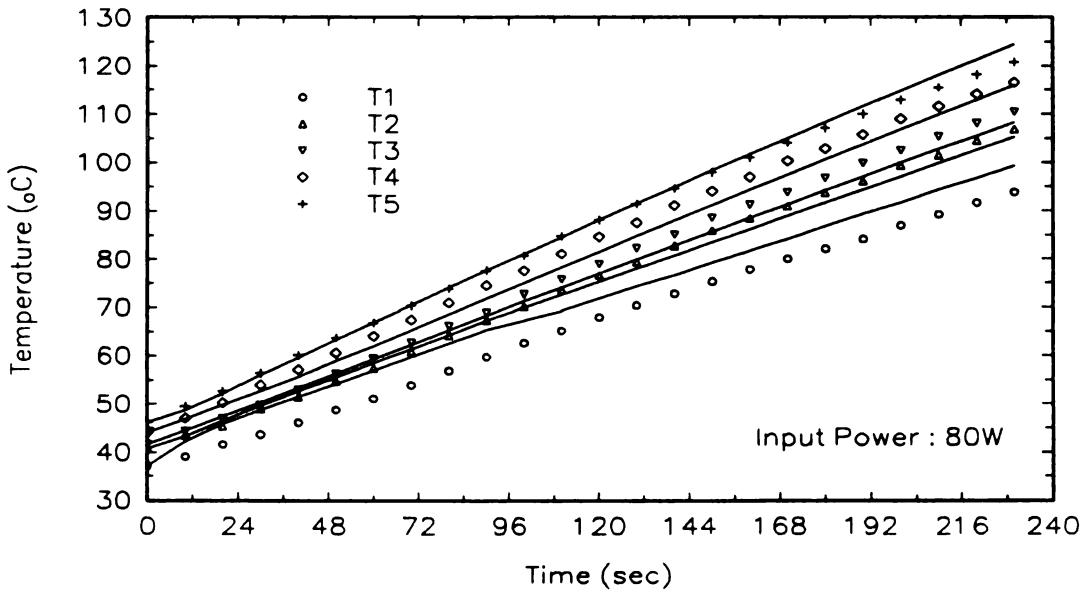

Figure 8.9 Temperature Distribution Across the Fully Cured 72-ply Unidirectional Hercules AS4/3501-6 composite during Microwave Heating at L_c=16.03 cm with 80W Input Power

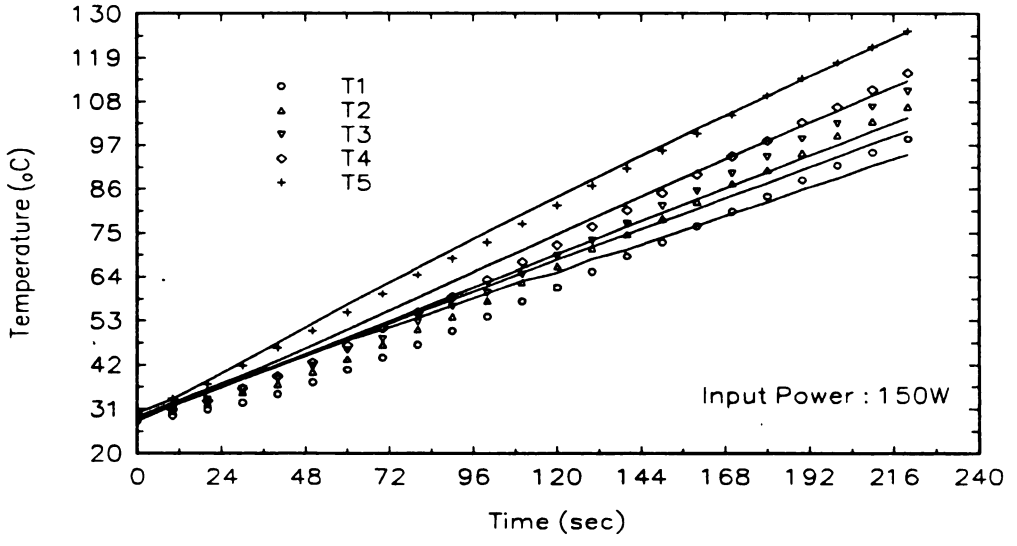

Figure 8.10 Temperature Distribution Across the Fully Cured 72-ply Unidirectional Hercules AS4/3501-6 Composite during Microwave Heating at L_c=16.03 cm with 150W Input Power

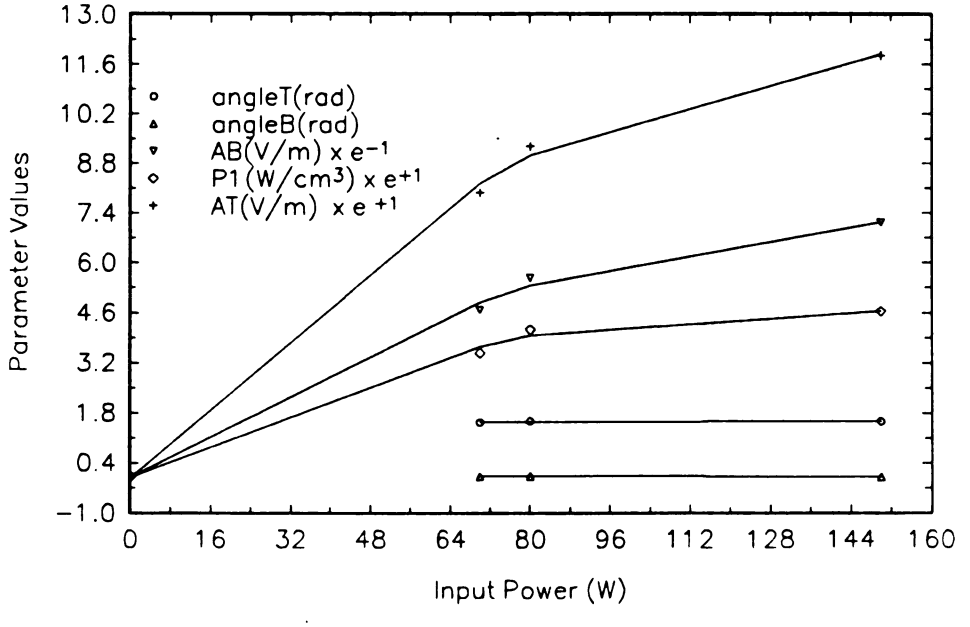

Figure 8.11 Input Power Effect on the Parameters in Microwave Power Absorption Model during Microwave Heating of Composite at Resonant Mode with L_c=16.03 cm

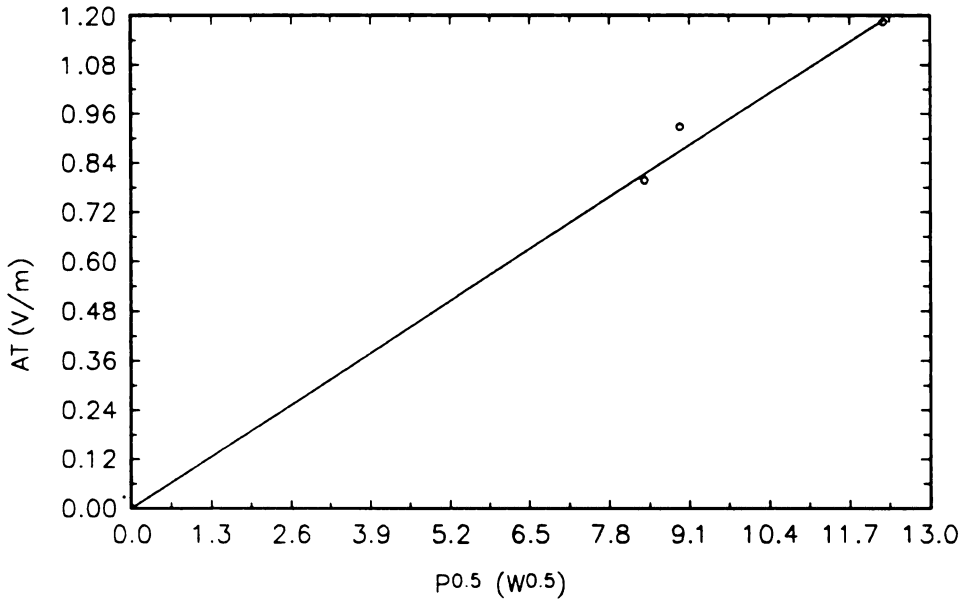

Figure 8.12 Linear Relationship Between A_T and $P^{½}$ During Microwave Heating of AS4/3501-6 Composite at Resonant Mode with L_c=16.03 cm

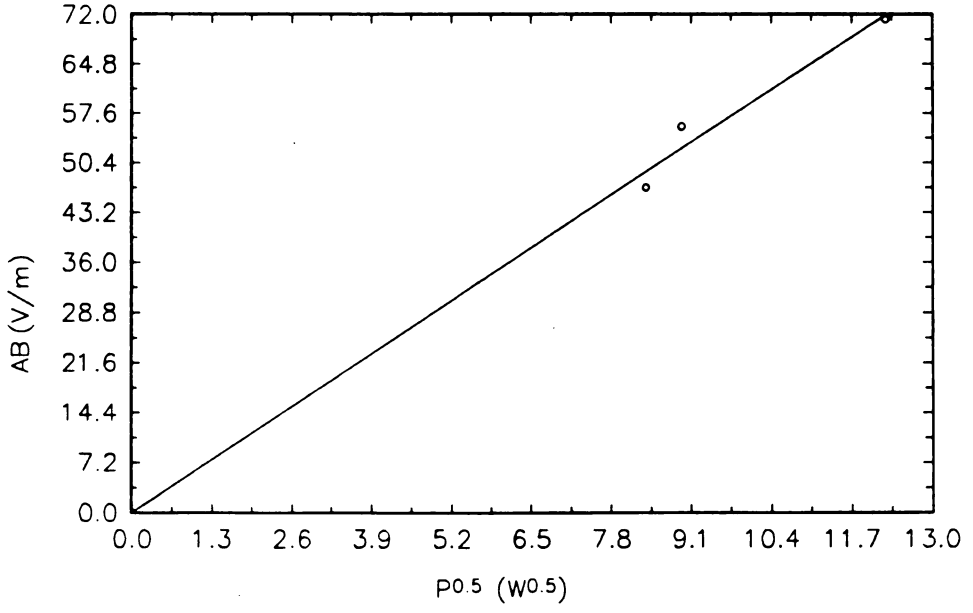

Figure 8.13 Linear Relationship Between A_B and $P^{½}$ During Microwave Heating of AS4/3501-6 Composite at Resonant Mode with L_c=16.03 cm

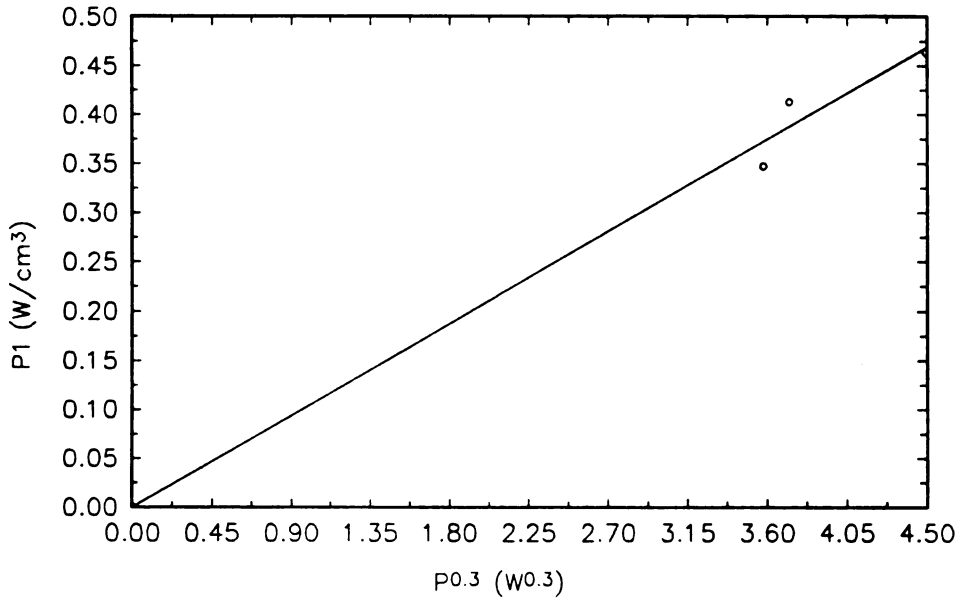

Figure 8.14 Linear Relationship Between P_1 and $P^{0.3}$ During Microwave Heating of AS4/3501-6 Composite at Resonant Mode with L_c=16.03 cm

8.6 Conclusion

A one-dimensional five-parameter microwave power absorption model was developed for microwave power dissipation inside the composite. A FORTRAN code combining the energy balance equation, the microwave power absorption model, and the least squares optimization was developed to generate the five parameters based on the temperature/time/position profiles obtained during microwave heating of a fully cured composite. A set of five parameters was generated for microwave heating of 72-ply unidirectional AS4/3501-6 composite at a resonant mode at L_c=16.03 cm. Among the five parameters, P_1 increases linearly with input power to the power of 0.3, A_T and A_B increase linearly with the square root of the input power, and θ_T and θ_B are not functions of the input power. With the relationship of the five parameters as functions of input power for the given mode, the temperature profiles during microwave cure can be readily simulated.

CHAPTER 9
PROCESSING MODEL FOR MICROWAVE AND THERMAL PROCESSING OF COMPOSITES

9.1 Introduction

In the previous chapters, the microwave and thermal cure of epoxy resins and composites was studied. Various processing techniques were investigated, and a microwave power absorption model was developed. This chapter will focus on the prediction and control of the temperature profile and extent of cure during microwave and thermal processing of Hercules AS4/3501-6 composites.

Optimum material properties and reliable processing parameters are often required for the processing of high performance thermoset composites. These are usually obtained through extensive testing of various processing conditions experimentally. However, the result for one geometry is not applicable to others. Therefore, this procedure of locating the optimum processing conditions is very costly. A fast and cost-effective way to find the optimum processing condition for various processing requirement is through simulation of processing using a processing model[132]. The model should include the chemical, physical, and mechanical behavior of the composite during processing. The chemical behavior and the temperature/time/position profiles during both microwave and thermal processing were discussed in previous chapters. A processing model that consists of coupled kinetic and energy submodels is developed in this chapter. The kinetic submodel describes the reaction rates and predicts the processing time. The energy submodel consists of the power absorbed from microwave radiation and the exotherm released from reaction. A computer code was written to simulate the processing under various conditions. The code can be used to predict the various properties of the composite on-line during microwave and thermal processing. It can be also used to

design an optimum processing condition based on the required properties of the final products.

9.2 Background

The review of kinetics can be found in Chapter 3. A general review on rheology is provided here. Rheology deals with viscosity and resin flow in the composite during cure. Unlike thermoplastics, the viscosity of thermoset is not only a function of temperature and flow geometry but also a function of the extent of cure. The effect of increasing temperature is complicated. On one hand, increasing temperature will lower the viscosity. On the other hand, increasing temperature will increase the reaction rate, and thus the extent of cure, and increase the viscosity. Resin flow is influenced by fiber compaction, flow velocity, actual resin pressure, and void formation. Because the "apparent" rheological data generated on the fiber-reinforced prepreg material closely resembles data generated on the neat resin as shown experimentally[133], the viscosity data for pure resins are usually used for processing modeling of composites.

9.2.1 Viscosity

There are two types of model for the prediction of the viscosity of epoxy resin during processing, WLF form and Arrhenius forms. Based on the free volume argument, the WLF equation was derived[134]

$$\log\left(\frac{\eta(T)}{\eta(T_s)}\right) = -\frac{c1(T-T_s)}{c2+T-T_s} \tag{9-1}$$

where c1=26.8, c2=13.4, T_s and $\eta(T_s)$ are functions of temperature and time. To fit the chemoviscosity data of epoxy system, a modified WLF equation was proposed by Tajima et. al. [135]

The modified WLF equation was used to fit the experimental data of non-isothermal cure of Hercules 3501-6[136]. The fitted parameters are c1=29.667, c2=36.926,

$$\ln\left(\frac{\eta(T)}{\eta(T_g)}\right) = -\frac{c1(T-T_g)}{c2+T-T_g} \tag{9-2}$$

$Tg=283.42 + 196.5\,\alpha - 925.4\,\alpha^2 + 3435\,\alpha^3 - 4715\,\alpha^4 + 2197\,\alpha^5$, and

$\ln(\eta(Tg))=20.72+8.56\alpha-9.69\alpha^2 + 41.17\alpha^3$.

A theoretical dependence of the viscosity η on molecular weight and temperature has been proposed for epoxy-amine systems using WLF-type of expressions[137].

$$\frac{\eta(t,\alpha)}{\eta(T_o)} = g\left[\frac{M_\alpha(\alpha)}{M_{\alpha o}}\right]^{3.4} \frac{\exp\left[\frac{c1(T_r-T_{go})}{c2+T_r-T_{go}}\right]}{\exp\left[\frac{c1(T_r-T_{go}(\alpha))}{c2+T_r-T_g(\alpha)}\right]} \tag{9-3}$$

Where η is the viscosity, M_α is the weight average molecular weight of the polymer, g is the ratio between the radii of gyration of a branched chain and a linear chain of the same molecular weight, T_r is the reference temperature, T_{go} is the glass transition temperature of the unreacted system, T_g is the glass transition temperature, α is the extent of cure, and c1, c2 are constants. This model requires knowledge of the composition and structure of the epoxy and the amine molecules and a knowledge of the reaction mechanism. The validity of this equation has been verified for TGDDM/DDS epoxy system at temperatures of low reactivity.

Another type of model is in Arrhenius form which is based on the assumption that flow is an activated process. The general form is [138,139]

$$\eta(T) = AT^n\exp(\Delta E/RT) \tag{9-4}$$

where A and n are constants, and ΔE is the activation energy. For thermoset polymers, an exponential function was proposed as the chemoviscosity equation

$$\eta(T,t) = \eta_o\exp(kt) \tag{9-5}$$

where η_o and k obey the Arrhenius relation. For non-isothermal cure, the above equation was expressed as [140]

$$\ln\eta(T,t) = \ln\eta_\infty + \Delta E_\eta/RT + \int_o^t k_\infty \exp(\Delta E_\eta/RT)dt \quad (9\text{-}6)$$

However, this type of model carries no information about the chemical conversion-time relationship. Higher orders of t and the introduction of an entanglement factor into k have been used for better fit to the experimental data[141]. The viscosity of Hercules 3501-6 resin under isothermal cure was modeled using equation [140]

$$\eta = \eta_\infty \exp(U/RT + K\alpha) \quad (9\text{-}7)$$

where η_∞ is a constant, U is the activation energy for viscosity, and K is a constant independent of temperature. This equation is only valid before gelation, that is $\alpha < 0.3$. For this specific system, K=14.1, U=9.08 x 10^4 J/mol, and η_∞= 7.93 x 10^{-14} Pa s.

The viscosity η was also assumed to be a function of the initial viscosity η_o of unreacted monomer and a term involving the reaction dependence of the bulk viscosity[142].

$$\eta = \eta_o * \textit{reaction term} \quad (9\text{-}8)$$

The initial viscosity can be expressed as either a WLF or Arrhenius-type equation. The reaction term of the viscosity is dependent upon the extent of cure. For 1st order kinetics under isothermal curing

$$\ln(\eta) = \ln(\eta_x) + E_\eta/RT + \phi k_x \exp(-E_k/RT)t \quad (9\text{-}9)$$

where η_x is initial viscosity at infinite temperature, E_η is the activation energy, R is the ideal gas constant, T is the absolute temperature, Φ is entanglement factor, k_x is the kinetic pre-exponential factor, E_k is the kinetic activation energy, and t is time. For nth-order kinetics under isothermal curing

$$\ln(\eta) = \ln(\eta_x) + E_\eta/RT + \frac{\phi}{n-1}\ln[1+(n-1)k_x \exp(-E_k/RT)t] \quad (9\text{-}10)$$

The dielectric properties of thermoset and thermoset composites have been used to monitor the viscosity. Based on Stoke's law and an assumption that the molecules are spherical, the viscosity of the resin η is found to be proportional to the

inverse of the ionic conductivity σ[143]. For resin systems with $R >> 1$, $1 < \epsilon' < 25$, and $12 << \epsilon'' << R$, the ionic conductivity can be expressed as[144]

$$\sigma = \omega \epsilon_o \epsilon'' = 2\pi f \epsilon_o \epsilon'' \tag{9-11}$$

Where ω is the angular frequency, f is the frequency in Hz, ϵ_o is the permittivity of free space, ϵ'' is the relative loss factor, ϵ' is the relative permittivity, and R is a constant which depends on the geometry of the sensor and the material[145]. Several experimental results have been reported on the comparison of viscosity and the inverse of the ionic conductivity for TGMDA/DDS based epoxy and prepreg. Approximate agreement was found for Fibredux HT/6376 carbon fiber/epoxy prepreg from CIBA-GEIGY[145] and good agreement was reported for Hercules 3501-6 epoxy[146]. However, differences between viscosity prediction and inverse ionic conductivity measurements were reported on Hercules AS/3501-6 prepreg[147].

9.2.2 Resin Flow

There are two main approaches to predict resin flow behaviors in the composite. One approach describes the resin flow in the composite in terms of Darcy's Law[148,149,150]. This approach requires knowledge of fiber network permeability, porosity, and resin viscosity, and predicts the consolidation of the plies across the thickness starting from the bleeder surface. The second approach uses a lubrication theory approximation to calculate the components of "squeezing flow" created by compaction of plies[151]. The second approach assumes a plane of symmetry at the horizontal midplane of the laminate and no fiber-to-fiber interaction which means the fibers do not touch each other and do not carry any load during compaction.

Two flow models exist in the first approach. One was proposed by Springer[148] assuming that the fiber bed carries no load, and that there is a compaction wavefront

travelling through the laminate which starts from the bleeder interface and eventually reaches the other end of laminate. This model predicts the resin flow as sequential, the layer closest to the bleeder becomes totally compacted, then the next layer, and so on. This model is over simplified and does not agree with experimental data[152]. Using Chlorine and Bromine as a tag to follow resin mixing, Pourstartip et al. observed considerable local resin mixing such that the excess resin of the tagged ply can go as far as 8 plies in the flow direction during processing. The second model was developed by Dave et al.[149] and Gutowski et al. [150] independently with identical models. This model assumes that the fiber bed is fully saturated with resin and allows for three-dimensional resin flow and one-dimensional consolidation of the composite. The fiber bed is considered to behave like a spring. This model can predict local resin mixing and agrees with the experimental data. A unified resin flow model in terms of Darcy's Law has been proposed which can be readily applied for most processing, including bleeder ply molding or autoclave processing, pultrusion, and resin transfer molding[153].

Assuming no resin flow in the horizontal direction and resin flow out of composite as flow through porous media, Springer[154] proposed an expression for the quasi-steady, seeping flow using Darcy's law. According to this model, the resin flow rate out of the composite is

$$\frac{d(hA)}{dt} = \frac{-1}{n + \frac{S_c}{S_b}\frac{h_b}{h_1}}\left(\frac{S_c F}{\mu h_1}\right) \qquad (9\text{-}12)$$

where h is the height of the liquid surface at time t, A is the cross sectional area of the composite perpendicular to the direction of the flow, S_c and S_b are the permeability of the composite and bleeder, h_b and h_1 are thickness of resin in the bleeder and compacted prepreg layer, μ is the resin viscosity, F is the applied force, and n is the number of compacted layers. The change in the composite thickness during processing is[154]

$$\frac{\Delta h}{h_o} = \frac{t^*}{n + \frac{S_c}{S_b}\frac{h_b}{h_1}} \qquad (9\text{-}13)$$

$$t^* \equiv \frac{S_c F}{\mu h_1 h_o A} t$$

where h_o is the initial thickness of the composite and t^* is dimensionless time. This model was tested by placing porous plates and rod layers in the oil having constant viscosities of 16000 cps and 1257600 cps and a good agreement was found.

Based on the second approach, the resin flow was modeled as a one-dimensional confined compression (no boundary motion in x, y directions) and a three-dimensional seepage flow in a porous medium[155]. The governing equation is

$$-m_v \frac{\partial(\sigma - p)}{\partial t} = [\frac{\partial}{\partial x}(\frac{k_x}{\eta}\frac{\partial p}{\partial x}) + \frac{\partial}{\partial y}(\frac{k_y}{\eta}\frac{\partial p}{\partial y}) + \frac{\partial}{\partial z}(\frac{k_z}{\eta}\frac{\partial p}{\partial z})] \qquad (9\text{-}14)$$

where k_x, k_y, k_z are stress dependant specific permeabilities in the x, y, and z directions, η is the resin viscosity, σ and p are the applied pressure and the hydraulic resin pressure, and m_v is the coefficient of volume change (the absolute change in porosity ϵ per unit increase in the axial (normal) stress).

The porosity here refers to the non-fiber portion of the medium. The coefficient of volume change, m_v, is equal to $a_v/(1+e_i)$, where e_i is the initial void ratio and a_v is the coefficient of compressibility, $a_v = -de/dp$. The porosity can be calculated from the void ratio, $\epsilon = e/(1+e)$. The simplest case of resin flow is one dimensional consolidation under a constant load with one dimensional seepage flow in the vertical direction. Once p is known, the resin velocity at any point and time in any direction can be evaluated using Darcy's law.

$$u_i(x,y,z,t) = -\frac{k_i}{\eta}\frac{\partial p(x,y,z,t)}{\partial i}$$

where i=x,y,z. The motion of the moving boundary layer in the thickness direction of the laminate has to be accounted for by changing the computational grid size after each time step during the consolidation process. This model can be simplified to Springer's model by assuming: 1) no flow in the y direction (perpendicular to both fiber and thickness directions), 2) spring-like fiber-to-fiber interaction is negligible, i.e. σ=p, 3) flow in the horizontal and vertical directions can be decoupled.

Three partial differential equations were proposed to model vertical and horizontal flows[156]. Assuming vertical resin flow to be a filtration compaction process through prepreg and bleeder, the Kozeny-Carman equation is used to describe the flow. Both vertical and horizontal resin flow in the bleeder is governed by the Kozeny-Carman equation.

$$-\frac{dP}{dL}=\frac{K\eta(1-\epsilon)^2 u_{bs}}{D^2 g_c \epsilon^3} \qquad (9\text{-}15)$$

where P is the pressure, L is the bed length, η is the viscosity, ϵ is the void fraction, u_{bs} is the superficial velocity, D is the mean effective fiber diameter, g_c is the gravitational constant, and K is the bed characterization constant.

For horizontal flow within fiber layers, a flow field equation is used to describe the velocity profile as a function of fiber spacing and diameter. Assuming fibers are uniformly distributed in a triangular pitch, the flow field equation becomes

$$\frac{\partial^2 u}{\partial y^2}+\frac{\partial^2 u}{\partial z^2}=-\frac{2g_c}{\eta}\frac{dP}{dx} \qquad (9\text{-}16)$$

where u is velocity and x is the length.

The horizontal flow between fiber layers is modeled as flow between parallel plates.

$$-\frac{dP}{dx}=\frac{12\eta u_{bs}}{g_c z_o^2} \tag{9-17}$$

Where z_o is distance between parallel plates.

The solution of these three partial differential equations can be calculated using the finite difference method.

$$-\Delta P = RU \tag{9-18}$$

Where ΔP is the pressure difference between two nodes, R is the flow resistance, and U is the mass/area flow velocity. The flow resistance R varies with the type of flow. For vertical flow,

$$R_v=\frac{K\eta(1-\epsilon)^2\Delta L}{D^2 g_c \epsilon^3 \rho}$$

Where ρ is the resin density. For horizontal flow within fiber layers,

$$R_H=K\frac{\eta\Delta x}{2g_c\rho}$$

Where K is the flow coefficient, $K=f(\epsilon)$. For horizontal flow between layers,

$$R_{HB}=\frac{12\eta\Delta x}{g_c z_o^2 \rho}$$

9.2.3 Voids

Void formation is a complicated problem. It is affected by factors such as prepreg variations, environmental history, layup variation, and cure cycles. It would be ideal to model the void formation, growth, transport during cure as well as the

relationship between applied pressure, resin hydrostatic pressure, and void formation. There are two possible sources for void formation, the moisture dissolved in the resin during prepregging and layup and the entrapped pockets of air. In order to prevent the potential for water void growth by diffusion, the resin pressure at any point within the curing laminate must satisfy the following inequality,[156]

$$P_{min} \geq 4.962 \times 10^3 \exp(\frac{4892}{T})(RH)_o \qquad (9\text{-}19)$$

Where P_{min} is the minimum resin pressure required to prevent water-vapor void growth by diffusion. $(RH)_o$ is the relative humidity (in %) exposure to which the prepreg is equilibrated prior to processing. A value of 60% is suggested.

Voids will become mobile when the viscous flow forces are large enough to overcome the surface tension forces. By considering the void transportation in a laminate as oil ganglia mobilization by water-flooding, a void mobilization criteria was suggested [156]

$$|\frac{dp}{dl}| > |\frac{dp}{dl}|_c = \frac{4\gamma_{LV}\cos\theta}{d_c L_v} \qquad (9\text{-}20)$$

Where dp/dl is the resin pressure gradient in the direction of flow, γ_{LV} is the resin-void surface tension, θ is the apparent contact angle, d_c is the diameter of the narrowest constriction perpendicular to the flow, and L_v is the void length projected in the flow direction. Contact angles between epoxy resins and graphite fibers, with and without surface oxiding treatment, are roughly 14° and 23°, respectively[157]. The effect of cure pressure on void content was examined. Two characteristics of voids during processing are similar size across the laminate and no migration through the resin[148].

The void formation will directly affect the compaction of the composite. For graphite fiber/epoxy laminate, experiments showed that the total compaction of the thin laminate was independent of cure temperature and pressure. However, the rate of compaction was dependent upon the cure temperature and pressure[158]. For

laminate consisting of 16 plies, the total relative compaction (the ratio of measured compaction and uncompacted laminate thickness) is about 22%. This is because the resin gels after the completion of compaction. For thick-section laminate, it may not be the case.

9.2.4 Composite Properties

Glass transition temperature is an important parameter for composite applications. To obtain the highest possible T_g, it is necessary to cure the composite as complete as possible. However, to obtain the highest possible flexural and tensile strength and the best resistance to compressive creep and water absorption, the cure has to be stopped after an optimum conversion is reached[159]. For thermal cure of several epoxy/amine systems, this conversion is located in the postgel stage at 0.10 to 0.15 higher than α_{gel} [160].

For Hercules 3501-6 resin, a tetraglycidyl 4,4′-diaminodiphenylmethane (TGDDM) with 33 phr curing agent 4,4′-diaminodiphenyl sulfone(DDS) epoxy resin, the DiBenedetto equation has been used to fit the T_g (°K) versus α data[161].

$$\frac{1}{T_g} = \frac{1-\alpha}{258} + \frac{\alpha}{505}$$

where α is the extent of cure. The maximum extent of cure at cure temperature 177°C was 0.873.

The residual stress, either due to thermal gradient or volume shrinkage during the cure, will reduce the mechanical properties of the composite. Although the volume of epoxy resin decreases during curing, the contractive stresses in the composite are only due to the volume contraction after gelation[162]. Tensile stresses were found to be present in the interior and compressive stresses near the surface in isothermal cured epoxy polymer. Higher stress magnitudes were obtained when higher curing temperatures were used[163].

The thermal conductivity of the composite may be calculated combining the thermal conductivities of the matrix, k_m, and the fiber, k_f. The thermal conductivity of AS4/EPON828/mPDA composite with 70% fiber weight percentage was measured experimentally. The measured values are 0.73 (W/m/K) and 4.18+0.032*T (W/m/K) for directions perpendicular to and along the fiber orientation of unidirectional composite, respectively[164].

9.3 Microwave and Thermal Processing Model

The microwave and thermal processing of composites is described as follow. Lamina are exposed to a thermal and/or microwave environment as shown in Figure 9.1. The edges of the lamina are surrounded by an adhesive cork dam during the processing to prevent resin flow out from the sides. The top is exposed to the environment directly and the bottom is covered by the bleeder and the support plate, either a steel plate in the case of thermal processing or a Teflon plate in the case of microwave processing. The heat flow at the interface only includes heat transferred by thermal conduction and convection. Heat flow caused by thermal radiation is neglected because the temperature of the system is much lower than 400°C. In this study, a one dimensional model was developed for the prediction of distributions of the extent of cure (α) and temperature (T) across the thickness of the composite as function of time (t).

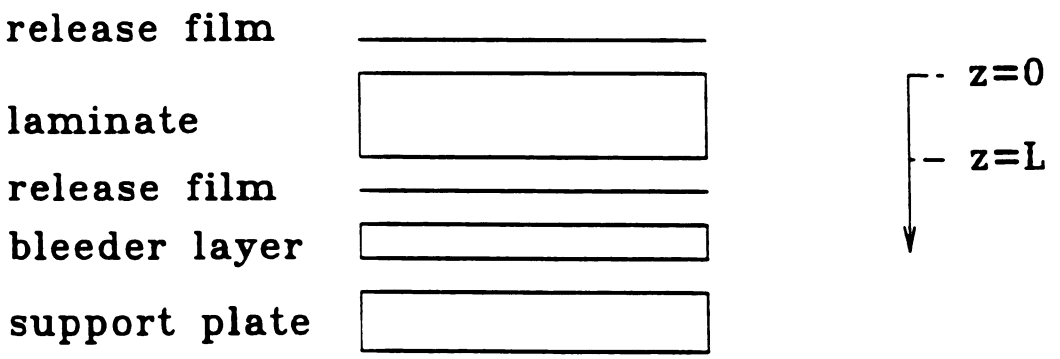

Figure 9.1. Composite Configuration for Processing Simulation

From an energy balance, the one-dimensional heat transfer equation was derived as

$$\rho C_p \frac{\partial T}{\partial t} = \frac{\partial}{\partial x}(K\frac{\partial T}{\partial x}) + \rho \dot{H} + P_m \tag{9-21}$$

with generalized temperature boundary conditions

$$a\frac{\partial T(s,t)}{\partial \hat{n}}_{s=0,L} + bT(s,t) + cT_a(t) = 0 \tag{9-22}$$

where ρ and C_p are the density and specific heat of the composite, K is the thermal conductivity of composite in the thickness direction, $\dot{H}$ is the rate of heat generation per unit weight by the chemical reaction, and P_m is the rate of heat generation per unit volume by the absorbed microwave energy. The power absorption P_m can be calculated using models from Chapter 8. In this study, the model simulation is focused on the microwave and thermal processing of unidirectional AS4/3501-6 composite. For cured Hercules AS4/3501-6 composite, $K=4.457\times10^{-3}$ (W/cm/°K), $C_p=0.942$ (J/g/°K), and $\rho=1.52$ (g/cm^3) [165]. The microwave power absorption model for unidirectional composite was described by Equations (8-63), (8-64), (8-66),

(8-68), and (8-69). For boundary conditions, $T_a(t)$ and T(s,t) are the environment and the composite surface temperatures, respectively. $\hat{n}$ is the outward unit vector normal to the top or bottom surfaces. The coefficients a,b, and c control the type of the boundary conditions. For the Dirichlet(prescribed) boundary condition, their values are a=0, b=-c=1. For the Neumann(insulated) boundary condition, their values are a=1, b=c=0. For the Robin(convective) boundary condition, a=1 and $b=-c=(h/k)_{eff}$, where $(h/k)_{eff}$ is the effective heat transfer coefficient. When the effective heat transfer coefficient is very large, the Robin boundary condition becomes the Dirichlet boundary condition. For autoclave processing, the effective heat transfer coefficient was due to forced convection and was usually very large. In general, the Robin boundary condition was used for the top surface and Neumann boundary condition was used for the bottom surface. The effective heat transfer coefficient for microwave processing was essentially due to free convection and needed to be measured experimentally. Therefore, the boundary conditions for the energy balance equation are

$$\frac{\partial T(z,t)}{\partial z}\Big|_{z=0} = -\left(\frac{h}{K}\right)_{eff}(T_a(t) - T(0,t))$$
$$\frac{\partial T(z,t)}{\partial z}\Big|_{z=L} = \left(\frac{h}{K}\right)_{eff}(T_a(t) - T(L,t)) \qquad (9\text{-}23)$$

The initial condition for Equation (9-21) is

$$T(z,0) = T_i(z) \qquad (9\text{-}24)$$

To solve for T(z,t) in an AS4/3501-6 composite during processing, the reaction kinetics for Hercules 3501-6 resin, the effective heat transfer coefficient of top surface, and the five parameters for microwave power absorption P_m are required. To simulate the temperature profile and extent of cure profiles across the thickness of composite as function of time, implicit method of Lee's[166] was used to code the non-linear parabolic equation, Equation (9-21). The use of Lee's algorithm gives a truncation error similar to that of the Crank-Nicolson method but leads to a higher

computational rate. The algorithm for Lee's method is based on the central-difference approximation. The finite-difference expressions for the partial derivatives are

$$\frac{\partial T}{\partial t} = \frac{T_{i,j+1} - T_{i,j-1}}{2\delta t} \tag{9-25}$$

$$\frac{\partial}{\partial z}\left(K\frac{\partial T}{\partial z}\right) = \frac{K(T_{i+\frac{1}{2},j})(T_{i+1,j} - T_{i,j}) - K(T_{i-\frac{1}{2},j})(T_{i,j} - T_{i-1,j})}{\delta z^2} \tag{9-26}$$

where $T_{i\pm\frac{1}{2},j}=(T_{i,j}+T_{i\pm1,j})/2$, $T_{i,j}=(T_{i,j-1}+T_{i,j}+T_{i,j+1})/3$, i represents nodes in space, j represents nodes in time, i,j=1,2,3,... The Crank-Nicolson method[167] was used to generate the first set of temperatures, $T_{i,1}$, i=0,1,2,...

9.3.1 Reaction Kinetics

Hercules 3501-6 resin is a catalyzed tetraglycidyl ether of methylenedianiline (TGMDA)/ diaminodiphenyl sulphone (DDS). The reaction kinetics for both tetraglycidyl ether of methylenedianiline (TGMDA)/ diaminodiphenyl sulphone (DDS) neat resins and TGMDA/DDS based carbon fiber reinforced prepreg have been studied[168]. The reaction kinetics of Hercules 3501-6 resin was modeled by the following reaction kinetics[119].

$$\frac{d\alpha}{dt} = \begin{cases} (k_1 + k_2\alpha)(1-\alpha)(B-\alpha) & \alpha < \alpha_{gel} \\ k_3(1-\alpha) & \alpha > \alpha_{gel} \end{cases} \tag{9-27}$$

where k_1, k_2, and k_3 are the reaction rate constants, B is the ratio of initial hardener equivalents to epoxide equivalents, and α_{gel} is the extent of cure at the gelation point. Their values are $\alpha_{gel}=0.3$, B=0.47, $k_1=2.101\times10^9 \exp(-8.07\times10^4/(RT))$, $k_2=-2.014\times10^9 \exp(-7.78\times10^4/(RT))$, and $k_3=1.960\times10^5 \exp(-5.66\times10^4/(RT))$. R is the gas constant R=8.314 (J/mol/K).

The rate of heat released by the polymerization reaction is

$$\dot{H} = \frac{d\alpha}{dt} H_R \tag{9-28}$$

where $\dot{H}$ is the rate of heat generated by polymerization reaction. H_R is the total heat of reaction that can be generated during cure. For Hercules AS4/3501-6 prepreg, $H_R = 175.2$ J/g as determined by DSC. The extent of cure during processing can be calculated by

$$\alpha = \int_0^t (\frac{d\alpha}{dt}) dt \tag{9-29}$$

The closed, multi-step, fourth-order Milne method[165] was used to code the reaction kinetic expression. The first order ordinary differential equation can be shortened to $\frac{d\alpha}{dt} = f(\alpha)$. The multistep method is chosen because it requires considerably less computation than the one-step method for results of comparable accuracy. The closed method is preferred because its local truncation error is considerably smaller than that of the open method. The Milne's algorithm is a predictor-corrector method. The predictor is

$$\alpha_{j+1} = \alpha_{j-3} + \frac{4\delta t}{3}(2f_j - f_{j-1} + 2f_{j-2}) \tag{9-30}$$

and the corrector is

$$\alpha_{j+1} = \alpha_{j-1} + \frac{\delta t}{3}(f_{j+1} + 4f_j + f_{j-1}) \tag{9-31}$$

The choice of δt must satisfy the convergence condition

$$\delta t < \left| \frac{3}{\frac{df(\alpha_{j+1})}{d\alpha}} \right| \tag{9-32}$$

The single-step Runge-Kutta method was used to generate the values of the first four points.

9.3.2 The Measurement of the Effective Heat Transfer Coefficient

The effective heat transfer coefficients for the top surface were different for microwave and thermal processing. For thermal processing, $(h/k)_{eff}$ was mainly due to forced convection and the value is very large. The top surface temperature of the composite was equal to the environment temperature during thermal processing. For microwave processing, $(h/k)_{eff}$ was mainly due to free convection and the value needed to be measured experimentally. A two-ply fully cured AS4/3501-6 composite was heated up and the temperature was measured as a function of time during cooling. The thickness of the composite was 0.058cm. Assuming all the heat lost is due to the heat loss at the surfaces, the effective heat transfer coefficient can be calculated from the temperature versus time data.

$$h_{eff} = \frac{\rho C_p V \frac{dT}{dt}}{2A(T_a - T(t))} \tag{9-33}$$

where T_a is the ambient temperature and A and V are the surface area and the volume of the composite respectively. Figure 9.2 shows the measured temperature during cooling. Assuming the temperature difference between the composite surface and the ambient temperature (T_a=23), T-T_a, decays exponentially with time:

$$T - T_a = ce^{\lambda t} \tag{9-34}$$

With this assumption, ln(T-T_a) is a linear function of time, t, with slope λ. This assumption holds very well within a certain temperature range as shown in Figure 9.3. Three straight lines were obtained, one before 60 sec, one between 60 and 110 sec, and one after 110 sec. In other words, the effective heat transfer coefficient is a step function of T-T_a. Once λ was obtained from Figure 9.3, the effective heat transfer coefficient for the straight line temperature range can be easily calculated.

$$h_{eff} = -\frac{\rho C_p V}{2A}\lambda \tag{9-35}$$

The slopes are λ=-0.0168, λ=-0.00944, and λ=-0.00150 for the lines before 60 sec, between 60 and 110 sec, and after 110 sec respectively. The experimentally determined effective heat transfer coefficients are h_{eff}=0.000698 (W/cm^2/K) if T-T_a > 43°C and h_{eff}=0.000392 (W/cm^2/K) if 27°C < T-T_a ≤ 43°C , and h_{eff}=0.0000623 (W/cm^2/K) if T-T_a ≤ 27°C.

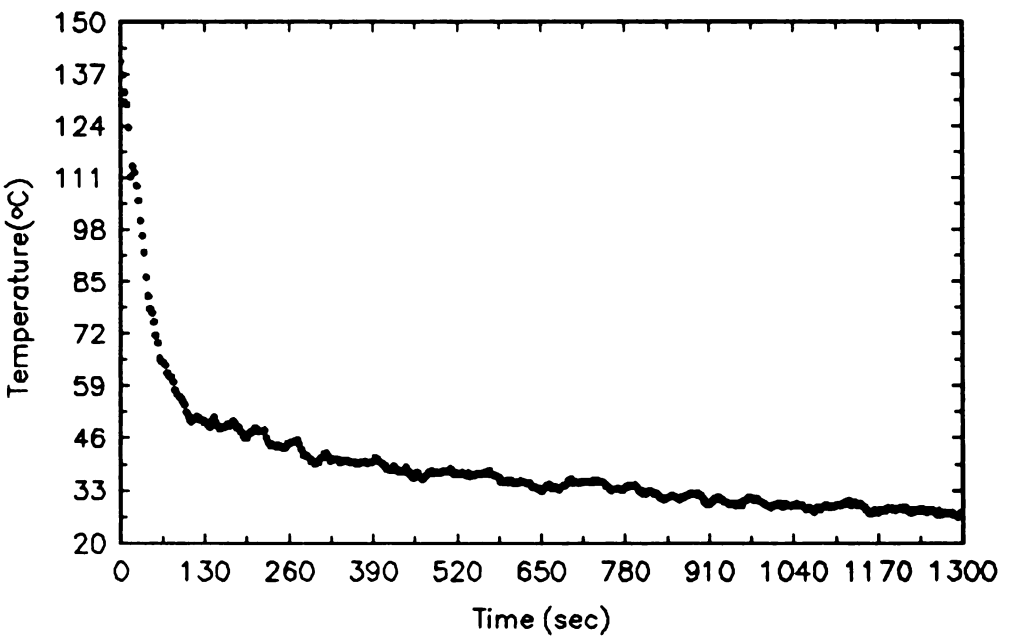

Figure 9.2 Temperature/time Profile During Cooling of 2-ply Hercules AS4/3501-6 composite

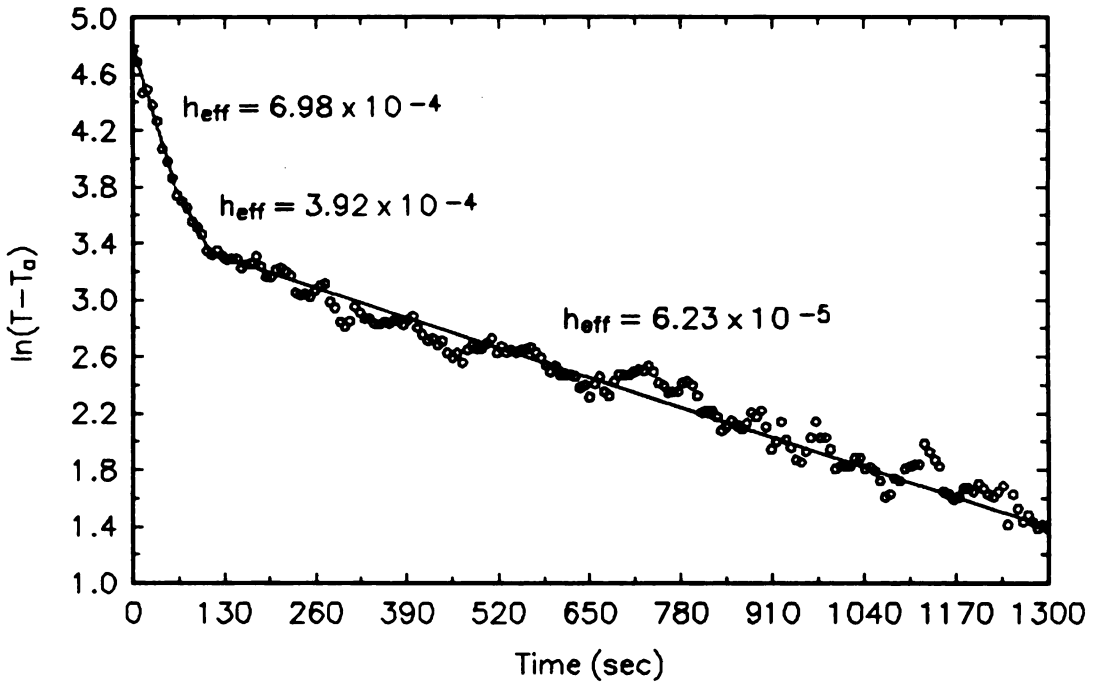

Figure 9.3 Ln(T-T_a) Versus Time Curve

9.4 Simulation

With the expression for P_m and $\dot{H}$, the temperature and extent of cure profiles inside the composites can be readily calculated. The computer simulation was carried out in two parts, thermal processing and microwave processing. The FORTRAN code for the simulation is attached in Appendix III. The composite thickness and effective heat transfer coefficient effects on the processing were studied.

9.4.1 Thermal Processing

In thermal processing, P_m equals 0. The temperature and extent of cure profiles as a function of time at the midplane and the bottom surface were simulated

during processing of 2.0 cm thick AS4/3501-6 laminate using the manufacturer suggested cure cycle. A Dirichlet and Neumann boundary conditions were used for the top and bottom surfaces respectively in this simulation. The cure cycle is a ramp from room temperature(25°C) to 116°C in 40 minutes, then hold at 116°C for 60 minutes, then ramp to 177°C in 30 minutes, then hold at 177°C for 120 minutes, and cool down to 95°C in 50 minutes. Figure 9.4 and Figure 9.5 show the temperature and extent of cure profiles respectively. In Figure 9.4, the straight line represents the cure cycle, i.e. the oven temperature. The solid and dot-dash curves are the temperatures at the bottom surface, z/L=1, and the midplane, z/L=0.5, respectively. In Figure 9.5, the solid and dot-dash curves are the extent of cure at the bottom surface, z/L=1, and the midplane, z/L=0.5, respectively.

As shown in Figure 9.4, the bottom surface temperature was higher than the midplane temperature except during the first 50 minutes. Both the midplane and the bottom surface have two temperature excursions, a small excursion during the 116°C isotherm and a large excursion at the beginning of the 177°C isotherm. Since the bottom surface temperature is only slightly higher than midplane temperature, the cure is only slightly faster at the bottom surface than the midplane as shown in Figure 9.5.

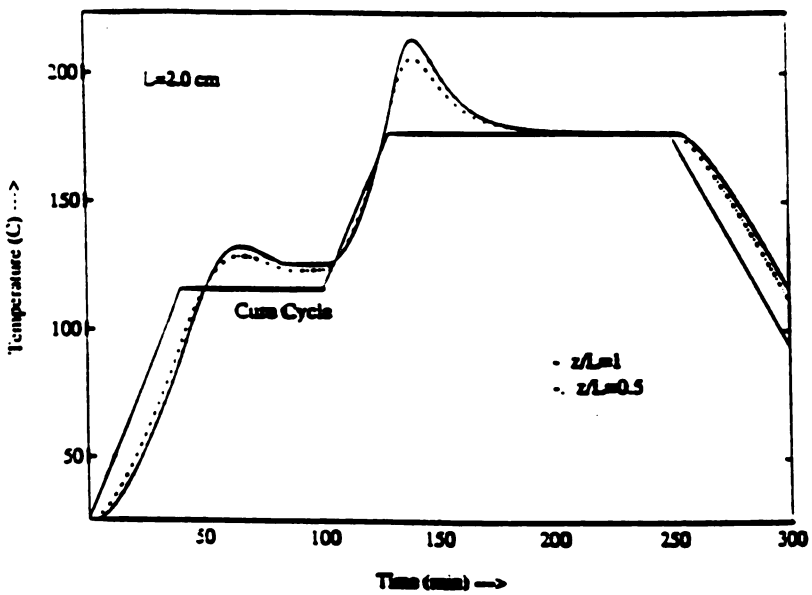

Figure 9.4 Temperature/time Profiles for Thermal Processing of AS4/3501-6 Laminate

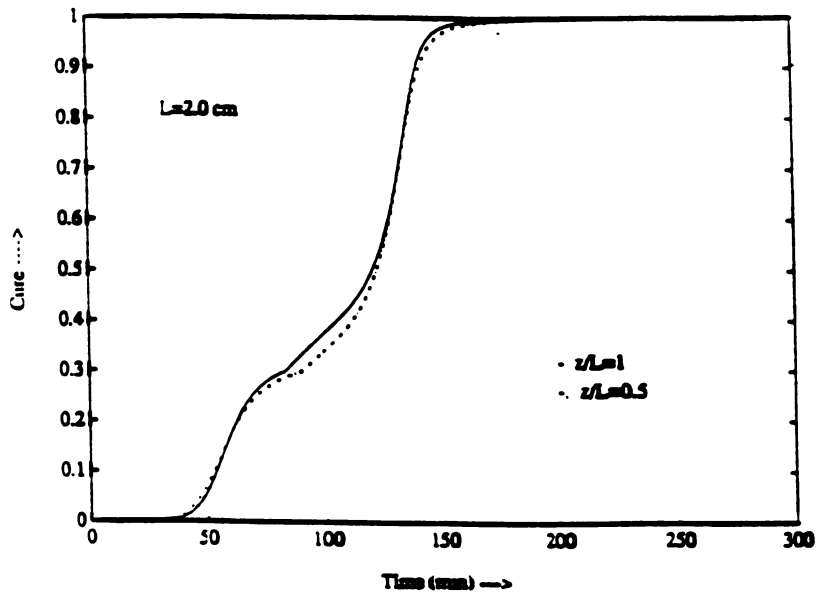

Figure 9.5 Extent of Cure Profiles for Thermal Processing of AS4/3501-6 Laminate

The effect of two parameters, the laminate thickness and the effective heat transfer coefficient at the top surface, on the temperature and extent of cure at the bottom surface were studied during thermal processing simulation. Using the same composite properties(K, C_p, ρ, and $(h/K)_{eff}$) and processing cycle, the temperature and extent of cure profiles at the bottom surface were simulated for four laminate thicknesses, 1.0, 2.0, 3.0, and 4.0 cm. Figure 9.6 and 9.7 show the temperature and the extent of cure profiles for the four different thicknesses. The numbers beside the curves represent the thickness of the laminate in centimeters used in the simulation. As shown in Figure 9.6, there are two temperature excursions during processing, a small one during the 116°C isotherm and a large one during the 177°C isotherm. The time needed for the occurrence of the first excursion is a strong function of laminate thickness and increases with the laminate thickness. For example, the time needed for first excursion to occur is 45, 60, 90, and 105 minutes for 1, 2, 3, and 4 cm thick laminates, respectively. However, the time required for occurrence of the second excursion is relatively independent of the laminate thickness within the thickness range studied. For the 1 cm thick laminate, the second excursion occurred at 140 minutes while for the other three thicknesses, the second excursion occurred at 145 minutes. As the laminate thickness increases, the occurrence of second excursion may start before completion of the first excursion. The two excursions become indistinguishable for thick laminates and the first excursion peak can be barely seen, such as in the simulation for 4 cm thick laminate. The magnitudes of both excursions increase with laminate thickness. The maximum temperature at the bottom surface reached 260°C for the 4 cm thick laminate. Since the thermal degradation temperature of Hercules AS4/3501-6 prepreg is 290°C as determined by thermogravimetric analysis (TGA), the maximum thickness of laminate that can be processed using the manufacture's cycle is 4 cm if the operation margin is set to 30°C. As shown in Figure 9.7, The laminate thickness has two effects on the extent of cure at the bottom surface, a delay of the initiation of the reaction and a shortening of the reaction time. For the 1 cm thick laminate, the reaction started at 35 minutes and ended at 200 minutes, total reaction time of 165 minutes. For the 4 cm thick

laminate, the reaction did not start until 60 minutes and ended at 140 minutes, total reaction time of only 80 minutes.

The effect of the effective heat transfer coefficient, $(h/K)_{eff}$, on the bottom surface temperature during thermal processing was studied while maintaining the other composite parameters(K, C_p, ρ, and L) constant. The laminate thickness, L, used in this simulation was 2.0 cm. Figure 9.8 shows the bottom surface temperature for $(h/K)_{eff} >> 1$, $(h/K)_{eff}=1$, $(h/K)_{eff}=0.5$, and $(h/K)_{eff}=0.1$. The simulation results show that once $(h/K)_{eff}$ is larger than 10 (cm^{-1}), the temperature profiles are very close to those for an infinite heat transfer coefficient. Comparing Figure 9.8 to Figure 9.6, the effect of $(h/K)_{eff}$ on the bottom surface temperature is similar to the effect of laminate thickness on the temperature profiles. A decrease in $(h/K)_{eff}$ has the same effect on the temperature profiles as an increase in laminate thickness. As shown in Figure 9.8, the maximum bottom temperature reached 280°C if $(h/K)_{eff}=0.1$ cm^{-1}, though the laminate thickness was only 2.0 cm. Thus, the thickest laminate that can be processed by the manufacture's cycle is 2.0 cm if the effective heat transfer coefficient is 0.1 cm^{-1}. This value is close to that of the boundary condition with free convection. Therefore, it is important to keep the effective heat transfer coefficient as high as possible during thermal processing of thick AS4/3501-6 laminate.

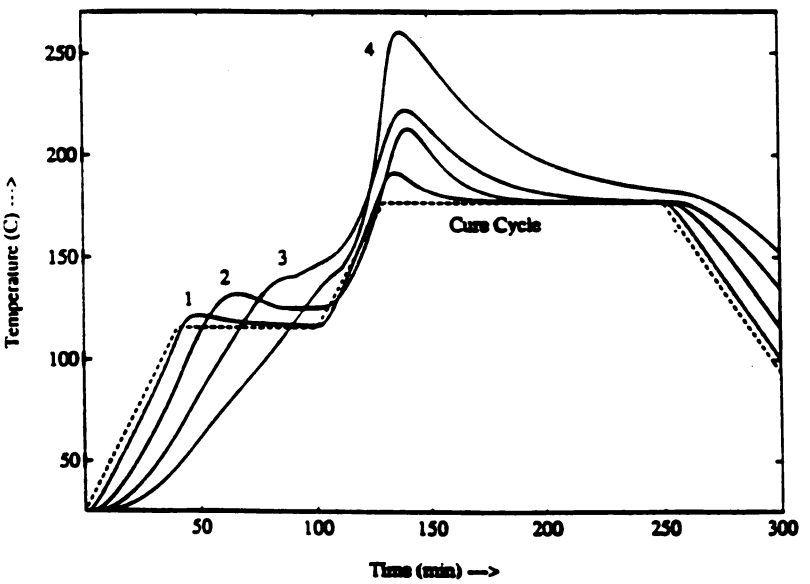

Figure 9.6 Temperature Profiles for Various Laminate Thickness

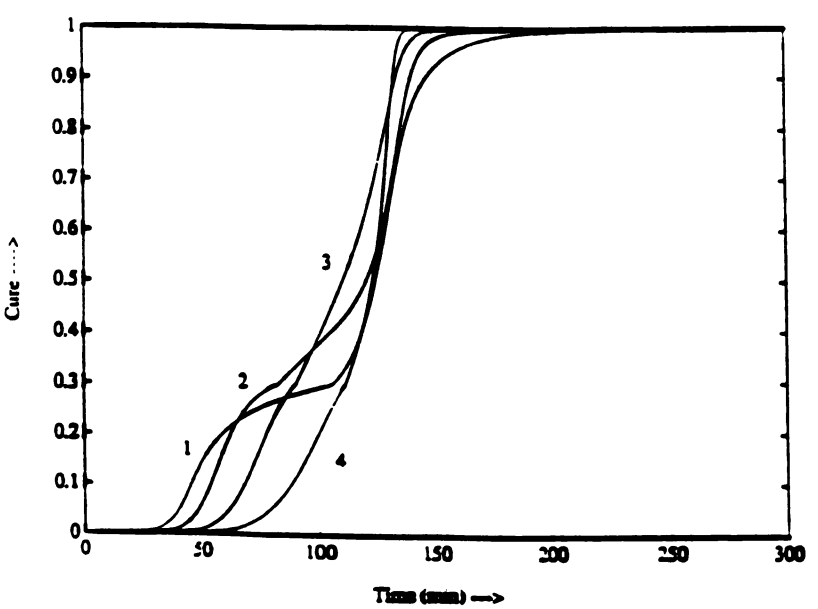

Figure 9.7 Extent of Cure Profiles for Various Laminate Thickness

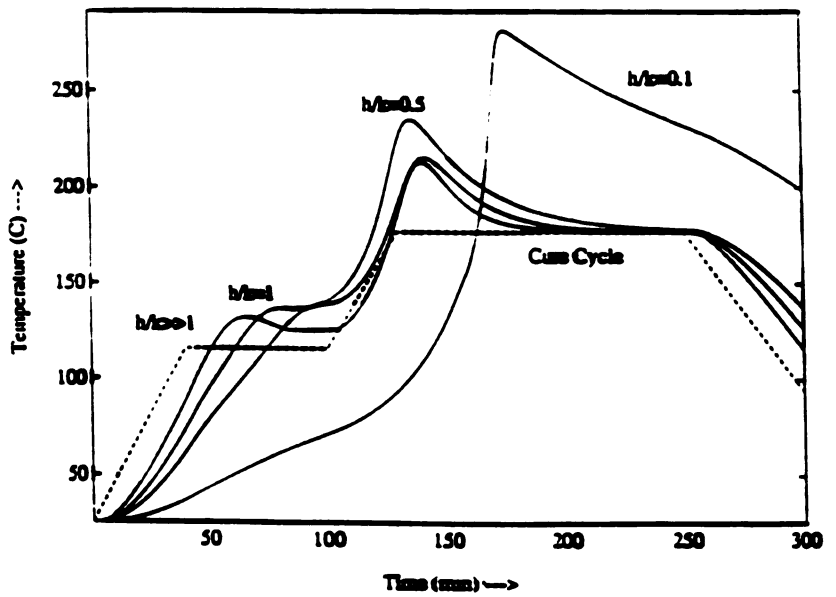

Figure 9.8 Temperature Profiles for Various Effective Heat Transfer Coefficient

9.4.2 Microwave Processing

Microwave processing of a 72-ply unidirectional AS4/3501-6 composite at a resonant mode, L_c=16.03 cm, and 70 W input power was simulated using the parameters generated in the Chapter 8. The five parameters for the microwave power absorption model in the given resonant mode and 70W input power are 0.347 W/m^3, 0.797 V/m, 46.79 V/m, 1.54 rad., and 0.0201 rad. for P_1, A_T, A_B, θ_T, and θ_B respectively. A free convection and insulated heat transfer boundary conditions are used at the top and bottom surfaces respectively. The measured effective heat transfer coefficients for free convection are $(h/K)_{eff}$=0.014 [1/cm] if T-$T_a \leq$ 27°C, $(h/K)_{eff}$=0.088 [1/cm] if 43°C $\geq$ T-T_a > 27°C, and $(h/K)_{eff}$=0.157 [1/cm] if T-T_a $\geq$ 43°C. The control temperature was set to 177°C during the simulation. Figure 9.9 and 9.10 show the simulated temperature and the extent of cure profiles at the top surface, midplane, and bottom surface during microwave processing.

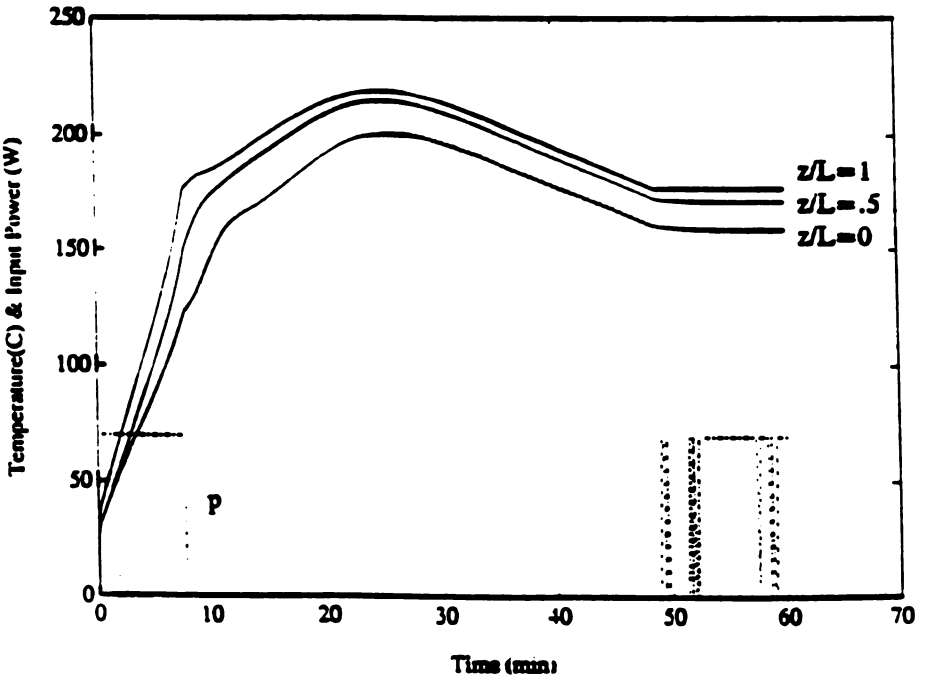

Figure 9.9 Temperature/time Profiles during Microwave Processing of 72-ply Unidirectional AS4/3501-6 Composite at L_c=16.03 cm and 70 W

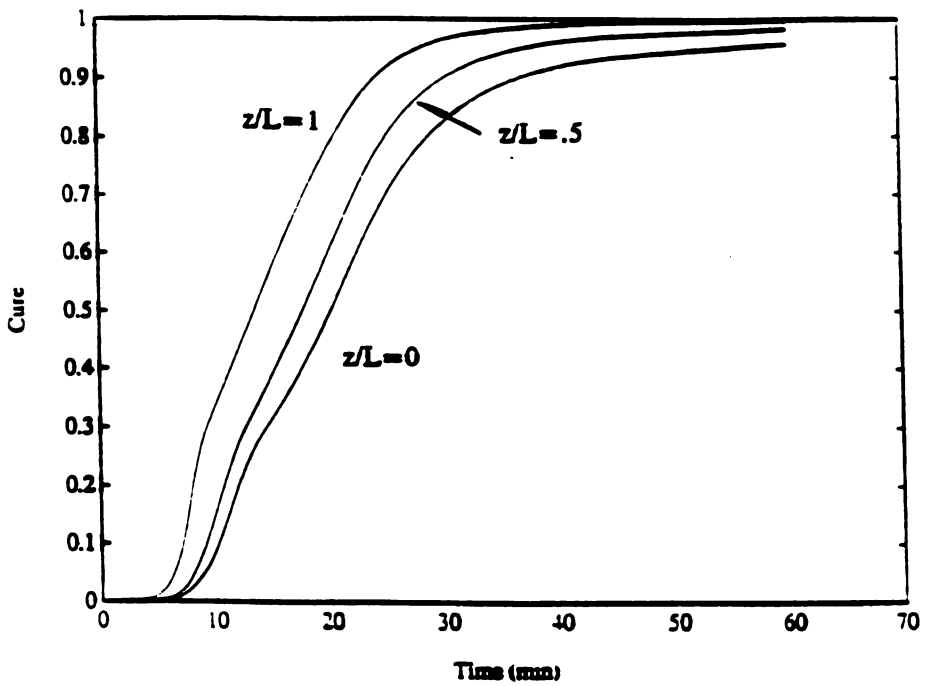

Figure 9.10 Extent of Cure Profiles during Microwave Processing of 72-ply Unidirectional AS4/3501-6 Composite at L_c=16.03 cm and 70 W

In Figure 9.9, the z/L=0, 0.5, and 1 curves represent the temperature profile at the bottom, midplane, and top surfaces of the composite, respectively. The dash line is the power input curve. The laminate can be heated directly to the desired temperature in 8 minutes at an input power of 70W. Though the power is turned off as the temperature reached 177°C, there still have small temperature excursion during the processing. This temperature excursion is due to the reaction exotherm and the small heat transfer coefficient at the composite surface and can be eliminated by increasing the heat transfer coefficients. As shown in Figure 9.10, the extent of cure reached 0.3 when the temperature reached 177°C at the bottom surface. The exotherm from the reaction was sufficient in maintaining the temperature once the reaction started until the composite was almost fully cured at the simulation condition.

Since the temperature excursion can be eliminated, the processing temperature can be raised to 250°C without any risk of composite degradation. Figure 9.11 shows the temperature profiles during microwave processing of the 72-ply AS4/3501-6 composite at the resonant mode L_c=16.03 cm and 500 W.

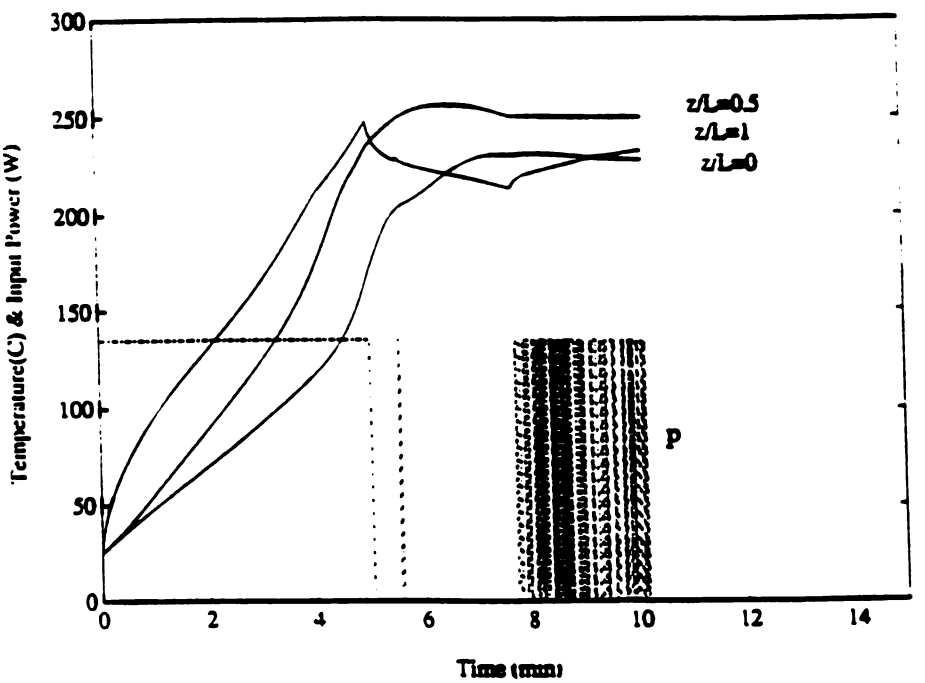

Figure 9.11 Temperature/time Profiles during Microwave Processing of 72-ply Unidirectional AS4/3501-6 Composite at L_c=16.03 cm and 500 W

The heat transfer coefficients used in Figure 9.11 are $1.5x10^{-3}$ and $2.0x10^{-3}$ ($W/cm^2/K$) for the top and bottom surfaces. As shown in Figure 9.11, the temperature of bottom surface reached 250°C in 5 minutes and no temperature excursion was observed. The time required to heat the composite up to the control temperature can be shortened with higher input power. Comparing Figure 9.11 to 9.4, the advantages of microwave processing over thermal processing can be summarized as: 1) The temperature excursion during microwave processing is eliminated. 2) High temperatures can be used during microwave processing. 3) The ideal heating profile is realized during microwave processing, that is directly heating the laminate to the desired temperature as quickly as possible then maintaining the laminate at the desired temperature.

9.5 Conclusion

A one-dimensional process model was developed for both microwave and thermal processing. The five-parameter microwave power absorption model was applied to calculate the microwave power dissipated inside the composite. The process model was coded numerically using Lee's algorithm and Milne's method. The computer code was used to simulate the temperature and extent of cure profiles across the composite thickness during autoclave and microwave processing. With the effective heat transfer coefficients for the top and bottom surfaces as infinite and zero, the thickest AS4/3501-6 composite that can be processed is 4.0 cm. A decrease in the effective heat transfer coefficient will increase the magnitude of the temperature excursion and decrease the thickness of composite that can be processed. The temperature excursion can be eliminated during microwave processing. The ideal heating profile is realized during microwave processing, that is directly heating the laminate to the desired temperature as rapidly as possible then maintaining the laminate at the desired temperature.

CHAPTER 10
SUMMARY OF RESULTS

The feasibility of using microwave energy to processing polymers and composites was systematically explored. Microwave radiation effects on epoxide polymerization, the properties of the cured epoxy resins and composites, and various microwave processing techniques were studied. This study shows that microwave processing offers a fast heating rate, fast polymerization rate, and better property products as compared to thermal processing.

In the study of the neat epoxy resins, stoichiometric DGEBA/DDS and DGEBA/mPDA epoxy systems were chosen. The main results are summarized in the following.

* Faster reaction rates were observed in the microwave cure when compared to those of thermal cure at the same cure temperature for both systems. Microwave radiation has stronger effects on the DGEBA/DDS system than the DGEBA/mPDA system.

* Autocatalytic kinetics model was successfully used to analyze the cure behavior of DGEBA/mPDA and DGEBA/DDS systems for both microwave and thermal cure.

* The reaction rate constants of microwave cure were higher than those of thermal cure at the same cure temperature for both DGEBA/DDS and DGEBA/mPDA systems.

* For the stoichiometric DGEBA/mPDA system,

  a) Microwave radiation increases the values of k_1/k_2 at low cure temperatures, but decrease the values of k_1/k_2 at high cure temperatures.

  b) In the model, the reaction rate constants of primary amine-epoxy are equal to secondary amine-epoxy and the etherification reaction is negligible for both microwave and thermal cure.

* For stoichiometric DGEBA/DDS system,

  a) Microwave radiation decreases the values of k_1/k_2

  b) The reaction rate constants of primary amine-epoxy are greater than those of secondary amine-epoxy and the etherification reaction is negligible at low cure temperatures for both microwave and thermal cure.

  c) Microwave radiation decreases the reaction rate constant ratio of primary amine-epoxy to secondary amine-epoxy and the ratio of primary amine-epoxy to the etherification reaction.

* Microwave radiation increases the activation energies of both k_1 and k_2 in the DGEBA/DDS system while it only increases the activation energies of k_2 in the DGEBA/mPDA system.

* Microwave radiation increases the glass transition temperature of cured epoxy after the extent of cure reaches α_{gel}. The increase was much more significant in the DGEBA/DDS system than the DGEBA/mPDA system. The DiBenedetto model was used to fit the experimental Tg data.

* The full-cure epoxy-monomer lattice energy is lower in microwave cure than in thermal cure and the full-cure epoxy-monomer segmental mobility is lower in microwave cure than in thermal cure for both DGEBA/DDS and DGEBA/mPDA.

* The TTT diagrams for both microwave and thermal cure were generated using data and models. A good agreement was found between the two.

* The vitrification time is shorter in microwave cure than in thermal cure, especially at higher isothermal cure temperatures. The minimum vitrification time is shorter in microwave cure than in thermal cure, especially for the DGEBA/DDS system.

In the microwave processing study, three processing techniques, batch processing, scale-up, and continuous processing, were investigated. The main results of the processing study are summarized as follows.

In the batch processing study

* Unidirectional and crossply graphite fiber/epoxy composite laminates consisting of 24, 72, and 200 plies were successfully processed in a 17.78 cm tunable resonant cavity using 2.45 GHz microwave radiation.

* The heating rate and the temperature uniformity were strong functions of the fiber orientation and the cavity length during microwave heating of fully cured 3.8 cm thick AS4/3501-6 composite. Both uniform planar temperature or overall temperature can be achieved at proper fiber orientation and resonant mode.

* Temperature uniformity during the processing and the flexural properties of

the processed samples were shown to be strong functions of the resonant heating modes.

* The flexural properties of the microwave processed unidirectional composites were also affected by the fiber orientation of the composites with respect to the electromagnetic coupling probe. The maximum flexural properties of unidirectional composites were observed when the sample was processed at an orientation of 45 degrees to the coupling probe.

* The flexural properties of microwave processed crossply samples have been found to be between those values measured for the microwave processed unidirectional laminates cured with fiber orientations perpendicular and parallel to the coaxial coupling probe.

* The concept of a processing mode (PM) is defined based on the flexural properties of the processed composites. Criteria defining a processing mode were obtained from a database of types of processing modes, radial field patterns during processing, and the flexural properties of processed composites.

* The flexural strength of the unpressurized thermally cured unidirectional and crossply composites were much lower than those of unpressurized microwave cured samples. The flexural modulus of the unpressurized thermally cured unidirectional composites was comparable to that of unpressurized microwave cured unidirectional samples with a fiber orientation of 0 degrees to the coupling probe, but lower than that of microwave cured unidirectional samples with other fiber orientations.

* Comparing the flexural properties of the microwave processed composites with a processing time of 90 minutes and no pressure to those of autoclave

processed samples with a processing time of 300 minutes and a pressure of 100 psig

a) A comparable flexural strength but lower flexural modulus were found in the microwave processed 24-ply unidirectional composites than those of the autoclave processed samples.

b) Both flexural strength and flexural modulus of microwave processed 24-ply crossply samples were lower than those of autoclave processed samples.

* The apparent interlaminar shear strengths (ISS) of microwave processed composites increased with increasing extent of cure.

* Scanning electron microscope analysis for the fracture surface revealed that

a) Graphite fiber/epoxy bonding was higher in microwave processed composites than in thermally processed samples.

b) Microwave processed composites failed in matrix failure mode for samples of high extent of cure and in a combination mode of interfacial and matrix failure mode for samples of low extent of cure.

c) The autoclave processed samples failed in a combination mode of interfacial and matrix failure mode.

In the scale up study

* Fully cured DGEBA/DDS epoxy and Hercules AS4/3501-6 composite squares were heated in a 17.78cm and a 45.72cm tunable cylindrical resonant cavities

with the same cavity geometry ratios, sample/cavity size ratios, and the input power density.

* A microwave source operating at 2.45GHz was used for the 17.78cm cavity and 915MHz was used for the 45.72cm cavity, in order to reproduce the same empty cavity resonant mode for the same cavity geometry ratio.

* The scale-up of cavity length during microwave heating of low to medium loss materials, such as an epoxy square, can be approximated by the scale-up factor of empty cavity for a given resonant mode.

* The maximum temperature was linearly related to the maximum temperature difference during microwave heating of graphite fiber/epoxy composite. This relationship was the same for both the 2.45 GHz system and 915 MHz system.

In the continuous processing study

* A unique microwave applicator was invented in which continuous graphite fiber reinforced prepreg tapes can be continuously processed using 2.45GHz microwave radiation without causing microwave leakage.

* The microwave power absorption efficiency was higher in the CH modes than in the PS modes.

* Fully cured products were obtained in the controlled-hybrid modes while only partially cured products were obtained in the pseudo-single modes under experimental conditions.

In order to predict and control the temperature and extent of cure of the composite during processing, a one dimensional processing model was developed for both microwave and thermal processing. The main results were summarized as follows.

* A five-parameter microwave power absorption model was derived to calculate the microwave power dissipated inside the composite during microwave processing.

* A FORTRAN program combining the energy balance equation, the microwave power absorption model, and the least squares optimization was coded to generate the five parameters based on the temperature/time/position profiles obtained from microwave heating of a fully cured composite.

* A set of five parameters was generated for a resonant mode at $L_c = 16.03$ cm and 0° fiber orientation in a 72-ply unidirectional AS4/3501-6 composite loaded cavity. For this mode, P_1 increases linearly with input power to the power of 0.3, A_T and A_B increase linearly with the square root of the input power, and θ_T and θ_B are not functions of the input power.

* The process model was coded numerically using Lee's algorithm and Milne's method for processing simulation.

* The thermal simulation results show that the thickest AS4/3501-6 composite that can be processed is 4.0 cm with the manufacture's suggested cure cycle and it is very important to keep a high effective heat transfer coefficient at the surface during thermal processing.

* The advantages of microwave processing over thermal processing were fully demonstrated by the computer simulation.

CHAPTER 11
FUTURE WORK

This study systematically demonstrated the feasibility and advantages of microwave processing as an alternative in the processing of polymers and composites. However, there are still some fundamental and application issues that need to be further explored.

In the neat resin study, the further work that need to be done is:

* To detect the crosslinked network structural difference in the microwave and thermally cured epoxy resins using wide-angle X-ray diffraction or solid-state NMR. This study will give insights into the question of why microwave cured epoxy samples have higher Tg.

* To determine the key functional groups in curing agents responsible for the enhancement of reaction rate and Tg using a curing agent having an intermediate dipole moment, such as diamino diphenyl methane. If an intermediate behavior is observed in diamino diphenyl methane with microwave radiation, the overall dipole moment of the curing agent is the determining factor for microwave cure behavior. If the microwave cure behavior is similar to the DDS system, the proximity of amines in mPDA have inhibiting effects on microwave radiation. If the microwave cure behavior is similar to mPDA, it means that the activity of the SO_2 group in DDS is responsible for the significant increase of reaction rates and T_g during microwave cure.

* To study the polymer rheology behavior during microwave processing.

* To study weight loss during microwave heating.

In the processing study, some application issues need to be further explored.

* Develop a pressure device to couple pressure into the processing.

* Study the microwave heating characteristics of complex shaped composites.

* Study the scalibility for the composite processing in the microwave environment with the samples only scaled in two dimensions.

* Study the scalibility of complex shaped composites.

* Apply the microwave energy in various continuous processing techniques using the microwave applicator invented in this study. These could include extrusion, pultrusion, carbon fiber or wire production, filament winding, and so on.

In the modeling, the current one dimensional process model needs to be extended into a three dimensional model and the rheology, mechanical property, and void formation behaviors need to be coupled into the model.

Appendix I FORTRAN code for generating the TTT diagram for the DGEBA/DDS system

```
C     TTT Diagram Calculating Program for DGEBA/DDS System
C     variables declaration
      REAL mwn,mwl,mwk1lna,mwk1e,mwk2lna, mwk2e,mwxvit
      REAL thn,thl,thk1lna,thk1e,thk2lna,thk2e,thxvit
      REAL n,l,tc(300),xgel,mwtggel,thtggel,p,f
      REAL g,gg,fi,delt,mwk1,mwk2,thk1,thk2
      REAL tht,mwt,thtgel(300),thtvit(300),thx0,mwx0
      REAL mwtgel(300),mwtvit1(300),mwtvit2(300),thx,mwx
c
      OPEN(9, FILE='tttdth.m')
      OPEN(11, FILE='tttdmw.m')
C     constants
      mwn=.15
      mwl=.0
      mwk1lna=23.21
      mwk2lna=34.8
      mwk1e=21000.0
      mwk2e=30000.0
      thn=.4
      thl=.0
      thk2lna=25.01
      thk1lna=16.07
      thk2e=23270.0
      thk1e=16040.0
      xgel=0.57
      mwtggel=339.7
      thtggel=334.6
      tg0=295.4
      DO 50 I=1,200
      mwtgel(i)=0.0
      mwtvit1(i)=0.0
      mwtvit2(i)=0.0
      thtgel(i)=0.0
50    thtvit(i)=0.0
      write(9,250)
      write(11,350)
250   format('%For thermal cure of DGEBA/DDS',//
     1 '%th(i,j), th(1,j)=temp in K; th(2,j)=thtgel, in min'/
     2 '% th(3,j)=thtvit,in min., th(4,j)=thxvit'///
     3 '% T(K), thtgel(min)  thtvit(min)  thxvit '/'th=[')
```

```
350   format('%For microwave cure of DGEBA/DDS',//
     1 '%mw(i,j), mw(1,j)=temp in K; mw(2,j)=mwtgel, in min'/
     2 '% mw(3,j)=mwtvit,in min.,at mwx=mwxvit'/
     3 '%mw(4,j)=mwtvit2, in min. where mwx=thxvit'/
     4 '%mw(5,j)=mwxvit'//
     5 '% T(K)  mwtgel(min) mwtvit1 mwtvit2 mwxvit',/'mw=[')
       DO 100 j=1,230
       tc(j)=273.2+25+j
       mwxvit=(tc(j)/tg0-1.0)/(tc(j)*.82/tg0-.68)
       thxvit=(tc(j)/tg0-1.0)/(tc(j)*.7/tg0-.56)
c      print *, tc(j),thxvit,mwxvit
       mwk1=exp(mwk1lna-mwk1e/1.987/tc(j))
       mwk2=exp(mwk2lna-mwk2e/1.987/tc(j))
       thk1=exp(thk1lna-thk1e/1.987/tc(j))
       thk2=exp(thk2lna-thk2e/1.987/tc(j))
c      print *, 'thk1=',thk1,'thk2=',thk2,'mwk1=',mwk1,'mwk2=',mwk2
C
       If (tc(j) .GE. 418.0) mwl=0.6
        If (tc(j) .GE. 438.0) thl=.8
       IF (thxvit .GT. 1.0) then
       thxvit=1.0
       go to 300
       end if
       thx0=0.0
       n=thn
       L=thl
       fi=1.0
       if (j .lt. 50) then
       delt=10.0
       else
       delt=1.0
       end if
       DO 200 i=1,10000000
       tht=(i-1)*delt
       f=1.0-((1.0-n)*fi+fi**(n/2.0))/(2.0-n)
       thx=((1.0-fi)*(1-n)*(2.0-L)+2.0*(1.0-fi**(n/2.0))*
     1       (1.0-L/n)-(2.0-n)*L*LOG(fi))/2.0/(2.0-n)
       p=((2.0*(1-n)*fi+n*fi**(n/2.0))/(2.0-n)+L*f)*
     1       (1.0-thx)*(thk1+thk2*f)
       g=-((1.0-n)*(2.0-L)+n*(1-L/n)*fi**(n/2.0-1.0)+
     1       (2.0-n)*L/fi)/2.0/(2.0-n)
       gg=p/g
       fi=fi+gg*delt
```

```
      IF ( (xgel-thx)*(xgel-thx0) .LT. 0.0) THEN
           thtgel(j)=tht
c     print *, 'thtgel(',j,')=',thtgel(j)
           end if
      IF ( (thxvit-thx)*(thxvit-thx0) .LT. 0.0) THEN
           thtvit(j)=tht
           print *, 'thtvit(',j,')=', thtvit(j)
           end if
      IF ( thtgel(j) .NE. 0.0 .AND. thtvit(j) .NE. 0.0 ) GO TO 25
      thx0=thx
200   CONTINUE
C
25    write (9,1000) tc(j),thtgel(j),thtvit(j),thxvit
300   n=mwn
      L=mwl
      mwx0=0.0
      fi=1.0
      if (mwxvit .gt. 1.0) go to 100
      if (j .le. 50) then
      delt=10.0
      else
      delt=1.0
      end if
      if (j .GT. 85 ) then
      delt=.1
      end if
      if (j .gt. 135) then
      delt=.01
      end if
      if (j .gt. 180) then
      delt=.001
      end if
      if (j .gt. 220) then
      delt=.0001
      end if
95    DO 400 i=1,100000000
      mwt=(i-1)*delt
      f=1.0-((1.0-n)*fi+fi**(n/2.0))/(2.0-n)
      mwx=((1.0-fi)*(1-n)*(2.0-L)+2.0*(1.0-fi**(n/2.0))*
     1      (1.0-L/n)-(2.0-n)*L*LOG(fi))/2.0/(2.0-n)
      p=((2.0*(1.0-n)*fi+n*fi**(n/2.0))/(2.0-n)+L*f)*
     1    (1.0-mwx)*(mwk1+mwk2*f)
      g=-((1.0-n)*(2.0-L)+n*(1.0-L/n)*fi**(n/2.0-1.0)+
     1      (2.0-n)*L/fi)/2.0/(2.0-n)
```

```
      gg=p/g
      fi=fi+gg*delt
c     print *, mwx
      IF ( (xgel-mwx)*(xgel-mwx0) .LT. 0.0) THEN
            mwtgel(j)=mwt
c     print *, 'mwtgel(',j,')=', mwtgel(j)
            end if
      IF ( (mwxvit-mwx)*(mwxvit-mwx0) .LT. 0.0) THEN
            mwtvit1(j)=mwt
c     print *, 'mwtvit1(',j,')=', mwtvit1(j),'at mwx=mwxvit'
            end if

      IF (thxvit .eq. 1) THEN
      mwtvit2(j)=1000
      go to 700
      end if
      IF ( (thxvit-mwx)*(thxvit-mwx0) .LT. 0.0) THEN
            mwtvit2(j)=mwt
c     print *, 'mwtvit2(',j,')=',mwtvit2(j),'at mwx=thxvit'
            end if
700   IF ( mwtgel(j) .NE. 0.0 .AND. mwtvit1(j) .NE. 0.0
     1        .AND. mwtvit2(j) .NE. 0.0) GO TO 11
      mwx0=mwx
400   CONTINUE
      print *, 'the result is wrong!'
11    print *, 'program is running'
      write (11,2000) tc(j),mwtgel(j),mwtvit1(j),
     1              mwtvit2(j),mwxvit
1000  format(2x,f7.3,2x,e15.7,2x,e15.7,2x,f7.3)
2000  format(2x,f7.3,2x,e15.7,2x,e15.7,2x,e15.7,2x,f7.3)

100   CONTINUE
      write(9,3000)
      write(11,4000)
3000  format('];'/'semilogx(th(:,2),th(:,1),th(:,3),th(:,1))'/
     1    'hold')
4000  format('];'/'semilogx(mw(:,2),mw(:,1),mw(:,3),mw(:,1))'/
     1      'hold'/'semilogx(mw(:,4),mw(:,1))')
      close(11)
      close (9)
      print *, 'end'
      end
```

Appendix II FORTRAN code for calculating the parameters for microwave power absorption model

```
Program fitparameters
implicit none
double precision pi,mn,tdx(72),sum,dx,dt,tdt(500), denm(500,72),er1,b(5), b1,
bet(72), er, ma(72,72), ttemp(500,72),expm(500,72),x(5,500,72),b(5),to,yin,a
integer cnt,m,pt,i,j,k,m1
common /blok8/ x
common /blk1/ yin,to,m
common /blk6/ expm,pt
common /blk7/ dx,dt,tdt
common /blk0/ ttemp
common /nwblk/ tdx,m1
open(unit=12,status='unknown',file='exn4.m')
open(unit=13,status='unknown',file='exx4.m')
call input(b)
pi=3.141592654
do i=1,5
bet(i)=0
enddo
call tempprof(b,ttemp)
call err(m1,pt,expm,ttemp,er)
write(*,*),'Iteration:',cnt,'    S=',er
write(*,*),'Parameters'
do i=1,5
write(*,*),b(i)
enddo
er1=er
mn=er
cnt=0
do while((abs((er1-er)/er1) .GT. 1.0e-3).OR.(cnt .LT. 1))
if (cnt .GT. 0) then
er=er1
endif
do i=1,5
call dpowc(b,i,denm)
do j=1,pt
do k=1,m1
x(i,j,k)=(denm(j,k)-ttemp(j,k))/(0.00001*b(i))
enddo
enddo
enddo
```

```
      do i=1,5
      call rhsum(m1,pt,x,expm,ttemp,i,a)
      ma(i,6)=a
      do j=1,5
      call lhsum(m1,pt,x,i,j,b1)
      ma(i,j)=b1
c     write(*,*),ma(i,j)
      enddo
      enddo
      call mat(ma,5,bet)
      do i=1,5
      b(i)=abs(b(i)+bet(i))
      if ((i.EQ.4).OR.(i.EQ.5)) then
      if(b(i).LT.0) then
      b(i)=b(i)-2*pi*(-1+int(b(i)/(2*pi)))
      else
      b(i)=b(i)-2*pi*int(b(i)/(2*pi))
      endif
      endif
      enddo
      call tempprof(b,ttemp)
      call err(m1,pt,expm,ttemp,er1)
      cnt=cnt+1
      write(*,*),'Iteration:',cnt,'    S=',er1
      write(*,*),'Parameters'
      do i=1,5
      write(*,*),b(i)
      enddo
      enddo
      write(*,*),'Parameters'
      do i=1,5
      write(*,*),b(i)
      enddo
      write(*,*),'    Temperatures    '
      write(*,*),'Experimental','   Fitted'
      write(12,*),'exp=['
      do i=1,pt
      write(*,*),'Time:',tdt(i)
      write(12,60),
tdt(i),expm(i,1),expm(i,2),expm(i,3),expm(i,4),expm(i,m1),ttemp(i,1),
ttemp(i,2),ttemp(i,3),ttemp(i,4),ttemp(i,m1)
      do j=1,m1
      write(*,59),expm(i,j),ttemp(i,j)
59    format(F9.5,3X,F9.5)
```

```
      enddo
60    format(F7.2,1X,F9.5,1X,F9.5,1X,F9.5,1X,F9.5,1X,F9.5,1X,F9.5,1X,F9.5,
1X,F9.5,1X,F9.5,1X,F9.5 )
      write(*,*)
      enddo
      write(12,*),'];'
      write(13,*),'xs1=['
      do j=1,pt
      write(13,61),tdt(j),x(1,j,1),x(1,j,2),x(1,j,3),x(1,j,4),x(1,j,m1)
61    format(F7.2,1X,F12.5,1X,F12.5,1X,F12.5,1X,F12.5,1X,F12.5)
      enddo
      write(13,*),'];'
      write(13,*),'xs2=['
      do j=1,pt
      write(13,62),tdt(j),x(2,j,1),x(2,j,2),x(2,j,3),x(2,j,4),x(2,j,m1)
62    format(F7.2,1X,F12.5,1X,F12.5,1X,F12.5,1X,F12.5,1X,F12.5)
      enddo
      write(13,*),'];'
      write(13,*),'xs3=['
      do j=1,pt
      write(13,63),tdt(j),x(3,j,1),x(3,j,2),x(3,j,3),x(3,j,4),x(3,j,m1)
63    format(F7.2,1X,F12.5,1X,F12.5,1X,F12.5,1X,F12.5,1X,F12.5)
      enddo
      write(13,*),'];'
      write(13,*),'xs4=['
      do j=1,pt
      write(13,64),tdt(j),x(4,j,1),x(4,j,2),x(4,j,3),x(4,j,4),x(4,j,m1)
64    format(F7.2,1X,F12.5,1X,F12.5,1X,F12.5,1X,F12.5,1X,F12.5)
      enddo
      write(13,*),'];'
      write(13,*),'xs5=['
      do j=1,pt
      write(13,65),tdt(j),x(5,j,1),x(5,j,2),x(5,j,3),x(5,j,4),x(5,j,m1)
65    format(F7.2,1X,F12.5,1X,F12.5,1X,F12.5,1X,F12.5,1X,F12.5)
      enddo
      write(13,*),'];'
      end

      subroutine rhsum(m1,pt,x,expm,ttemp,n,a)
      integer i,j,n,m,pt,m1
      double precision a,ttemp(500,72),expm(500,72),x(5,500,72)
      a=0
      do i=1,pt
      do j=1,m1
```

```
a=a+(expm(i,j)-ttemp(i,j))*x(n,i,j)
enddo
enddo
return
end

subroutine lhsum(m1,pt,x,n,q,b)
integer m1,n,q,i,j,pt,m
double precision b,x(5,500,72)
b=0
do i=1,pt
do j=1,m1
b=b+x(q,i,j)*x(n,i,j)
enddo
enddo
return
end

subroutine err(m1,pt,expm,ttemp,er)
double precision er,ttemp(500,72),expm(500,72)
integer m1,i,j,pt
er=0
do i=1,pt
do j=1,m1
er=er+((expm(i,j)-ttemp(i,j))**2)
enddo
enddo
return
end


subroutine dpowc(b,q,dtem)
double precision dtem(500,72),c(5),b(5)
integer q,i
do i=1,5
if (i .EQ. q) then
c(i)=b(q)+0.00001*b(q)
else
c(i)=b(i)
endif
enddo
call tempprof(c,dtem)
return
end
```

```
      subroutine tempprof(b,rtemp)
      implicit none
      integer k,m1,m,i,j,tpt,pt
      double precision
slpe,diff,hdl1,hdh1,hdh2,cf,tdx(72),ptot,ft,hd2,expm(500,72),b(5),hd1,
rtemp(500,72),y5(72),pc(72),b(5),d1,wf,yav3,p1,p2,y2(72),y1(72),y3(72,72),
dt,dx,to,kav1,kav2,kav3,kav,yav1,yav2,t,yin,dmt,tdt(500),intl(72)
      common /blk1/ yin,to,m
      common /blk6/ expm,pt
      common /blk7/ dx,dt,tdt
      common /sblk8/ hdl1,hdh1,hdh2,hd2
      common /nwblk/ tdx,m1
      common /blnk/ cf,intl(72)
      t=0
      do i=1,m+1
      if(tdt(1).EQ.0.0) then
      do j=1,m1-1
      if(((i-1)*dx.LT.tdx(j+1)).AND.((i-1)*dx.GE.tdx(j))) then
      slpe=(intl(j+1)-intl(j))/(tdx(j+1)-tdx(j))
      y1(i)=1.0/to*(intl(j)+slpe*((i-1)*dx-tdx(j)))
      endif
      enddo
      if(((i-1)*dx.GE.tdx(m1))) then
      y1(i)=intl(m1)/to
      endif
      else
      y1(i)=1.00
      endif
      y5(i)=y1(i)
      enddo
      do i=1,m+1
      do j=1,m+2
      y3(i,j)=0.00
      enddo
      enddo
      tpt=1
      call unimwp(b(1),b(2),b(3),b(4),b(5),m*dx,m,pc,ptot)

      do while(tpt .LE. pt)
            if (abs(t-tdt(tpt)).LT.1.0e-12) then
            k=1
            do while (k.LE.m1)
            do i=1,m+1
            if (abs((i-1)*dx-tdx(k)).LE.1.0e-6) then
```

```
                rtemp(tpt,k)=to*y5(i)
                k=k+1
                endif
                enddo
                enddo
                tpt=tpt+1
                endif
C
C       Lees Method
                if (t.GT.0) then
                dmt=2*dt/(3*(dx**2.0))
                yav3=0.50*(y2(2)+y2(1))
                call Th(yav3*to,1,kav3)
                call Th(y2(1)*to,1,kav)
                call prod(y2(1)*to,1,p2,wf,d1)
                diff=to*abs(yin-y2(1))
                if (diff.LE.27) then
                hd1=hdl1
                endif
                if ((diff.LE.43).AND.(diff.GT.27)) then
                hd1=hdh1
                endif
                if (diff.GT.43) then
                hd1=hdh2
                endif
                y3(1,1)=dmt*(2*dx*hd1+kav3+kav)+p2
                y3(1,2)=-(kav3+kav)*dmt

y3(1,m+2)=p2*y1(1)+dmt*((y2(1)+y1(1))*(-2*dx*hd1-(kav+kav3))+
(kav+kav3)*(y2(2)+y1(2))+6*yin*hd1*dx)+2*dt*pc(1)/to+p1*y1(i)
                do i=2,m
                yav1=0.50*(y2(i)+y2(i+1))
                yav2=0.50*(y2(i)+y2(i-1))
                call Th(yav1*to,1,kav1)
                call Th(yav2*to,1,kav2)
                call prod(y2(i)*to,1,p1,wf,d1)
                y3(i,i-1)=-kav2*dmt
                y3(i,i)=p1+dmt*(kav1+kav2)
                y3(i,i+1)=-dmt*kav1

y3(i,m+2)=dmt*(kav1*(y2(i+1)+y1(i+1))-(kav1+kav2)*(y2(i)+y1(i))+
kav2*(y2(i-1)+y1(i-1)))+p1*y1(i)+2*dt*pc(i)/to
                enddo
                yav3=0.50*(y2(m+1)+y2(m))
```

```
                call Th(yav3*to,1,kav3)
                call Th(y2(m+1)*to,1,kav)
                call prod(y2(m+1)*to,1,p2,wf,d1)
                y3(m+1,m+1)=dmt*(2*dx*hd2+kav+kav3)+p2
                y3(m+1,m)=-dmt*(kav+kav3)

y3(m+1,m+2)=p2*y1(m+1)+dmt*((y2(m+1)+y1(m+1))*(-2*dx*hd2-
(kav+kav3))+(kav+kav3)*(y2(m)+y1(m))+6*yin*hd2*dx)+2*dt*pc(m+1)/to
                call tridag(y3,m+1,y5)
                do i=1,m+1
                y1(i)=y2(i)
                y2(i)=y5(i)
                enddo
                endif
C
C       Crank Nicolson  Method
                if (t.EQ.0) then
                dmt=dt/(2*(dx**2))
                yav3=0.50*(y1(2)+y1(1))
                call Th(yav3*to,1,kav3)
                call Th(y1(1)*to,1,kav)
                call prod(y1(1)*to,1,p2,wf,d1)
                diff=to*abs(yin-y1(1))
                if (diff.LE.27) then
                hd1=hdl1
                endif
                if ((diff.LE.44).AND.(diff.GT.27)) then
                hd1=hdh1
                endif
                if (diff.GT.44) then
                hd1=hdh2
                endif
                y3(1,1)=dmt*(2*dx*hd1+kav+kav3)+p2
                y3(1,2)=-dmt*(kav3+kav)
                y3(1,m+2)=y1(1)*(p2-dmt*2*dx*hd1-(kav3+kav)*dmt)+
dmt*(kav3+kav)*y1(2)+4*yin*hd1*dx*dmt+pc(1)*dt/to
                do i=2,m
                yav1=0.50*(y1(i)+y1(i+1))
                yav2=0.50*(y1(i)+y1(i-1))
                call Th(yav1*to,1,kav1)
                call Th(yav2*to,1,kav2)
                call prod(y1(i)*to,1,p1,wf,d1)
                y3(i,i-1)=-kav2*dmt
                y3(i,i)=p1+dmt*(kav1+kav2)
```

```
                y3(i,i+1)=-dmt*kav1

y3(i,m+2)=dmt*(kav1*(y1(i+1))-(kav1+kav2)*(y1(i))+kav2*(y1(i-1)))+
dt*pc(i)/to+p1*y1(i)
                enddo
                yav3=0.50*(y1(m+1)+y1(m))
                call Th(yav3*to,1,kav3)
                call Th(y1(m+1)*to,1,kav)
                call prod(y1(m+1)*to,1,p2,wf,d1)
                y3(m+1,m+1)=dmt*(2*dx*hd2+kav+kav3)+p2
                y3(m+1,m)=-dmt*(kav3+kav)

y3(m+1,m+2)=p2*y1(m+1)+dmt*((y1(m+1))*(-2*dx*hd2-(kav+kav3))+
(kav+kav3)*(y1(m))+4*yin*hd2*dx)+dt*pc(m+1)/to
                call tridag(y3,m+1,y5)
                do i=1,m+1
                y2(i)=y5(i)
                enddo
                endif
        t=t+dt
        enddo
        return
       end

        subroutine Th(a,x1,k1)
        double precision a,x1,k1,kf,km
        common /blk2/ kf
        km=(0.161+x1*(0.00147*a-0.417))/100.0
        k1=(0.02514*km)/(.02514+km)
        return
        end

        subroutine prod(y,x2,ret1,ret2,ret3)
        double precision y1,x1,y,x2,r2,rho,sp,ret1,ret2,ret3
        y1=y
        x1=x2
        call den(y1,x1,rho)
        call Cp(y1,x1,sp,r2)
        ret1=rho*sp
        ret2=r2
        ret3=rho
        return
        end
```

```
      subroutine den(a,x1,ret)
      double precision a,ret,rf,rm,x1
      common /blk5/ rf
      ret=rf
      return
      end

      subroutine Cp(a,x1,ret1,ret2)
      double precision intl(72),a,x1,rf,tem,wf,vf,cf,ret1,ret2
      common /blk4/ vf
      common /blk5/ rf
      common /blnk/ cf,intl(72)
      call den(a,x1,tem)
      wf=tem*vf/rf
      ret1=cf
      ret2=wf
      return
      end

      SUBROUTINE
UNIMWP(P1,AT,AB,ANGLET,ANGLEB,L,N,PTOTAL,psum)
C
C     P1,P2,PTOTAL - POWER ABSORPTION RATE DUE TO SIDE WAVES,
TOP
C                  AND BOTTOM WAVES, AND ALL TEM WAVES, IN W/M^3
C     AB,AT - MAGNITUDES OF BOTTOM AND TOP INCIDENT TEM
      WAVES IN V/M
C     L - COMPOSITE THICKNESS,IN M.
C     ANGLEB,ANGLET - POLARIZATION ANGLE OF BOTTOM AND TOP
      TEM WAVES,
C                  0 TO 2*PI.
C     N - THE NUMBER OF OUTPUT DATA DESIRED.
C     implicit none

      INTEGER N,I
      double precision P1, AT, AB, ANGLET,ANGLEB,EPS0,MU0,FREQ,L
      double precision PI,P2(72),PTOTAL(72),PSUM, DELTH,PI2,EXY(100)
      DOUBLE COMPLEX  J,EX(72),EY(72)
      DOUBLE COMPLEX EPSPC, EPSQC,EXT,EYT,EXB,EYB
C     COMPLEX*16  EPSPU, EPSQU
      DOUBLE COMPLEX   KP, KQ
      DOUBLE COMPLEX EXAVG(100),EYAVG(100)
      EPSPC=(1.0,-25000)
C     DATA EPSQU /(33.0,-53.3)/
```

```
      EPSQC=(14.5,-75.8)

C     OPEN INPUT AND OUTPUT DATA FILES
C      CONSTANTS
      PI=3.14159
      J=(0.0,1.0)
C     write(*,*),J
      FREQ=2.45*1.0E+9
      EPS0=1.0/(36*PI)*1.0E-9
      MU0=4*PI*1.0E-7
       EPSPC=EPSPC*EPS0
       EPSQC=EPSQC*EPS0
C
C     INCIDENT TOP AND BOTTOM TEM WAVES
      EXT=AT*COS(ANGLET)
      EYT=AT*SIN(ANGLET)
      EXB=AB*COS(ANGLEB)
      EYB=AB*SIN(ANGLEB)
      KP=2*PI*FREQ*SQRT((MU0*EPSPC))
      KQ=2*PI*FREQ*SQRT((MU0*EPSQC))
C
      DELTH=0.01*L/N
      DO 200 I=1,N+1
      EX(I)=EXB*EXP(J*KP*(I-N-1)*DELTH)+
     1      EXT*EXP(-J*KP*(i-1)*DELTH)
      EY(I)=EYB*EXP(J*KQ*(I-N-1)*DELTH)+
     1      EYT*EXP(-J*KQ*(i-1)*DELTH)
      EXY(I)=sqrt(abs(EX(I))**2+abs(EY(I))**2)

      P2(I)=-FREQ*PI*(imag(EPSPC)*ABS(EX(I))**2+
     1             imag(EPSQC)*ABS(EY(I))**2)
200   PTOTAL(I)=P1+1.0e-6*P2(I)
C
      PSUM=0.0
      DO 225 I=1,N
      EXAVG(I)=(EX(I)+EX(I+1))/2
      EYAVG(I)=(EY(I)+EY(I+1))/2
      PI2=-FREQ*PI*(IMAG(EPSPC)*ABS(EXAVG(I))**2+
     1          IMAG(EPSQC)*ABS(EYAVG(I))**2)
225   PSUM=PSUM+(P1+PI2)*9.0*.0254*.0254*DELTH
c
      return
      END
```

```
      SUBROUTINE TRIDAG(c,n,b)
      DOUBLE PRECISION c(72,72),bet(72),g(72),b(72)
      INTEGER n,i,j
      bet(1)=c(1,1)
      g(1)=c(1,n+1)/bet(1)
      do i=2,n
      bet(i)=c(i,i)-c(i,i-1)*c(i-1,i)/bet(i-1)
      g(i)=(c(i,n+1)-c(i,i-1)*g(i-1))/bet(i)
      enddo
      b(n)=g(n)
      j=n
      do while(j.GE.1)
      b(j)=g(j)-c(j,j+1)*b(j+1)/bet(j)
      j=j-1
      enddo
      return
      END

      SUBROUTINE MAT(C,N,B)
      DOUBLE PRECISION amx,C(72,72),A(72,72),B(72),TEMP,MAX,RAT
      INTEGER r,xm,mx(72),N,I,J,K,M,tr
      K=1
      DO I=1,N
      DO J=1,N+1
      A(I,J)=C(I,J)
      ENDDO
      ENDDO
      do i=1,n
      mx(i)=i
      enddo
1     DO WHILE (K.LE.N)
      MAX=A(K,K)
      tr=0
      do i=1,n
      if (abs(a(i,k)).GT.abs(max)) then
      max=a(i,k)
      tr=1
      r=i
      endif
      enddo
      if (tr.EQ.1) then
      do j=1,n+1
      temp=a(k,j)
      a(k,j)=a(r,j)
```

```
      a(r,j)=temp
      enddo
      endif
            amx=abs(max)
            tr=0
            do i=1,n
            if (amx.LT.abs(a(k,i))) then
            amx=a(k,i)
            r=i
            tr=1
            endif
            enddo
            if (tr.EQ.1) then
            xm=mx(r)
            mx(r)=mx(k)
            mx(k)=xm
            do i=1,n
            temp=a(i,k)
            a(i,k)=a(i,r)
            a(i,r)=temp
            enddo
            endif
            max=a(k,k)
            DO 25 J = 1,N+1
            A(K,J)=A(K,J)/MAX
25          CONTINUE
            DO 30 I = 1,N
                  IF (I .NE. K) THEN
                  RAT=A(I,K)
                        DO 27 J = 1,N+1
                        A(I,J)=A(I,J)-RAT*A(K,J)
27                      CONTINUE
                  ENDIF
30          CONTINUE
      K=K+1
      ENDDO
      DO 40 I = 1,N
      B(mx(i))=A(I,N+1)
40    CONTINUE
      RETURN
      END
```

```
      subroutine input(b)
      implicit none
      integer ch1,ch,m,i,m1
      double precision
intl(72),hdh2,cf,spx,fx,tb,sdx,tdx(72),expm(500,72),hdl1,hdh1,hd2,vf,rf,kf,dt,dx,l,to,
tin,yin,tf,td,tdt(500),b(5)
      integer j,pt
      common /blk1/ yin,to,m
      common /blk2/ kf
      common /blk4/ vf
      common /blk5/ rf
      common /blk6/ expm,pt
      common /blk7/ dx,dt,tdt
      common /sblk8/ hdl1,hdh1,hdh2,hd2
      common /nwblk/ tdx,m1
      common /blnk/ cf,intl(72)
      read(*,*),ch,ch1,rf,vf,kf,cf,hdl1,hdh1,hdh2,hd2,l,tin,to,dt,m
      do i=1,5
      read(*,*),b(i)
      enddo
      if (ch1.EQ.0) then
      read(*,*),sdx,fx,m1
      spx=(fx-sdx)/m1
      do i=1,m1
      tdx(i)=sdx+(i-1)*spx
      enddo
      else
      read(*,*),m1
      do i=1,m1
      read(*,*),tdx(i)
      enddo
      endif
      if (ch.EQ.0) then
      read(*,*),tb,td,pt
      pt=(tf-tb)/td+1
      do i=1,pt
      tdt(i)=(i-1)*td
      enddo
      else
      read(*,*),pt
      do i=1,pt
      read(*,*),tdt(i)
      do j=1,m1
      read(*,*),expm(i,j)
```

```
if((i.EQ.1).AND.(tdt(i).EQ.0)) then
intl(j)=expm(i,j)
endif
enddo
enddo
endif
yin=tin/to
dx=l/m
return
end
```

Appendix III FORTRAN code for processing model

```
      PROGRAM MWCURE
      implicit none
      integer st,timcnt,i,j,cntr
      double precision
endt,diff,hdl1,hdh1,ptot,pc(72),b(5),vf,cf,emt(10),em(10,2),a3,e3,
hd1,hd2,rf,kf,d1,wf,xav1,xav2,xav3,xt(72),r1(72),yav3,p1,p2,y2(72),y1(72),y3(72,72
),x(72),x1(72),x2(72),x3(72),dt,dx,l,td,tf,to,tin,a1,a2,e1,e2,kav1,kav2,kav3,kav,yav1,
yav2,t,dh,tdt,
yin,dmt,hdh2,templ(5),rte(72),y5(72),error,y4(72),sudt,dt1,r2(72),r3(72),r4(72),xt1(72
), f1(72),f2(72),f3(72),f4(72),y0(72),error1
      integer m,o
      common /blk1/ a1,a2,a3,e1,e2,e3,to
      common /blk2/ kf
      common /blk3/ x1,x2,x3
      common /blk5/ rf
      common /blok/ st
      common /blok1/ em,emt
      common /blnk/ cf
      common /nblk/ vf
      common /tblk1/ m
      common /tblk2/ endt
      common /block/ rte
      common /ovlk/ y0,y1,y2
      common /fblk/ f1,f2,f3,f4

      read(*,*),rf,cf,kf,vf,hdl1,hdh1,hdh2,hd2,l,dh,st,to,endt
      write(*,*),rf,cf,kf,vf,hdl1,hdh1,hdh2,hd2,l,dh,st,to,endt
      read(*,*),emt(1)
      em(1,1)=0
      do i=2,st+1
      read(*,*),em(i,1)
      write(*,*),em(i-1,1),'<=t<=',em(i,1)
      write(*,*),'Final Temperature:'
      read(*,*),emt(i)
      em(i,2)=(emt(i)-emt(i-1))/(em(i,1)-em(i-1,1))
      write(*,*),'Slope=',em(i,2)
      enddo
      read(*,*),a1,a2,a3,e1,e2,e3,dt,m,tf,td
C     write(*,*),a1,a2,a3,e1,e2,e3,dt,m,tf,td
      do i=1,5
      read(*,*),b(i)
```

```
      enddo
      dx=l/m
      do i=1,5
      read(*,*), templ(i)
      enddo
C     open(unit=10,status='unknown',file='n4.m')
      open(unit=11,status='unknown',file='n5.m')
      open(unit=12,status='unknown',file='n6.m')
C     write(*,*),dx
      call unimwp(b(1),b(2),b(3),b(4),b(5),l,m,rte,ptot)
      do i=1,72
      pc(i)=0
      enddo
      dh=dh/to
      do 10 i = 1,m+1
      y0(i)=1.00
      y1(i)=1.00
      y2(i)=1.000
      x(i)=0.0000
      x1(i)=0.0000
      x2(i)=0.0000
      x3(i)=0.0000
10    continue
      t=0
      tdt=0
      timcnt=1
      yin=emt(1)/to
      do i=1,m+1
      do j=1,m+2
      y3(i,j)=0.00
      enddo
      enddo
      write(12,*),'tt=['
      write(11,*),'xt=['

C
C     Start Loop In Time
C
      do while (t.LE.tf)
      if (t.GT.0) then
      call powst(y2,pc)
      else
      call powst(y1,pc)
      endif
```

```
      if (abs(t-tdt).LT.1.0e-6) then
C     write(*,*)
C     write(*,11),t
11    format(5X,'Time :',F12.4)
C     write(*,12)
C     write(*,*),'Cure Temp',yin*to
12    format (5X,'Distance',8X,'Cure',9X,'Temperature',4X,'Power',4X,'Rate')
C     write(10,13),int(100*t/60)
13    format ('txd',I5,'=[')

write(11,48),t/60.00,x(int(templ(1)/dx)+1),x(int(templ(2)/dx)),x(int(templ(3)/dx)),
x(int(templ(4)/dx)),x(int(templ(5)/dx))
14    format(F12.3,' ',F10.6,' ',F10.6,' ',F10.6)
      if (t.GT.0) then
      write(12,48),t/60.00,to*y2(int(templ(1)/dx)+1)-273.15,to*y2(int(templ(2)/dx))
-273.15,to*y2(int(templ(3)/dx))-273.15,to*y2(int(templ(4)/dx))-273.15,to*y2(int(templ
(5)/dx))-273.15,pc(1)
      else
       write(12,48),t/60.00,to*y1(int(templ(1)/dx)+1)-273.15,to*y1(int(templ(2)/dx))
-273.15,to*y1(int(templ(3)/dx))-273.15,to*y1(int(templ(4)/dx))-273.15,to*y1(int(templ
(5)/dx))-273.15,pc(1)
      endif
48    format(F12.3,1X,F8.3,1X,F8.3,1X,F8.3,1X,F8.3,1x,F8.3,1x,F8.3)
      do i=1,m+1
      if (t.GT.0) then
C     write(*,15),(i-1)*dx,x(i),to*y2(i),pc(i),r2(i)
C     write(10,20),to*y2(i),x(i)
      else
C     write(*,15),(i-1)*dx,x(i),to*y1(i),pc(i),r1(i)
C     write(10,20),to*y1(i)-273.15,x(i)
      endif
15    format (5X,F8.5,5X,F8.5,5X,F12.5,5X,F8.5,5X,F8.5)
20    format (F10.6,1X,F12.6)
      enddo
C     write(10,*),'];'
      tdt=tdt+td
      endif

      if (t.GT.0) then
      cntr=0
      sudt=0
      dt1=dt
      error1=100
       do while (sudt.LT.dt)
```

```
      do i=1,m+1
      y5(i)=y2(i)
      xt(i)=x(i)
      call rate(y2(i),x(i),r2(i))
      enddo
      dmt=2*dt1/(3*(dx**2.0))
      o=0
      error=0
       do while (((o.EQ.0).OR.(error.GT.1.0e-4)).AND.(o.LE.50))
           call powst(y5,pc)
            do i=1,m+1
            y4(i)=y5(i)
            xt1(i)=xt(i)
            call rate(y5(i),xt(i),r3(i))
            r4(i)=1.0/3.0*(r1(i)+r2(i)+r3(i))
            enddo
            yav3=0.50*(y2(2)+y2(1))
            xav3=0.50*(x(2)+x(1))
            call Th(yav3*to,xav3,kav3)
            call Th(y2(1)*to,x(1),kav)
            call prod(y2(1)*to,x(1),p2,wf,d1)
            diff=to*abs(yin-y2(1))
      if (diff.LE.27) then
      hd1=hdl1
      endif
      if ((diff.LE.43).AND.(diff.GT.27)) then
      hd1=hdh1
      endif
      if (diff.GT.44) then
      hd1=hdh2
      endif
      y3(1,1)=(dmt*(2*dx*hd1+kav3+kav)+p2)
      y3(1,2)=-y5(2)*(kav3+kav)*dmt
      y3(1,m+2)=p2*y1(1)+dmt*((y2(1)+y1(1))*(-2*dx*hd1-(kav+kav3))+
(kav+kav3)*(y2(2)+y1(2))+6*yin*hd1*dx)-2*dt*r4(1)*dh*(1-wf)*d1+2*dt*pc(1)/to
      y5(1)=(y3(1,m+2)-y3(1,2))/y3(1,1)

      do i=2,m
      yav1=0.50*(y2(i)+y2(i+1))
      yav2=0.50*(y2(i)+y2(i-1))
      xav1=0.50*(x(i)+x(i+1))
      xav2=0.50*(x(i)+x(i-1))
      call Th(yav1*to,xav1,kav1)
      call Th(yav2*to,xav2,kav2)
```

```
      call prod(y2(i)*to,x(i),p1,wf,d1)
C     write(*,*),kav1,kav2,p1,wf,d1,r1
      y3(i,i-1)=-kav2*dmt*y5(i-1)
      y3(i,i)=p1+dmt*(kav1+kav2)
      y3(i,i+1)=-dmt*kav1*y5(i+1)
      y3(i,m+2)=dmt*(kav1*(y2(i+1)+y1(i+1))-(kav1+kav2)*(y2(i)+y1(i))+
kav2*(y2(i-1)+y1(i-1)))-2*dt*r4(i)*dh*(1-wf)*d1+p1*y1(i)+2*dt*pc(i)/to
      y5(i)=(y3(i,m+2)-y3(i,i-1)-y3(i,i+1))/y3(i,i)
      enddo

      yav3=0.50*(y2(m+1)+y2(m))
      xav3=0.50*(x(m+1)+x(m))
      call Th(yav3*to,xav3,kav3)
      call Th(y2(m+1)*to,x(m+1),kav)
      call prod(y2(m+1)*to,x(m+1),p2,wf,d1)
C     write(*,*),kav3,kav,p2,wf,d1,r2
      y3(m+1,m+1)=dmt*(2*dx*hd2+kav+kav3)+p2
      y3(m+1,m)=-dmt*(kav3+kav)*y5(m)
      y3(m+1,m+2)=p2*y1(m+1)+dmt*((y2(m+1)+y1(m+1))*
(-2*dx*hd2-(kav+kav3))+(kav+kav3)*(y2(m)+y1(m))+6*yin*hd2*dx)-2*dt*r4(m+
1)*dh* (1-wf)*d1+2*dt*pc(m+1)/to
      y5(m+1)=(y3(m+1,m+2)-y3(m+1,m))/y3(m+1,m+1)
      error=0
      call cure(timcnt,y5,xt1,m+1,dt1,xt)
      do i=1,m+1
      if (error.LE.abs((y5(i)-y4(i))/y5(i))) then
      error=abs((y5(i)-y4(i))/y5(i))
      endif
      if (xt(i).GT.1.0e-7) then
      if (error.LE.abs((xt(i)-xt1(i))/xt(i))) then
      error=abs((xt(i)-xt1(i))/xt(i))
      endif
      endif
      enddo
      o=o+1
      enddo

      if (o.GT.100) then
      if(error1.LE.error) then
      goto 21
      else
      dt1=dt1/2
      error1=error
      cntr=cntr+1
```

```
      endif
      else
21    sudt=sudt+dt1
      do i=1,m+1
      x1(i)=x2(i)
      x2(i)=x3(i)
      x3(i)=x(i)
      x(i)=xt(i)
      y0(i)=y1(i)
      y1(i)=y2(i)
      y2(i)=y5(i)
      r1(i)=r2(i)
      r2(i)=r3(i)
      if (timcnt.GT.3) then
      f1(i)=f2(i)
      f2(i)=f3(i)
      f3(i)=f4(i)
      endif
      enddo
      timcnt=timcnt+1
      endif
C     write(*,*),o,' ',error,' ',dt1,' ',sudt
      enddo
      endif
C
            if (t.EQ.0) then
            call cure(timcnt,y1,x,m+1,dt,xt)
            do i=1,m+1
            x1(i)=x2(i)
            x2(i)=x3(i)
            x3(i)=x(i)
            x(i)=xt(i)
            call rate(y1(i),x(i),r1(i))
            enddo
            call powst(y1,pc)
            dmt=dt/(2*(dx**2.0))
            yav3=0.50*(y1(2)+y1(1))
            xav3=0.50*(x(2)+x(1))
            call Th(yav3*to,xav3,kav3)
            call Th(y1(1)*to,x(1),kav)
            call prod(y1(1)*to,x(1),p2,wf,d1)
            diff=to*abs(yin-y1(1))
            if (diff.LE.27) then
            hd1=hdl1
```

```
                endif
                if ((diff.LE.43).AND.(diff.GT.27)) then
                hd1=hdh1
                endif
                if (diff.GT.44) then
                hd1=hdh2
                endif
                y3(1,1)=dmt*(+2*dx*hd1+kav+kav3)+p2
                y3(1,2)=-dmt*(kav3+kav)
                y3(1,m+2)=y1(1)*(p2-dmt*2*dx*hd1-(kav3+kav)*dmt)+
dmt*(kav3+kav)*y1(2)+4*yin*hd1*dx*dmt-d1*(1-wf)*dt*r1(1)*dh+dt*pc(1)/to

                do i=2,m
                yav1=0.50*(y1(i)+y1(i+1))
                yav2=0.50*(y1(i)+y1(i-1))
                xav1=0.50*(x(i)+x(i+1))
                xav2=0.50*(x(i)+x(i-1))
                call Th(yav1*to,xav1,kav1)
                call Th(yav2*to,xav2,kav2)
                call prod(y1(i)*to,x(i),p1,wf,d1)
                y3(i,i-1)=-kav2*dmt
                y3(i,i)=p1+dmt*(kav1+kav2)
                y3(i,i+1)=-dmt*kav1

y3(i,m+2)=dmt*(kav1*(y1(i+1))-(kav1+kav2)*(y1(i))+kav2*(y1(i-1)))-
d1*(1-wf)*dt*r1(i)*dh+p1*y1(i)+dt*pc(i)/to
                enddo

                yav3=0.50*(y1(m+1)+y1(m))
                xav3=0.50*(x(m+1)+x(m))
                call Th(yav3*to,xav3,kav3)
                call Th(y1(m+1)*to,x(m+1),kav)
                call prod(y1(m+1)*to,x(m+1),p2,wf,d1)
                y3(m+1,m+1)=dmt*(2*dx*hd2+kav+kav3)+p2
                y3(m+1,m)=-dmt*(kav3+kav)

y3(m+1,m+2)=p2*y1(m+1)+dmt*((y1(m+1))*(-2*dx*hd2-(kav+kav3))+
(kav+kav3)*(y1(m))+4*yin*hd2*dx)-d1*(1-wf)*dt*r1(m+1)*dh+dt*pc(m+1)/to
                call mat(y3,m+1,y2)
                timcnt=timcnt+1
                endif
        t=t+dt
        call tinp(t,dt,yin*to,tin)
        yin=tin/to
```

```
enddo
write(12,*),'];'
write(11,*),'];'
close(10)
close(11)
close(12)
end

subroutine Th(a,x,k1)
double precision a,x,k1,kf,km
common /blk2/ kf
km=(0.161+x*(0.00147*a-0.417))/100
k1=(0.02514*km)/(.02514+km)
return
end

subroutine prod(y,x,ret1,ret2,ret3)
double precision y1,x1,y,x,r2,rho,sp,ret1,ret2,ret3
y1=y
x1=x
call den(y1,x1,rho)
call Cp(y1,x1,sp,r2)
ret1=rho*sp
ret2=r2
ret3=rho
return
end

subroutine den(a,x,ret)
double precision a,ret,rf,x
common /blk5/ rf
ret=rf
return
end

subroutine Cp(a,x,ret1,ret2)
double precision rf,tem,vf,cf,a,x,ret1,ret2
common /blnk/ cf
common /blk5/ rf
common /nblk/ vf
call den(a,x,tem)
ret2=tem*vf/rf
ret1=cf
return
```

```
      end

      subroutine tinp(ti,dt,yp,re)
      double precision yp,ti,dt,re,em(10,2),emt(10)
      integer fnd,i,st
      common /blok/ st
      common /blok1/ em,emt
      i=2
      fnd=0
      do while((i.LE.st+1) .AND. (fnd.EQ.0))
      if ((ti.GE.em(i-1,1)) .AND. (ti.LE.em(i,1))) then
      re=yp+dt*em(i,2)
      fnd=1
      endif
      i=i+1
      enddo
      if (ti.GT.em(st+1,1)) then
      re=yp+dt*em(st+1,2)
      endif
      return
      end


      subroutine powst(yd,px)
      implicit none
      double precision a1,a2,a3,e1,e2,e3,tdx,endt,to,yd(72),px(72),ptot,mxa,rte(72)
      integer i,m
      common /blk1/ a1,a2,a3,e1,e2,e3,to
      common /tblk1/ m
      common /tblk2/ endt
      common /block/ rte
      mxa=yd(1)*to
      do i=2,m+1
      if (mxa.LE.to*yd(i)) then
      mxa=to*yd(i)
      endif
      enddo
C     write(*,*), mxa
      if (mxa.GE.endt) then
      do i=1,m+1
      px(i)=0
      enddo
      endif
      if (mxa .LT. endt) then
```

```
      do i=1,m+1
      px(i)=rte(i)
      enddo
      endif
C     write(*,*),px(1),px(5),px(m+1)
      return
      end


      subroutine cure(j,t,x,n,h,xi)
      integer n,i,j
      double precision temp2,f1(72),f2(72),f3(72),f4(72),con,t(72),x(72),xi(72),h,
x1(72),x2(72),x3(72),tm1(72),tm2(72),tm3(72),nx(72),orr
      common /blk3/x1,x2,x3
      common /ovlk/ tm1,tm2,tm3
      common /fblk/ f1,f2,f3,f4
      con=1.0/sqrt(2.0)
      if (j.LE.3) then
      do i=1,n
      call rate(t(i),x(i),f1(i))
      call rate(t(i),x(i)+0.50*h*f1(i),f2(i))
      call rate(t(i),x(i)+(con-0.50)*h*f1(i)+(1-con)*h*f2(i),f3(i))
      call rate(t(i),x(i)-con*h*f2(i)+(1+con)*h*f3(i),f4(i))
      Xi(i)=x(i)+h/6.0*(f1(i)+2*(1-con)*f2(i)+2*(1+con)*f3(i)+f4(i))
      if ((real(xi(i))-1.000).GE.1.0e-7) then
      xi(i)=1.0000
      endif
      enddo
      endif

      if (j.GT.3) then
      do i=1,n
      if (j.EQ.4) then
      call rate(tm1(i),x1(i),f1(i))
      call rate(tm2(i),x2(i),f2(i))
      call rate(tm3(i),x3(i),f3(i))
      endif
      call rate(t(i),x(i),f4(i))
      xi(i)=x1(i)+4.0*h/3.0*(2*f4(i)-f3(i)+2*f2(i))
      orr=1000
      do while(orr.GT.1.0e-2)
      nx(i)=xi(i)
      call rate(t(i),nx(i),temp2)
      xi(i)=x3(i)+h/3.0*(temp2+4*f4(i)+f3(i))
```

```
orr=abs((xi(i)-nx(i))/xi(i))
enddo
if ((real(xi(i))-1.000).GE.1.0e-10) then
xi(i)=1.0000
endif
enddo
endif
return
end

subroutine  rate(y,x,ra)
double precision a1,a2,a3,e1,e2,e3,to,y,x,ra
common /blk1/ a1,a2,a3,e1,e2,e3,to
double precision k2,k3,k4,R
R=8.314
if ((real(x)-1.000).LT.1.0e-8) then
k2=a1*exp(-e1/(R*y*to))
k3=a2*exp(-e2/(R*y*to))
k4=a3*exp(-e3/(R*y*to))
if (x.LE.0.30) then
ra=((k2+k3*x)*(1-x)*(0.47-x))
else
ra=(k4*(1-x))
endif
endif
if ((real(x)-1.000).GE.1.0e-10) then
ra=0.0000
endif
return
end
```

REFERENCES

1. N. Vlahakis and D. Van Dorn, 25th joint Propulsion Conference, Monterey, CA, July, (1989).

2. B. Tittmann, MRS Bulletin, April, p. 21, (1988).

3. J. Wei, J. Jow, J.D. DeLong, and M.C. Hawley, SAMPE Journal, 27 (1),33 (1991).

4. W.I. Lee and G.S. Springer, J. Composite Materials, 18, p. 387 (1984).

5. J. Wei, Y. Chang, B. Thomas, and M.C. Hawley, Proceeding of ICCM/VIII, 1, 10-L (1991).

6. Agrawal, R. and L. T. Drazl, J. Adhesion, (1989).

7. J. Jow, Ph.D dissertation, Chem. Eng. Depart., MSU, (1988).

8. W.I. Lee and G.S. Springer, J. Composite Materials, 18, p. 357 (1984).

9. J. Wei, J. Jow, J.D. DeLong, and M.C. Hawley, 2nd Topical Conf. on Emerging tech. in mat., AIChE annual meeting, Nov. 1989, SF, CA.

10. J. Wei, J.D. DeLong, M. DeMeuse, and M.C. Hawley, "Comparison of Microwave and Thermal Cure of Epoxy Resins", Polym. Eng. & Sci. (in press) (1992).

11. J. Wei, B. Thomas, and M. C. Hawley, ANTEC'92, Detroit, May, (1992).

12. J. Wei, M. DeMeuse, and M. C. Hawley, ACS meeting, SF, CA, April, (1992).

13. J. Wei, B. Thomas, and M. C. Hawley, 37th Intern. SAMPE, Anaheim, CA, March, (1992).

14. U. Hottong, J. Wei, R. Dhulipala, and M.C. Hawley, Ceramic Transactions, 21, 587 (1991).

15. M.C. Hawley and J. Wei, MRS Symp. Proc. , 189, 413 (1990).

16. J. Wei, J.D. DeLong, and M.C. Hawley, Proceeding of 5th Amer. Soc. Comp., 239 (1990).

17. Larry Fellows and Martin C. Hawley, 37th Intern. SAMPE, Anaheim, CA, March, (1992).

18. J. Mijovic and J. Wijaya, Macromolecules, 23(15), 3677 (1990).

19. J. Mijovic, A. Fishbain, and J. Wijaya, Macromolecules, 25(25), 986 (1992).

20. A. Gourdenne, Proceedings, International Conference on reactive Proceeding of Polymers, p. 23, (1982).

21. J. Jow, J. DeLong, and M. C. Hawley, SAMPE Quart., 20(2), 46 (1989).

22. D. A. Lewis, J. C. Hedrick, T. C. Ward and J. E. McGrath, Polymer Preprint, 28(2), 330, (1987).

23. J. Jow, M. C. Hawley, M. Finzel, J. Asmussen, and R. Fritz, AIChE Conf. Emerg. Tech. Mat., Aug. (1987).

24. J. Jow, M. C. Hawley, and M. Finzel, Rev. Sci. Instr., 60(1), 96 (1989).

25. J.D. DeLong, J. Jow, and M.C. Hawley, AIChE 2nd Conf. Emerg. Tech. Mat., Nov, (1989).

26. Lewis,D.,T.Ward,J.Summers,and T.Ward,Polymer Prep., 29, 1 (1988).

27. G.L. Vogel, J. Jow, J.D. DeLong, and M.C. Hawley, Proc. Am. Soc. Comp. 4th Tech. Conf. Comp. Mat., Oct., (1989).

28. L. K. Wilson and J. P. Salerno, Technical Report, AVRADCOM TR-78-46, (1978).

29. Normans Strand, Modern Plastics, 54, 64 (1980).

30. A. Gourdenne et al., 3rd International Conference on Composite Materials, Paris, 2, 1514 (1980).

31. A. Gourdenne and Le Q. Van, Polymer Preprints, 22, 125 (1981).

32. E. Karmazsin and P. Satre, Thermochemics Acta, 93, 305 (1985).

33. J. Jow, M. C. Hawley, M. Finzel and T. Kern, Polym. Eng. Sci., 28, 1450 (1988).

34. Jullien, H., and H. Valot, Polymer, 26, 506 (1985).

35. J. Wei, Fabrication of experimental setup and procedure for microwave curing of AS4/3501-6 composite laminate, Research Complex, MSU, (1989).

36. J. Wei, V. Adegbite, Y. Chang, and M.C. Hawley, 6th annual ASM/ESD Advanced Comp. Conf./Exp., Session of Emerg. Struct. Comp. tech. I, Oct., (1990).

37. Chen, Y. F., and C. Y. C. Lee, Polym. Mat. Sci. Eng. (Am. Chem. Soc.) 60 (1989), 680-684.

38. J. Mijovic, and J. Wijaya, Polymer Composites, 11, 184 (1990).

39. E.E.W. Kassner,"Apparatus For the Generation of Short Electromagnetic Energy" U.S. Patent 2 109 843, Oct. 5, (1937).

40. M. Rothstein, "Dielectric Heating" in Encyclopedia of polymer science, vol 5., New York: Interscience Publisher, (1966).

41. R.W. Bruce, Mat. Res. Soc. Symp. Proc., 124, 3,(1988).

42. R.F. Harrington,"Time-Harmonic Electromagnetic Fields", McGraw-Hill Book Company,Inc., (1987).

43. C.C. Ku and R. Liepins, "Electrical Properties of Polymers: chemical principles", Macmillan Publishing Company, (1987).

44. P. Debye, Polar Molecules, Chemical Catalog Co., New York, Chap. V., (1929).

45. T.W. Gault and J.B. Wilson, "Radio Frequency Redrying of Veneer - A Case Study", J. Microwave Power, p.179, (1987).

46. Irving J. Chabinsky, Mat. Res. Soc. Symp., 124, 17, (1988).

47. G. Lightsey, et. al. , J. Microwave Power and Electromagnetic Energy, 23(1), 11 (1988).

48. Jean-Marie Thiebaut, C. Akyel, and G. Roussy, IEEE Trans. Instrum. Meas., 37(1), 114 (1988).

49. G. Lightsey, C. George, and L.D. Russell, J. Microwave Power, p.86, (1986).

50. R.D. Smith, EPRI Report EM-3645, (1984).

51. Stuart O. Nelson, J. Microwave Power, p.65, (1985).

52. J.P. Vetsuypens and W. Van Loock, J. Microwave Power, p.110, (1986).

53. N.S. Strand, Modern Plastics, p.64, (1980).

54. D.A. Lewis, MRS Symp. Proc., 269, L1.2 (1992).

55. W.H. Sutton, MRS Symp. Proc., 269, L1.1 (1992).

56. L. Dauerman, MRS Symp. Proc., 189, L3.3 (1990).

57. J. Suzuki, et. al, J. Microwave Power, 25(3), 168 (1990).

58. S.J. Oda, Inter. Microwave Power Inst., 26th Symp. Proc., Buffalo, NY, (1991).

59. S.J. Oda, MRS Symp. Proc., 269, L10.1, (1992).

60. R.J. Giguere, et. al, J. Tetrahedron Lett., 27, 4945 (1986).

61. R.N. Gedye, F.E. Smith, and K.C. Westaway, Can. J. Chem., 66, 17 (1987).

62. R.J. Giguere et. al, J. Tetrahedron Lett., 28, 6553 (1987).

63. R.J. Giguere, MRS Symp. Proc., 269, L11.1, (1992).

64. R.C. Collin, "Field Theory of Guided Waves", 2nd ed., IEEE Press, (1990).

65. Haw-Hwa Lin, Ph.D. dissertation, Michigan State University, (1989).

66. E. Karmazsin, P. Satre, and J. F. Rochas, Thermochimica Acta, 93, 305 (1985).

67. J.Brandrup, E.H.Immergut,polymer handbook,3rd edition John Wiley&sons,inc., (1989).

68. Turi, Edith, Thermal Characterization of Polymeric Materials, Academic Press Inc. (1981).

69. B.A. Rozenberg, Kinetics, Thermodynamics and Mechanism of Epoxy Oligomers with Amines. Advances in Polymer Science, Ed. K. Dusek, Part

II, 750, 113, (1985).

70. Acitelly,M.A.,Prime,R.B.,and Sacher,E.,Polymer,pp 335-342, 1971.

71. Hagnauer,G.L., Pearce, P.J., LaLiberte,B.R., and Roylance, M.E., Thermorheology of Thermosetting Polymers, pp 25-47, 1983.

72. Dutta, A. and Ryan, M.E., Journal of Applied Polymer Science, 24, 635 (1979).

73. Mijovic, J.,Journal of Applied Polymer Science, 31, 1177 (1986).

74. Moroni, A., Mijovic,J., Pearce, E.M., and Foun, C.C.,Journal of Applied Polymer Science, 32, 3761 (1986).

75. Sichina, W.J.,Dupont Company Applications Brief, No. TA-93.

76. J.K. Gillham, "Developments in Polymer characterization -3", J.V. Dawkins, p. 159, Applied Science, London (1982).

77. Sourour, S. and Kamal, M.R., Thermochimic Acta, 14, 41 (1976).
78. L. Schechter, J. Wynstra, and R.P. Kurkjy, Ind. Eng. Chem. 48, 94 (1956).

79. L.A. O'Neil and C.P. Cole, J. Appl. Chem. (London) 6, 356 (1956).

80. H. Dannenberg, Soc. Plast. Eng. Trans, 3, 78 (1963).

81. K. Horie, H. Hiura, M. Sawada, I. Mita, and H. Kambe, J. Polym. Sci., A-1, 8, 1337 (1970).

82. K. Dusek, M. Ilavsky, and S. Lunak, J. Polym. Sci. Polym. Symp., 53, 29 (1976).

83. C.C. Riccardi, H.E. Adabbo, and R.J.J. Williams, J. Appl. Polym. Sci., 29, 2481 (1984).

84. Mark Finzel, Ph.D. Dissertation, Michigan State University, 1991.

85. C.C. Riccardi and R.J.J. Williams, "Crosslinked Epoxies",B. Sedlacek, and J. Kahovec Eds., Walter de Gruyter & Co. NY, (1987).

86. Mark Finzel, Lab notes, Depart. Chem.Eng., MSU. (1989).

87. W.I. Lee, A.C. Loos and G.S. Springer, J. Comp. Mater., 16, 510 (1982).

88. I. Havlicek and K. Dusek,"Crosslinked Epoxies",B. Sedlacek, and J. Kahovec Eds., Walter de Gruyter & Co. NY, (1987).

89. E. Rabinowitch, Trans. Faraday Soc., 33, 1225 (1937).

90. M. Gordon, and W. Simpson, Polymer, 2(4), 383 (1961).

91. M.L. Williams, R.F. Landel, J.D. Ferry, J. Am. Chem. Soc., 77, 3701 (1955).

92. K.C. Rusch, J. Macromol. Sci-phys., B2(2), 179(1968).

93. G. Wisanrakkit and J.K. Gillham, Journal of Coatings Technology, 62(783), 35 (1990).

94. C.W. Macosko and D.R.Miller, Macromolecules, 9, 199 (1976).

95. Flory, P.J., Principles of Polymer Chemistry, Cornell unv. press., Ithacas,New York,1953.

96. D.R. Miller and C.W. Macosko, Macromolecules, 9(2), 206, (1976).

97. R.F.Boyer,Rubber Chem. Technol., 63, 1303 (1963).

98. Wisanrakkit, G.; Gillham,J.K. Polym. Mater. Sci. Eng., 59, 969 (1988).

99. Bair, H.E., Polym. Prepr. (Am.Chem.Soc., Div.Polym.Chem.), 26(1), 10 (1985).

100. W.H. Jo and K.J. Ko, Polym. Eng. Sci., 31(4), 239, Feb. (1991).

101. I. Havlick and K Dusek, in Crosslinked Epoxy, B. Sedlacek and J. Kahovec Eds. p417, De. Gruyter, Berlin, 1987.

102. DiBenedetto, A.T., J. Polym. Sci., Part B: Polym. Phys., 25(9), 1949 (1987).

103. J.P. Pascault and R.J.J. Williams, J. Polym. Sci., Part B: Polym. Phys., 28, 85 (1990).

104. E. Mertzel and J. Koening, Adv. Polym. Sci., Part B: Polym. Phys., 28, 85 (1990).

105. D.W. Schiering, J.E. Katon, L.T. Drzal, and V.B. Gupta, J. Appl. Polym.

Sci., 34, 2367 (1987).

106. A. Moroni, J. Mijovic, E.M. Pearce, and C.C. Foun, J. Appl. Polym. Sci., 32, 3761 (1986).

107. J.B. Enns, and J.K. Gillham, J. of Appl. Polym. Sci., 28, 2567 (1983).

108. P.G. Babayevsky, and J.K. Gillham, J. of Appl. Polym. Sci., 17, 2067 (1973).

109. J.K. Lee, and K.D. Pae, J. of Polym. Sci., part C: Polymer letters, 28, 323 (1990).

110. J. Galy, J.P. Pascault, and M.F. Grenier-Loustalot, in Crosslinked Epoxy, B. Sedlacek and J. Kahovec Eds., De. Gruyter, Berlin, 1987.

111. Bidstrup, S.A., Sheppard, N.F. Jr., and Senturia, S.D., Technical Report 8, Office of Naval Research, 1986.

112. M. DeMeuse, unpublished results.

113. N.F. Sheppard, Jr. and Senturia, Polym. Eng. & Sci., 26(5), 354 (1986).

114. Nielsen, L.E.,J. Macromol. Sci.-Revs. macromol. Chem., c3(1), 69, 1969.

115. S.M. Singer, J. Jow, J. DeLong and M.C. Hawley, Sampe Q. p14,Jan 1989.

116. S.Y. Lee and G.S. Springer, J. Composite Mater. vol. 22, 15, Jan 1988.

117. Asmussen. J., H. H. Lin, B. Manring and R. Fritz, Rev. Sci. Instrum. 58, p. 1477, (1987).

118. J. Jow, M.C. Hawley, M.C. Finzel, J. Asmussen, H.H. Lin, and B. Manring, IEEE, Microwave Theory and Techniques, 35(12), 1435 (1987).

119. J. Jow, M.C. Hawley, M.C. Finzel, and J. Asmussen, Rev. Sci. Instrum., 60, 1, p. 96, (1989).

120. W. I. Lee, A. C. Loos and G. S. Springer, J. Composite Material, 16, 510, (1982).

121. Threshold limit values and biological exposure indices for 1988-1989, American Conference of Governmental Industrial Hygienists, Cincinnati, Ohio,

p103, (1988).

122. A.L. VanKoughnett and J.G. Dunn, J. Microwave Power, 8 (1), 101 (1973).

123. J. Ippen, Rubber Chem. Technol., 44 (1), 294 (191).

124. C.S. Wang, Rubber Chem. Technol., 57 (1), 134 (1984).

125. Ben Manring, Ph.D. thesis, Michigan State University, (1992).

126. W.I. Lee and G.S. Springer, J. Comp. Mater., 17, 135 (1983).

127. W.M. Sun, unpublished results, MSU, 1990.

128. V. Volpe, J. Comp. Mater., 14, 189 (1980).

129. M.A. Morgan, D.L. Fisher, and E.A. Milne, IEEE Transaction on Antennas and Propagation, Ap-35(2), 191 (1987).

130. O. Hashimoto and Y. Shimizu, IEEE transactions on Microwave Theory and Techniques, MTT-34(11), 1202 (1986).

131. J.V. Beck and K.J. Arnold, "Parameter Estimation Engineering and Science", p410, John Wiley & Sons, Inc. (1977).

132. J. Wei, A. Sundaram, and M.C. Hawley, MRS Symp. Proc., 269, L11.8, (1992).

133. M.R. Dusi, et. al., J. Appli. Polym. Sci., 30, 1847 (1985).

134. M.L. Williams, R.F. Landel, and J.D. Ferry, J. Am. Chem. Soc., 77, 3701 (1955).

135. Y.A. Tajima, and D.G. Crozier, Polym. Engr. Sci., 28, 491 (1986).

136. T.H. Hou and J.M. Bai, "Chemoviscosity Modeling for Thermosetting Resin systems - III", NASA-CR-181718, NASA Langley Research Center (1988).

137. J.C. Halpin, A. Apicella, and L. Nicolais, Polymer Processing and Properties, G. Astarita and L. Nicolais, eds, Plenum Press, New York, p143, (1984).

138. E.N. Da C. Andrade, Phil. Mag., 17, 699 (1934).

139. F. Bueche, "physical Properties of Polymers", p.91, Interscience Publishers, New York (1962).

140. M.B. Roller, Polym. Engr. Sci., 15(6), 406 (1975).

141. M.R. Dusi, C.A. May, and J.C. Seferis, Organic Coatings and Applied Polymer Science Proceedings, 47, 635 (1982).

142. J.W. Lane, J.C. Seferis, and M.A. Bachmann, Polym. Eng. & Sci., 26(5), 346 (1986).

143. J.M. Kenny, SAMPE J. 27(2), 39 (1991).

144. D.R. Day, International SAMPE Symp., 31, 1095 (1986).

145. D.R. Day, T.J. Lewis, H.L. Lee and S.D. Senturia, J. Adhesion, 18, 73 (1985).

146. D. Kranbuehl, S. Delos, M. Hoff and L. Weller, International SAMPE Symp., 31, 1087 (1986).

147. P.R. Ciriscioli and G.S. Springer, International SAMPE Sypm., 31, 312 (1989).

148. Loos A.C., G.S. Springer, J. Comp. Mater. 17, 135 (1983).

149. Dave, R. J.L. Kardos and M.P. Dudukovic, Polym. Comp., 8, 29 (1987).

150. Gutowski, T.G., T. Morigaki, and Z. Cai, J. Comp. mater. 21, 172 (1987).

151. Lindt, J.T., SAMPE Quarterly, 5,14 (1982)

152. A. Pourstartip, G. Riahi, and G. Smith, Proceedings of ICCM/8, 10-G-3, Honolulu, (1991).

153. R. Dave, J. Comp. Mater., 24, 22 (1990).

154. Springer J. Comp. Mater., 16, 400 (1982)

155. R. Dave, J.L. Kardos, and M.P. DuDuKovic, Proc. of Amer. Soc. for Comp., p137, (1986).

156. A.R. Mallow, F.R. Muncaster and F.C. Campbell, Proc. of Amer. Soc. for Comp., p171, (1986).

157. J-B. Donnet and R.C. Bansal, Carbon Fibers, Marcel Dekker, Inc., New York, p151, (1984).

158. K.Y. Yoon, T.W. Kim, W.I. Lee, and E.J. Jun, Proc. of 6th ICCM & 2nd ECCM, vol. 1, p1.81, (1987).

159. A. Noordam et al. in "crosslinked Epoxies", B. Sedlacek and J. Kahovec eds., W. de Gruyter, Berlin, p373, (1987).

160. R.J.J. Williams et al., Polym. Eng. & Sci., 30(18), 1140 (1990).

161. I. Dobas et al., in "Crosslinked Epoxies", B. Sedlacek and J. Kahovec eds., p81, W. de Gruyter, Berlin, (1987).

162. T. Igarashi, et. al. , Polymer, 20, 301 (1979).

163. A.K. Srivastava and J.R. White, J. Appl. Polym. Sci., 29, 2155 (1984).

164. M.H. Loh and J.V. Beck, ASME winter annual meeting, Atlanta, GA, December, (1991).

165. T.A. Bogetti and J.W. Gillespie, Jr., J. Comp. Mat., 25, 239 (1991).

166. G. D. Smith, Numerical Solutions of Partial Differential Equations: Finite Difference Methods, 2nd ed., Oxford University Press, Oxford (1978).

167. B. Carnahan, H.A. Luther, and J.O. Wilkes, "Applied Numerical Methods", Robert E. Krieger Publishing Company, Inc. (1990).

168. J.M. Kenny, A. Trivisano, and L.A. Berglund, SAMPE J. 27(2),39 (1991).